Investigations of Complex Guidance Cues for Nerve Regeneration Using Novel *In Vitro* Platforms

By Celinda Michelle Kofron

Sc.B., Brown University, 2004

Submitted in partial fulfillment of the requirements for the degree of Doctor of Philosophy in Biomedical Engineering, a joint program in the Division of Biology and Medicine and the Division of Engineering, at Brown University

Providence, Rhode Island

May 2009

This dissertation by Celinda M. Kofron is accepted in its present form by the program in Biomedical Engineering, a joint program in the Division of Biology and Medicine and the Division of Engineering, as satisfying the dissertation requirement for the degree of Doctor of Philosophy.

Date _____ _____
Diane Hoffman-Kim, Ph.D., Director

Recommended to the Graduate Council

Date _____ _____
Jeffrey Morgan, Ph.D., Reader

Date _____ _____
G. Tayhas Palmore, Ph.D., Reader

Date _____ _____
Thomas Webster, Ph.D., Reader

Date _____ _____
Deanna Thompson, Ph.D., External Reader

Approved by the Graduate Council

Date _____ _____
Sheila Bonde, Dean of the Graduate School

Curriculum Vitae for Celinda Michelle Kofron

Date and Place of Birth

February 9, 1982, Warwick, RI

Education

Expected May 2008	Brown University, Providence, RI
	Ph.D. Biomedical Engineering
	Advisor: Diane Hoffman-Kim, Ph.D.
	Title of Dissertation: Investigations of Complex Guidance Cues for Nerve Regeneration Using Novel *In Vitro* Platforms
May 2004	Brown University, Providence, RI
	Sc.B. Biomedical Engineering with Honors
	Concentration Advisor: Michael Lysaght, Ph.D.
	Research Advisor: Edith Mathiowitz, Ph.D.
	Title of Thesis: The Effects of Surfactants on the Physical Properties of Poly(fumaric-co-sebacic anhydride) Microspheres Fabricated with Phase Inversion Nanoencapsulation
June 2000	Coventry High School, Coventry, RI
	Valedictorian

Fellowships and Awards

2009	Sigma Xi Scientific Honor Society – Full Membership
2008	Sigma Xi Scientific Honor Society – Student Membership American Association of University Women Selected Professions Dissertation Writing Fellowship
2004	Brown University – University Fellowship
1999	Yale Science and Engineering Science Fair Award Rensselaer Polytechnic Institute Mathematics and Science Medal

Publications

Journal Articles

- **Kofron CM** and Diane Hoffman-Kim. Optimization by response surface methodology of confluent aligned monolayers of glial and non-glial cells. Submitted, 2009.
- **Kofron CM**, Fong VF, and Hoffman-Kim D. Neurite outgrowth at the interface of 2D and 3D growth environments. *Journal of Neural Engineering* 6: 12pp, 2009.
- Li GN, Livi LL, **Gourd CM**, Deweerd ES, and Hoffman-Kim D. Genomic and morphological changes of neuroblastoma cells in response to three-dimensional matrices. *Tissue Engineering* 13: 1035-1047, 2007.
- Furtado S, Abramson D, Burrill R, Olivier G, **Gourd C**, Bubbers E, and Mathiowitz E. Oral Delivery of Insulin Loaded Poly(fumaric-co-sebacic) Anhydride Microspheres. *Int J Pharmaceutics* 347 (1-2): 149-155, 2007.

Abstracts

- Nath N, Zhang P, **Kofron C**, King M, Hoffman-Kim D, and Mende U. Cardiac Myocyte Behavior in Micropatterned and Continuously Paced Short-term Cultures. *International Society for Heart Research,* May 2009.
- Nath N, Zhang P, **Kofron C**, King M, Hoffman-Kim D, and Mende U. Novel in Vitro Culture Model for Cardiac Myocyte Investigation. *New England Science Symposiom,* April 2009.
- Kim K, Richardson J, Kim S, **Kofron C**, Hoffman-Kim D, and Palmore GTR. Electrical stimulation of nerve cells: Image analysis of cell behavior. *Materials Research Society Fall Meeting,* December 2008.
- Johnson C, **Kofron C**, and Hoffman-Kim D. Combination of Schwann cell topography and patterned chondroitin sulfate proteoglycans influences dorsal root ganglia neuron growth. *Annual Meeting of the Biomedical Engineering Society,* October 2008.
- Richardson J, Kim K, **Kofron C**, Kim S, Hoffman-Kim D, and Palmore GT. Neurite outgrowth in repsonse to electrical and molecular cues. *Annual Meeting of the Biomedical Engineering Society,* October 2008.
- **Kofron CM**, Pallay JE, and Hoffman-Kim D. Biomimetic materials presenting Schwann cell topography direct growth of neurons and support cells. *Annual Meeting of the Biomedical Engineering Society,* October 2008.
- **Kofron CM**, Rollo JC, Johnson CM, Bruder JM, and Hoffman-Kim D. Neurite outgrowth on aligned glial cell topographies. *35th New England Complex Fluids Meeting,* June 2008.
- Richardson J*, Kim K-M*, **Kofron C***, Kim SY, Hoffman-Kim D, and Palmore GT (*co-first authors). Novel platform to assess neurite outgrowth in response to multiple cues. *34th Annual Northeast Bioengineering Conference,* April 2008.
- **Kofron CM**, Rollo JC, Johnson CM, Bruder JM, and Hoffman-Kim D. Alignment of glial cell topographies for directed neurite outgrowth. *34th Annual Northeast Bioengineering Conference,* April 2008.
- **Gourd C**, Rollo J, Bruder J, and Hoffman-Kim D. Neurite outgrowth on aligned glial cell topographies. *Annual Meeting of the Biomedial Engineering Society*, September 2007.
- **Gourd C**, Fong V, and Hoffman-Kim D. Neuronal growth at the interface of 2D and 3D cues. *Annual Meeting of the Biomedical Engineering Society*, October 2006.

- **Gourd C**, Fong V, and Hoffman-Kim D. Neurite outgrowth in response to micropatterned molecular cues and three dimensional matrices. *Annual Meeting of the Society for Biomaterials*, April 2006.
- **Gourd C**, Deweerd E, Livi L, Li G, and Hoffman-Kim D. Genomic and morphological analysis of human neuroblastoma cell growth in three-dimensional matrices. *Annual Meeting of the Society for Biomaterials*, April 2006.
- Furtado S, Burrill R, Reineke J, Morello AP, Harrison M, Olivier G, **Gourd C**, Qian H, Jong Y, and Mathiowitz E. A Method to Investigate the Stability of Poly(fumaric-co-sebacic) anhydride (p(FASA)) microspheres. *Annual Meeting of the Controlled Release Society,* November 2005.
- Furtado S, Burrill R, Reineke J, Morello A, Harrison M, Olivier G, **Gourd C**, Qian H, and Mathiowitz E. Oral Delivery of Insulin Microspheres to Type 1 Diabetic Dogs. *Annual Meeting of the Controlled Release Society*, November 2005.

Manuscripts in progress

- **Kofron CM**, Liu Y-T, Rollo JR, Pallay JE, and Hoffman-Kim D. Anisotropic biomimetic and bioinspired topographies guide neurite outgrowth. In preparation, 2009.
- **Kofron CM***, Johnson CM*, Bruder JM*, Lee AP, and Hoffman-Kim D (*co-first authors). Combinations of Schwann cell topography and patterned molecular cues influence neuron growth. In preparation, 2009.
- Nath N*, Zhang P*, **Kofron C**, King M, Hoffman-Kim D, and Mende U (*co-first authors). Cardiac Myocyte Behavior in Micropatterned and Continuously Paced Short-term Cultures. In preparation, 2009.

Professional Affiliations

- Biomedical Engineering Society
- Society for Biomaterials

Teaching Experience

Undergraduate Research and Honors Thesis Mentor in Neuroscience and Biomedical Engineering, Brown University

- Christina Johnson, Summer 2007-present, Biomedical Engineering Honors Thesis Title: *Combinations of Schwann cell topography and patterned proteins influence dorsal root ganglia growth and alignment,* presented at fall meeting of Biomedical Engineering Society 2008, author of manuscript in progress and three abstracts
- Carmichael Ong, Summer 2008
- Jennifer Pallay, Summer 2007-Spring 2008, Biomedical Engineering Honors Thesis Title: *Investigations of Cellular Growth on Biomimetic Materials Presenting Schwann Cell Topography*, presented at fall meeting of Biomedical Engineering Society 2007, author of manuscript in progress and one abstract

- Johnathon Rollo, Summer 2006-Spring 2007, Neuroscience Honors Thesis Title: *Neurite Alignment in Response to Cellular Topography*, author of manuscript in progress and three abstracts
- Vivian Fong, Summer 2005-Spring 2006, Biomedical Engineering Honors Thesis Title: *Neurite Outgrowth in Response to Micropatterned Molecular Cues and Three-Dimensional Matrices*, author of published manuscript and two abstracts

Teaching Assistant, Brown University

- Tissue Engineering (BI114), Diane Hoffman-Kim, Spring 2007
- Biotechnology Management (BI8), Michael Lysaght & Barrett Bready, Spring 2006
- Biotechnology in Medicine (BI17), Michael Lysaght & Edward Hawrot, Fall 2005
- Foundations of Living Systems (BI10), Kenneth Miller and John Stein, Spring 2003, Spring 2004
- Genetics (BI47), Jeffrey Laney and Michael McKeown, Fall 2003
- Computer Control of Scale Model Vehicles, Jerry Daniels, Summer 2003
- Genetics (BI47), Marc Tatar and Arthur Landy, Fall 2002
- Foundations of Living Systems (BI20), Peter Heywood, Jonathan Waage, and John Stein, Spring 2002

Partnerships and Research Investigations with Mathematicians, Engineers, and Scientists (PRIMES)

- Development of after-school science clubs at Citizens Memorial Elementary, Harris Elementary, and Kevin K. Coleman Elementary schools in Woonsocket, RI 2007-2008
- Development of after-school science club at Harris Elementary school in Woonsocket, RI 2008-2009

Interests and Activities

Ultimate Frisbee

- Member of RI People's Ultimate League, 2002-present (captain 2004)
- Member of Tandem, a nationally ranked coed club team, 2006-present
- Brown University women's team assistant coach, 2008
- Ultimate Players Association Southern New England Sectionals Coordinator, Spring 2004-2008
- Member of Brown's nationally ranked women's team Disco Inferno, 2001-2006

Acknowledgements

First, I would like to thank Diane Hoffman-Kim for being a wonderful mentor and role model in the last five years. I have truly grown as a scientist and as a person under her influence. There have often been times when she has shown more faith, support, and trust in me than I have shown in myself. I am thankful for her patience, encouragement, and advice, and I consider myself very fortunate to have had the opportunity to not only be part of her laboratory and research program but to also have been under her personal tutelage.

I would also like to thank my thesis committee – Jeffrey Morgan, Tayhas Palmore, Thomas Webster, and Deanna Thompson – for their generosity in spending time evaluating my work and for their valuable scientific and professional advice.

I would also like to thank my past mentors Michael Lysaght and Edith Mathiowitz for beginning to shape my scientific perspective and skills as an undergraduate and for continuing to encourage and guide me as a graduate student.

I am thankful to all of the members of the Hoffman-Kim lab that I have collaborated and commiserated with over the last five years: George Aninwene II, Elke Bremus-Koebberling, Jan Bruder, Elizabeth Deweerd, Grace Li, Yu-Ting Liu, Liane Livi, Cristina Lopez-Fagundo, Jennifer Mitchel, Jennifer Pallay, and Julie Richardson. I have appreciated the wealth of knowledge, encouragement, and teamwork that we have all shared. I would especially like to thank Grace for her friendship and guidance. I would not have gotten this far personally or academically without her camaraderie. Also of particular mention are Jan, for patient technical assistance and helpful scientific

input; Jen and Julie, for serving as sound boards for my ideas; Cristina, Jenny, and UT, for bringing renewed spirit of exploration and teamwork to the lab this year; and Liane, for continuous encouragement and generosity.

The undergraduate students that I have worked with have been wonderfully gifted, energetic, and synergetic. Thank you, Vivian Fong, Johnathon Rollo, Jennifer Pallay, Christina Johnson, and Carmichael Ong, for your wealth of ideas and assistance.

I would also like to thank the Lysaght, Mathiowitz, and Morgan labs for friendship, support, and encouragement. I would especially like to thank Roshni Patel and Danya Decoteau for offering sound advice and allowing me to vent my frustrations.

I am tremendously thankful to my parents Peter and Susan Gourd, my grandparents Isidore and Clara Rondeau and Normand and Irma Gourd, my brother Nathan Gourd, and the rest of our family. Their sacrifices and support have given me great opportunities in my life. Their strength makes me stronger. Thanks for staying back and watching me shine.

Lastly, I would like to thank my husband Michael Kofron for limitless support and encouragement. This adventure has definitely been better together, and I look forward to facing whatever the future has in store for us together.

Contents

Figures

Tables

Chapter 1 Introduction

This work has focused on innovative platforms to investigate nerve regeneration. This project has integrated a comprehensive toolbox of engineering and biological techniques to bear on this problem, creating *in vitro* environments that are closer to *in vivo* than traditional tissue culture specifically addressing the important roles of topography and dimensionality of the human body in nerve repair. I have characterized the response of neurons to cues that have not previously been isolated such as cellular topography independent of cellular biochemical factors as well as the response of neurons to several combinations of cues that have each been studied extensively individually, but had not yet been characterized together. These studies provide insights into the neuronal response to complex, multi-cue environments informing future research in neurodevelopment and nerve guidance in post-injury environments.

The chapters of this thesis are presented in the style of sequential journal articles including Introduction, Materials and Methods, Results, Discussion, and Reference sections for each primary research chapter. The first chapter provides background and literature review of current strategies for neuronal guidance with a focus on the types of cues that are present in the post-injury environment and the strategies by which they have been investigated extensively *in vitro*.

The primary aim of Chapter 2 was to characterize and optimize alignment of glia and support cells for investigation of their topographical features as directive guidance cues. Novel application of the statistical experimental design method Design of Experiments and the experimental analysis method

Response Surface Methodology is described to improve efficiency and utility of determining optimal experimental conditions. This study also provided insights into the general mechanisms of cellular adhesion, alignment, and monolayer formation. The study has been submitted to the Cellular and Molecular Bioengineering.

Chapter 3 investigates the topographical features that encode critical guidance information to a navigating neuron, focusing on the topographical information presented by support cells and the capacity for these topographies to guide navigating neurons. Several anisotropic cellular topographies are shown to be sufficient for guiding neuronal growth despite distinct topographies and anisotropies presented by these materials.

Chapter 4 demonstrates the complex response of neurons to multi-cue environments. A hierarchy of directive cues is demonstrated. The roles of type of cue presented and the relative strength of each cue individually in determining the response of neurons to simultaneous presentation of these cues were investigated.

Chapter 5 characterizes the influence of 2D substrate bound molecular cues on neurite growth in conjunction with a more complex 3D environment. Insights into the spatial integration of permissive and inhibitory molecular cues and 3D architecture are described. This study was published in the Journal of Neural Engineering in 2009.

1.1 Specific aims

The lack of optimistic outcomes for spinal cord injury (SCI) patients lies in the fact that nerve regeneration does not occur spontaneously within the central nervous system (CNS). Inherent

differences between CNS and peripheral nervous system (PNS) post-injury environments explain their contrasting capacities for regeneration. While the Schwann cells (SCs) in the PNS provide supportive cues to regeneration in the post-injury environment, oligodendrocytes and reactive astrocytes in the CNS contribute inhibitory cues. The field of neural tissue engineering studies the cues neurons must be given to overcome this inhibitory post-injury environment and aims to generate therapies to improve the quality of life of SCI patients. Growing neurons *in vitro* and *in vivo* navigate complex environments by integrating a variety of cues, including diffusible factors, substrate-bound factors, electric and magnetic fields, and topographical features. *In vitro* systems for studying neuronal growth typically limit the cues presented to a single type of cue on a flat, two dimensional (2D) substrate; this may in turn limit the resulting growth and our ability to interpret that growth. The limitations of these methods lie in the poor approximation that the flatness of 2D surfaces provides of the complex three dimensional (3D) architecture neurons navigate *in vivo,* including astrocytes and their derived extracellular matrix (ECM) in the CNS and SCs and their derived basement membrane in the PNS. To determine their full potential as guidance cues *in vivo*, these cells and molecules must be evaluated in more complex 3D or topographical culture systems *in vitro*. My research focuses on incorporating these cues in *in vitro* platforms and presenting them to growing neurons. **Our working hypothesis is that neurons integrate multiple structural and chemical cues to make net growth decisions.** Our plan to test this hypothesis has three primary aims:

Aim 1: Determine which topographical features – dimension and/or shape – encode critical guidance information to navigating neurons.

Aim 1.1: Optimize the alignment of confluent monolayers of astrocytes, endothelial cells, and Schwann cells for the presentation of anisotropic cellular topography to navigating neurons.

Aim 1.2: Determine the topographical guidance information provided by optimally aligned astrocytes, endothelial cells, and Schwann cells and characterize the influence of biomimetic and bioinspired topography on cellular and neurite guidance.

Previous work has shown that neurons are guided by anisotropic tissue structures *in vitro* and *in vivo*, and neurons have been shown to respond to topographical features in their environment as narrow as 50 nm, as wide as 100 μm, as shallow as 14 nm, and as deep as 40 μm. Previous studies used simple geometries of curves (fibrils) or 90° angles, and recent work in our lab showed guidance by polymer replicas presenting aligned SC topographies. A systematic analysis of topographical parameters that influence neurite growth has not previously been carried out. It is well recognized that the different chemical cues presented by SCs and astrocytes after injury contribute to the varied capacities for regeneration in the PNS and CNS. This work will reveal the contribution of physical features of these distinct glia to the promotion of axon regrowth and guidance. We will also look at a non-glial cell type, endothelial cells (ECs), to determine if anisotropy of any tissue or cell type is sufficient for neuronal guidance or if a glial phenotype is necessary. We will generate comparable confluent and aligned monolayers of SCs, astrocytes, and ECs. The influence of protein patterning parameters on cellular confluence and alignment will be statistically modeled and analyzed quantitatively, and optimal conditions will be determined for each cell type. Biomimetic materials that reproduce astrocyte, EC, and SC topography with nanoscale resolution will then be generated. These poly(dimethylsiloxane) (PDMS) substrates will be characterized for degree of alignment, length, height, width, and frequency of features using scanning electron microscopy, white light interferometry, and phase and fluorscence microscopy. Further, we aim to generate substrates with a comprehensive array of features in order to determine the topographical parameters that guide neurite outgrowth. We will use computer assisted design and lithography to fabricate PDMS materials with topographies ranging from simple plateaus and grooves to complex geometries that mimic cellular features. We will evaluate the growth of dorsal root ganglia (DRG) on all of these topographical substrates with phase contrast, immunofluorescence, and confocal microscopy in order to investigate the ability of these topographical features to guide axon growth.

Aim 2: Determine conditions necessary for biomimetic materials presenting cellular topographies to influence neuron guidance when presented with conflicting substrate bound molecular cues.

Aim 2.1: Compare LN and CSPG directive cues for their capacity for competition, synergy, and balance with biomimetic materials presenting SC topography.

Aim 2.2: Determine if there exists a set of conditions where the cellular topography dominates over chemical patterning, and neurons preferentially align to the underlying topography.

Neuronal response to individual cues has been studied extensively. Studies of complex, multi-cue environments are imperative for understanding the decisions neurons make *in vivo*. We will investigate the additive and hierarchical effects of combinations of permissive or inhibitory molecular cues and biomimetic materials presenting topography on directed neuronal growth. 50 μm stripes of permissive laminin (LN, 50 μg/ml) or a mix of inhibitory chondroitin sulfate proteoglycans (CSPGs, 10 μg/ml) and LN (50 μg/ml) will be micro-contact printed on PDMS biomimetic replicas presenting SC topography. LN or CSPG/LN will be patterned either parallel or perpendicular to aligned SC topography. Platforms with a single directive cue will include LN or CSPG/LN coated SC topographical replicas and flat PDMS patterned with LN or CSPG/LN. Flat PDMS with LN or CSPG/LN coating will be non-directive controls. We will evaluate the growth of DRG on these substrates with phase contrast and immunofluorescence in order to investigate the relative abilities of these cues to guide axon growth. We will also investigate the effects of protein concentration, pattern dimensions, and pattern type on the preference of neurons to align on directive biomimetic replicas. Larger stripes of permissive LN (500 μm), smaller spaces between stripes of LN (10 μm), or repeating geometries inspired by the features of aligned SCs will be micro-contact printed either perpendicular to aligned SC topography or on flat PDMS with lower concentrations of LN (5 or 10 mg/ml), and DRG cells will again be cultured for 5 days.

Aim 3: Characterize the influence of 2D substrate bound molecular cues on neurite growth in conjunction with a more complex 3D environment.

Parallel stripes of substrate bound guidance proteins presented on 2D substrates can align neurites *in vitro*. This classic cell culture approach does not reflect the complex 3D environment neurons must navigate *in vivo*. We and others have observed differences in the gene expression and morphology of neurons grown in 2D versus 3D. For example, neurite extensions within a 3D collagen matrix were longer than on a 2D collagen substrate. Effects of dimensionality on neurite outgrowth have been shown, but the effects of dimensionality on the ability of neurons to interpret guidance cues have not been investigated. To determine their full potential as guidance molecules *in vivo*, these molecules must be evaluated in more complex 3D culture systems *in vitro*. We have developed a novel cell culture system which combines microcontact printing of guidance proteins with collagen I matrices in order to culture cells at the interface of 2D chemical and 3D structural cues (hereafter, "interface cultures"). This method will allow us to present these cues simultaneously. We will use lithography to fabricate silicon wafers as templates for poly(dimethyl siloxane) (PDMS) microstamps for microcontact printing of 2D tracks of proteins which promote (LN) or inhibit (CSPGs) neurite extension. DRG will be cultured at the interface of a 2D substrate and a 3D matrix in a novel cell culture system. Neurite outgrowth will be assessed under phase contrast and confocal microscopy, and a customized analysis system will be developed to compare neurite outgrowth across conditions.

At the conclusion of this project, we will have characterized the response of neurons to several platforms that are a better representation of the *in vivo* nervous system than those studied in the past. We will have characterized the topographical guidance information presented by astrocytes, ECs, and SCs as well as distinguished the substrate architecture necessary to promote adhesion and guidance from those which do not guide outgrowth. We will have determined the relative contribution of biochemical cues and biomimetic cellular topographies to direct nerve growth.

Finally, we will have insights into the spatial integration of permissive or inhibitory substrate bound cues and 3D architecture by growing neurons. Significantly, these findings will increase the understanding of neuronal response to structurally complex environments and allow future biomaterials to be designed with these principles in mind.

1.2 Relevance

> "… a neuroblast, though being the source of the axon, cannot also provide its itinerary. A growing nerve fiber has no inherent tendency to move in any particular direction at certain points, not to branch and terminate after having reached a certain length. For all these actions it is dependent on directive influences of the environment, and its own endowment in this respect consists merely of the faculty of letting itself be guided."
>
> -Weiss 1939[1]

The nervous system is a magnificently complex, intricate network of cells that communicate information about surroundings and self, process this information, and cause reactions to one's surrounding and self. Neurons are the processors and transmitters of information in the nervous system, but in order for this intricate network to be formed and maintained, neurons must be triggered to grow, follow the directed path, and connect or reconnect to the appropriate targets. Neurons are often recognized for their highly developed pathfinding ability, but in any part of the nervous system, during development or after the challenge of injury, the itinerary provided by its local environment is essential and extremely complex. Navigating neurons are endowed with a variety of cues to sense and integrate, including substrate bound and diffusible chemical cues, electrical signals from neighboring cells, and physical and topographical cues from the morphology of surrounding cells and the ECM. These cues have been studied *in vitro* extensively, but such studies oversimplify the complex environment neurons must navigate *in vivo*, therefore underestimating the

precision to which the neurons respond to the itinerary provided by their local environment. *In vitro* systems for studying neuronal growth typically limit the cues presented to a single type of cue often in platforms that are classified as having overall positive or negative influence on growth. These cues are often classified as permissive, inhibitory, outgrowth promoting, outgrowth suppressing, attractive, repulsive, or directive, but integration of these cues in competing, synergistic, or balancing platforms is not well understood. Our goal is to study the collective influences of the rich mixture of cues in the local environment, and the mechanisms by which a neuron allows itself to be guided by these directive influences.

1.3 Background and significance

Each year 12,000 new spinal cord injuries (SCI) occur in the US.[2] Depending on the extent of the injury, the expense of caring for a patient in which injury occurs at the age of 25 can be over $3 million over their lifetime,[2] and this toll is only increasing as the medical technology to sustain these patients continues to improve. Spinal cord injury, which severs the connection between central and peripheral nerves, is among the most debilitating, life altering conditions a person can sustain. Most injuries occur as a result of car accidents (46.9%) and the mean age at time of injury is only 38 years. The most frequent consequence of SCI is incomplete quadriplegia (partial loss of function in all limbs, as well as compromised control of the torso, 34.3%), followed by complete paraplegia (complete loss of function in the legs and abdomen, 25.1%), complete quadriplegia (22.1%) and incomplete paraplegia (17.5%). Alarmingly, the majority of afflicted patients never functionally recover. Although the life expectancy of patients with SCI continues to improve, the devastation of the disease lies in its sizeable impact on patient quality of life. A commonly used clinical measure of quality of life is the time-tradeoff (TTO) test. TTO poses the choice between living a fixed amount of time in the patient's current medical state – usually the residual length of one's life expectancy – and alternatively living a shorter amount of time in full health. The point of indifference between the two options is recorded, and a TTO score is computed as the proportion of the variable length of time (in full health) over the fixed amount of time (with their medical condition). A recent study reports a

median TTO value of 0.50 from their sample of 187 patients with SCI.[3] This is a strong statement, especially considering that many diseases commonly regarded as highly insidious frequently receive higher TTO values. Patients with chronic obstructive pulmonary disease, congestive heart failure, colon cancer and lung cancer reported average TTO values greater than 0.7 in one study, with multi-organ system failure resulting in an average score of 0.6.[4] SCI is thus a significant financial and emotional burden.

1.4 Challenges to spinal cord injury

The lack of optimistic outcomes for SCI patients lies in the fact that trauma to the delicate structures of the nervous system is particularly damaging because nerve regeneration does not occur spontaneously within the CNS. This lack of regeneration was formerly attributed to the incapacity of neurons in the CNS to regenerate, a property fundamentally different from their counterparts in the PNS which have some capacity to reconnect after injury. This model was contradicted in the 1980s when elongation of injured axons in the brain and spinal cord was achieved with the use of peripheral nerve grafts.[5, 6] Since then, focus was adjusted from inherent differences between CNS and PNS neurons to the post-injury environment to explain their contrasting capacity for regeneration. As in most tissue damage, CNS injuries induce a reactive inflammation response, with an influx of fibrotic and immune cells to isolate the injury. Astrocytes, common glial cells specializing in metabolic support, also flood the area. It is thought that these cells function to restore the blood brain barrier after injury, preventing a wide scale, destructive inflammatory response.[7] The unfortunate side effect of this response is the construction of a mechanical and chemical barrier to neural regrowth known as the glial scar. The hardened, disorganized matrix of the glial scar acts to mechanically and topographically inhibit neurite path finding. Reactive astrocytes increase CSPG production, which has been shown to be an extremely inhibitory molecular cue for neurons.[8, 9] CSPGs have been shown to inhibit nerve regeneration both in the *in vivo* glial scar environment and *in vitro*.[9-12] There is also upregulation of the anti-adhesive protein tenascin causing a reduction in neuronal attachment and migration at the injured site.[9] Microglia and oligodendrocytes also migrate

towards the injury site. Combinations of myelin inhibitory molecules from mature oligodendrocytes and macrophage action of microglia also contribute to the inhibitory nature of the glial scar.[7, 13] The few axons that persist after CNS injury are found in close proximity with a subpopulation of astrocytes that transiently up-regulate polysialic acid (PSA), a negatively charged sugar chain carried by neural cell adhesion molecules (NCAMs).[14, 15] Today, the field of neural tissue engineering aims to study the cues neurons must be given to overcome this inhibitory post-injury environment to generate therapies to restore function and improve the quality of life of SCI patients.

In the PNS, which includes the nerves that innervate the extremities and the organs, the post injury environment is more permissive towards nerve regrowth. For small injuries (< 1 mm), nerve regeneration is possible. After injury, neurites extend from nodes of Ranvier proximal to the transection.[16] These naked extensions are joined by migrating SCs that line up, form a scaffold-like structure to guide subsequent nerve growth, and become closely associated with the extending neurites.[17] Not only do SCs act as a physical scaffold for neurons, they also express positive chemotactic cues to support nerve growth. One of these essential molecules for nerve regeneration expressed by SCs is LN, an adhesive molecule shown to promote neuronal growth and act as a guidance cue.[18] Neural extension is limited without associated SCs, demonstrating the important guidance function for these cells.[19]

In the clinical setting, the gold standard for peripheral nerve repair is to use nerve autografts to reconnect severed nerve stumps. This approach has several inherent limitations, especially in application to the CNS. Appropriate donor sites must be available, and there is also a degree of morbidity associated with the donor sites following harvesting. This procedure is not realistic for the CNS as it is not ideal for large diameter nerves or gaps larger than 1 mm.[20] Because of autograft limitations, recent work in nerve regeneration has largely centered on tissue engineered constructs for neural repair, namely the fabrication of neural guidance conduits (NGCs). This strategy attempts

to entubulate the severed ends of nerves, as well as the intervening gap between. Currently, only empty tubes made from Slubria hydrogel, collagen, and polyglycolic acid have been FDA approved as a nerve regeneration therapy, and only for use in the peripheral nervous system.[21] Studies of this product have been encouraging, demonstrating increased rates of elongation, reconnection, and action potential recovery, as well as an overall superior functional recovery as compared to conventional autografting. Use of these NGCs in comparison with autografting resulted in thicker and more dense myelinated axons and less swelling, necrosis, and discontinuity.[22] These empty NGCs are not ideally suited to overcome the more complex CNS environment. The challenge of repairing the CNS will require synergistic presentation of an environment containing multiple cues that guide axons.

1.5 Neuron pathfinding and growth cones

Neurons have the most highly developed pathfinding ability of any cell type. The specialized structures responsible for pathfinding decisions called growth cones are active and agile structure.[23] They are able to penetrate tissues, insinuate themselves between cells, and burrow through ECM while navigating the path of axon elongation.[23] Studies of guidance cues *in vitro* often focus on the result of growth cone navigation, neurite outgrowth and alignment. This resulting path is dependent on the interactions of the growth cone with the environment. On smooth surfaces, growth cones end in numerous branched fine filopodia at the leading edge of a small lamella. The filopodia are less than 0.2 μm wide and up to 30 μm long, and the lamellae are usually 5-20 μm in diameter. When an axon extends within a groove for more prolonged time, the morphology of its growth cone gradually simplifies. The lamella decreases and the number of filopodia declines.[24] This simplified growth cone structure is also observed in neurons growing on isolated tracks of LN.[25] The structure of growth cones becomes most elaborate in regions where the need for accurate direction finding is most acute.[23] For example, it has been shown that the growth cones of neurons grown in 3D agarose appear more globular than the lamellar morphology of grown cones in 2D.[26] There has been little characterization of the morphology of growth cones navigating such environments.

While the growth cone is considered archetypal in its ability to sense differences in chemical information, growth cone sensing in the local environment does not effectively explain the integration and response of neurons to other guidance information such as topography or electrical stimulation. For example, the lack of response shown by neurons to ultrafine gratings may be better explained by their lack of high-order F-actin and focal adhesions, and their alignment by larger topographies is suggested to be mediated through smaller networks of actin filaments.[27] Dunn also predicted that cells lacking focal contacts and actin cables are likely to be less sensitive to substratum shape.[28] There is also evidence that neuronal responses such as adhesion, extension, and guidance may be mediated by processes distinct from each other. For example, neurites are directed by the border between A7 and Neu7 astrocytes. Increasing the capacity of the astrocyte substrate to permit neurite extension by enzymatic treatment did not reduce guidance by this boundary indicating that the processes of extension and guidance are separable. Unpublished work in our lab also points to separation of adhesion and extension mechanisms. To maximize cellular adhesion and neurite outgrowth on gradients with opposing slopes of LN and CSPG, Li found that LN should be presented at 50 μg/ml and CSPG at 10 μg/ml. To maximize cellular adhesion and neurite outgrowth on gradients with parallel slopes of LN and CSPG, Li found that LN should be presented at 50 μg/ml with CSPG as 1 μg/ml.[29] These optimal values of slope and direction do not coincide to maximize both adhesion and neurite length suggesting that promoting adhesion and extension may be differentially regulated.

1.6 Substrate bound molecular cues

Substrate bound chemical cues have been studied for their effectiveness as cell and neurite guidance molecules. *In vivo*, these chemical cues are expressed by surrounding cells and integrated into the ECM. Using techniques such as microcontact printing, surface modification for selective adsorption, and microfluidics, specific patterns of chemicals have been created and used as platforms for

studying nerve guidance *in vitro*. Boundary lines or parallel stripes of these molecules are commonly employed on 2D cell culture substrates in order to investigate their ability to direct growth.[10, 25, 30] Molecules that have been investigated in this manner include those that are purely adhesive such as poly-L-lysine (pLL),[31] poly-D-lysine,[32] polyorinthine,[33] and silane derivatives[34]; those that are growth promoting such as LN, fibronectin (FN), and collagen[35]; those that are non-adhesive such as tenascin[36]; and those that are inhibitory such as CSPG.[37] It has been recognized, however, that guidance factors cannot properly be characterized in standard dissociated cell culture conditions.[18] The limitations of these methods lie in the poor approximation that the flatness of these 2D surfaces provides of the more complex 3D architecture neurons must navigate *in vivo* including the astrocyte derived ECM in the CNS[38] and the SC-derived basement membrane in the PNS.[39] To determine their full potential as guidance molecules *in vivo*, these molecules must be evaluated in more complex 3D and topographical culture systems *in vitro*.

1.6.1 LN guidance

LN has been studied in depth as a molecule used to direct and promote neurite growth.[18] LN is a glycoprotein localized in the basement membrane and the ECM that is present in developing and regenerating axon tracts. LN has many functional domains[18] and influences many aspects of neurite growth including promoting outgrowth, axon specification,[30] and guidance.[25, 40-43] Hammarback et al. demonstrated that neurites follow tracks of LN *in vitro*,[40, 44, 45] and growth cones were able to follow 7 and 10 μm wide tracks of LN.[45] Since then, studies have demonstrated neurite guidance on LN stripes as narrow as 2 μm and as wide as 50 μm.

A common assay to investigate the ability of LN to direct growth *in vitro* is presentation of boundary lines or parallel stripes. Several parameters contribute to the effectiveness of LN in this assay, including the width of LN tracks, the width of the space between tracks, and the concentration of LN. It has been demonstrated that the width of the track and the spacing between tracks jointly

contribute to LN effectiveness as a directive cue. When embryonic chick cerebral neurons were cultured on LN tracks with equal stripe and space width, a high degree of alignment was observed on substrates with 6, 12, and 25 μm tracks, but not on substrates with 2 or 3 μm tracks.[25] However, neurons did align to 2 μm tracks with 50 μm spaces pointing to the hypothesis that the tight packing of cues rather than overall size made it difficult for growth cones to align on substrates with narrow width and spacing. Hippocampal neurite outgrowth on a hexagonal lattice pattern was most precisely guided on substrates with narrow chemical tracks (2.3 μm wide) and larger spaces.[46] Recently, Song and Uhrich examined the effect of varying LN stripe width with constant spacing.[43] Chick embryo DRGs on substrates with 10, 20, 30, 40 or 50 μm LN stripes and 40 μm spaces aligned on substrates with 30-50 μm wide stripes with the highest degree of alignment on 40 μm stripes. That guidance by LN stripes was most effective when there were larger spaces between the tracks points to the importance of studying this cue in a more complex environment. In the more complex *in vivo* environment, cues are presented simultaneously, not in a spaced and controlled manner. It is not clear whether neurites would still have this degree of alignment if cells were allowed to overgrow the spaces and interact with each other or if the spaces were filled with cues of complicating influence.

The concentration of LN used to pattern substrates may also influence its effectiveness at guiding neurite outgrowth. Previous work in our lab used a microfluidic mixer to create gradients of substrate bound chemical cues. In a gradient where LN concentration theoretically ranged from 50 to 0 μg/ml, cell adhesion dropped significantly when the LN concentration dropped to 10 μg/ml or below, and outgrowth was directed toward increasing concentration of LN.[47] Few studies have examined the effect on LN concentration on overall cell alignment in a patterned substrate.

1.6.2 CSPG guidance

CSPGs are generally considered inhibitory towards neurite growth and are often used as negative guidance molecules. CSPGs are expressed in many regions of the developing nervous system that axons avoid, but their role in neuron guidance may be much more complex. For example, in the developing mouse neocortex, efferent axons follow a pathway with very little CSPG, whereas afferent pathways grow within the CSPG-rich cortical subplate. The different preferences of the two types of neurons suggest that CSPG may act to segregate the neurons and that the CSPG actually provides a pathway for the afferent axons. Similarly, in both the subventricular zone and the subependymal zones, the patterns of tenascin and CSPG appear to regulate cell migration and proliferation rather than neurite extension, since the neurites advance into tenascin/CSPG-rich regions.[9] In the glial scar, CSPGs contribute to the inherently inhibitory environment and must be overcome for successful regeneration. *In vivo*, astrocytes in the glial scar upregulate production of inhibitory CSPGs such as neurocan, phosphocan, NG2 and versican.[11, 12] *In vitro*, CSPGs also have an inhibitory effect on neurite growth. Neurite extension has been shown to decrease on homogeneous substrates of CSPG.[10] Studies have been done using CSPGs in combination with other molecules to analyze neurite behavior at CSPG borders. When embryonic chick DRGs were cultured on alternating 350 μm wide stripes of CSPGs and LN, greater neurite outgrowth was observed on LN stripes.[10] When neurites encountered a CSPG border, they would either stop or turn and grow along the border. Further, to balance the anti-adhesive effects of CSPG, it was mixed with LN and used to form alternating stripes of CSPG/LN and LN. Neurites continued to stop or turn at CSPG/LN borders until the LN concentration was much greater than the CSPG concentration. Later studies by Snow et al. found that the ratio of adsorbed LN and CSPG affected neurite behavior. For LN/CSPG ratios <0.48, neurites turned sharply at CSPG borders. When LN/CSPG was intermediate (~12.9), some neurites were able to cross the border, and at high ratios of LN/CSPG (~250), almost all neurites were able to cross into the region containing CSPG.[48] It has been demonstrated that growth cones sense the inhibitory molecule in the nearby environment and initiate the turning response of the neurite.[49] However, most studies using CSPGs examined neurite crossing at a border and not overall cell alignment in a

larger pattern. *In vivo*, neurons must integrate information from both LN and CSPGs at multiple borders and concentrations in the glial scar.

CSPGs have also been studied in the context of gradients. When CSPG was presented as a gradient, the resulting distribution of postnatal DRG neurite outgrowth was directed toward lower concentrations of CSPG, and when the CSPG gradient slope was increased, the neurite angle distribution change from directed to not significantly directed. There was a thresholded response for neuron adhesion along the CSPG gradient with relatively small increases in adhesion in the direction of decreasing CSPG concentration.[47] When LN and CSPG were presented in gradients together in opposing orientation, neurite outgrowth was directed toward increasing LN and decreasing CSPG in a stronger manner than on the single-cue gradients. Neurons showed similar adhesion patterns on the LN/CSPG opposing gradient as on the single-cue LN gradient, but decreasing the inlet concentration of LN or increasing the inlet concentration of CSPG dramatically reduced cell adhesion. When LN and CSPG were presented in parallel gradients, growth was not directed and adhesion was lower.[47] Cellular adhesion was affected by LN concentration and slope in double cue LN and CSPG gradients. Cellular adhesion was affected by CSPG inlet concentration and slope in double cue LN and CSPG gradients presenting a shallow LN gradient. Neurite length was affected by CSPG inlet concentration and slope in double cue LN and CSPG gradients presenting a steep LN gradient, suggesting that CSPG gradients play a larger role in adhesion than extension, where inhibition occurs regardless of the slope of LN presented. LN and CSPG concentrations elicited differential effects on neurite outgrowth dependent on gradient direction.

1.6.3 NCAM and L1 guidance

The NCAM is a prototypic member of the immunoglobulin (Ig) superfamily of cellular adhesion molecules (CAMs) and mediates adhesion through homophilic and heterophilic interactions, thereby modulating a range of biological processes.[50] NCAM is expressed in most tissues, but is expressed in particularly large amounts in the nervous system, where it is involved in numerous processes,

including neural development, regeneration, and learning and memory formation. NCAM can glycosylate with the unusual carbohydrate polysialic acid (PSA). PSA acts as a modulator of NCAM-mediated cell adhesion and affects processes such as cell migration, neurite outgrowth, and synaptic plasticity. NCAM is known to mediate cell-cell adhesion through a Ca^{2+}-independent homophilic mechanism in which NCAM on the surface of one cell interacts with NCAM on an opposing cell. NCAM also interacts heterophilically with several other molecules including heparin sulfate, L1, and brain spectrin.[51] NCAM does not appear to be involved in peripheral neurite outgrowth on astrocytes or Schwann cells or on the surfaces of other peripheral axons, but as NCAM is expressed on astrocytes in culture, it remains a candidate for mediating interactions that lead to neurite outgrowth by some types of neurons on astrocytes.[52] The developmentally and topographically changing associations of cell surface molecules are important for the regulation of cell behavior by triggering intracellular signals depending on the partner molecules with which they are associated.[53] Their ability to influence developmental events, including cell migration, proliferation, and differentiation can result from both their adhesive properties as well as induction of signaling pathways.

NCAMs are most often studied *in vitro* in co-culture platforms where underlying cell monolayers are induced to express NCAMs. Neurite outgrowth is induced by trans-homophilic NCAM interactions occurring in co-cultures of NCAM-expressing neurons growing on top of a layer of NCAM-expressing cells.[14] Similarly, rat dorsal root ganglia neurons (DRGs) grown on monolayers of cells transfected to express NCAM increased their expression of neurofilament, indicating morphological differentiation to a neuronal phenotype.[54] Transfection of glial scar astrocytes to express PSA resulted in a substantial portion of severed axons growing through the scar.[15] Similarly, transplantation of grafts of SCs expressing PSA-NCAM promoted functional recovery after SCI in mice.[55]

NCAM also mediates interactions between cells and the ECM. Two CSPGs, neurocan and phosphocan, have been shown to interact with NCAM. The expression of phosphocan is confined to neural tissue,

where it is produced by astrocytes. The biological significance of the interactions between NCAM and CSPGs is not well understood. Both neurocan and phosphocan inhibit the aggregation of NCAM-coated beads, indicating that the interaction of these molecules with NCAM interferes with homophilic NCAM interactions and thereby potentially with NCAM- dependent cell adhesion and neurite outgrowth. No direct binding between NCAM and laminin has been demonstrated, but they are likely to constitute parts of the same extracellular networks.

L1 is one of four CAMs belonging to the L1 family of the Ig superfamily of CAMs. The interaction between NCAM and L1 is mediated by a lectin-like sequence in the NCAM Ig4 module that binds to carbohydrates expressed by L1. This interaction induces L1 phosphorylation. Blocking this interaction inhibits neurite outgrowth in cerebellar neurons.[53]

1.6.4 Receptors and the cytoskeleton

The signal transduction mechanisms involved in neurite outgrowth are interconnected, such that the perturbance of one may influence another signaling cascade.[53] Neurons have receptors to both collagens and LNs,[56, 57] and DRG neurons have been specifically shown to express $\alpha_1\beta_1$ integrin, $\alpha_3\beta_1$ integrin and low levels of $\alpha_6\beta_1$ integrin.[58] The integrins include both heterodimers that recognize many ligands, e.g. $\alpha_3\beta_1$, which binds LN, FN, and collagen, and heterodimers that bind only one ligand, e.g. $\alpha_6\beta_1$ and $\alpha_5\beta_1$, which are specific for LN and FN, respectively. Both FN and LN receptors are dynamically regulated on neurons. N-cadherin is a 130-kD cell surface glycoprotein that mediates calcium dependent adhesion between neural cells. Neurite outgrowth by peripheral neurons grown on astrocytes depends strongly on the function of N-cadherin. N-cadherin also functions in peripheral neuron outgrowth on skeletal myotubes and Schwann cells.[52] The cell surface receptors mediating neurite outgrowth on pLL are not known.[53]

The cytoplasmic portion of the integrin receptor is connected through talin, vinculin, and α-actinin to actin filaments of the cytoskeleton. NCAM is also coupled to the cytoskeleton through spectrin suggesting that NCAM may be important for relaying mechano-physical information to the cell.[14]

1.7 Topographical cues

Another type of directive cue that has been evaluated substantially *in vitro* is substrate topography. The concept of "contact guidance" was first developed with regard to the experiments of Weiss[59, 60] and Curtis[61] which demonstrated that cells aligned along oriented fibers. Edges, fibers, and repeating grooves in the nanometer and micrometer range have been shown to guide and promote neurite outgrowth depending on the depth and width of such features. While grooves and fibers as narrow as 50 nm, as wide as 200 μm, as shallow as 14 nm, and/or as deep as 40 μm have been investigated, the minimal dimensions required for guidance by topographical substrates have yet to be determined. Many methods to study these effects, such as oriented fibers, hollow tubes, porous materials, simple scratches and underlying cells, do not inform us of the distinct topographical cue that leads to an effect, but they give insight into the general scale and scope that influence neuronal features.

1.7.1 Single feature topographies

Some studies have focused on cellular responses to isolated topographical features. Two particular topographies examined were a step[62] and single scratches on glass slides.[24] Embryonic chick neural cells were found to align parallel to the long axis of the step, and the degree of this alignment increased as the step height increased from 1 μm to 5 μm.[62] When a chick embryo DRG neurite encountered an isolated scratch approximately 0.15 μm wide and 0.5 μm deep, the growth cone would turn and elongate in the direction of the scratch and subsequent neurite growth would follow

the scratch.[24] This demonstrates how feature size can play a role in cellular response. It is possible that there is a threshold for neuron and growth cone detection of feature sizes.

1.7.2 Fibrillar topographies

Aligned collagen fibrils have been shown to orient chick embryo ganglia neurites and increase extension along the alignment axis.[63] It was proposed that filopodia from the growth cone contacted collagen fibers and tended to orient further growth along that point of contact. In the first application of magnetically aligned collagen, fibroblasts were also shown to orient along the collagen axis.[64] Neural cell response to multiple features has also been examined. One type of topography examined is aligned collagen fibrils. When chick embryo DRG explants were placed in an aligned collagen gel, outgrowing neurons preferentially aligned in the direction of the fibers.[63, 65] Neurite alignment appeared to be mediated by growth cones of navigating neurons.[63] It was proposed that the growth cone contacted the feature and turned along the axis of the feature, filopodia anchored to the feature, and the subsequent neurite growth followed the feature. In a more systematic approach, Dubey et al. used magnetically aligned collagen fibers (50-500nm diameter) to study rat and chick dorsal root ganglia. They found a 50% increase in mean elongation for chick DRG neurites grown in aligned collagen gels compared with unaligned collagen. Importantly, Schwann cell co-invasion was observed in rat DRG cultures, and SC were particularly conspicuous at the leading end of associated neurite elongation.[65] Increased neurite elongation on aligned substrates has been observed on different substrates and suggests that the topography of a substrate can influence internal cellular processes in addition to the alignment and morphology of the cell.

A more systematic analysis of fiber dimension influence on extension and alignment was conducted by Smeal et al.[66] Polypropylene filaments have been found to direct DRG neurites and SCs from DRG explants along the long axis of the filaments tested with an optimal filament diameter of 5 μm. The addition of FN and LN coatings on the filaments led to greater maximal neurite lengths than with

uncoated controls and resulted in neurite outgrowth that preceded migrating SCs (Wen and Tresco 2006). It seemed in this study that topographies in the range of cell features (<30um) were more relevant to guiding axons. Growth cone filopodia may not detect fibril features greater than 30 μm, or it may not have been energetically favorable to alter course in response to them.

1.7.3 Microgrooved topographies

Techniques from the field of electronics such as etching and photolithography have been used to create substrates with more precisely defined topography. Typically, these substrates present surfaces with repeated grooves and plateaus, and the plateau width, groove width, and groove depth can be varied to test neurite response to different topography dimensions. Depending on neuron type, different responses to grooved topography have been observed. Most PNS neurons align parallel to the long axis of grooves while hippocampal and other CNS neurons have shown a more complex response to grooved topography.[67, 68] When mouse CNS neurons were cultured on grooves of between 1-8 μm width and 0.05-0.8 μm depth, neurites oriented both parallel and perpendicular to the long axis of the grooves.[68] A similar study demonstrated the response of hippocampal neurons to grow parallel or perpendicular depended on topographical feature size. On grooves with larger dimensions (1.1 μm depth and 4 μm width), neurites were more likely to align to the long axis of the grooves.[67]

The first studies of alignment and neurite activity on varied topographies showed that neurites prefered to align in ways that minimized the overcoming of obstacles. Cells tended to not extend around angles in substrates.[69] On substrates with repeating groove patterns, increasing groove depth decreased the rate at which neurites crossed boundaries,[70] and increased the percent of neurites aligned with the pattern. Feature depth has since been shown to be an important contributor to topographical guidance. Though some cells have aligned to nanometer scale features, some studies have found that postnatal rat DRGs and chick embryo cerebral neurons only responded to features

with a depth greater than 1 μm.[70, 71] In each of the studies, the strongest degree of parallel alignment was seen on deeper grooves.[25, 67, 71] An analysis of groove depth and guidance revealed that when depth was varied from 2.5um to 69um, mouse cortical neurons increased alignment as depth increased until the 20um mark was reached.[32]

Topographical feature width also plays a role in neurite response. When cultured on substrates with 1-8 μm groove and plateau width, CNS and PNS neurites oriented parallel to any features wider than 4 μm.[68] This finding was confirmed by a second study which found the strongest parallel neurite alignment on 4 μm grooves as compared to 1 and 2 μm width features.[67] Britland et al. studied postnatal rat DRG neurite alignment on feature widths of 12, 25, 50, and 100 μm and observed the strongest parallel alignment on surfaces with 12 μm wide grooves and plateaus.[71] Strong alignment was also observed on 25 μm wide features. On the previous substrates mentioned, the plateaus and grooves were equal width on each substrate. Mahoney et al. cultured PC12 cells on microchannels of 20 to 60 μm in width and 11 μm in depth. Neurites were directed along the axis of the grooves, with microchannels of 20 to 30 μm being most effective at neurite direction.[72] Studies have not effectively examined the effect of varying plateau width with fixed grooves or varying both plateau and groove width independently.

A systematic study of pattern period has not been conducted, but a number of studies point to inter-feature distances that guide neurons. PC-12 cells have been shown to align greater than 90% to intergroove distances as small as 400 nm[73] and as great as 10 μm.[72] In general, patterns with period on the cellular scale (10um-20um) tend to align neurites best. Ultra fine topographies of 260 nm have been shown to not affect orientation of chick embryo cerebral neurons. In the range of 0.5 to 5 μm inter-feature distances, Dowell-Mesfin et al. found that 1 μm high by 2 μm wide pillars optimally aligned neurites with gaps of 1.5 μm.[74] Other cell types, such as fibroblasts, have been found to be relatively unaffected by pattern grating and aligned to features as small as 70 nm.[75] Although varying

between cell types, it appears that primary neuronal cell types align best to patterns of cellular dimensions.

Based on the scope of the previously mentioned studies, it can be concluded that topography plays a significant role in cell growth and alignment. In the micrometer range, a feature depth of at least 1 μm is necessary for neurite alignment, and neurons demonstrated increased alignment to feature with increased the feature depth. A top threshold, if any, has not been found. Optimal neurite alignment occurred on feature widths between 4 and 30 μm. These findings are interesting, because the features shown to be effective for neurite alignment have the same approximate dimension range as cells.

Perhaps the most interesting aspect of topographical guidance of axons is topography's effect on cell morphology. It has been well documented that neuronal cells of most types exhibit longer processes with more bipolar features and fewer neurites on topographically orienting substrates. Oriented neurites have also been reported to extend at a faster rate than undirected extensions.[76] Not surprisingly, the path-finding growth cones of extending neurites are also affected by topography. They tend to become thinner and more elongated when encountering small features. Chick embryo DRG growth cones typically extend many radial filopodia, but when they encounter a scratch in glass (0.1 to 1 μm deep) the filopodia adhere to the scratch, anchoring the growth cone and decreasing its orthogonal width.

Although much work has been done on substrate topography, there are a number of limitations in the current analysis in the literature. Previous studies are limited in application because they use simple grooves, 90^{o} angles or fibrils to guide neurons, and are not able to study complex structures systematically. In addition, it has been suggested that simple geometries are less permissive to neurite outgrowth and adhesion.[77] Cell co-culture guidance paradigms are likewise limited because

they cannot isolate the topographical cues of the underlying monolayer from their chemo-adhesive or secretory molecular contributions to guidance. The contribution of cell density has often been ignored in the analysis, a factor that could have significant topographical influences. A comprehensive, systematic analysis of topographical parameters that guide axons has thus far not been conducted.

In vivo, surrounding cells and ECM provide topographical guidance for navigating neurons. While co-cultures are a useful model of the *in vivo* environment (discussed in the next section), it is difficult to separate the influence of topography from the chemical and electrical influences of the guiding cells. To circumvent this, our lab developed a novel technique to form polymer replicas of cellular topography that are accurate to the micro- and nano-scale.[78] In a later study, dissociated postnatal rat DRGs were cultured on biomimetic replicas displaying aligned SC topography. DRG cells showed increased adhesion to substrates presenting SC topography as compared to flat substrates. When cultured as a dense monolayer, DRG neurites, cell bodies, and nuclei aligned to the direction of the underlying SC topography.[79] This study illustrates the influence of cellular topography on neurite growth and guidance and is an important step toward breaking down contributors in the complex environment *in vivo*.

1.8 Cellular cues

Glial cells are critical participants in every major aspect of brain development, function, and disease.[80] Guidepost cells are thought to play an integral part in directing neurites to their appropriate targets during development. Primitive glia are thought to lay a blueprint which growing neurites follow toward their desitination. The trace pathways are envisioned as mechanical-chemical itineraries which the neurites follow according to their individual affinities.[81] In addition to providing specific highways for regenerating axons the blueprint hypothesis implies that individual axons recognize and follow particular itineraries even when challenged by multiple highways. This

hypothesis has elements of two classical theories of axonal guidance, namely that axons are directed by mechanical pathways to their destination and by chemical cues (not mutually exclusive). This does not imply that regenerating axons are incapable of following other pathways than their original ones, but that they are most able to follow the one to which they have special affinity and persist in that one until the target is attained. Further, developing neurons use the various tracks of neurons before them (pioneering neurons) to determine their own pathway. This is largely done through growth cone preference for CAMs expressed on the axons of pioneer neurons.[82]

To that end, many studies have examined neurite outgrowth on oriented cellular topographies. Nagata et al. dissected a myriad of rat neuronal cells, including olfactory bulb, cerebral cortical, hippocampus and DRG and cultured them on a cerebellum micro-explant that contained naturally oriented neurite bundles.[83] Grown in explant-conditioned media, some cell types including olfactory, hypothalamus and hippocampus grew perpendicular to the cerebellum bundles (75-77%). DRG cells, on the other hand, significantly preferred to align parallel to the bundles (92-96%).[83] In further studies on oriented cellular topographies, the underlying monolayer of cells is aligned via a topographical,[84-86] chemical,[87] electrical,[88] or mechanical cue,[84] and then neurons are cultured on top of this monolayer. Neurite alignment has been observed on different cell types, such as astrocytes,[84, 85, 88, 89] SCs,[87, 90] meningeal cells,[91] olfactory ensheathing cells,[85] and fibroblasts.[24]

1.8.1 Astrocytes

Astrocytes can contribute both permissive and inhibitory cues to navigating neurons. They are largely responsible for glial scarring that inhibits severed CNS axons from regenerating, but studies of central nervous system development and regeneration have demonstrated that astrocytes provide and effective cellular substrate for axonal elongation.[52] The perceived role of astrocytes in the developing brain has evolved from their providing a passive support mechanism for neurons to their

functioning actively in regulating neurite extension and patterning. Various properties of astrocytes contribute to this function. Astrocytes release a range of cytokines, proteases, and protease inhibitors. They have, on their surface, a number of adhesion molecules that can influence axon growth and can produce a variety of extracellular matrix molecules.[92] One major mechanism by which astrocytes influence neurites is by forming boundaries that restrict neurite extension. This role is most apparent after CNS injury. Astrocytes in close proximity to the injury become hypertrophied and increase their expression of GFAP and some of the same ECM molecules as those found during development, especially tenascin and CSPG.

Astrocytes are thought to be a heterogeneous population of cells. Astrocytes have been reported to vary in their response to injury, especially in the upregulation of ECM molecules.[92] Multiple distinct populations of astrocytes have been identified by clonal analysis in the neonatal rat spinal cord.[93] The A7 cell line, which was derivec from immortalized rat optic nerve astrocytes has been shown to permit neurite extension. Whereas neurite outgrowth on A7 as well as cell lines derived from neonatal cortical astrocytes is less than that on primary astrocytes. Neu7 astrocytes are the least permissive of these cell lines. Further characterization, by using Western blot and immunocytochemistry analyses, has revealed that the restrictive Neu7 cells express relatively high levels of the ECM molecules tenascin and CSPG, whereas these molecules are almost undetectable in A7 cells.[92] The Neu7 cells also secrete a soluble factor that restricts neurite extension by negating the promotional effects of laminin.[94] Astrocytes isolated from embryonic or early postnatal brain are good substrates for rapid neurite extension by both central and peripheral neurons *in vitro*.[95, 96] In particular, neurons extend profuse, unfasciculated neurites on astrocyte surfaces while they do not respond well to fibroblast monolayers.[95] Astocytes thus express active neurite outgrowth-promoting factors. Laminin is expressed on the surfaces of cultured astrocytes,[97] but using antibodies to block the integrin β_1 subunit which blocks neuronal attachment and process outgrowth on LN, FN, collagens, and native ECM, only mildly inhibits neurite outgrowth of peripheral neurons on astrocytes.[98]

Aligned astrocytes have been shown to orient rat DRG cells to a high degree of correlation.[88] Even in the presence of substrates providing contrasting directional cues of parallel substrata and perpendicular astrocytes, DRG neurons preferred aligning to the astrocyte monolayer.[84] Recknor et al. cocultured astroctyes with neural progenitor cells (NPCs) and observed that confluent, directed astrocyte monolayers can direct adult rat NPCs and may contribute to the differentiation process.[89]

1.8.2 Schwann cells

Oligodendrocytes and Schwann cells have an intimate interaction with neurons wrapping their membranes around axons to form myelin. In addition to providing insulation and trophic support to neurons, myelinating glia are active participants in nervous system function, sculpting the structural and electrical properties of axons be controlling their diameter, as well as the spacing and clustering of ion channels at nodes and paranodes.[80] Inhibition of SC proliferation and migration reduces axon regrowth.[19] *In vitro*, DRGs strongly aligned to underlying SC monolayers.[87] In addition, DRG neurons produced more primary neurites on SCs than on LN alone.

1.8.3 Other glial cells

DRGs cultured on grooved polystyrene with an oriented cranial meningi monolayer surface were statistically more aligned and exhibited longer outgrowth when cultured on the oriented meningeal monolayer compared to the laminin-coated grooved substrate.[91] Deumens et al. cultured neonatal cerebral cortical neurons with olfactory ensheathing cells (OECs), glial cells thought to be responsible for continuous growth of peripheral axons in the olfactory system, and their associated olfactory nerve fibroblasts (ONF) or neonatal astrocytes. Cortical neurites were oriented in the direction of the underlying aligned OEC/ONF or astrocyte culture, and greater neurite elongation was observed on OEC/ONF cultures than on neonatal astrocyte cultures.

1.8.4 Other types of cells

Chick DRGs exhibited increased alignment and faster outgrowth when cultured on oriented human skin fibroblasts.[24] Vascular cells are a major cellular constituent of the brain and have recently emerged as important, though relatively neglected, contributors of brain development and function. Vascular cells guide developing axons, provide trophic support and differentiation signals to neurons and stem cells, and provide a niche for neural stem cells.[80] Vascular cells also provide guidance information to developing sympathetic neurons. A model has been suggested in which developing sympathetic neurons are predetermined to choose between distinct vascular trajectories, and thus destined to innervate select end organs. This choice of vascular route is guided, at least in part, by the actions of vascular-derived endothelins, proteins that constrict blood vessels.[99]

1.9 3D cues

Much of the current knowledge regarding neuron growth has been gained from cells grown on the two dimensional (2D) surfaces of dishes and flasks. This not only fails to reflect the complex three dimensional (3D) environment which nerves must navigate *in vivo*, but also fails to address the necessity for cells to infiltrate and interact with materials used in neural tissue engineering for conduits, electrodes, and drug delivery systems.[17, 100, 101] Materials are often used to promote innervation, but the rationale behind much of this use is on a trial and error basis. There is a lack of knowledge in to the molecular mechanisms by which neurons grow in three dimensions.

The use of scaffold materials to mimic the 3D cellular environment is not novel. The use of hydrogels for *in vitro* study of neurons has been popular for over a decade.[102] Hydrogels are a class of polymer

materials in which water accounts for greater than 30% of the material's weight. They have proven to be useful biomaterials because their properties can be optimized so that they are capable of gelling without damaging cells suspended in the matrix, are nontoxic, allow diffusion of nutrients, and have enough mechanical integrity to support the growth of cells.[103] A variety of synthetic polymers such as polyethylene glycol (PEG) and polyvinyl alcohol (PVA) are often used as hydrogels, and many of the natural components of the ECM can be used *ex vivo*. Natural hydrogels include agarose, alginate, chitosan, collagen, fibrin, gelatin, and hyaluronic acid.[104-107] Established hydrogels are compatible with cell culture and readily available, so characterization of the molecular interactions of neurons with these hydrogels is a useful endeavor.

The high water content of hydrogels makes them very useful for cell culture, but also makes them very difficult to characterize. The microscopy and mechanical techniques that have been utilized to characterize hydrogels have consistently revealed the trends that stiffness and neurite outgrowth are inversely correlated while pore size is positively correlated to neurite outgrowth,[26, 108-112] but the absolute values of these properties have differed by orders of magnitude even when measured by the same group on the same gels.[108, 109] In addition to inconsistency, another shortcoming in measurement of the stiffness and porosity of hydrogels is that while both have been correlated to changes in neurite outgrowth, the contributions of these properties are difficult to separate from each other. The porosity and stiffness of agarose,[26, 108-110] collagen,[113] polyacrylamide,[111] and PEG[112] have each been studied individually, but since they have not been studied and compared together the contributions of the chemical and topographical features intrinsic to the materials have also not been evaluated. The optimal porosity, stiffness, and topographical structure of a hydrogel for the culture of neurons *in vitro* have thus not yet been determined.

Hydrogel materials usually contain or mimic the natural components of the extracellular matrix in order to promote cell adhesion and neurite extension. Molecules known to promote cell adhesion

such as laminin or fibronectin have been added to common culture gels such as collagen, agarose, and fibrin.[110, 113-115] The addition of these molecules was intended to promote neurite outgrowth, but the results have not completely supported this hypothesis. In one study, the addition of laminin and fibronectin to a collagen hydrogel was shown to enhance outgrowth at 2 days and then inhibit outgrowth by day 4 of culture.[113] A later study in collagen showed that fibronectin had an inhibitory effect at both 2 and 4 days, and that the addition of laminin yielded similar results to an unmodified collagen gel.[110] These unpredictable results are probably due to physical changes in the gel such as reduction in porosity or a decrease in migration due to the large increase in the number of potential binding sites by the addition of these molecules, but because physical properties are seldom studied in conjunction with these chemical additions to the matrix, these findings are difficult to apply to future biomaterials.

In order to reduce the physical changes invoked by the addition of these molecules, several groups have included small oligopeptides with the binding sequences of these proteins rather than the whole protein.[112, 116, 117] These results have also been unpredictable. The addition of the RGDS domain of fibronectin was shown to enhance neurite outgrowth in agarose[116] and PEG.[112] The addition of YIGSR, a binding domain of laminin, increased outgrowth in agarose[116] gels and not in PEG,[112] but the IKVAV domain of laminin increased extension in PEG.[112] The physical changes caused by the addition of large molecules were reduced in these cases, but the unpredictable results leave a gap in the understanding of the importance of the presence and type of adhesive properties in 3D cell culture.

Comparison of neuron growth in unmodified versions of the many of the aforementioned gels is also a study of the effects of chemical properties. Agarose, for example, does not have any known adhesion sites for cells while ECM molecules such as fibrin and collagen are rich in adhesion sites. Collagen and fibrin gels have been shown to promote neurite extension and neuron viability when

compared to agarose gels.[118, 119] These experiments support the use of natural matrices as biomaterials for neural tissue engineering, but their conclusions are limited by the fact that the differences in neurite outgrowth are attributed to the adhesive properties of these gels despite the possible contribution of physical differences in the gels. The application of hydrogels for tissue engineering would thus be advanced by a study which takes into account the physical and adhesive properties of these hydrogels.

Differences in the morphology of neurons grown in 2D versus 3D are often observed. For example, neurite extensions within a 3D fibrin matrix are shorter as compared to extension on the surface of the matrix,[115] and the growth cones of neurons grown in 3D agarose appear more globular than the lamellar morphology of neuronal grown cones in 2D.[26] Most of these studies have not been able to correlate these morphological changes with molecular regulation in the cell. One study not only observed increased fascicle and network formation in the 3D morphology of cells grown on a polystyrene matrix rather than on flat tissue culture plastic, but also correlated these observations to Western blot analysis of the protein expression of these cells. Proteins associated with growing, maturing neurons such as neurofilament 68kDa, neuroD, and MAP2ab were upregulated in 3D cultures indicating that these networks are continuing to expand and extend neurites.[120] This study is a step in the right direction, but their protein analysis is limited to the proteins they chose to investigate. Our lab performed a more rigorous comprehension of the cellular and molecular mechanisms underlying axon growth in a matrix that is physiologically relevant in its 3D geometry. We compared the gene expression of SH-SY5Y cells grown in 3D collagen I matrices with that of SH-SY5Y cells grown on 2D collagen I substrates. Microarray analysis identified more than 1,700 genes that were differentially regulated. Seven genes with roles in cytoskeleton, ECM, and neurite growth were selected for further analysis, and their differential expression in 3D and 2D culture conditions in 2 distinct matrices was confirmed using RT-PCR. We hypothesized that the differences in gene expression were related to differences in the geometry of the culture and were independent of the type of ECM material used. RT-PCR experiments tested this hypothesis and confirmed that genes for

filamin A, actinin 1α1, capping proteinα2, fibronectin, and midkine were differentially regulated in response to culture geometry and that expression patterns were similar between collagen I and Matrigel. Neuroblastoma cell soma morphology also varied with culture geometry; in collagen I and Matrigel, cells were rounder in 3D cultures and more spread in 2D cultures. More complex results were seen for patterns of neurite outgrowth. For collagen I, growth in 3D cultures was longer than growth on 2D substrates, but the opposite trend was seen for Matrigel. Collagen I matrices were also found to be more fibrillar, stiffer, and more porous than Matrigel. The findings of this study suggest that the regulation of these responses is complex and depends on the geometry of the matrix as well as on its composition, structure, and mechanical properties.

1.10 Diffusible factors

A third type of cue that neurons have responded to *in vitro* as well as *in vivo* is diffusible neurotrophic factors.[121-127] Of the neurotrophic molecules, nerve growth factor (NGF) has been used the most extensively in a guidance role. NGF has been reported to promote both the growth and survival of axons of the PNS and CNS.[128] Diffusible and immobilized gradients have been shown to guide outgrowth *in vitro*.[123, 125] In fact, gradients of NGF as small as 133 ng/ml per millimeter have been shown to guide neurites toward the source.[123] If NGF is to be used to enhance outgrowth and guidance, in combination with other cues, small inconsistencies in its release could induce gradients that actually interfere with the guidance of other cues. Inclusion of growth factors in nerve guide conduits *in vivo* has been shown to promote regeneration.[129-131] The success of these studies has prompted several attempts to fabricate drug delivery systems for sustained release of NGF.[121, 122, 126, 127] Most of these systems incorporate degradable polymers in order to achieve sustained and controlled delivery. In order to combine these drug delivery systems with topographical cues, a balance must be achieved between degradability of the polymer for release and the integrity of topographical features required for guidance.

1.11 Combinations of cues

The response of neurons to these more complex multi-cue environments are only beginning to be investigated. Li and Folch studied opposing molecular and topographical cues in the response of mouse cortical neurons to pDL coated PDMS grooves covered with a Matrigel matrix and found that axons initially on plateaus chose to grow into the Matrigel matrix in contrast to growth along the plateaus when grooves are filled with media rather than matrix.[32] In a study of parallel molecular and topographical cues, rat DRG neurites demonstrated a high degree of alignment to those substrates presenting parallel chemical and topographical cues. When groove depths from 1-4 μm and groove and stripe widths of 10 and 20 μm were tested, the highest degree of alignment was observed on substrates with 10 μm wide and >3 μm deep features in combination with 200 μg/ml LN.[132] Other studies of combinations of defined topographical and molecular cues revealed synergies between cues. Gomez et al. studied the combined effects of NGF and microtopography of microchannels on axon initiation, polarization and elongation of hippocampal neurons.[133] When presented with microchannel substrates of 1- to 2-μm widths and 400- to 800-μm depths containing immobilized NGF on the surface, hippocampal neurons responded to the combination of molecular and topographical stimulation with the longest neurites. Zhang et al. developed hybrid templates that combine topographical and molecular cues with channels 5 μm deep and 20 to 40 μm wide connecting to nodes of 50 to 100 μm widths and pLL to achieve geometric control over neurite connections for the application of microelectronic circuits.[76] Hippocampal neurites extended on pLL tracks and avoided regions where no pLL was present.

Britland et al. studied the combination of adhesive tracks and topography presented together, in parallel or orthogonally opposed. Guidance was enhanced by parallel cues. Neurites aligned preferentially to adhesive tracks perpendicular to shallow grooves, but aligned increasingly to grooves with increasing depth. Britland et al. tested feature sizes ranging from 12-100 μm wide and 0.05-6 μm deep.[71] On substrates with parallel guidance cues, the highest degree of alignment (>80% of neurites aligned within 10° of the pattern) was observed on substrates with 25 μm width and 6 μm

depth, though a high degree of alignment was observed on all substrates with 25 and 50 μm width features. On substrates where perpendicular cues were presented, slightly more complex behavior was observed. Britland et al. found that more neurites aligned parallel to the LN tracks when groove depth was less than 1 um, but neurites preferentially aligned parallel to the grooves when they were >1 um deep. This demonstrates a complex growth response to cues in opposing directions. As more is understood about how neurons respond to patterned chemical and topographical cues, more complex environments can be investigated to understand how neurons integrate and respond to multiple guidance cues. By combining cues, we can use multiple parallel cues to generate more highly aligned neuron cultures and cues presented in opposing directions to determine the preferred neuronal alignment.

Our lab has begun to examine neurite alignment on biomimetic topographical substrates with parallel and orthogonal guidance cues. This allows us to more closely mimic the *in vivo* environment and to determine the strength of cellular topography as a directive cue. When the topography and LN stripes were presented in a parallel orientation, results suggested more neuronal alignment than on substrates with either single cue. On substrates where the cellular topography and LN tracts were presented in an orthogonal orientation, DRG cells demonstrated preferential alignment to the chemical tracks. This degree of alignment suggests a decrease from those substrates presenting LN stripes only.[134] This result parallels those found in the study by Britland et al., as SC are typically on the order of 1 μm in height.

The results of these studies help unravel neuronal response to multi-cue environments, but they also demonstrate the complexity of this response. Topographical feature shape, height, and width and chemical type, concentration, and pattern dimensions could all impact the guidance of growing neurons. In order to understand neuronal behavior in complex environments, more studies must be done to determine the impact of each of these variables.

1.12 Methods to determine anisotropy or density of outgrowth

1.12.1 Use and analysis of dissociated DRGs

DRGs are commonly used to study neurite guidance in response to *in vitro* platforms for axon guidance. Recent studies demonstrating successful cryopreservation of neurons with or without transfection increases the ease with which they can be used as an experimental model.[135] DRG contain multiple cell types that are found both in the PNS and the CNS, of which neurons are a major component. Other important cell types that make up DRG are SCs and fibroblasts. Measuring the alignment of neurons and neurites is very important in determining the efficacy of substrates for aiding aligned nerve regeneration. Evaluation of neurite outgrowth *in vitro* has included qualitative scoring systems with grouped categorical quantification.[27, 86, 136, 137] There are many different methods for measuring the angular orientation of various cell types on different substrates, where some focus on neurites, if present,[84] and others use nuclei as representative of cellular alignment.[138] Most rely on imaging and image analysis techniques. Manually tracing cells and neurites with respect to the substrate or image is a simple method that can be tedious so does not allow for analysis of a large number of cells or samples, but it can be very accurate since short neurites can be ignored and large clusters of cells can be individually scored for alignment. Most alignment studies currently use computer automated tracing, line fitting, or pixel intensity calculations, which allow for high precision and the ability to analyze many cells and samples.

More advanced methods use pixel intensity or spectrum analysis of such confluent substrate images. Alexander et al. determined the response of DRG neurites to aligned astrocytes by Fast Fourier Transformation processing and analysis.[88] The intensity and distribution of the pixels in the FFT images represent the frequency content, which is related to the direction distribution of the original images. FFT analysis was compared to individual neurite tracing and each showed pixel intensity peaks corresponding to directed orientation. Corey et al. demonstrated the utility of FFT processing when determining alignment of DRG neurites cultured on aligned electrospun fibers.[139] Spectral

analysis via Fourier power spectra has also been utilized to determine anisotropy in image analysis.[85, 140]

Li and Hoffman-Kim demonstrated that circular statistical methods may be used to analyze biological data containing directional biases and anisotropy, particularly to quantify neurite outgrowth.[141] The geometry of neurite outgrowth is most meaningfully parameterized in a circular coordinate system centered on the cell and rotationally aligned to the stimulus applied. The distribution of neurite angles in culture can be described by circular statistical parameters, such as mean direction and length of the mean vector. Circular statistical methods show sufficient power and are a better model than linear statistical methods to analyze directional neurite outgrowth. Circular histograms allow easy visualization of data clustering.

1.12.2 Use and examination of DRG explants

Researchers have frequently utilized DRG explants within experimental models aimed to evaluate the neurotrophic effects of growth factors and other bioassays. However, characterization of DRG explant growth has often been problematic. Due to the highly complicated networks of extensions and migrant cells surrounding the explant body, it is often impossible to distinguish the path of a single extension from others occupying the same space. Branching and fasciculation further compound this problem, making neurite counts exceedingly labor intensive and time consuming. Three-dimensional assessment of explants is even more challenging as one must account for neurite weaving through vertical planes. In the past, this additional factor has made quantitative assessments of 3D DRG explant growth essentially unrealistic, especially when unitizing approaches developed for 2D growth characterization.

A common strategy to evaluate DRG explant growth in 2D is assignment of qualitative labeling. Ratings of low, medium, and high are used to describe robustness in growth in terms of observed overall neurite length and density.[142] In other cases, ratings are completely omitted, and images are used as the sole demonstration of growth results.[143, 144] There are numerous drawbacks with these forms of qualitative assessment. These evaluations are potentially biased, and it is difficult to make truly direct comparisons between samples. Statistical analysis is not possible with these qualitative results, and some growth patterns cannot be detected through observation alone.

Other groups have assessed neurite growth of DRG explants through the measurement of the longest observed neurite, or a fixed number of the longest neurites.[145, 146] However, these approaches do not account for overall growth, and can be misleading depending on outgrowth variability. For example, an explant with several long processes would appear to have had better outgrowth than an explant that grows many robust medium length extensions. There is high variability between individual results using this analysis, due to the natural inconsistencies between explant growth that stem from such variables as age of explant source (P0-P5), extraction location (midsection versus distal end of the spinal column), and the initial size of explant. Similar to the longest neurite analysis approach, some groups have counted the number of processes that were able to grow past a defined barrier, such as in the study previously visited by Yu and Bellamkonda.[110] While this approach was appropriate for the purposes of that study, it is not useful when characterizing overall growth of explants. Also, assessing ability to grow through a barrier may be difficult given that explants often exhibit asymmetrical growth. Therefore, comparisons may be confounded by initial orientation of the explant. For the purposes of our study, this analysis method was not useful.

Bilsland et al. pioneered an approach to quantitatively measure explant growth based on densitometry.[147, 148] Using the grain counting function and optical density analysis of imaging software, they were able to assess the total area occupied by neurites and migrant cell bodies. The

resulting number is an indication of neurite density. Advantages of this system include automation, which limits subjectivity while maximizing processing speed, and incorporation of neurite length, branching, and fasciculation in its resulting characteristic number. This strategy also allows the possibility of statistical analysis. The drawbacks to this approach include the fact that it doesn't provide a spatial description of growth, and that the method is unable to differentiate between a small number of long neurites and a large number of short neurites. Additionally, this method is problematic for 3D systems where a number of neurites are observable and optically significant but ultimately out of focus.

In the minority of studies, explant growth was limited to the point of feasible neurite counting.[149] However, these circumstances are very limited. Through counting alone, it is difficult to account for branching and neurite fasciculation. Additionally, pure counting of extensions does not differentiate between long and short neurites. For this reason, some researchers utilize longest neurite analysis along with neurite counting. However, explants often have such complicated networks of extensions that it is tedious to separate out entire tracks of individual neurites to perform an overall count.

1.13 Closing remarks

A variety of neuronal guidance cues have been identified, but in order to determine their full potential as guidance cues for therapeutic application, these cues must be evaluated in more complex platforms that take into account the local environment *in vivo*. Tissue engineering and biomaterial approaches are well equipped to develop precisely defined microenvironments that incorporate three dimensions, topography, controlled molecules, electric fields, and other guidance cues individually, in parallel, or in a competitive manner. Successful therapies for nerve regeneration will require the coordinated presentation of several of these cues. Determining net neuronal responses to temporal and spatial combinations of molecular, cellular, and geometric cues is an important step toward generating therapies to improve expectations of optimistic outcomes for SCI patients.

1.14 References

1. Weiss, P. Principles of development. New York: Henry Holt, 1939.

2. Foundation for Spinal Cord Injury Prevention, C., and Cure, Spinal cord injury facts, 2004.

3. Lin, M. R., H. F. Hwang, K. P. Chung, C. Huang and C. Y. Chen. Rating scale, standard gamble, and time trade-off for people with traumatic spinal cord injuries. Phys Ther. 86: 337-44, 2006.

4. Tsevat, J., E. F. Cook, M. L. Green, D. B. Matchar, N. V. Dawson, S. K. Broste, A. W. Wu, R. S. Phillips, R. K. Oye and L. Goldman. Health values of the seriously ill. Support investigators. Ann Intern Med. 122: 514-20, 1995.

5. Aguayo, A. J., S. David and G. M. Bray. Influences of the glial environment on the elongation of axons after injury: Transplantation studies in adult rodents. J Exp Biol. 95: 231-40, 1981.

6. Bray, G. M., M. Vidal-Sanz and A. J. Aguayo. Regeneration of axons from the central nervous system of adult rats. Prog Brain Res. 71: 373-9, 1987.

7. Silver, J. and J. H. Miller. Regeneration beyond the glial scar. Nat Rev Neuroscience. 5: 146-156, 2004.

8. McKeon, R. J., R. C. Schreiber, J. S. Rudge and J. Silver. Reduction of neurite outgrowth in a model of glial scarring following cns injury is correlated with the expression of inhibitory molecules on reactive astrocytes. J Neurosci. 11: 3398-411, 1991.

9. Powell, E. M., J. W. Fawcett and H. M. Geller. Proteoglycans provide neurite guidance at an astrocyte boundary. Molecular and Cellular Neurosciences. 10: 27-42, 1997.

10. Snow, D. M., V. Lemmon, D. A. Carrino, A. I. Caplan and J. Silver. Sulfated proteoglycans in astroglial barriers inhibit neurite outgrowth in vitro. Exp Neurol. 109: 111-30, 1990.

11. Fawcett, J. W. and R. A. Asher. The glial scar and central nervous system repair. Brain Research Bulletin. 49: 377-391, 1999.

12. Margolis, R. U. and R. K. Margolis. Chondroitin sulfate proteoglycans as mediators of axon growth and pathfinding. Cell and tissue research. 290: 343-348, 1997.

13. Fry, E. J. Central nervous system regeneration: Mission impossible? Clinical and Experimental Pharmacology and Physiology. 28: 253-258, 2001.

14. El Maarouf, A., A. K. Petridis and U. Rutishauser. Use of polysialic acid in repair of the central nervous system. Proceedings of the National Academy of Sciences. 103: 16989, 2006.

15. Rutishauser, U. Specific alteration of ncam-mediated cell adhesion by an endoneuraminidase. Journal of Cell Biology. 101: 1842-1849, 1985.

16. Torigoe, K., H. F. Tanaka, A. Takahashi, A. Awaya and K. Hashimoto. Basic behavior of migratory schwann cells in peripheral nerve regeneration. Exp Neurol. 137: 301-8, 1996.

17. Schmidt, C. E. and J. B. Leach. Neural tissue engineering: Strategies for repair and regeneration. Annu Rev Biomed Eng. 5: 293-347, 2003.

18. Bixby, J. L. and W. A. Harris. Molecular mechanisms of axon growth and guidance. Annu Rev Cell Biol. 7: 117-59, 1991.

19. Chen, Y. Y., D. McDonald, C. Cheng, B. Magnowski, J. Durand and D. W. Zochodne. Axon and schwann cell partnership during nerve regrowth. Journal of Neuropathology and Experimental Neurology. 64: 613, 2005.

20. Rummler, L. S. and R. Gupta. Peripheral nerve repair: A review. Curr Opin Ortho. 15: 215-9, 2004.

21. Phillips, J. B., S. C. Bunting, S. M. Hall and R. A. Brown. Neural tissue engineering: A self-organizing collagen guidance conduit. Tissue Eng. 11: 1611-7, 2005.

22. Nakamura, T., Y. Inada, S. Fukuda, M. Yoshitani, A. Nakada, S. Itoi, S. Kanemaru, K. Endo and Y. Shimizu. Experimental study on the regeneration of peripheral nerve gaps through a polyglycolic acid-collagen (pga-collagen) tube. Brain Res. 1027: 18-29, 2004.

23. Bray, D. and P. J. Hollenbeck. Growth cone motility and guidance. Annu Rev Cell Biol. 4: 43-61, 1988.

24. Stepien, E., J. Stanisz and W. Korohoda. Contact guidance of chick embryo neurons on single scratches in glass and on underlying aligned human skin fibroblasts. Cell Biol Int. 23: 105-16, 1999.

25. Clark, P., S. Britland and P. Connolly. Growth cone guidance and neuron morphology on micropatterned laminin surfaces. J Cell Sci. 105 (Pt 1): 203-12, 1993.

26. Balgude, A. P., X. Yu, A. Szymanski and R. V. Bellamkonda. Agarose gel stiffness determines rate of drg neurite extension in 3d cultures. Biomaterials. 22: 1077-84, 2001.

27. Webb, A., P. Clark, J. Skepper, A. Compston and A. Wood. Guidance of oligodendrocytes and their progenitors by substratum topography. J Cell Sci. 108 (Pt 8): 2747-60, 1995.

28. Dunn, G. A. How do cells respond to ultrafine surface contours? Bioessays. 13: 1991.

29. Li, G. N. Y. Axon guidance by molecular and topographical cues. Ph.D. dissertation, Brown University, 2008.

30. Esch, T., V. Lemmon and G. Banker. Local presentation of substrate molecules directs axon specification by cultured hippocampal neurons. J Neurosci. 19: 6417-26, 1999.

31. Gundersen, R. W. Response of sensory neurites and growth cones to patterned substrata of laminin and fibronectin in vitro. Dev Biol. 121: 423-31, 1987.

32. Li, N. and A. Folch. Integration of topographical and biochemical cues by axons during growth on microfabricated 3-d substrates. Exp Cell Res. 311: 307-16, 2005.

33. Letourneau, P. C. Cell-to-substratum adhesion and guidance of axonal elongation. Dev Biol. 44: 92-101, 1975.

34. Kleinfeld, D., K. H. Kahler and P. E. Hockberger. Controlled outgrowth of dissociated neurons on patterned substrates. J Neurosci. 8: 4098-120, 1988.

35. Luckenbill-Edds, L. Laminin and the mechanism of neuronal outgrowth. Brain Research Reviews. 23: 1-27, 1997.

36. Faissner, A. and J. Kruse. J1/tenascin is a repulsive substrate for central nervous system neurons. Neuron. 5: 627-37, 1990.

37. Hoke, A. and J. Silver. Proteoglycans and other repulsive molecules in glial boundaries during development and regeneration of the nervous system. Prog Brain Res. 108: 149-63, 1996.

38. Silver, J. and J. H. Miller. Regeneration beyond the glial scar. Nature Reviews Neuroscience. 5: 146-156, 2004.

39. Chernousov, M. A. and D. J. Carey. Schwann cell extracellular matrix molecules and their receptors. Histol Histopathol. 15: 593-601, 2000.

40. Hammarback, J. A., S. L. Palm, L. T. Furcht and P. C. Letourneau. Guidance of neurite outgrowth by pathways of substratum-adsorbed laminin. J Neurosci Res. 13: 213-20, 1985.

41. Yeung, C. K., L. Lauer, A. Offenhausser and W. Knoll. Modulation of the growth and guidance of rat brain stem neurons using patterned extracellular matrix proteins. Neurosci Lett. 301: 147-50, 2001.

42. Song, H. K., B. Toste, K. Ahmann, D. Hoffman-Kim and G. T. Palmore. Micropatterns of positive guidance cues anchored to polypyrrole doped with polyglutamic acid: A new platform for characterizing neurite extension in complex environments. Biomaterials. 27: 473-84, 2006.

43. Song, M. and K. E. Uhrich. Optimal micropattern dimensions enhance neurite outgrowth rates, lengths, and orientations. Ann Biomed Eng. 35: 1812-20, 2007.

44. Hammarback, J. A. and P. C. Letourneau. Neurite extension across regions of low cell-substratum adhesivity: Implications for the guidepost hypothesis of axonal pathfinding. Dev Biol. 117: 655-62, 1986.

45. Hammarback, J. A., J. B. McCarthy, S. L. Palm, L. T. Furcht and P. C. Letourneau. Growth cone guidance by substrate-bound laminin pathways is correlated with neuron-to-pathway adhesivity. Dev Biol. 126: 29-39, 1988.

46. Kam, L., W. Shain, J. N. Turner and R. Bizios. Axonal outgrowth of hippocampal neurons on micro-scale networks of polylysine-conjugated laminin. Biomaterials. 22: 1049-54, 2001.

47. Li, G. N., J. Liu and D. Hoffman-Kim. Multi-molecular gradients of permissive and inhibitory cues direct neurite outgrowth. Annals of Biomedical Engineering. 36: 889-904, 2008.

48. Snow, D. M., J. D. Smith and J. A. Gurwell. Binding characteristics of chondroitin sulfate proteoglycans and laminin-1, and correlative neurite outgrowth behaviors in a standard tissue culture choice assay. Journal of Neurobiology. 51: 2002.

49. Challacombe, J. F., D. M. Snow and P. C. Letourneau. Dynamic microtubule ends are required for growth cone turning to avoid an inhibitory guidance cue. Journal of Neuroscience. 17: 3085-3095, 1997.

50. Nielsen, J., N. Kulahin and P. S. Walmod. Extracellular protein interactions mediated by the neural cell adhesion molecule, ncam: Heterophilic interactions between ncam and cell adhesion molecules, extracellular matrix proteins, and viruses. Neurochemical Research. 1-19,

51. Rao, Y., X. Zhao and C. H. Siu. Mechanism of homophilic binding mediated by the neural cell adhesion molecule ncam. Evidence for isologous interaction. Journal of Biological Chemistry. 269: 27540-27548, 1994.

52. Neugebauer, K. M. N-cadherin, ncam, and integrins promote retinal neurite outgrowth on astrocytes in vitro. The Journal of Cell Biology. 107: 1177-1187, 1988.

53. Horstkorte, R. The fourth immunoglobulin-like domain of ncam contains a carbohydrate recognition domain for oligomannosidic glycans implicated in association with l1 and neurite outgrowth. Journal of Cell Biology. 121: 1409-1421, 1993.

54. Doherty, P. Neuronal process outgrowth of human sensory neurons on monolayers of cells transfected with cdnas for five human n-cam isoforms. Journal of Cell Biology. 109: 789-798, 1989.

55. Papastefanaki, F., J. Chen, A. A. Lavdas, D. Thomaidou, M. Schachner and R. Matsas. Grafts of schwann cells engineered to express psa-ncam promote functional recovery after spinal cord injury. Brain. 130: 2159, 2007.

56. Reichardt, L. F. and K. J. Tomaselli. Extracellular matrix molecules and their receptors: Functions in neural development. Annual review of neuroscience. 14: 531-570, 1991.

57. Venstrom, K. A. and L. F. Reichardt. Extracellular matrix. 2: Role of extracellular matrix molecules and their receptors in the nervous system. The FASEB Journal. 7: 996-1003, 1993.

58. Tomaselli, K. J., P. Doherty, C. J. Emmett, C. H. Damsky, F. S. Walsh and L. F. Reichardt. Expression of beta 1 integrins in sensory neurons of the dorsal root ganglion and their functions in neurite outgrowth on two laminin isoforms. Journal of Neuroscience. 13: 4880-4888, 1993.

59. Weiss, P. Experiments on cell and axon orientation in vitro: The role of colloidal exudates in tissue organization. J Exp Zool. 100: 353-386, 1945.

60. Weiss, P. Cell contact. Int. Rev. Cytol. 7: 391-423, 1958.

61. Curtis, A. S. and M. Varde. Control of cell behavior: Topological factors. J Natl Cancer Inst. 33: 15-26, 1964.

62. Clark, P., P. Connolly, A. S. Curtis, J. A. Dow and C. D. Wilkinson. Topographical control of cell behaviour. I. Simple step cues. Development. 99: 439-48, 1987.

63. Ebendal, T. The relative roles of contact inhibition and contact guidance in orientation of axons extending on aligned collagen fibrils in vitro. Exp Cell Res. 98: 159-69, 1976.

64. Guido, S. and R. T. Tranquillo. A methodology for the systematic and quantitative study of cell contact guidance in oriented collagen gels. Correlation of fibroblast orientation and gel birefringence. J Cell Sci. 105 (Pt 2): 317-31, 1993.

65. Dubey, N., P. C. Letourneau and R. T. Tranquillo. Guided neurite elongation and schwann cell invasion into magnetically aligned collagen in simulated peripheral nerve regeneration. Exp Neurol. 158: 338-50, 1999.

66. Smeal, R. M., R. Rabbitt, R. Biran and P. A. Tresco. Substrate curvature influences the direction of nerve outgrowth. Ann Biomed Eng. 33: 376-82, 2005.

67. Rajnicek, A., S. Britland and C. McCaig. Contact guidance of cns neurites on grooved quartz: Influence of groove dimensions, neuronal age and cell type. J Cell Sci. 110 (Pt 23): 2905-13, 1997.

68. Nagata, I., A. Kawana and N. Nakatsuji. Perpendicular contact guidance of cns neuroblasts on artificial microstructures. Development. 117: 401-8, 1993.

69. Dunn, G. A. and J. P. Heath. A new hypothesis of contact guidance in tissue cells. Exp Cell Res. 101: 1-14, 1976.

70. Clark, P., P. Connolly, A. S. Curtis, J. A. Dow and C. D. Wilkinson. Topographical control of cell behaviour: Ii. Multiple grooved substrata. Development. 108: 635-44, 1990.

71. Britland, S., C. Perridge, M. Denyer, H. Morgan, A. Curtis and C. Wilkinson. Morphogenetic guidance cues can interact synergistically and hierarchically in steering nerve cell growth. Experimental Biology Online. 1: 1-15, 1997.

72. Mahoney, M. J., R. R. Chen, J. Tan and W. M. Saltzman. The influence of microchannels on neurite growth and architecture. Biomaterials. 26: 771-8, 2005.

73. Foley, J. D., E. W. Grunwald, P. F. Nealey and C. J. Murphy. Cooperative modulation of neuritogenesis by pc12 cells by topography and nerve growth factor. Biomaterials. 26: 3639-44, 2005.

74. Dowell-Mesfin, N. M., M. A. Abdul-Karim, A. M. Turner, S. Schanz, H. G. Craighead, B. Roysam, J. N. Turner and W. Shain. Topographically modified surfaces affect orientation and growth of hippocampal neurons. J Neural Eng. 1: 78-90, 2004.

75. Clark, P., P. Connolly, A. S. Curtis, J. A. Dow and C. D. Wilkinson. Cell guidance by ultrafine topography in vitro. J Cell Sci. 99 (Pt 1): 73-7, 1991.

76. Zhang, N., C. Zhang and X. Wen. Fabrication of semipermeable hollow fiber membranes with highly aligned texture for nerve guidance. J Biomed Mater Res A. 75: 941-9, 2005.

77. Curtis, A. S., B. Casey, J. O. Gallagher, D. Pasqui, M. A. Wood and C. D. Wilkinson. Substratum nanotopography and the adhesion of biological cells. Are symmetry or regularity of nanotopography important? Biophys Chem. 94: 275-83, 2001.

78. Bruder, J. M., N. C. Monu, M. W. Harrison and D. Hoffman-Kim. Fabrication of polymeric replicas of cell surfaces with nanoscale resolution. Biomaterials. 27: 460-472, 2006.

79. Bruder, J. M., A. P. Lee and D. Hoffman-Kim. Biomimetic materials replicating schwann cell topography enhance neuronal adhesion and neurite alignment in vitro. Journal of Biomaterials Science, Polymer Edition. 18: 967-982, 2007.

80. Barres, B. A. The mystery and magic of glia: A perspective on their roles in health and disease. Neuron. 60: 430-40, 2008.

81. Singer, M., R. H. Nordlander and M. Egar. Axonal guidance during embryogenesis and regeneration in the spinal cord of the newt: The blueprint hypothesis of neuronal pathway patterning. J Comp Neurol. 185: 1-21, 1979.

82. Sanes, D. H., T. A. Reh and W. A. Harris. Development of the nervous system. Academic Press, 2005.

83. Nagata, I. and N. Nakatsuji. Rodent cns neuroblasts exhibit both perpendicular and parallel contact guidance on the aligned parallel neurite bundle. Development. 112: 581-90, 1991.

84. Biran, R., M. D. Noble and P. A. Tresco. Directed nerve outgrowth is enhanced by engineered glial substrates. Exp Neurol. 184: 141-52, 2003.

85. Deumens, R., G. C. Koopmans, C. G. Den Bakker, V. Maquet, S. Blacher, W. M. Honig, R. Jerome, J. P. Pirard, H. W. Steinbusch and E. A. Joosten. Alignment of glial cells stimulates directional neurite growth of cns neurons in vitro. Neuroscience. 125: 591-604, 2004.

86. Sørensen, A., T. Alekseeva, K. Katechia, M. Robertson, M. O. Riehle and S. C. Barnett. Long-term neurite orientation on astrocyte monolayers aligned by microtopography. Biomaterials. 28: 5498-5508, 2007.

87. Thompson, D. M. and H. M. Buettner. Neurite outgrowth is directed by schwann cell alignment in the absence of other guidance cues. Ann Biomed Eng. 34: 161-8, 2006.

88. Alexander, J. K., B. Fuss and R. J. Colello. Electric field-induced astrocyte alignment directs neurite outgrowth. Neuron Glia Biol. 2: 93-103, 2006.

89. Recknor, J. B., D. S. Sakaguchi and S. K. Mallapragada. Growth and differentiation of astrocytes and neural progenitor cells on micropatterned polymer films. Ann N Y Acad Sci. 1049: 24-7, 2005.

90. Miller, C., S. Jeftinija and S. Mallapragada. Micropatterned schwann cell-seeded biodegradable polymer substrates significantly enhance neurite alignment and outgrowth. Tissue Eng. 7: 705-15, 2001.

91. Walsh, J. F., M. E. Manwaring and P. A. Tresco. Directional neurite outgrowth is enhanced by engineered meningeal cell-coated substrates. Tissue Eng. 11: 1085-94, 2005.

92. Powell, E. M., S. Meiners, N. A. DiProspero and H. M. Geller. Mechanisms of astrocyte-directed neurite guidance. Cell and tissue research. 290: 385-393, 1997.

93.

94. Smith-Thomas, L. C., J. Stevens, J. Fok-Seang, A. Faissner, J. H. Rogers and J. W. Fawcett. Increased axon regeneration in astrocytes grown in the presence of proteoglycan synthesis inhibitors. J Cell Sci. 108 (Pt 3): 1307-15, 1995.

95. Fallon, J. R. Preferential outgrowth of central nervous system neurites on astrocytes and schwann cells as compared with nonglial cells in vitro. Journal of Cell Biology. 100: 198-207, 1985.

96. Tomaselli, K. J. Distinct molecular interactions mediate neuronal process outgrowth on non-neuronal cell surfaces and extracellular matrices. Journal of Cell Biology. 103: 2659-2672, 1986.

97. Liesi, P. Laminin is produced by early rat astrocytes in primary culture. The Journal of Cell Biology. 96: 920-924, 1983.

98. Tomaselli, K. J. Purification and characterization of mammalian integrins expressed by a rat neuronal cell line (pc12): Evidence that they function as alpha/beta heterodimeric receptors for laminin and type iv collagen. Journal of Cell Biology. 107: 1241-1252, 1988.

99. Makita, T., H. M. Sucov, C. E. Gariepy, M. Yanagisawa and D. D. Ginty. Endothelins are vascular-derived axonal guidance cues for developing sympathetic neurons. Nature. 452: 759-63, 2008.

100. Blackshaw, S. E., S. Arkison, C. Cameron and J. A. Davies. Promotion of regeneration and axon growth following injury in an invertebrate nervous system by the use of three-dimensional collagen gels. Proc Biol Sci. 264: 657-61, 1997.

101. Liu, X., D. B. McCreery, R. R. Carter, L. A. Bullara, T. G. Yuen and W. F. Agnew. Stability of the interface between neural tissue and chronically implanted intracortical microelectrodes. IEEE Trans Rehabil Eng. 7: 315-26, 1999.

102. Dai, W., J. Belt and W. M. Saltzman. Cell-binding peptides conjugated to poly(ethylene glycol) promote neural cell aggregation. Biotechnology (N Y). 12: 797-801, 1994.

103. Drury, J. L. and D. J. Mooney. Hydrogels for tissue engineering: Scaffold design variables and applications. Biomaterials. 24: 4337-51, 2003.

104. Gelse, K., E. Poschl and T. Aigner. Collagens--structure, function, and biosynthesis. Adv Drug Deliv Rev. 55: 1531-46, 2003.

105. Hoffman, A. S. Hydrogels for biomedical applications. Ann N Y Acad Sci. 944: 62-73, 2001.

106. Lee, K. Y. and D. J. Mooney. Hydrogels for tissue engineering. Chem Rev. 101: 1869-79, 2001.

107. Wallace, D. G. and J. Rosenblatt. Collagen gel systems for sustained delivery and tissue engineering. Adv Drug Deliv Rev. 55: 1631-49, 2003.

108. Bellamkonda, R., J. P. Ranieri, N. Bouche and P. Aebischer. Hydrogel-based three-dimensional matrix for neural cells. J Biomed Mater Res. 29: 663-71, 1995.

109. Dillon, G. P., X. Yu, A. Sridharan, J. P. Ranieri and R. V. Bellamkonda. The influence of physical structure and charge on neurite extension in a 3d hydrogel scaffold. J Biomater Sci Polym Ed. 9: 1049-69, 1998.

110. Yu, X. and R. V. Bellamkonda. Dorsal root ganglia neurite extension is inhibited by mechanical and chondroitin sulfate-rich interfaces. J Neurosci Res. 66: 303-10, 2001.

111. Flanagan, L. A., Y. E. Ju, B. Marg, M. Osterfield and P. A. Janmey. Neurite branching on deformable substrates. Neuroreport. 13: 2411-5, 2002.

112. Gunn, J. W., S. D. Turner and B. K. Mann. Adhesive and mechanical properties of hydrogels influence neurite extension. J Biomed Mater Res A. 72: 91-7, 2005.

113. Krewson, C. E., S. W. Chung, W. Dai and W. M. Saltzman. Cell aggregation and neurite growth in gels of extracellular matrix molecules. Biotechnology and Bioengineering. 43: 555-62, 1994.

114. Baldwin, S. P., C. E. Krewson and W. M. Saltzman. Pc12 cell aggregation and neurite growth in gels of collagen, laminin and fibronectin. Int J Dev Neurosci. 14: 351-64, 1996.

115. Pittier, R., F. Sauthier, J. A. Hubbell and H. Hall. Neurite extension and in vitro myelination within three-dimensional modified fibrin matrices. J Neurobiol. 63: 1-14, 2005.

116. Borkenhagen, M., J. F. Clemence, H. Sigrist and P. Aebischer. Three-dimensional extracellular matrix engineering in the nervous system. J Biomed Mater Res. 40: 392-400, 1998.

117. Sakiyama, S. E., J. C. Schense and J. A. Hubbell. Incorporation of heparin-binding peptides into fibrin gels enhances neurite extension: An example of designer matrices in tissue engineering. Faseb J. 13: 2214-24, 1999.

118. O'Connor, S. M., D. A. Stenger, K. M. Shaffer and W. Ma. Survival and neurite outgrowth of rat cortical neurons in three-dimensional agarose and collagen gel matrices. Neurosci Lett. 304: 189-93, 2001.

119. Lin, P. W., C. C. Wu, C. H. Chen, H. O. Ho, Y. C. Chen and M. T. Sheu. Characterization of cortical neuron outgrowth in two- and three-dimensional culture systems. J Biomed Mater Res B Appl Biomater. 75: 146-57, 2005.

120. Hayman, M. W., K. H. Smith, N. R. Cameron and S. A. Przyborski. Enhanced neurite outgrowth by human neurons grown on solid three-dimensional scaffolds. Biochem Biophys Res Commun. 314: 483-8, 2004.

121. Camarata, P. J., R. Suryanarayanan, D. A. Turner, R. G. Parker and T. J. Ebner. Sustained release of nerve growth factor from biodegradable polymer microspheres. Neurosurgery. 30: 313-9, 1992.

122. Cao, X. and M. S. Schoichet. Delivering neuroactive molecules from biodegradable microspheres for application in central nervous system disorders. Biomaterials. 20: 329-39, 1999.

123. Cao, X. and M. S. Shoichet. Defining the concentration gradient of nerve growth factor for guided neurite outgrowth. Neuroscience. 103: 831-40, 2001.

124. Grill, R., K. Murai, A. Blesch, F. H. Gage and M. H. Tuszynski. Cellular delivery of neurotrophin-3 promotes corticospinal axonal growth and partial functional recovery after spinal cord injury. J Neurosci. 17: 5560-72, 1997.

125. Kapur, T. A. and M. S. Shoichet. Immobilized concentration gradients of nerve growth factor guide neurite outgrowth. J Biomed Mater Res A. 68: 235-43, 2004.

126. Powell, E. M., M. R. Sobarzo and W. M. Saltzman. Controlled release of nerve growth factor from a polymeric implant. Brain Res. 515: 309-11, 1990.

127. Xu, X., W. C. Yee, P. Y. Hwang, H. Yu, A. C. Wan, S. Gao, K. L. Boon, H. Q. Mao, K. W. Leong and S. Wang. Peripheral nerve regeneration with sustained release of poly(phosphoester) microencapsulated nerve growth factor within nerve guide conduits. Biomaterials. 24: 2405-12, 2003.

128. Sofroniew, M. V., C. L. Howe and W. C. Mobley. Nerve growth factor signaling, neuroprotection, and neural repair. Annu Rev Neurosci. 24: 1217-1281, 2001.

129. Aebischer, P., A. N. Salessiotis and S. R. Winn. Basic fibroblast growth factor released from synthetic guidance channels facilitates peripheral nerve regeneration across long nerve gaps. J Neurosci Res. 23: 282-9, 1989.

130. Ho, P. R., G. M. Coan, E. T. Cheng, C. Niell, D. M. Tarn, H. Zhou, D. Sierra and D. J. Terris. Repair with collagen tubules linked with brain-derived neurotrophic factor and ciliary neurotrophic factor in a rat sciatic nerve injury model. Arch Otolaryngol Head Neck Surg. 124: 761-6, 1998.

131. Wells, M. R., K. Kraus, D. K. Batter, D. G. Blunt, J. Weremowitz, S. E. Lynch, H. N. Antoniades and H. A. Hansson. Gel matrix vehicles for growth factor application in nerve gap injuries repaired with tubes: A comparison of biomatrix, collagen, and methylcellulose. Exp Neurol. 146: 395-402, 1997.

132. Miller, C., S. Jeftinija and S. Mallapragada. Synergistic effects of physical and chemical guidance cues on neurite alignment and outgrowth on biodegradable polymer substrates. Tissue Eng. 8: 367-78, 2002.

133. Gomez, N., Y. Lu, S. Chen and C. E. Schmidt. Immobilized nerve growth factor and microtopography have distinct effects on polarization versus axon elongation in hippocampal cells in culture. Biomaterials. 28: 271-284, 2007.

134. Bruder, J. M. Neuron guidance by biomimetic topographical cues. Ph.D. dissertation, Brown University, 2008.

135. Seggio, A. M., K. S. Ellison, M. R. Hynd, W. Shain and D. M. Thompson. Cryopreservation of transfected primary dorsal root ganglia neurons. Journal of Neuroscience Methods. 173: 67-73, 2008.

136. Dertinger, S. K. W., X. Jiang, Z. Li, V. N. Murthy and G. M. Whitesides. Gradients of substrate-bound laminin orient axonal specification of neurons. Proceedings of the National Academy of Sciences. 99: 12542-12547, 2002.

137. Sonigra, R. J., P. C. Brighton, J. Jacoby, S. Hall and C. B. Wigley. Adult rat olfactory nerve ensheathing cells are effective promoters of adult central nervous system neurite outgrowth in coculture. Glia. 25: 256-269, 1999.

138. Schmalenberg, K. E. and K. E. Uhrich. Micropatterned polymer substrates control alignment of proliferating schwann cells to direct neuronal regeneration. Biomaterials. 26: 1423-30, 2005.

139. Corey, J. M., D. Y. Lin, K. B. Mycek, Q. Chen, S. Samuel, E. L. Feldman and D. C. Martin. Aligned electrospun nanofibers specify the direction of dorsal root ganglia neurite growth. Journal of Biomedical Materials Research Part A. 2007.

140. Blacher, S., V. Maquet, F. Schils, D. Martin, J. Schoenen, G. Moonen, R. Jerome and J. P. Pirard. Image analysis of the axonal ingrowth into poly (d, l-lactide) porous scaffolds in relation to the 3-d porous structure. Biomaterials. 24: 1033-1040, 2003.

141. Li, G. N. Y. and D. Hoffman-Kim. Evaluation of neurite outgrowth anisotropy using a novel application of circular analysis. Journal of Neuroscience Methods. 2008.

142. Ebendal, T.Nerve growth factors. Bath: Wiley, 1989.

143. Borasio, G. D., S. Horstmann, J. M. Anneser, N. T. Neff and M. A. Glicksman. Cep-1347/kt7515, a jnk pathway inhibitor, supports the in vitro survival of chick embryonic neurons. Neuroreport. 9: 1435-9, 1998.

144. Steiner, J. P., G. S. Hamilton, D. T. Ross, H. L. Valentine, H. Guo, M. A. Connolly, S. Liang, C. Ramsey, J. H. Li, W. Huang, P. Howorth, R. Soni, M. Fuller, H. Sauer, A. C. Nowotnik and P. D. Suzdak.

Neurotrophic immunophilin ligands stimulate structural and functional recovery in neurodegenerative animal models. Proc Natl Acad Sci U S A. 94: 2019-24, 1997.

145. Masuda, T., N. Okado and T. Shiga. The involvement of axonin-1/sc2 in mediating notochord-derived chemorepulsive activities for dorsal root ganglion neurites. Dev Biol. 224: 112-21, 2000.

146. Wen, X. and P. A. Tresco. Effect of filament diameter and extracellular matrix molecule precoating on neurite outgrowth and schwann cell behavior on multifilament entubulation bridging device in vitro. J Biomed Mater Res. 76A: 626-37, 2006.

147. Bilsland, J., M. Rigby, L. Young and S. Harper. A rapid method for semi-quantitative analysis of neurite outgrowth from chick drg explants using image analysis. J Neurosci Methods. 92: 75-85, 1999.

148. Bilsland, J. G. and S. J. Harper. Cep-1347 promotes survival of ngf responsive neurones in primary drg explants. Neuroreport. 14: 995-9, 2003.

149. Harper, S., J. Bilsland, L. Young, L. Bristow, S. Boyce, G. Mason, M. Rigby, L. Hewson, D. Smith, R. O'Donnell, D. O'Connor, R. G. Hill, D. Evans, C. Swain, B. Williams and F. Hefti. Analysis of the neurotrophic effects of gpi-1046 on neuron survival and regeneration in culture and in vivo. Neuroscience. 88: 257-67, 1999.

Chapter 2 Optimization by response surface methodology of confluent and aligned cellular monolayers for nerve guidance

Anisotropic tissue structures provide guidance for navigating neurons *in vitro* and *in vivo*. Here we optimized the generation of comparable anisotropic monolayers of astrocytes, endothelial cells, and Schwann cells as a first step toward determining which properties of anisotropic cells are sufficient for nerve guidance. The statistical experimental design method Design of Experiments and the experimental analysis method Response Surface Methodology were applied to improve efficiency and utility. Factors investigated included dimensions of microcontact printed protein patterns, cell density, and culture duration. Protein patterning spacing had the strongest influence. When cells initially aligned at borders and proliferated to fill in spaces, space between stripes was most effective when it was comparable to cell size. Maximizing the area of adhesive molecule coverage was also important for confluence of these types of cells. When cells adhered and aligned over the width of a stripe and broadened to fill spaces, space width about half the cell width was most effective. These findings suggest that if the mechanism of alignment, alignment at borders or over the width of the stripe, is predetermined and the cell size determined, the optimal size of the micropatterning for aligned monolayers of other cell types can be predicted.

2.1 Introduction

The generation of anisotropic tissues is important for a variety of biomedical engineering applications including devising organ replacements, guiding tissue regeneration, designing biomimetic materials, and modeling cellular interactions. The formation of highly organized tissues is also critically important in development i.e. vasculogenesis and angiogenesis,[1, 2] skeletogenesis,[3] myogenesis,[4] etc. Anisotropic guidance is of particular importance in the nervous system. Oriented glial cells and vasculature guide the formation of precise neuronal connections during development.[5-8] Injury to the central nervous system (CNS) results in an inhibitory biochemical barrier to regeneration, but furthermore disrupts the geometric organization of the surrounding tissue.[9] The inherent injury response in the peripheral nervous system (PNS) includes reorganization of the injury site with a favorable anisotropic geometry as well as permissive biochemical factors.[10] As nerves attempt to regenerate after injury in either the CNS or PNS, oriented tissues are important for effective nerve guidance.

Many studies have established that many cell types have the ability to orient to specific guidance cues in their local environments. Endothelial cells (ECs) have been aligned with shear stress,[11, 12] underlying substrate topography,[13] and protein patterns.[13-16] Astrocytes have been aligned with electric fields,[17, 18] mechanical strain,[19] and substrate topography.[19-22] Schwann cells (SCs) have been aligned with substrate topography[23] and protein patterns.[24-26] Oligodendrocytes and fibroblasts have been aligned with topography.[20, 21, 27-30] Generally, cell alignment has been demonstrated, but optimization of alignment is less completely understood.

In the particular case of the nervous system, previous work has shown that neurons are guided by anisotropic tissue structures *in vitro* and *in vivo*. Neurons can align to tissues such as nerve,[31, 32] white matter,[9] muscle,[33-35] and blood vessels;[36-38] to transplanted olfactory ensheathing cells,[39] marrow stromal cells,[40] and tracks of SCs;[41] and in co-cultures with aligned astrocytes,[17, 19, 20, 42] SCs,[23,

[43, 44] meningeal cells,[45] olfactory ensheathing cells,[20] and fibroblasts.[45, 46] In motivating strategies to promote nerve regeneration, this work gives rise to several questions: Is anisotropy of any tissue or cell type sufficient for nerve guidance? Which cellular properties are important for guidance?

In this study, we generated comparable confluent and aligned monolayers of SCs, astrocytes, and ECs. The influence of protein patterning parameters on cellular confluence and alignment was statistically modeled and analyzed quantitatively, and optimal conditions were determined for each cell type. The systematic optimization of biochemical conditions to enhance cellular alignment and confluence was investigated as a first step toward generating anisotropic tissues and biomimetic substrates for studying neuron guidance. Successful application of the statistical experimental design method Design of Experiments (DOE), the experimental analysis method Response Surface Methodology (RSM), and statistical optimization to surface engineering and cell culture parameters was also demonstrated.

2.2 Materials and methods

A summary of the sequence of experimental design and analysis elements involved in this study are presented in Figure 1.

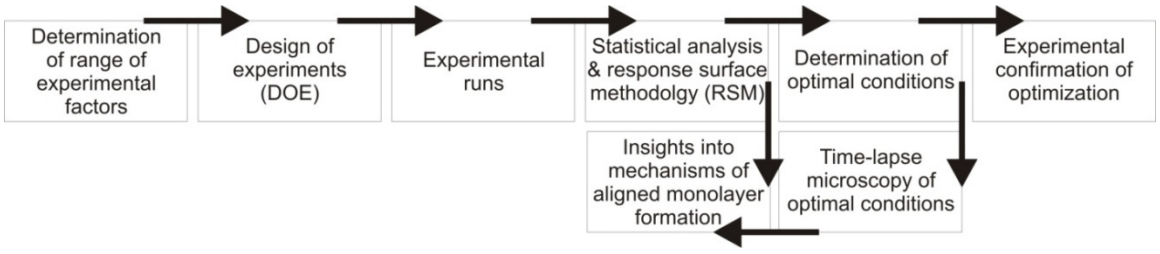

Figure 2.1. Methods of experimental design and analysis

2.2.1 Experimental design and statistical analysis

Statistical software package Design-Expert (Version 7, Stat-Ease, Minneapolis, MN, USA) was used to design and analyze the experiment. A four-factor d-optimal design with a full set of replicates was calculated to model alignment and confluence. The same experimental design was used for the three cell types investigated: astrocytes (A7s), human umbilical vein ECs (HUVECs), and SCs. The four factors investigated for effects on alignment and confluence were width of space between protein stripes, width of protein stripes, starting cell density, and time in culture (Table 1). The first and second factors had five levels each: 10, 20, 30, 40, and 50 μm. The third factor had three levels (determined from confluence experiments): 17K cells cm^{-2}, 26K cells cm^{-2}, and 49K cells cm^{-2}. The fourth factor had two levels: 24h and 48h for A7s and HUVECs, and 48h and 72h for SCs. The number of cells cm^{-2} and the mean vector length (MVL) of the clustering of nuclear alignment at the end of each run were measured with the analysis described below (Table 2).

Table 2.1. Factors investigated for effects on cell alignment and confluence

Factor	Low Value	High Value
A-space width	10 μm	50 μm
B-stripe width	10 μm	50 μm
C-plating density	17K cells cm^{-2}	49K cells cm^{-2}
D-culture time	24h (48h for SCs)	48h (72h for SCs)

2.2.2 Cell culture

Cell culture reagents were from Invitrogen Life Technologies (Carlsbad, CA, USA) unless otherwise indicated. Cultures were incubated at 37°C with 5% CO_2 in a humidified environment.

SCs from rat sciatic nerve, a generous gift of Dr. Mary Bunge (University of Miami, Coral Gables, FL, USA), were cultured on tissue culture plastic dishes coated with 100 μg ml^{-1} poly(L-lysine) (PLL; Sigma, St. Louis, MO, USA) in Dulbecco's modified eagle's medium (DMEM) with 10% fetal bovine serum (FBS), 4 mM L-glutamine, 100 U ml^{-1} penicillin and 100 μg ml^{-1} streptomycin supplemented

with 2 μM forskolin (Sigma), 10 μg ml^{-1} bovine pituitary extract (Sigma) and 2 μM heregulin (generous gift from Genentech, Vacaville, CA, USA) (SC media). Cells used in experiments were between passages 5 and 9.

A7s, a generous gift of Dr. Herbert Geller (Developmental Neurobiology Section, NHLBI, NIH, Bethesda, MD, USA), were cultured on tissue-culture plastic dishes in DMEM with 10% FBS, 4 mM L-glutamine, 100 U ml^{-1} penicillin and 100 μg ml^{-1} streptomycin supplemented with 5 μg ml^{-1} insulin from bovine pancreas. Cells used in experiments were between passages 9 and 13.

HUVECs (PCS-100-010, ATCC, Manassas, VA, USA) were cultured on tissue-culture plastic dishes in endothelial growth media-2 (EGM-2) (Cambrex, Rockland, ME, USA). Cells used in experiments were between passages 5 and 11.

Table 2.2. Responses recorded in 118 experimental runs for each cell types

Response	Low Value	High Value	Average
A7			
mean vector length	0.095	0.693	0.443
terminal cell density	7,979 cells cm^{-2}	106,252 cells cm^{-2}	45,395 cells cm^{-2}
HUVEC			
mean vector length	0.127	0.418	0.282
terminal cell density	4,663 cells cm^{-2}	54,974 cells cm^{-2}	26,776 cells cm^{-2}
SC			
mean vector length	0.532	0.806	0.705
terminal cell density	15,310 cells cm^{-2}	100,933 cells cm^{-2}	50,771 cells cm^{-2}

2.2.3 Determination of cell density at confluence

Cells were allowed to grow to confluence in T25 culture flasks. Samples were fixed with 2% paraformaldehyde (Sigma) in 0.1 M phosphate-buffered saline (PBS). Cells were then stained with 4',6'-diamidino-2-phenylindole (DAPI, Sigma) and analyzed for cell density as described below.

2.2.4 Alignment study

Substrates were prepared as previously described.[47] For SCs and A7s, poly(dimethyl siloxane) (PDMS) microstamps with plateaus of 10 mm length, 10-50 μm width and 10-50 μm pitch were coated with laminin (LN) and stamped onto glass coverslips *via* micro-contact printing. For HUVECs, coverslips were microstamped with human fibronectin (FN) stripes. SCs, A7s, and HUVECs were plated on the appropriate substrates at 17K, 26K, or 49K cells cm^{-2} and incubated for 24-72 h. Cells were fixed with 2% paraformaldehyde (Sigma) in 0.1 M phosphate-buffered saline (PBS), stained with DAPI and analyzed for alignment as described below. Control coverslips coated uniformly with LN or FN were also plated at these cell densities, fixed at appropriate time points, and analyzed.

2.2.5 Confirmation of protein patterning

Fixed samples were blocked for 1 h at room temperature with 10% goat serum (Jackson Immuno Research Laboratories, West Grove, PA, USA) and 1% bovine serum albumin (Sigma) in 0.1 M PBS (blocking buffer) with the addition of 0.1% Triton X-100 (VWR, West Chester, PA, USA) for permeabilization. Samples were incubated overnight at 4°C with a rabbit polyclonal anti-LN primary antibody (Biomedical Technologies Inc., Stoughton, MA, USA) or monoclonal anti-cellular FN primary antibody (Sigma), diluted 1:200 in blocking buffer. Samples were rinsed in PBS, incubated for 1 h at room temperature with Cy2 or Cy3-conjugated goat anti-rabbit secondary antibody or Cy2 or Cy3-conjugated goat anti-mouse secondary antibody (Jackson Immuno Research Laboratories) diluted 1:200 in blocking buffer, rinsed in PBS and viewed under fluorescence microscopy.

2.2.6 Microscopy

12-bit fluorescent images were obtained at 100× magnification with a 30-ms exposure for imaging of DAPI, 100-ms exposure for imaging of immunohistochemistry, and 10-ms exposure for imaging of phase contrast and analyzed as described below.

To visualize alignment and proliferation of support cells on micropatterned substrates, ten 664 μm × 872 μm fields of view (FOVs) were acquired at 100× magnification on a Nikon Eclipse TE2000-S microscope equipped with phase-contrast and epifluorescence optics and software-controlled motorized stage. Samples were oriented so that substrate pattern direction was uniform between samples. Corresponding phase and epifluorescence images were captured using a Hamamatsu Orca-ER camera, an Orbit shutter controller, and a Ludl stage controller, outputting to OpenLab v4.0.4 (Improvision, Lexington, MA, USA). A custom stage automation was written which allows the user to select the area of protein patterning, choose 10 points at random within this area, and obtain corresponding images of phase, DAPI, and stained micropattern.

DAPI images for adhesion and cell density analysis were converted to 8-bit greyscale with Adobe Photoshop CS2, inverted, and the contrast was adjusted using the level and curve functions. Nuclei number were assessed with ImageJ v1.36, using the Otsu function of the multithresholder plugin and the particle analyzer plugin with size filter set to 50–850 pixels to exclude image artifacts and cell clusters. For alignment and confluence analysis, DAPI images were processed as described, and nuclei number and angle of orientation were assessed with ImageJ. This data was analyzed with Oriana v2.02c (Kovach Computing Services, Pentraeth, UK).

2.2.7 Statistical analysis

Circular analysis was used to analyze the angular distributions of the major axes of the nuclei.[48] Circular mean vectors were calculated, where the length of the mean vector corresponds to the degree of clustering of the data, and the direction of the mean vector corresponds to the mean direction of the data. Uniformity of the distribution of nuclei was assessed using a Rao's spacing test and alignment of nuclei in the direction of the substrate pattern was assessed with a V-test. Oriana

2.02c software was used for circular analysis. For all cases, a *P* value of 0.05 was taken to be significant. Design results were analyzed by standard analysis of variance (ANOVA) and fitted to a second-order polynomial equation.

2.3 Results

2.3.1 Design of experiments

In this study, we investigated the effects of protein pattern dimensions, cell plating density, and time in culture on the generation of aligned, confluent monolayers of three cell types. In order to optimize the experimental efficiency, DOE was utilized. A D-optimal design, which is generated by an iterative search algorithm that minimizes the covariance of the parameter estimates for a specified model, was selected and reduced the number of required experiments from 150 to 59 for each cell type. We hypothesized that several factors would interact to affect the monolayers, i.e. that plating density and culture time would interact to affect the terminal cell density. Therefore, a second order interaction model was chosen so that both the main effects of each individual factor as well as any dual factor interactions could be investigated. The following model was proposed to describe the monolayers.

$$Y = x + x_1A + x_2B + x_3C + x_4D + x_{12}AB + x_{13}AC + x_{14}AD + x_{23}BC + x_{24}BD + x_{34}CD$$

Where Y is the response (either mean vector length or terminal cell density), A is the space between protein stripes, B is the width of protein stripes, C is the initial plating density, D is the culture time, and x_i and x_{ij} are the coefficients.

2.3.2 Factors and responses analyzed

The space between protein stripes and the width of protein stripes were varied from 10-50 μm in 10 μm intervals. The initial plating densities and culture times were determined from pilot experiments that established the density of each cell type at confluence (Figure 2A). At confluence, the density of

A7s was 105,000 ± 20,000 cells cm^{-2} (Figure 2B), the density of HUVECs was 41,000 ± 9,000 cells cm^{-2} (Figure 2C), and the density of SCs was 55,000 ± 14,000 cells cm^{-2} (Figure 2D). Initial plating densities for the experiments of the study were chosen to correspond to approximately half of the cell density of each cell type at confluence, i.e. 49K, 17K, and 26K cells cm^{-2}. In pilot experiments plating cells on LN coated coverslips at these densities, most samples were confluent within 48h (A7s, HUVECs) or 72h (SCs). Thus culture times of 24h, 48h, and 72h were chosen for investigation. Mean vector length of the distribution of nuclear angles was used as a measure of overall alignment (Figure 3), and the number of cells stained by DAPI and counted was used as a measure of the final confluence.

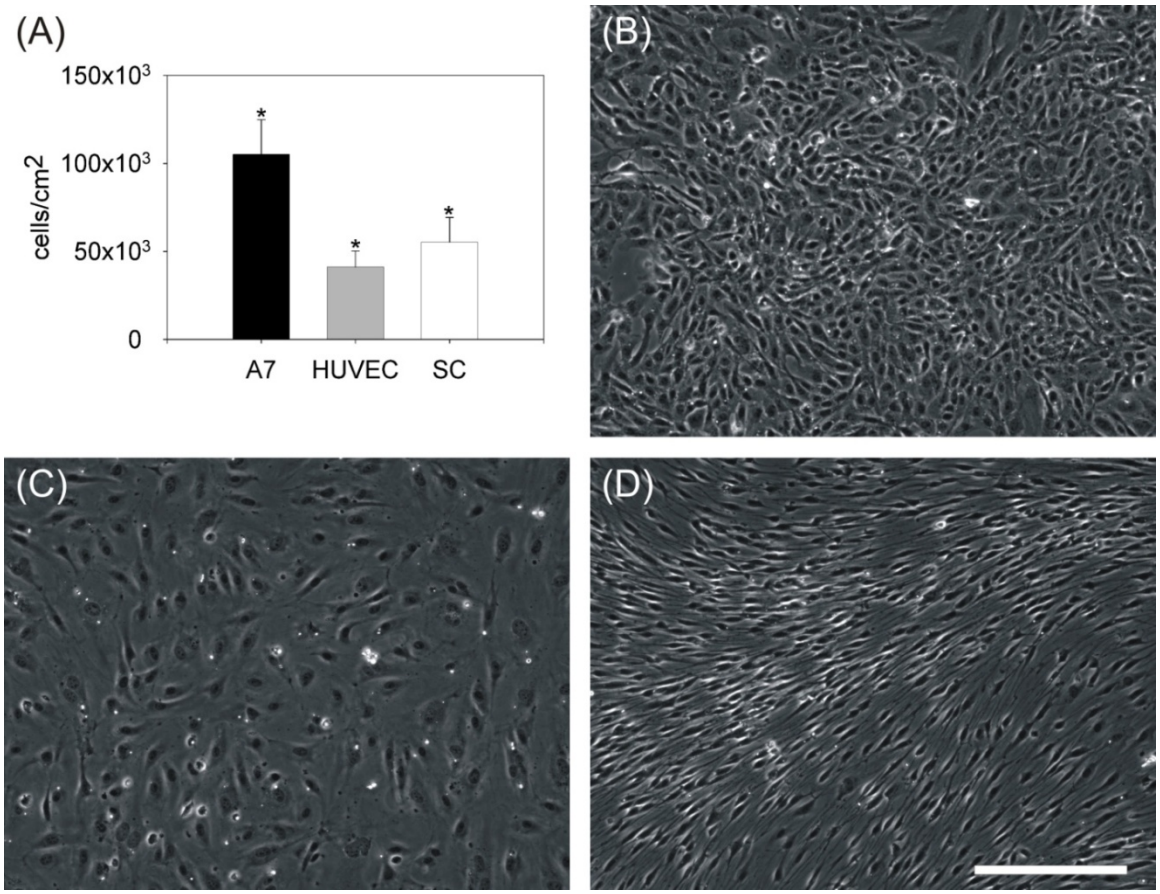

Figure 2.2. Cell density at confluence varied among A7s, HUVECs, and SCs.
(A) Graph of the cell density of A7s, HUVECs, and SCs grown to confluence and counted (n=3). Phase contrast micrographs of A7s (B), HUVECs (C), and SCs (D) at confluence. * Indicates difference from other cell types with $p<0.05$. Scale bar, 200 μm.

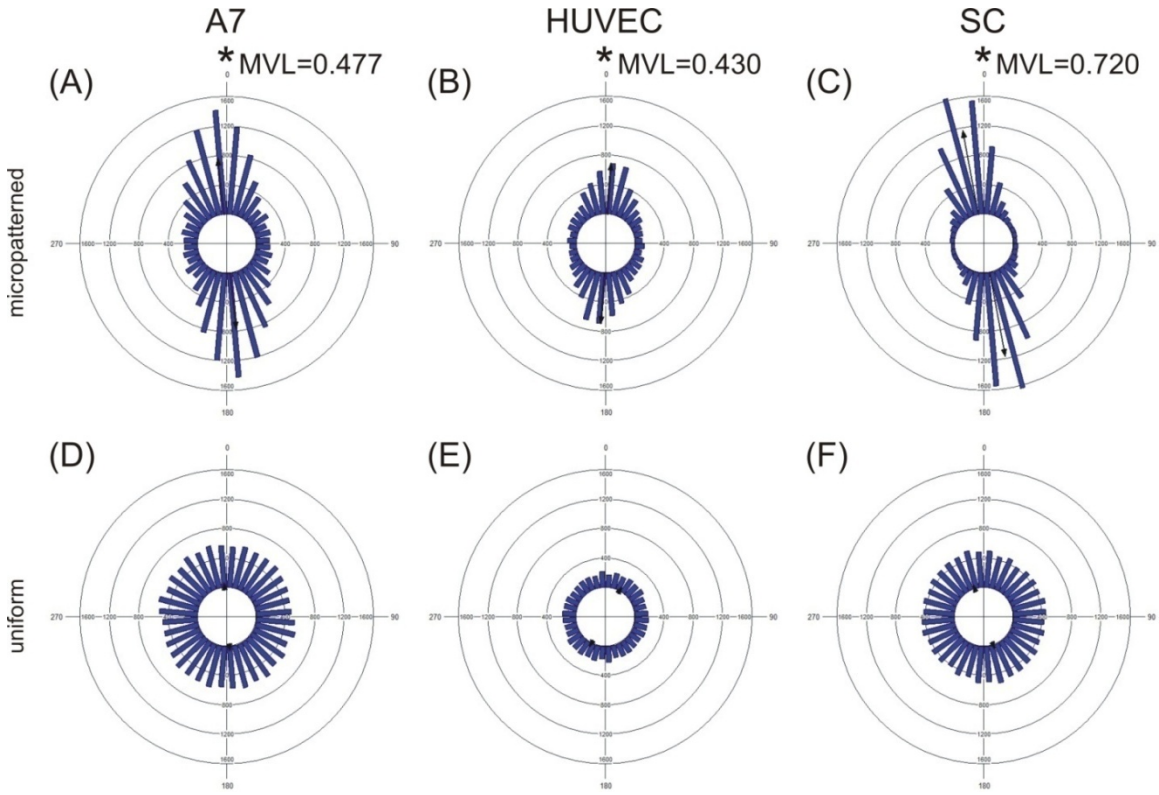

Figure 2.3. Cellular alignment on micropatterned substrates was clustered in the direction of the micropatterns. Circular histograms of A7s (A,D), HUVECs (B,E), and SCs (C,F) plated at 49K cm^{-2} and cultured for 48h on optimal protein micropatterned substrates (A-C) or on uniformly protein coated substrates (D-F). * Indicates difference from a uniform distribution with $p<0.05$ by Rao's spacing test.

The D-optimal mixture design and response results for each run can be found in supplementary materials. From the 150 candidate points for each cell type, 59 experimental points were chosen by Design Expert software to establish the model and assess the fit of the model. These experimental points included vertices, centers of the edges, blends of the inner experimental space, and overall centroid. Each run was replicated for a total of 118 runs for each cell type. All runs were carried out in the order given by the software. Of the 354 runs in the study, 21 runs were repeated at the end of all trials to replace runs that contained sub-optimal microstamping or cell health as revealed by immunohistochemistry. The high, low, and average responses recorded for each cell type are presented in Table 2.

The RSM models for all cell types are presented in Tables 3 and 4 and Figures 4-7. The models are presented in two ways: (1) with coefficients that correspond to the actual experimental variables (i.e. protein stripe width in μm); and (2) with coded coefficients that are transformed so the high value of the variable becomes +1 and the low value becomes -1 (i.e. transformation of the equation such that protein stripe width of 50 μm would equal +1 and protein stripe width of 10 μm would equal -1). Coded coefficients allowed for comparison across conditions. In each case tested, the model explained the response well, as the lack of fit was not significant ($p>0.05$). Stepwise regression was performed; where the coefficients with the largest p-value were consecutively deleted until only significant coefficients remained. The coefficients and contributions before elimination of insignificant variables can be found in supplementary materials.

2.3.3 Protein pattern dimensions influenced A7 alignment.

The width of protein patterning and spacing had significant effects on the alignment of A7s (Table 3). Interactions between spacing and culture time and interactions between starting density and culture time were also significant (Table 3). The following model for A7 alignment was obtained, with coefficients corresponding to actual factors:

$$mean\ vector\ length = 0.643 + 2.09 \times 10^{-3}A - 2.85 \times 10^{-3}B - 6.56 \times 10^{-6}C - 1.16 \times 10^{-3}D - 1.01 \times 10^{-4}AD + 1.57 \times 10^{-7}CD$$

Where A is the space between protein stripes (μm), B is the width of protein stripes (μm), C is the initial plating density (cells cm^{-2}), and D is the culture time (h). Contour plots based on this equation are shown in Figure 4. The resulting model suggests that at low starting cell density and shorter culture time, alignment increased with decreasing stripe width (Figure 4A). At higher starting density and longer culture time, alignment increased with decreasing space width (Figure 4D). The contribution of the influence of stripe width on A7 alignment was stronger than the contribution of space width in the range of conditions tested (contribution of 47.7% for stripe width vs. 14.9% for

space width). The interaction terms of AD (9.0%) and CD (19.6%) also significantly contributed to the model.

Table 2.3. Effect estimates for alignment from the result of Design Expert analysis.
Coded coefficients are transformed so the high value of the factor becomes +1 and the low value becomes -1 (i.e. for A, 50μm becomes +1 and 10 μm becomes -1). *Indicates the factor as a significant contributor to the model with p<0.05, **Indicates an insignificant lack of fit with p>0.05

	Factor	Coefficient (Actual Factor)	Coefficient (Coded Factor)	Standard Error (Coded)	Percent Contribution	P-value
A7	Model					<0.0001*
	Intercept	0.643	0.440	0.009		
	A-space width	2.09×10^{-3}	-0.031	0.012	14.9%	0.0109*
	B-stripe width	-2.85×10^{-3}	-0.057	0.012	47.7%	<0.0001*
	C-plating density	-6.56×10^{-6}	-0.015	0.01	4.5%	0.1621
	D-culture time	-1.16×10^{-3}	0.012	0.009	4.2%	0.1728
	AD	-1.01×10^{-4}	-0.024	0.012	9.0%	0.0468*
	CD	1.57×10^{-7}	0.03	0.01	19.6%	0.0037*
	Lack of fit					0.9172**
HUVEC	Model					<0.0001*
	Intercept	0.338	0.290	0.006		
	A-space width	-1.34×10^{-3}	-0.027	0.009	32.6%	0.0032*
	B-stripe width	1.64×10^{-3}	-0.033	0.009	47.3%	0.0005*
	C-plating density	1.13×10^{-6}	0.018	0.008	20.1%	0.019*
	Lack of fit					0.7534**
SC	Model					<0.0001*
	Intercept	0.633	0.710	0.005		
	A-space width	3.42×10^{-3}	-0.013	0.006	11.2%	0.0432*
	C-plating density	1.34×10^{-6}	0.022	0.006	42.7%	<0.0002*
	D-culture time	8.22×10^{-4}	-0.015	0.005	28.1%	0.0019*
	AD	-6.81×10^{-5}	-0.016	0.007	18.0%	0.0140*
	Lack of fit					0.5838**

2.3.4 Protein stripe pattern, plating density, and culture time influenced terminal density of A7s.

The width of protein stripes, starting cell density, and culture time had significant effects on the terminal density of A7s (Table 4). The interaction between stripe width and plating density was also significant. The following model for A7 terminal density was obtained, with coefficients corresponding to actual factors:

$$density = -41900 + 538B - 0.698C + 1620D + 0.0188BC - 22.7BD$$

Where B is the width of protein stripes (μm), C is the initial plating density (cells cm^{-2}), and D is the culture time (h). Contour plots based on this equation are shown in Figures 6 and 7. Final cell density increased as plating density and culture time increased (Figure 6A, D). As stripe width increased, the final cell density increased (Figure 7A). The influence of plating density on A7 confluence was stronger than the influence of culture time in the range tested (contributions of 61.1% for plating density vs. 28.3% for culture time), and both were stronger than the influence of stripe width (contribution of 4.7%). The interaction terms of BC (2.7%) and BD (3.2%) also contributed to the model.

2.3.5 Protein pattern dimensions and plating density influenced HUVEC alignment.

The width of protein patterning and spacing had significant effects on the alignment of HUVECs (Table 3). The effect of the starting cell density was also significant. The following model for HUVEC alignment was obtained, with coefficients corresponding to actual factors:

$$mean\ vector\ length = 0.338 - 1.34 \times 10^{-3}A - 1.64 \times 10^{-3}B + 1.13 \times 10^{-6}C$$

Where A is the space between protein stripes (μm), B is the width of protein stripes (μm), and C is the initial plating density (cells cm^{-2}). Contour plots based on this equation are shown in Figures 4 and 5. The resulting model shows that alignment increased with decreasing protein stripe width and decreasing spacing independent of the starting density and culture time (Figure 4B and 4E). Alignment also increased as the starting cell density increased (Figure 5A). The contribution of the influence of stripe width was stronger than the contribution of space width to HUVEC alignment in the range tested (contributions of 47.3% for stripe width vs. 32.6% for space width), and both were stronger than the influence of cell density (20.1%).

Table 2.4. Effect estimates for terminal density from the result of Design Expert analysis.
Coded coefficients are transformed so the high value of the factor becomes +1 and the low value becomes -1 (i.e. for A, 50μm becomes +1 and 10 μm becomes -1). *Indicates the factor as a significant contributor to the model with p<0.05, **Indicates an insignificant lack of fit with p>0.05

	Factor	Coefficient (Actual Factor)	Coefficient (Coded Factor)	Standard Error (Coded)	Percent Contribution	P-value
A7	Model					<0.0001*
	Intercept	-41900	49700	1430		
	B-stripe width	538	6880	2060	4.7%	0.0011*
	C-plating density	0.698	20200	1680	61.1%	<0.0001*
	D-culture time	1620	11200	1380	28.3%	<0.0001*
	BC	0.0189	6030	2380	2.7%	0.0127*
	BD	-22.7	-5450	1980	3.2%	0.0068*
	Lack of fit					0.1557**
HUVEC	Model					<0.0001*
	Intercept	-1960	28000	811		
	C-plating density	0.445	7120	951	57.7	<0.0001*
	D-culture time	424	5090	795	42.3	<0.0001*
	Lack of fit					0.9799**
SC	Model					<0.0001*
	Intercept	1330	53300	1030		
	A-space width	248	-5930	1480	6.4%	0.0001*
	B-stripe width	-666	7580	1490	10.3%	<0.0001*
	C-plating density	1.43	15000	1230	59.3%	<0.0001*
	D-culture time	38.7	6730	1020	17.3%	<0.0001*
	AC	-0.0165	-5280	1790	3.5%	0.004*
	BD	17.4	4180	1480	3.2%	0.0057*
	Lack of fit					0.1925**

2.3.6 Plating density and culture time influenced HUVEC terminal density.

Starting cell density and culture time had significant effects on the confluence of HUVECs (Table 4). The following model for HUVEC terminal density was obtained, with coefficients corresponding to actual factors:

$$density = -1960 + 0.445C + 424D$$

Where C is the initial plating density (cells cm^{-2}) and D is the culture time (h). Contour plots based on this equation are shown in Figure 6. Final cell density increased as plating density and culture time

increased (Figure 6B, E). The influence of plating density on HUVEC confluence was stronger than the influence of culture time in the range tested (contributions of 57.7% for plating density vs. 42.3% for culture time).

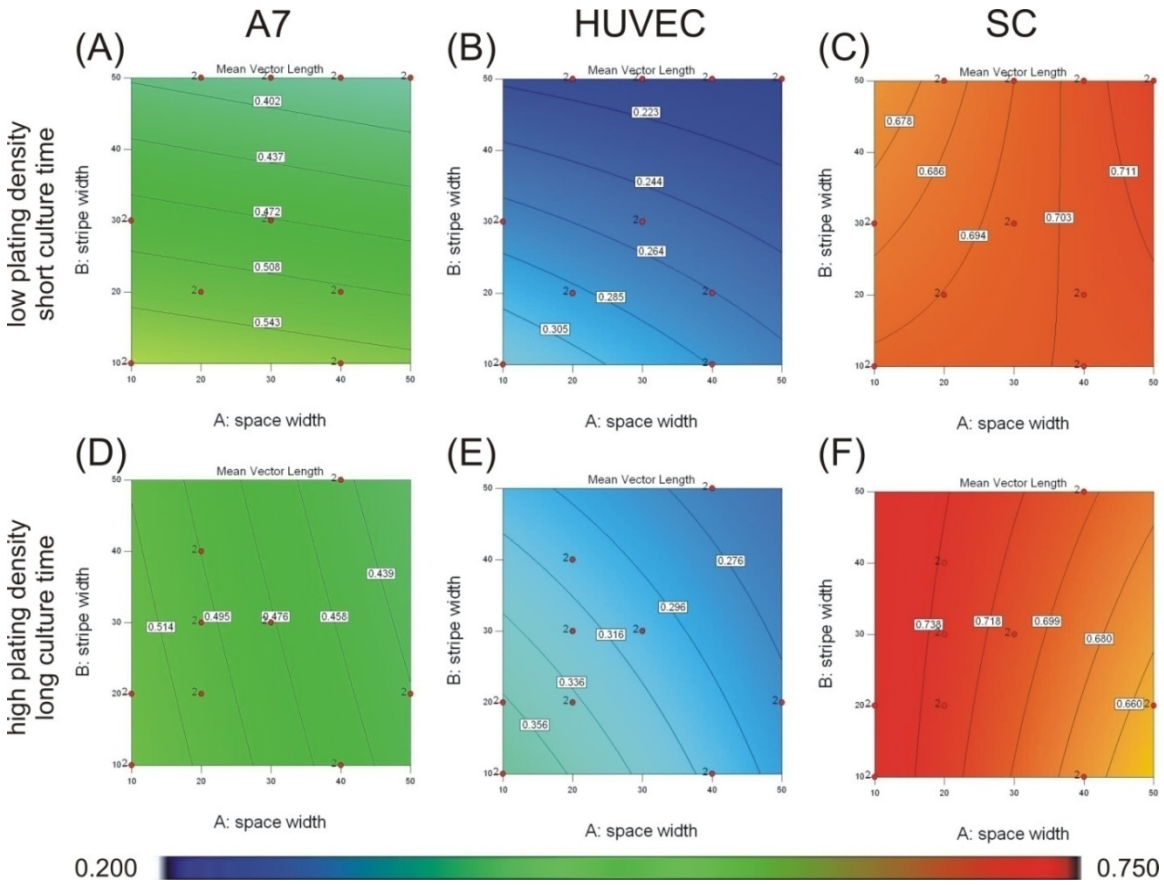

Figure 2.4. Micropattern dimensions affected alignment of cells.
Contour graphs showing the effects of protein stripe and space width on mean vector length when plated at 17K cells cm^{-2} for 24h (48h for SCs) (A-C) or plated at 49K cells cm^{-2} for 48h (72h for SCs) (D-F). Experimental conditions were determined and analyzed with Design Expert 7 software. An ANOVA model of mean vector length was calculated and graphed for A7s (A,D), HUVECs (B, E), and SCs (C, F). Mean vector magnitudes are indicated by contour lines and colorimetric scale, blue-red, 0.20-0.75. Design points carried out experimentally are indicated with red dots.

2.3.7 Plating density and culture time influenced SC alignment.

Starting cell density and culture time had significant effects on the alignment of SCs (Table 3). The space between protein stripes was also significant. The following model for SC alignment was obtained, with coefficients corresponding to actual factors:

$$mean\ vector\ length = 0.633 + 3.42 \times 10^{-3}A + 1.34 \times 10^{-6}C + 8.22 \times 10^{-4}D - 6.81 \times 10^{-5}AD$$

Where A is the space between protein stripes (μm), C is the initial plating density (cells cm^{-2}), and D is the culture time (h). Contour plots based on this equation are shown in Figures 4 and 5. The resulting model shows that at low starting cell density and shorter culture time, alignment increased with increasing space width (Figure 4C). At higher starting density and longer culture time, alignment increased with decreasing space width (Figure 4F). Alignment increased with increased starting cell density and culture time (Figure 5B). The contribution of plating density was stronger than the contributions of culture time (contributions of 42.7% for plating density vs. 28.1% for culture time), and both were stronger than the contribution of space width to SC alignment (11.2%). The interaction term AD also contributed (18.0%).

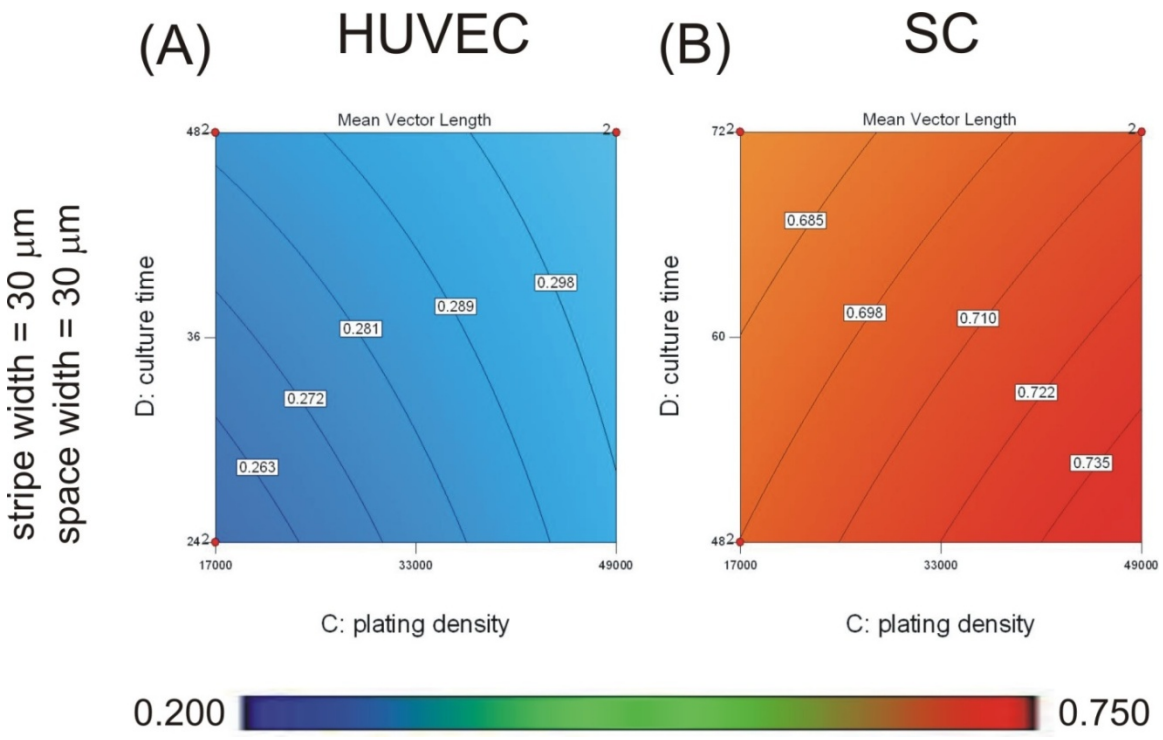

Figure 2.5. Plating density affected alignment of HUVECs and SCs.
Contour graphs showing the effects of plating density and culture time on mean vector length when plated on micropatterns with 30 μm protein stripe and space width. Experimental conditions were determined and analyzed with Design Expert 7 software. An ANOVA model of mean vector length was calculated and graphed for HUVECs (A), and SCs (B). Mean vector magnitudes are indicated by contour lines and colorimetric scale, blue-red, 0.20-0.75. Design points carried out experimentally are indicated with red dots.

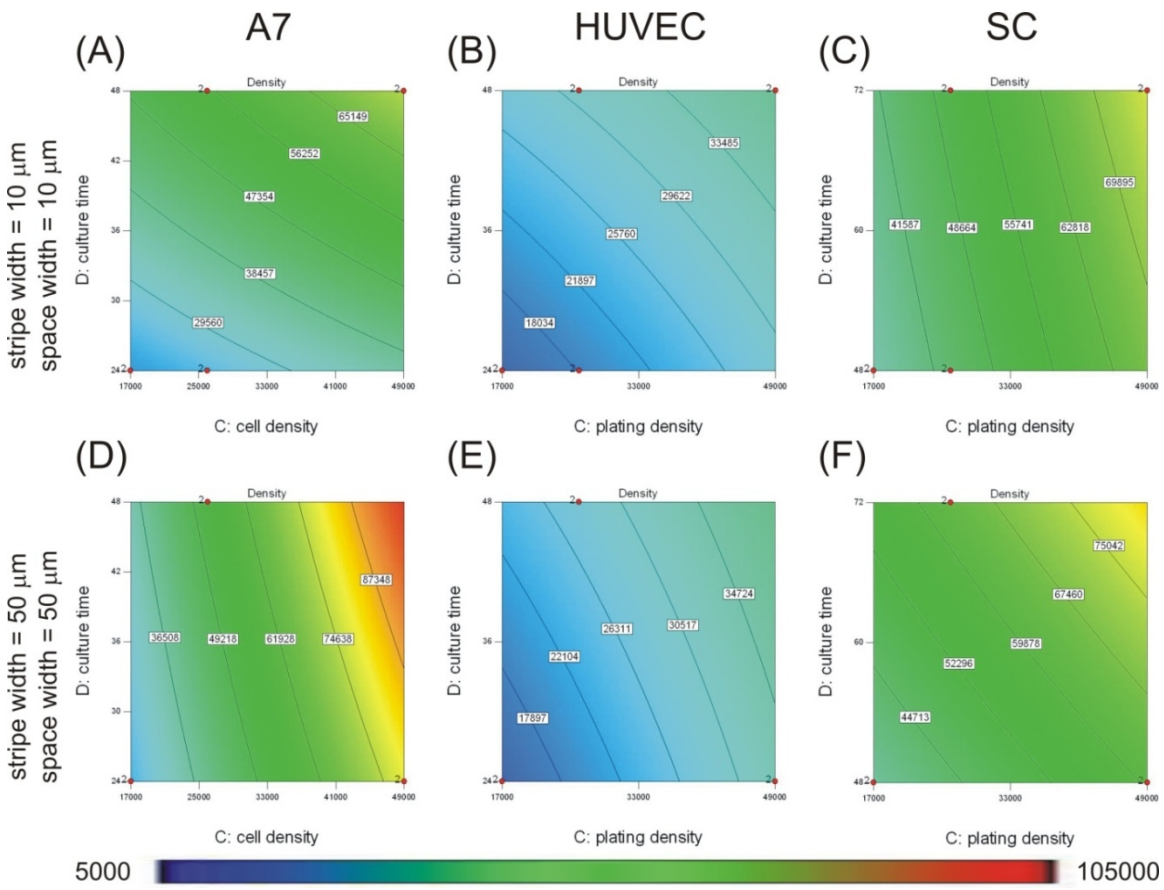

Figure 2.6. Plating density and culture time affected terminal density of cells.
Contour graphs showing the effects of protein stripe and space width on cell number when plated on micropatterns with 10 µm protein stripe and space width (A-C) or micropatterns with 50 µm protein stripe and space width (D-F). Experimental conditions were determined and analyzed with Design Expert 7 software. An ANOVA model of final cell number was calculated and graphed for A7s (A,D), HUVECs (B, E), and SCs (C, F). Cell number magnitudes are indicated by contour lines and colorimetric scale, blue-red, 5K-105K cells cm^{-2}. Design points carried out experimentally are indicated with red dots.

2.3.8 Pattern dimensions, plating density, and culture time influenced SC terminal cell density.

All four factors had significant effects on the terminal density of SCs (Table 3). The interaction between space width and plating density and between stripe width and culture time were also significant (Table 4). The following model for SC confluence was obtained, with coefficients corresponding to actual factors:

$$density = 1330 + 248A - 666B + 1.43C + 38.7D - 0.0165AC + 17.4BD$$

Where A is the space between protein stripes (μm), B is the width of protein stripes (μm), C is the initial plating density (cells cm^{-2}), and D is the culture time (h). Contour plots based on this equation are shown in Figures 6 and 7. Final cell density increased as plating density and culture time increased (Figure 6C, F). As stripe width increased, the terminal cell density increased, and as space width increased, cell density decreased (Figure 7B). The influence of cell density had the strongest influence on SC confluence (contribution of 59.3%). The influences of stripe width and culture time in the range tested were weaker (contributions of 10.3% for stripe width and 17.3% for culture time) with the smallest influence coming from space width (6.4%). The interaction terms of AC and BD also contributed (3.5% for AC and 3.2% for BD).

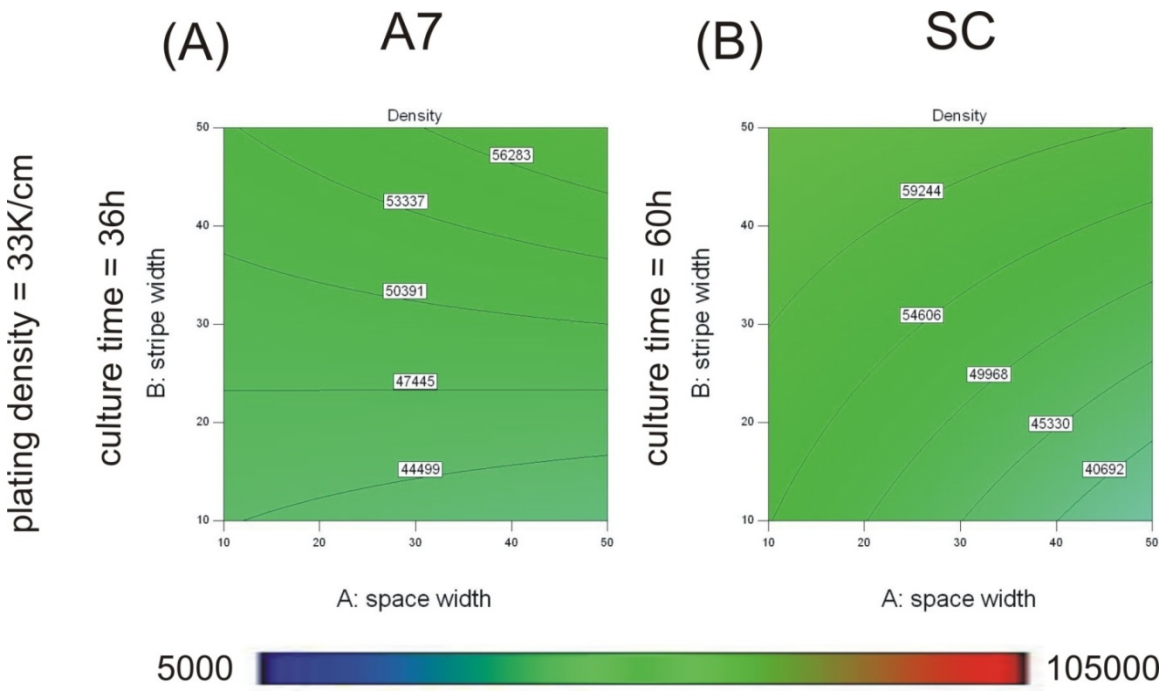

Figure 2.7. Protein stripe width affected the confluence of A7s and SCs.
Contour graphs showing the effect of protein stripe and space width on cell number when plated at 33K/cm2 for 36h for A7s (A) and 60h for SCs (B). Experimental conditions were determined and analyzed with Design Expert 7 software. An ANOVA model of cell number was calculated and graphed for A7s (A) and SCs (B). Cell number magnitudes are indicated by contour lines and colormetric scale, blue-red, 5K-105K cells cm-2. Design points carried out experimentally are indicated with red dots.

2.3.9 Contributions of factors varied across cell types.

Presentation of coded coefficients allowed us to compare the relative contributions of experimental parameters to cell responses across cell types. Cellular alignment of all three cell types was affected by pattern spacing. The contribution of pattern spacing to alignment was similar for A7s and HUVECs (coded coefficients of -0.031 for A7s and -0.027 for HUVECs), but reduced by half for SCs (coded coefficient of -0.013). The contribution of stripe width to the alignment of A7s was greater than that for HUVECs (coded coefficients of -0.057 for A7s vs. -0.033 for HUVECs). The contribution of plating density to the alignment of HUVECs and SCs was similar (coded coefficients of 0.018 for HUVECs and 0.022 for SCs).

Monolayer terminal cell density of all three cell types was affected by plating density and culture time. The contribution of plating density to terminal cell density was smallest for HUVECs (coded coefficient of 7120), intermediate for SCs (coded coefficient of 15000), and strongest for A7s (coded coefficient of 20200). The contribution of culture time to the terminal cell density was weakest for HUVECs (coded coefficient of 5090), intermediate for SCs (coded coefficient of 6730), and strongest for A7s (coded coefficient of 11200). The contribution of stripe width to the terminal cell density of

SCs was stronger than the contribution to the terminal cell density of A7s (coded coefficients of 7580 for SCs vs 6880 for A7s).

2.3.10 Optimal conditions for culture of confluent, aligned monolayer varied among cell types.

To determine the optimal conditions for confluent and/or aligned monolayers, a series of rules was applied systematically. To determine the conditions by which confluence would be achieved for monolayers of each cell type, the following criteria were applied: the space and stripe width must be

between 10 and 50 μm, the starting cell density must be between 17K and 49K cells cm^{-2}, the culture time must be between 24 and 48h for A7s and HUVECs and be between 48 and 72h for SCs, and the cell density must be between 85-125K cells cm^{-2} for A7s, 32-50K cells cm^{-2} for HUVECs, and 41-69K cells cm^{-2} for SCs. The required conditions for each cell type are presented in Table 5.1. For A7 confluence, there were 60 answers with equal desirability. These combinations can be found in supplementary materials. Space widths ranged from 17-50 μm, stripe widths ranged from 17-50 μm, plating density ranged from 45,000-49,000 cells cm^{-2}, and culture time ranged from 33-48h. For HUVEC confluence, there were 80 answers with equal desirability. These combinations can be found in supplementary materials. Space widths ranged from 10-49 μm, stripe widths ranged from 10-50 μm, plating density ranged from 29,000-49,000 cells cm^{-2}, and culture time ranged from 27-48h. For SC confluence, there were 80 answers with equal desirability. These combinations can be found in supplementary materials. Space widths ranged from 10-50 μm, stripe widths ranged from 10-50 μm, plating density ranged from 17,000-49,000 cells cm^{-2}, and culture time ranged from 48-72h.

To determine the best alignment under the conditions tested (sub-confluent or confluent), the same bounds were applied for the factors, no bound was placed on the terminal density, and the mean vector length had to be maximized. The strongest alignment conditions for each cell type are presented in Table 5.2. SC optimal alignment (MVL = 0.763 ± 0.014) was notably higher than A7 optimal alignment (MVL = 0.578 ± 0.035) and HUVEC optimal alignment (MVL = 0.373 ± 0.017).

For optimization of a confluent, aligned monolayer of each cell type, the same rules were applied for the factors, the mean vector length of nuclear angles had to be maximized, and the cell number had to be between 85-125K cells cm^{-2} for A7s, 32-50K cells cm^{-2} for HUVECs, and 41-69K cells cm^{-2} for SCs. The optimal conditions for each cell type are presented in Table 5.3. Within the bounds applied to the factors, SC optimal alignment (MVL = 0.759 ± 0.014) was higher than A7 optimal alignment (MVL

Table 2.5. Numerical optimizations of culture conditions with Design Expert.

Factor	Input Bounds	Model Output		
		A7	*HUVEC*	*SC*
5.1 CONFLUENT				
space width	10-50 µm	17-50 µm	10-49 µm	10-50 µm
stripe width	10-50 µm	17-50 µm	10-50 µm	10-50 µm
plating density	17-49K cm^{-2}	45-49K cm^{-2}	29-49K cm^{-2}	17K-49K cm^{-2}
culture time	24-48h 48-72h (SC)	33-48h	27-48h	48-72h
terminal density	85-125K cm^{-2} (A7) 32-50K cm^{-2} (HUVEC) 41-69K cm^{-2} (SC)	85-96K cm^{-2}	32-41K cm^{-2}	41-68K cm^{-2}
Desirability		1.000 (60 answers)	1.000 (80 answers)	1.000 (80 answers)
5.2 OPTIMAL ALIGNMENT				
space width	10-50 µm	10 µm	10 µm	10 µm
stripe width	10-50 µm	10 µm	10 µm	50 µm
plating density	17-49K cm^{-2}	17K cm^{-2}	49K cm^{-2}	49K cm^{-2}
culture time	24-48h 48-72h (SC)	24h	48h	48h
mean vector length	Maximize	0.578 ± 0.035	0.373 ± 0.017	0.763 ± 0.014
Desirability		0.808	0.752	0.844
5.3 OPTIMAL ALIGNMENT AT CONFLUENCE (IN RANGE OF EXPERIMENTS)				
space width	10-50 µm	16 µm	10 µm	10 µm
stripe width	10-50 µm	50 µm	10 µm	49 µm
plating density	17-49K cm^{-2}	49K cm^{-2}	49K cm^{-2}	46K cm^{-2}
culture time	24-48h 48-72h (SC)	48h	48h	48h
mean vector length	Maximize	0.498 ± 0.046	0.373 ± 0.017	0.759 ± 0.014
terminal density	85-125K cm^{-2} (A7) 32-50K cm^{-2} (HUVEC) 41-69K cm^{-2} (SC)	85K ± 8K cm^{-2}	32K ± 2K cm^{-2}	69K ± 6K cm^{-2}
Desirability		0.674	0.752	0.829
5.4 MATCHED ALIGNMENT AT CONFLUENCE				
space width	10-50 µm	50 µm	10 µm	50 µm
stripe width	10-50 µm	50 µm	10 µm	28 µm
plating density	17-49K cm^{-2}	49K cm^{-2}	49K cm^{-2}	17K cm^{-2}
culture time	24-48h 48-72h (SC)	31h	48h	72h
mean vector length	0.373 minimize (SC)	0.376 ± 0.036	0.373 ± 0.017	0.659 ± 0.011
terminal density	85-125K cm^{-2} (A7) 32-50K cm^{-2} (HUVEC) 41-69K cm^{-2} (SC)	85K ± 6K cm^{-2}	32K ± 2K cm^{-2}	41K ± 3K cm^{-2}
Desirability		1.000	0.752	0.533
5.5 OPTIMAL ALIGNMENT AT CONFLUENCE (LARGER RANGE)				
space width	1-100 µm	1-31 µm	1 µm	1-84 µm
stripe width	1-100 µm	1-100 µm	1 µm	1-98 µm
plating density	0-100K cm^{-2}	50-81K cm^{-2}	100K cm^{-2}	45-68K cm^{-2}
culture time	0-72h 0-96h (SC)	58-72h	18h	<1-36h
mean vector length	Maximize	0.693-0.784	0.435 ± 0.037	0.806-0.863
terminal density	85-125K cm^{-2} (A7) 32-50K cm^{-2} (HUVEC) 41-69K cm^{-2} (SC)	95-125K cm^{-2}	50K ± 5K cm^{-2}	42-68K cm^{-2}
Desirability		1.000 (75 answers)	0.941	1.000 (77 answers)

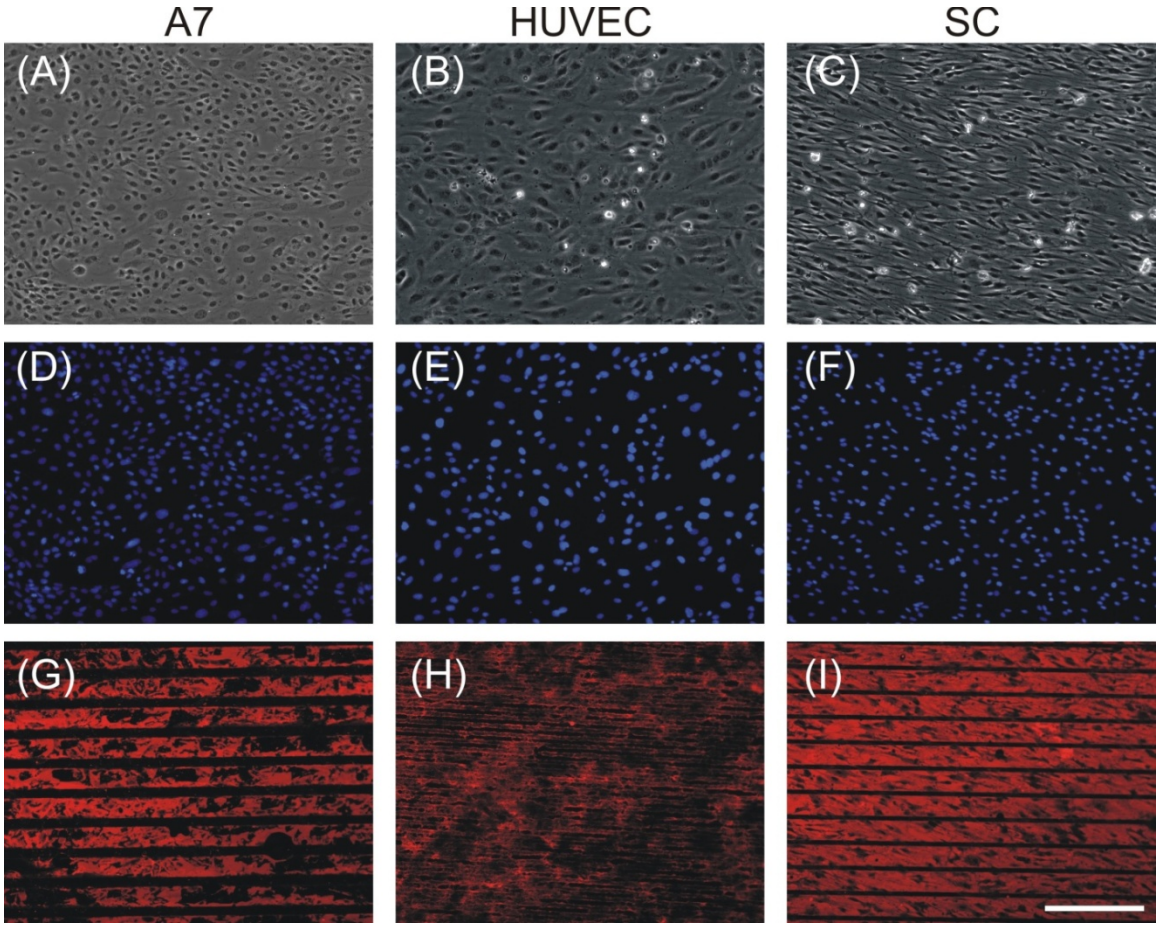

Figure 2.8. Experimental runs support model predictions.
Phase contrast (A-C) and epifluorescent images (D-I) of A7s plated at 49K cells cm^{-2} for 48h on LN stripes of 50 μm with 20 μm spaces (A, D, G), HUVECs plated at 49K cells cm^{-2} for 48h on FN stripes of 10μm with 10 μm spaces (B, E, H), and SCs plated at 49K cells cm^{-2} for 48h on LN stripes of 50 μm with 10 μm spaces (C, F, I). Cultures were stained with DAPI (D-F), with anti-LN (G,I) or anti-FN (H). Scale bar, 200 μm.

= 0.498 ± 0.046) and HUVEC optimal alignment (MVL = 0.373 ± 0.017). Alignment at confluence for HUVECs and SCs did not vary from alignment at any terminal density.

Monolayers of all three cell types were cultured under these conditions (Figure 3, 8). A7 alignment (MVL = 0.477) and confluence (87K cells cm^{-2}) were in the range of the predicted results (0.498 ±0.046 and 85,000±7,531). HUVEC alignment (MVL = 0.430) and confluence (48K cells cm^{-2}) were higher than the predicted results (0.373±0.017 and 32,000±2,180). SC alignment (MVL = 0.720) was

lower than the predicted result (0.759±0.014), while the confluence (67K cell cm^{-2}) was in the range of the predicted result (69,000±5,632).

2.3.11 Cellular dynamics underlying alignment varied among cell types.

Timelapse microscopy under optimal conditions for each cell type revealed further differences in cellular alignment among the cell types. Timelapse movies can be found in supplementary materials. At one hour after plating, A7s had just begun to adhere to the substrate (Figure 9A) while SCs had adhered and a few cells had begun to orient in the direction of the pattern (Figure 9C). The SCs initially appeared to be aligning along the boundaries of the stripes as they were in single file lines that were spaced 50 μm apart. By one hour, most of the HUVECs had adhered and elongated in the direction of the pattern, over the width of the stripe (Figure 9B). By four hours, SCs and HUVECs had similar elongation and confluence (Figure 9F and 9E), but elongation of A7s had just begun (Figure 9D). While most of the HUVECs and SCs at these time points appeared to move only parallel to the direction of the pattern, there were a number of astrocytes that moved in other directions, even perpendicular to the pattern and crossing several stripes. SCs rarely crossed over more than one stripe, and HUVECs remained confined to the 10 μm stripes. Between 4h and 10h, little change in alignment or confluence was seen in any of the cell types (Figure 9G-I), but the cells remained motile, moving mostly parallel to the pattern direction. HUVEC cell bodies were no longer as confined to the 10 μm stripes with their cell bodies broadened into the spaces between stripes. Between 10h and 24h, there was marked proliferation of all three cell types (Figure 9J-L). By 24h, A7s were 75% confluent, SCs were 90% confluent, and HUVECs were 95% confluent. At 48h, the cultures were confluent and remained aligned in the direction of the underlying protein pattern (Figure 9M-O).

2.4 Discussion

The central goal of this study was to generate confluent and aligned monolayers of support cells for

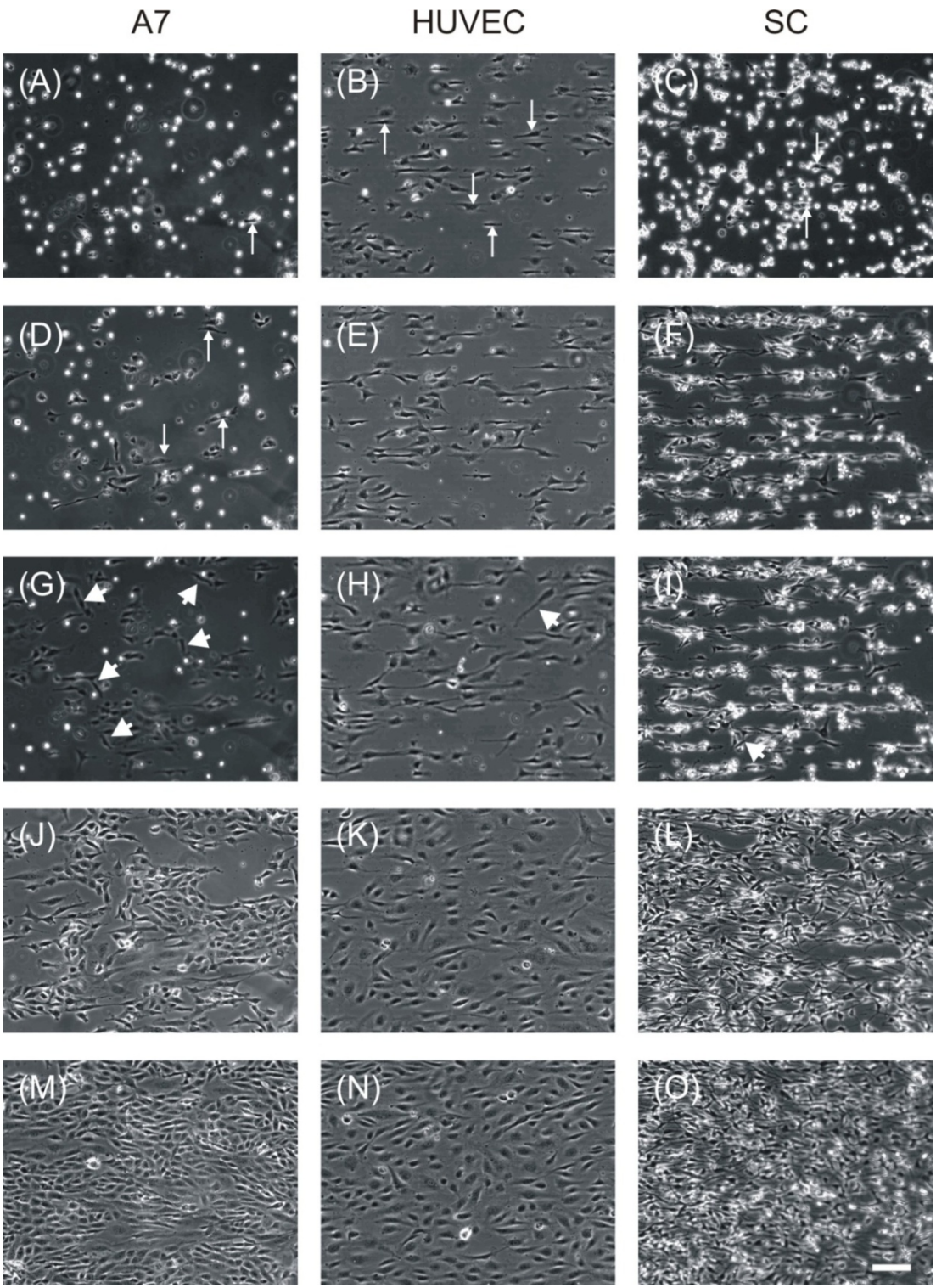

Figure 2.9. Timelapse microscopy of aligned monolayer generation reveals differences among cells types. Phase contrast images obtained by timelapse microscopy of A7s plated at 49K cells cm^{-2} after 1h (A), 4h (D), 10h (G), 24h (J), and 48h (M) on LN stripes of 50 μm with 20 μm spaces, HUVECs plated at 49K cells/cm^2 after 1h (B), 4h (E), 10h (H), 24h (K), and 48h (N) on FN stripes of 10μm with 10 μm spaces, and SCs plated at 49K cells/cm^2 after 1h (C), 4h (F), 10h (I), 24h (L), and 48h (O) on LN stripes of 50 μm with 10 μm spaces. Arrows indicate cells beginning elongation along micropattern. Arrow heads indicate cells moving in directions different from the pattern. Scale bar, 100 μm.

studying neuron guidance. Toward this end, the influence of protein patterning and culture parameters on cellular confluence and alignment were statistically modeled and analyzed quantitatively, and optimal conditions were determined from these models for each cell type. Confluent and aligned monolayers of A7s, HUVECs, and SCs were achieved through culture on micropatterned proteins, and the predicted optimal conditions by which these monolayers can be achieved varied among the cell types tested.

2.4.1 Design of experiments

Statistical experimental design was applied to improve the experimental efficiency of modeling confluence and alignment of these cell types. DOE has been demonstrated to be efficient and satisfactory for the acquisition of information to correlate independent factors with response in formulation composition and/or manufacturing processing parameters.[49, 50] Most of the experimentation in cellular alignment optimization is performed by changing the levels of each variable separately while keeping the remaining variables constant, leading to a large number of experiments.[24-26] One-factor-at-a-time investigations also ignore interactions between factors and do not elucidate which factors are most important and thus often do not provide information about the overall optimum. One of the most well-utilized experimental analysis methods for examination of factors is RSM.[49-52] RSM is a set of statistical methods which consists of using a set of designed experiments to obtain an optimal response. Experimental factors are modeled as a continuous function to approximate the optima of individual or multiple responses. Contour plots are often used to represent the response to two variables. Points on these plots are generated from a number of experimental trials and intermediate values between them are determined by mathematical interpolation. Results that can be analyzed by RSM can be designed *D*-optimally. The reasons for using optimal design instead of standard classical design, i.e the simplex design, are that standard factorial designs require numbers of runs that are prohibitively large for reasonable allocation of resources and time, and/or the design space is constrained i.e. the process space contains factor

settings that are not feasible or are impossible to run.[53] A *D*-optimal design is generated by an iterative search algorithm and seeks to minimize the covariance of the parameter estimates for a specified model. This is equivalent to maximizing the determinant $D = |X^T X|$, where X is the design matrix of model terms (the columns i.e. space width, stripe width, etc.) evaluated at specific treatments in the design space (the rows i.e. 10 μm, 20 μm, etc.). When the responses of interest are expressed in a model as a continuous function of the factors involved, the model could reveal, graphically and mathematically, regions of desirable formulation compositions that satisfy the criteria imposed by the experimenter.[53]

A7s and SCs were chosen for modeling and generation of anisotropic cultures because while it has been well recognized that the different chemical cues presented by SCs and astrocytes after injury contribute to the varied capacities for regeneration in the PNS and CNS, the contributions of the physical features of these distinct glia to the promotion of axon regrowth and guidance have not been studied together. We were also interested in determining if guidance by anisotropic tissues was limited to the features of glial cells, so HUVEC was chosen for characterization as a non-glial cell type. Astrocytes, ECs, and SCs have been cultured to aligned confluence previously, but not under similar conditions so that their influence on neuron growth can be compared in the same experiments. Generation of confluent layers is important so that the influence of the cellular cue can be evaluated. Micropatterning was chosen as a common alignment method since previous work with SCs and ECs has shown it effective, and because of its ease and flexibility.[54] Protein stripe and space width were varied at 10 um intervals from 10-50 um as these dimensions are on the scale of cellular dimensions and are in the range of dimensions that have been employed to align these and other cell types in our lab as well as other labs. Cell plating density was chosen as the number of cells that would be required to cover half of the substrate for each cell type. Culture time was chosen based on pilot experiments where it was qualitatively determined that the cells had reached confluence.

In order to study these cell types as anisotropic substrates, we were interested in achieving cultures that were both aligned and confluent. Circular statistical analysis and mean vector length of nuclear angles were chosen to measure alignment because circular orientation data such as alignment is better described by a resultant vector rather than an arithmetic mean[48] and the mean vector length corresponds to the clustering of the angles of the nuclei.[47] Changes in cellular shape have been shown to affect the shape of the nucleus,[30, 55] and previous work has shown that the angle of the major axis of the nucleus is an effective measure of cellular orientation.[44, 56] Other studies have utilized the nuclear form factor (NFF) as a measure of cellular alignment.[13] Because compared alignment across cell types, this method was not used as nuclear shape of the three cell types varied.

Table 2.6. Summary of key findings.
*Note: optimal conditions may be outside range tested.

	A7	HUVEC	SC
Most important factor for aligned monolayer:	Protein stripe width	Cell density	Cell density
Other key factors:	Protein space width Cell density Culture time	Protein stripe width	Culture time Protein space width
How well optimized: (MVL)	0.498 model 0.443 experimental	0.373 model* 0.418 experimental*	0.759 model 0.705 experimental
Suggested mechanism:	1. Align to stripes. 2. Fill spaces between stripes by proliferating.	1. Align to entire stripes. 2. Fill spaces between stripes by broading to fill spaces.	1. Align to stripe edges. 2. Fill spaces between stripes by proliferating and aligning to each other.

2.4.2 Contributions of factors and interpretation of responses

Our models and analysis of cellular alignment and confluence revealed different contributions of factors among the cell types tested (Table 6). SCs had the highest degree of alignment of the cell types, and plating density had the largest contribution to both their alignment and their confluence. Culture time and space width each contributed to SC alignment and confluence as well. Our multi-factorial approach also revealed that the effect of space width changed when influenced by other factors; for short cultures, increased space width increased alignment, but for longer cultures,

increased space width decreased alignment. As the aligned SC monolayers were forming, SCs showed a high capacity for alignment to protein patterns. The size of protein stripe was not a significant factor to SC alignment as SCs initially aligned to stripe borders and demonstrated a high affinity for alignment to each other as they filled in. The optimal conditions for SC alignment at confluence were the largest stripe width tested (50 μm), the smallest space width tested (10 μm), the highest plating density tested (49K cells cm^{-2}), and the shortest culture time tested (48h).

HUVECs had the lowest alignment of the cell types tested. The most important factor in achieving anisotropic HUVEC monolayers was plating density as it was the strongest contributing factor to confluence of HUVECs and also played a role in alignment. Stripe width was also an important factor for HUVEC alignment, as the cells' initial confinement to small stripes was imperative for achieving aligned monolayers. The optimal conditions for HUVEC alignment and confluence were small stripe and space width (10 μm) and high cell density (49K cells cm^{-2}) and culture time (48h).

A7s' alignment was intermediate between the HUVECs and the SCs. The most important factor in achieving confluent, aligned monolayers of A7s was protein stripe width as it was the strongest contributing factor to mean vector length and also significantly influenced terminal cell density. Our multi-factorial approach revealed several interesting interactions of factors that influenced this cell type. At low starting cell density and shorter culture time, alignment increased with decreasing stripe width, whereas at higher starting density and longer culture time, alignment increased with decreasing space width. Space width played an important role at longer culture times, suggesting that the way cells fill in the spaces is critical for the maintenance of alignment at confluence. The optimal conditions for confluent, aligned A7s were the largest stripe width tested (50 μm), space width of approximately the width of A7s (17 μm), and high plating density (49K cells cm^{-2}), and culture time (48h).

2.4.3 Potential mechanisms of aligned monolayer formation

With our combinatorial approach, we observed and analyzed the complexity of cellular interactions with micropatterned materials under a range of conditions; taking these observations together points toward possible mechanisms that underlie the formation of confluent, aligned monolayers of cells. SCs achieved their highly aligned monolayers by aligning first to the protein stripe edges, then proliferating and aligning to each other. Thus initial plating density strongly affected SC alignment and confluence. Increased width of the protein stripes increased terminal cell density by providing larger areas of adhesive substrate for initial adhesion and proliferation, but was inconsequential for alignment in these studies. Further, when space widths between the protein stripes were on the order of the size of a single SC, cells could fill in and align within the spaces more efficiently and overall alignment was enhanced.

The relatively low alignment of HUVECs achieved in this study may indicate a lower capacity for alignment to protein tracks by these cells, or may suggest that the optimal conditions for aligning HUVECs were outside the range tested. For example, timelapse microscopy revealed that HUVECs aligned to stripes much earlier than A7s and SCs, so their optimal alignment may be achieved at an earlier timepoint than those studied here. While SCs initially aligned to the edges of stripes, optimally aligned HUVECs adhered and aligned onto the entire 10μm wide stripes and initially remained confined to the stripes. HUVECs then broadened by 24h to fill the spaces between the stripes.

The intermediately aligned A7 cultures exhibited the widest range of responses among the cell types to the range of factors tested, and had clear optimal conditions for achieving aligned, confluent monolayers. A7s adhered and aligned to the 50μm protein stripes, then filled in the 20 μm spaces between the stripes, taking the longest time of the three cell types to adhere and spread. Steric

hindrance and/or cell-cell interactions likely allowed the A7s to fill in most effectively when the spaces were on the scale of cellular size. A7s differed from SCs and HUVECs in their dynamics, with a number of A7s moving in directions non-parallel to the protein patterns, most likely because they were larger than 20 μm and could interact with more than one stripe at a time. Of note, A7s were the most closely packed together cell type at confluence, and required the highest plating density and the longest time in culture to achieve their confluence.

Our study of the generation of anisotropic monolayers of three cell types revealed general trends of importance across cell types. The spacing of the protein patterning was the most important. When cells initially adhered and aligned at borders and proliferated to fill in spaces (A7s or SCs), space between the protein stripes was most effective when it was on the order of cell width (20 μm for A7s and 10 μm for SCs). When cells adhered and aligned over the width of a stripe and broadened to fill spaces (HUVECs), space width about half the size of the cell was most effective. Some cell types appeared to have an aligned morphology that was not dependent on stripe width (A7s and SCs), but the aligned shape of other cells was strongly influenced by the pattern on which they were aligned (HUVECs). Maximizing the area of adhesive molecule coverage was also important for confluence unless cells were large enough to broaden to fill spaces between the stripes. Taken together, these results suggest that if the mechanism of alignment is predetermined and the cell size determined, the optimal size of the micropatterning for aligned monolayers of other cell types can be predicted.

2.4.4 Comparisons to single factor approaches

Several of these culture parameters have also been studied previously, but typically in one-at-a-time approaches. Vartanian et al. studied the effect of culture time on baboon carotid artery ECs plated at 50,000 cells cm^{-2} on 25 μm collagen I stripes with 100 μm spaces and found that alignment increased from 0 to 24h, but was not changed between 24 and 48h.[14] While culture time was not a significant

contributing factor to HUVEC alignment in the present study, our choice of FN may have provided a stronger molecule for alignment of these cells. Feinberg et al. also studied the effect of pattern dimension on the alignment of primary porcine vascular ECs and found that while ECs did not align to 5 μm stripes of FN with 5 μm spaces, they did align to 50 μm stripes and spaces.[13] The smaller stripe and space sizes may have been too small to be detected by ECs which are larger than 5 μm. In comparison, HUVECs aligned to stripes tested in our study, where the smallest features tested were larger than this threshold. Wu et al. studied the effect of FN stripe width on the alignment of HUVECs and found a similar trend to our results; as width decreased from 60 to 15 μm, alignment increased.[15] They also found that cell area decreased, the length of the short axis of the cell decreased, and apoptosis increased. While we did not test for apoptosis directly, HUVECs were plated at confluence for many of our conditions, and it was clear from timelapse microscopy that not all of the cells survived. Similar to the Wu study, our cells were also qualitatively less broad on micropatterns than on flat substrates.

Schmalenberg and Uhrich studied the effects of pattern dimensions and culture time on SC alignment and found that there was no difference in the alignment of SCs plated at 100K cells cm^{-2} at 4h and at confluence and that pattern spacing of 40 μm did not direct alignment as well as spacing of 20 and 30 μm.[26] This trend also agrees with our finding that decreased space width increases alignment at confluence. Thompson and Buettner also studied the effects of pattern dimension, plating density, and culture time on SC alignment, but not in a multi-factorial approach. They employed micropatterns with LN stripe width ranging from 20-30 μm and space width ranging from 2-20 μm and found no significant effect on the degree of orientation.[25] Our study supports these findings as we also showed that stripe width was not a significantly contributing factor to SC alignment. Our study also extends this work since by testing a wider range of space widths we were able to determine an optimal space width (10 μm). They found that seeding density had no effect on alignment at 6 and 24 h,[24] while in longer cultures, alignment dipped at 48h but increased by 120h.[25] Of note, though our starting densities were higher, we also found that 48h was our optimal culture

time for SC alignment. With timelapse microscopy, Thompson and Buettner found that most SC elongation occurred in the first 12h of culture, and cells were motile throughout the experiment, continuing to move up and down the pattern even after they were completely aligned. Crossing to neighboring stripes was also noted, although crossing behavior diminished following alignment. Our timelapse results for SCs were similar despite the differences in plating densities.

2.4.5 Versatility of response surface methodology

RSM of confluence and alignment of the three cell types also allows the possibility for the alignment and/or terminal cell density of the cell types investigated to be matched. To determine the conditions by which cultures could be generated in which the three cell types have similar alignments, the same input parameters were applied, but rather than maximizing the mean vector for each cell type, the mean vector length was set to 0.373, the optimal value for HUVECs. The predicted conditions are shown in Table 5.4. The optimal HUVEC value is outside of the range of possible SC values predicted by the model in the range of conditions tested. Minimization of the alignment of SCs in the range of conditions tested toward matching the optimal alignment of the HUVECs predicts a mean vector length of 0.659 ± 0.011. Of note, because SCs align more strongly than HUVECs to the tested micropatterns, matching mean vector lengths cannot be achieved in this range of conditions.

This model can also be used to predict the alignment and confluence of cells cultured outside the range of the conditions tested. For example the bounds can be expanded such that the space and stripe width must be between 1 and 100 μm, the starting cell density must be between 0K and 100K cells cm^{-2}, the culture time must be between 0 and 72h for A7s and HUVECs and be between 0 and 96h for SCs, the mean vector length of nuclear angles must be maximized, and the cell number must be between 85-125K cells cm^{-2} for A7s, 32-50K cells cm^{-2} for HUVECs, and 41-69K cells cm^{-2} for SCs.

The predictions under these conditions are presented in Table 5.5. For A7 and SC, there were multiple answers with equal desirability. These combinations can be found in supplementary materials.

2.5 Conclusion

In conclusion, the formation of aligned monolayers of three cell types was optimized by response surface methodology as a first step toward generation of anisotropic tissues and biomimetic substrates for the study of nerve guidance. A strength of biomedical engineering approaches is the combination of design and problem solving techniques of engineers with the multifaceted experiments of biological sciences. The problem-solving power of DOE and RSM tools has been well recognized in chemical and pharmaceutical engineering; here we have demonstrated the benefits of applying these powerful tools to biomedical engineering areas such as tissue engineering and biomaterials. Current approaches to biological problems that require large number of variables can suffer from the expense of large amounts of time and resources, ignore interactions between inputs, and importantly, are not always well equipped to determine the relative contributions of inputs. The approaches utilized in this study offer a more efficient, economical, informative, and rigorous way to probe cellular responses to various and multiple factors. Finally, this study has also provided insights into the general mechanisms of cellular adhesion, alignment, and monolayer formation – key events that underlie the development of cell- and biomaterial-based therapeutics.

2.6 Acknowledgements

The authors would like to thank Christina Johnson and Grace Li for helpful discussion of the initial experimental set-up. They would also like to thank Carmichael Ong, Liane Livi, Cameron Rementer, and Jesse Thon for assistance with imaging and analysis. Si wafers were fabricated at the BioMEMS

Resource Center with the generous assistance of Octavio Hurtado. This work was funded by an NSF Career Award to DHK and an AAUW Selected Professions dissertation fellowship to CK.

2.7 References

1. Tomanek, R. J. Formation of the coronary vasculature during development. Angiogenesis. 8: 273-84, 2005.

2. Schmidt, A., K. Brixius and W. Bloch. Endothelial precursor cell migration during vasculogenesis. Circ Res. 101: 125-36, 2007.

3. Wood, A. and P. Thorogood. An ultrastructural and morphometric analysis of an in vivo contact guidance system. Development. 101: 363-381, 1987.

4. Sabourin, L. A. and M. A. Rudnicki. The molecular regulation of myogenesis. Clinical genetics. 57: 16, 2000.

5. Singer, M., R. H. Nordlander and M. Egar. Axonal guidance during embryogenesis and regeneration in the spinal cord of the newt: The blueprint hypothesis of neuronal pathway patterning. J Comp Neurol. 185: 1-21, 1979.

6. Gomes, F. C., T. C. Spohr, R. Martinez and V. Moura Neto. Cross-talk between neurons and glia: Highlights on soluble factors. Braz J Med Biol Res. 34: 611-20, 2001.

7. Silver, J., M. A. Edwards and P. Levitt. Immunocytochemical demonstration of early appearing astroglial structures that form boundaries and pathways along axon tracts in the fetal brain. The Journal of Comparative Neurology. 328: 415-436, 1993.

8. Makita, T., H. M. Sucov, C. E. Gariepy, M. Yanagisawa and D. D. Ginty. Endothelins are vascular-derived axonal guidance cues for developing sympathetic neurons. Nature. 452: 759-63, 2008.

9. Pettigrew, D. B. and K. A. Crutcher. White matter of the cns supports or inhibits neurite outgrowth in vitro depending on geometry. J Neurosci. 19: 8358-66, 1999.

10. Bunge, R. P. and C. Fernandez-Valle. The biology of schwann cells. Neuroglia. H. Kettenmann and BR Ransom, editors. Oxford University Press, Oxford. 44: 57, 1995.

11. Nerem, R. M., M. J. Levesque and J. F. Cornhill. Vascular endothelial morphology as an indicator of the pattern of blood flow. J Biomech Eng. 103: 172-6, 1981.

12. Malek, A. M. and S. Izumo. Mechanism of endothelial cell shape change and cytoskeletal remodeling in response to fluid shear stress. J Cell Sci. 109 (Pt 4): 713-26, 1996.

13. Feinberg, A. W., W. R. Wilkerson, C. A. Seegert, A. L. Gibson, L. Hoipkemeier-Wilson and A. B. Brennan. Systematic variation of microtopography, surface chemistry and elastic modulus and the state dependent effect on endothelial cell alignment. J Biomed Mater Res A. 2007.

14. Vartanian, K. B., S. J. Kirkpatrick, S. R. Hanson and M. T. Hinds. Endothelial cell cytoskeletal alignment independent of fluid shear stress on micropatterned surfaces. Biochem Biophys Res Commun. 371: 787-92, 2008.

15. Wu, C. C., Y. S. Li, J. H. Haga, R. Kaunas, J. J. Chiu, F. C. Su, S. Usami and S. Chien. Directional shear flow and rho activation prevent the endothelial cell apoptosis induced by micropatterned anisotropic geometry. Proc Natl Acad Sci U S A. 104: 1254-9, 2007.

16. Chen, C. S., M. Mrksich, S. Huang, G. M. Whitesides and D. E. Ingber. Geometric control of cell life and death. Science. 276: 1425-8, 1997.

17. Alexander, J. K., B. Fuss and R. J. Colello. Electric field-induced astrocyte alignment directs neurite outgrowth. Neuron Glia Biol. 2: 93-103, 2006.

18. Borgens, R. B., R. Shi, T. J. Mohr and C. B. Jaeger. Mammalian cortical astrocytes align themselves in a physiological voltage gradient. Exp Neurol. 128: 41-9, 1994.

19. Biran, R., M. D. Noble and P. A. Tresco. Directed nerve outgrowth is enhanced by engineered glial substrates. Exp Neurol. 184: 141-52, 2003.

20. Deumens, R., G. C. Koopmans, C. G. Den Bakker, V. Maquet, S. Blacher, W. M. Honig, R. Jerome, J. P. Pirard, H. W. Steinbusch and E. A. Joosten. Alignment of glial cells stimulates directional neurite growth of cns neurons in vitro. Neuroscience. 125: 591-604, 2004.

21. Webb, A., P. Clark, J. Skepper, A. Compston and A. Wood. Guidance of oligodendrocytes and their progenitors by substratum topography. J Cell Sci. 108 (Pt 8): 2747-60, 1995.

22. Recknor, J. B., J. C. Recknor, D. S. Sakaguchi and S. K. Mallapragada. Oriented astroglial cell growth on micropatterned polystyrene substrates. Biomaterials. 25: 2753-67, 2004.

23. Miller, C., H. Shanks, A. Witt, G. Rutkowski and S. Mallapragada. Oriented schwann cell growth on micropatterned biodegradable polymer substrates. Biomaterials. 22: 1263-9, 2001.

24. Thompson, D. M. and H. M. Buettner. Schwann cell response to micropatterned laminin surfaces. Tissue Eng. 7: 247-65, 2001.

25. Thompson, D. M. and H. M. Buettner. Oriented schwann cell monolayers for directed neurite outgrowth. Ann Biomed Eng. 32: 1120-30, 2004.

26. Schmalenberg, K. E. and K. E. Uhrich. Micropatterned polymer substrates control alignment of proliferating schwann cells to direct neuronal regeneration. Biomaterials. 26: 1423-30, 2005.

27. Clark, P., P. Connolly, A. S. Curtis, J. A. Dow and C. D. Wilkinson. Topographical control of cell behaviour. I. Simple step cues. Development. 99: 439-48, 1987.

28. den Braber, E. T., J. E. de Ruijter, L. A. Ginsel, A. F. von Recum and J. A. Jansen. Quantitative analysis of fibroblast morphology on microgrooved surfaces with various groove and ridge dimensions. Biomaterials. 17: 2037-44, 1996.

29. Walboomers, X. F., H. J. Croes, L. A. Ginsel and J. A. Jansen. Contact guidance of rat fibroblasts on various implant materials. J Biomed Mater Res. 47: 204-12, 1999.

30. Dalby, M. J., M. O. Riehle, S. J. Yarwood, C. D. Wilkinson and A. S. Curtis. Nucleus alignment and cell signaling in fibroblasts: Response to a micro-grooved topography. Exp Cell Res. 284: 274-82, 2003.

31. David, S. and A. J. Aguayo. Axonal elongation into peripheral nervous system "Bridges" After central nervous system injury in adult rats. Science. 214: 931-3, 1981.

32. Richardson, P. M., U. M. McGuinness and A. J. Aguayo. Axons from cns neurons regenerate into pns grafts. Nature. 284: 264-5, 1980.

33. Glasby, M. A., S. G. Gschmeissner, R. J. I. Hitchcock and C. L. H. Huang. The dependence of nerve regeneration through muscle grafts in the rat on the availability and orientation of basement membrane. Journal of Neurocytology. 15: 497-510, 1986.

34. Keynes, R. J., W. G. Hopkins and L. H. Huang. Regeneration of mouse peripheral nerves in degenerating skeletal muscle: Guidance by residual muscle fibre basement membrane. Brain Res. 295: 275-81, 1984.

35. Hall, S. Axonal regeneration through acellular muscle grafts. Journal of Anatomy. 190: 57-71, 1997.

36. Anderson, P. N. and M. Turmaine. Axonal regeneration through arterial grafts. Journal of Anatomy. 147: 73, 1986.

37. Chiu, D. T., I. Janecka, T. J. Krizek, M. Wolff and R. E. Lovelace. Autogenous vein graft as a conduit for nerve regeneration. Surgery. 91: 226-33, 1982.

38. Foidart-Dessalle, M., A. Dubuisson, A. Lejeune, A. Severyns, Y. Manassis, P. Delree, J. M. Crielaard, R. Bassleer and G. Lejeune. Sciatic nerve regeneration through venous or nervous grafts in the rat. Experimental Neurology. 148: 236-246, 1997.

39. Rambali, B., G. Verreck, L. Baert and D. L. Massart. Itraconazole formulation studies of the melt-extrusion process with mixture design. Drug Development and Industrial Pharmacy. 29: 641-652, 2003.

40. Hofstetter, C. P., E. J. Schwarz, D. Hess, J. Widenfalk, A. El Manira, D. J. Prockop and L. Olson. Marrow stromal cells form guiding strands in the injured spinal cord and promote recovery. Proc Natl Acad Sci U S A. 99: 2199-204, 2002.

41. Brook, G. A., J. M. Lawrence, B. Shah and G. Raisman. Extrusion transplantation of schwann cells into the adult rat thalamus induces directional host axon growth. Exp Neurol. 126: 31-43, 1994.

42. Recknor, J. B., D. S. Sakaguchi and S. K. Mallapragada. Growth and differentiation of astrocytes and neural progenitor cells on micropatterned polymer films. Ann N Y Acad Sci. 1049: 24-7, 2005.

43. Dubey, N., P. C. Letourneau and R. T. Tranquillo. Guided neurite elongation and schwann cell invasion into magnetically aligned collagen in simulated peripheral nerve regeneration. Experimental Neurology. 158: 338-350, 1999.

44. Thompson, D. M. and H. M. Buettner. Neurite outgrowth is directed by schwann cell alignment in the absence of other guidance cues. Ann Biomed Eng. 34: 161-8, 2006.

45. Walsh, J. F., M. E. Manwaring and P. A. Tresco. Directional neurite outgrowth is enhanced by engineered meningeal cell-coated substrates. Tissue Eng. 11: 1085-94, 2005.

46. Stepien, E., J. Stanisz and W. Korohoda. Contact guidance of chick embryo neurons on single scratches in glass and on underlying aligned human skin fibroblasts. Cell Biol Int. 23: 105-16, 1999.

47. Bruder, J. M., A. P. Lee and D. Hoffman-Kim. Biomimetic materials replicating schwann cell topography enhance neuronal adhesion and neurite alignment in vitro. Journal of Biomaterials Science, Polymer Edition. 18: 967-982, 2007.

48. Li, G. N. Y. and D. Hoffman-Kim. Evaluation of neurite outgrowth anisotropy using a novel application of circular analysis. Journal of Neuroscience Methods. 2008.

49. El-Malah, Y., S. Nazzal and N. M. Khanfar. D-optimal mixture design: Optimization of ternary matrix blends for controlled zero-order drug release from oral dosage forms. Drug Development and Industrial Pharmacy. 32: 1207-1218, 2006.

50. Kalil, S. J., F. Maugeri and M. I. Rodrigues. Response surface analysis and simulation as a tool for bioprocess design and optimization. Process Biochemistry. 35: 539-50, 2000.

51. Li, X., T. Xu, X. Ma, K. Guo, L. Kai, Y. Zhao, X. Jia and Y. Ma. Optimization of culture conditions for production of cis-epoxysuccinic acid hydrolase using response surface methodology. Bioresource Technology. 99: 5391-5396, 2008.

52. Lumor, S. E. and C. C. Akoh. Enzymatic incorporation of stearic acid into a blend of palm olein and palm kernel oil: Optimization by response surface methodology. Journal of the American Oil Chemists' Society. 82: 421-426, 2005.

53. Croarkin, C., P. Tobias, C. Zey, S. International, S. National Institute of and Technology. Engineering statistics handbook. The Institute; International SEMATECH, 2001.

54. Falconnet, D., G. Csucs, H. Michelle Grandin and M. Textor. Surface engineering approaches to micropattern surfaces for cell-based assays. Biomaterials. 27: 3044-3063, 2006.

55. Maniotis, A. J., C. S. Chen and D. E. Ingber. Demonstration of mechanical connections between integrins, cytoskeletal filaments, and nucleoplasm that stabilize nuclear structure. Proc Natl Acad Sci U S A. 94: 849-54, 1997.

56. Yim, E. K., R. M. Reano, S. W. Pang, A. F. Yee, C. S. Chen and K. W. Leong. Nanopattern-induced changes in morphology and motility of smooth muscle cells. Biomaterials. 26: 5405-13, 2005.

Supplementary Tables

Table 2.7. Experimental runs and responses

Run	Stripe width (μm)	Space width (μm)	Plating density (cells/cm^2)	Culture time (h)	Mean vector length	Terminal density (cells/cm^2)
A7						
1	10	30	17000	24	0.315	25215.89
2	50	40	26000	24	0.239	14611.4
3	10	40	17000	48	0.328	19412.78
4	30	10	26000	24	0.693	26960.28
5	40	30	49000	24	0.176	33557.86
6	20	20	49000	48	0.534	76960.28
7	20	10	49000	24	0.095	25492.23
8	30	20	49000	24	0.341	24041.45
9	30	10	49000	24	0.143	16545.77
10	50	50	26000	48	0.355	43765.11
11	20	50	26000	48	0.373	29689.12
12	30	10	17000	48	0.253	24352.33
13	10	10	26000	24	0.267	13419.69
14	10	30	26000	48	0.541	39637.31
15	50	20	49000	48	0.31	75440.41
16	10	40	49000	24	0.297	33039.72
17	40	20	17000	24	0.392	7979.275
18	30	50	26000	48	0.318	39965.46
19	10	10	17000	24	0.621	20880.83
20	10	10	49000	48	0.306	103903.3
21	10	20	49000	48	0.441	70259.07
22	50	10	49000	24	0.478	40362.69
23	40	40	26000	48	0.293	55474.96
24	20	40	49000	48	0.327	60207.25
25	20	30	17000	48	0.465	23471.5
26	30	20	26000	48	0.561	65595.85
27	50	10	17000	48	0.371	18203.8
28	50	20	26000	24	0.497	19343.7
29	40	40	26000	24	0.418	34421.42
30	40	30	26000	48	0.475	53696.03
31	50	40	49000	24	0.386	72538.86
32	20	30	26000	24	0.479	34507.77
33	20	40	17000	48	0.431	20569.95
34	20	20	17000	24	0.565	11036.27
35	20	50	17000	24	0.407	16822.11
36	10	50	17000	48	0.41	39965.46
37	30	30	17000	48	0.428	28773.75

38	30	30	49000	48	0.483	74784.11
39	50	20	17000	48	0.426	26459.41
40	10	20	26000	24	0.535	36269.43
41	50	50	17000	24	0.318	13592.4
42	30	50	17000	24	0.376	17599.31
43	30	40	49000	24	0.415	67150.26
44	30	40	26000	48	0.414	76994.82
45	40	10	17000	24	0.61	24905.01
46	40	50	49000	48	0.419	77392.06
47	40	50	17000	24	0.43	16649.4
48	40	40	17000	48	0.407	35664.94
49	20	40	26000	24	0.462	64006.91
50	20	20	49000	24	0.533	88031.09
51	50	30	26000	24	0.419	52970.64
52	20	30	49000	48	0.532	60915.37
53	30	30	17000	24	0.509	15941.28
54	50	50	49000	24	0.371	97253.89
55	40	20	26000	48	0.379	74075.99
56	50	30	17000	48	0.374	28480.14
57	10	50	26000	24	0.4	58393.78
58	40	10	49000	48	0.497	67910.19
59	10	10	26000	48	0.621	60500.86
60	50	40	49000	24	0.381	96373.06
61	20	30	17000	48	0.486	22452.5
62	40	20	26000	48	0.436	71329.88
63	10	50	26000	24	0.43	68013.82
64	30	10	17000	48	0.559	36873.92
65	50	50	49000	24	0.371	79464.59
66	20	20	17000	24	0.547	32884.28
67	30	40	26000	48	0.452	67582.04
68	40	10	49000	48	0.5	66511.23
69	30	50	17000	24	0.441	29430.05
70	50	20	26000	24	0.399	38341.97
71	20	50	26000	48	0.433	48704.66
72	30	10	49000	24	0.553	50155.44
73	40	40	26000	24	0.492	17098.45
74	50	30	17000	48	0.343	40915.37
75	30	20	49000	24	0.577	40466.32
76	40	30	26000	48	0.444	49136.44
77	10	40	17000	48	0.538	37046.63
78	50	10	49000	24	0.496	30466.32
79	20	40	49000	48	0.509	68359.24

80	40	50	17000	24	0.345	17063.9
81	50	50	17000	24	0.433	17979.27
82	30	20	26000	48	0.501	40172.71
83	10	40	49000	24	0.398	59948.19
84	50	50	26000	48	0.402	77236.61
85	20	10	49000	24	0.565	42141.62
86	40	10	17000	24	0.577	16804.84
87	10	30	26000	48	0.577	72141.62
88	20	20	49000	48	0.549	91468.05
89	40	40	17000	48	0.36	40379.97
90	30	50	26000	48	0.415	53298.79
91	40	30	49000	24	0.364	49084.63
92	20	50	17000	24	0.325	24853.2
93	20	30	26000	24	0.416	37754.75
94	30	10	26000	24	0.589	18013.82
95	40	50	49000	48	0.448	106114
96	10	20	49000	48	0.603	86597.58
97	30	30	49000	48	0.515	88946.46
98	10	20	26000	24	0.498	24231.43
99	50	20	49000	48	0.496	103557.9
100	10	30	17000	24	0.464	13108.81
101	20	40	17000	48	0.452	39585.49
102	10	10	26000	48	0.647	65682.21
103	10	10	17000	24	0.611	8065.63
104	20	30	49000	48	0.578	106252.2
105	50	30	26000	24	0.421	31796.2
106	10	10	49000	48	0.633	68117.44
107	30	30	17000	24	0.482	19360.97
108	40	20	17000	24	0.557	15388.6
109	30	40	49000	24	0.375	50690.85
110	10	50	17000	48	0.482	65889.46
111	50	20	17000	48	0.455	52487.05
112	20	40	26000	24	0.398	28670.12
113	50	10	17000	48	0.426	49758.2
114	40	40	26000	48	0.43	61830.74
115	10	10	26000	24	0.594	25561.31
116	20	20	49000	24	0.49	43626.94
117	30	30	17000	48	0.365	31675.3
118	50	40	26000	24	0.379	23575.13

Run	Stripe width (μm)	Space width (μm)	Plating density (cells/cm^2)	Culture time (h)	Mean vector length	Terminal density (cells/cm^2)
HUVEC						
1	10	30	17000	24	0.454	20500.86

2	50	40	26000	24	0.379	19516.41
3	10	40	17000	48	0.37	18842.83
4	30	10	26000	24	0.266	26908.46
5	40	30	49000	24	0.383	30518.13
6	20	20	49000	48	0.415	35889.46
7	20	10	49000	24	0.169	8687.392
8	30	20	49000	24	0.418	28445.6
9	30	10	49000	24	0.34	35354.06
10	50	50	26000	48	0.262	21329.88
11	20	50	26000	48	0.215	25336.79
12	30	10	17000	48	0.313	25889.46
13	10	10	26000	24	0.387	28290.16
14	10	30	26000	48	0.318	26908.46
15	50	20	49000	48	0.213	32849.74
16	10	40	49000	24	0.311	36459.41
17	40	20	17000	24	0.35	24421.42
18	30	50	26000	48	0.269	24542.31
19	10	10	17000	24	0.347	23005.18
20	10	10	49000	48	0.415	33488.77
21	10	20	49000	48	0.392	33592.4
22	50	10	49000	24	0.36	40656.3
23	40	40	26000	48	0.248	27789.29
24	20	40	49000	48	0.326	26839.38
25	20	30	17000	48	0.37	29499.14
26	30	20	26000	48	0.377	32815.2
27	50	10	17000	48	0.298	28773.75
28	50	20	26000	24	0.316	33436.96
29	40	40	26000	24	0.392	32694.3
30	40	30	26000	48	0.354	31191.71
31	50	40	49000	24	0.365	42297.06
32	20	30	26000	24	0.414	31502.59
33	20	40	17000	48	0.308	35492.23
34	20	20	17000	24	0.385	30379.97
35	20	50	17000	24	0.315	24697.75
36	10	50	17000	48	0.371	36303.97
37	30	30	17000	48	0.339	35647.67
38	30	30	49000	48	0.18	26217.62
39	50	20	17000	48	0.239	34386.87
40	10	20	26000	24	0.391	34576.86
41	50	50	17000	24	0.127	17737.48
42	30	50	17000	24	0.184	20794.47
43	30	40	49000	24	0.21	25975.82

44	30	40	26000	48	0.27	37029.36
45	40	10	17000	24	0.227	13575.13
46	40	50	49000	48	0.167	24283.25
47	40	50	17000	24	0.159	12020.73
48	40	40	17000	48	0.198	32677.03
49	20	40	26000	24	0.232	15025.91
50	20	20	49000	24	0.304	34386.87
51	50	30	26000	24	0.2	26062.18
52	20	30	49000	48	0.29	30673.58
53	30	30	17000	24	0.277	6131.261
54	50	50	49000	24	0.222	36977.55
55	40	20	26000	48	0.29	15924.01
56	50	30	17000	48	0.208	11191.71
57	10	50	26000	24	0.194	18290.16
58	40	10	49000	48	0.336	27789.29
59	10	10	26000	48	0.305	26545.77
60	50	40	49000	24	0.315	36787.56
61	20	30	17000	48	0.287	13488.77
62	40	20	26000	48	0.277	29913.64
63	10	50	26000	24	0.265	23298.79
64	30	10	17000	48	0.26	21934.37
65	50	50	49000	24	0.31	29585.49
66	20	20	17000	24	0.279	7478.411
67	30	40	26000	48	0.235	40310.88
68	40	10	49000	48	0.178	41640.76
69	30	50	17000	24	0.199	10017.27
70	50	20	26000	24	0.266	20362.69
71	20	50	26000	48	0.233	25993.09
72	30	10	49000	24	0.346	30207.25
73	40	40	26000	24	0.155	18411.05
74	50	30	17000	48	0.16	14386.87
75	30	20	49000	24	0.315	30673.58
76	40	30	26000	48	0.358	51658.03
77	10	40	17000	48	0.258	28445.6
78	50	10	49000	24	0.277	27132.99
79	20	40	49000	48	0.314	54265.98
80	40	50	17000	24	0.161	6787.565
81	50	50	17000	24	0.159	10155.44
82	30	20	26000	48	0.413	46683.94
83	10	40	49000	24	0.219	40466.32
84	50	50	26000	48	0.288	39274.61
85	20	10	49000	24	0.367	35837.65

86	40	10	17000	24	0.231	12072.54
87	10	30	26000	48	0.352	40362.69
88	20	20	49000	48	0.374	47720.21
89	40	40	17000	48	0.258	27582.04
90	30	50	26000	48	0.259	40379.97
91	40	30	49000	24	0.226	28013.82
92	20	50	17000	24	0.157	12504.32
93	20	30	26000	24	0.285	26200.35
94	30	10	26000	24	0.253	7322.971
95	40	50	49000	48	0.325	51744.39
96	10	20	49000	48	0.395	54974.09
97	30	30	49000	48	0.373	50207.25
98	10	20	26000	24	0.152	11122.63
99	50	20	49000	48	0.283	30829.02
100	10	30	17000	24	0.156	4663.212
101	20	40	17000	48	0.175	19447.32
102	10	10	26000	48	0.32	30898.1
103	10	10	17000	24	0.207	5388.601
104	20	30	49000	48	0.325	43609.67
105	50	30	26000	24	0.179	8359.24
106	10	10	49000	48	0.383	38411.05
107	30	30	17000	24	0.306	7547.496
108	40	20	17000	24	0.267	5820.38
109	30	40	49000	24	0.198	18756.48
110	10	50	17000	48	0.208	24680.48
111	50	20	17000	48	0.239	22400.69
112	20	40	26000	24	0.251	16459.41
113	50	10	17000	48	0.284	28013.82
114	40	40	26000	48	0.233	32348.88
115	10	10	26000	24	0.347	7202.073
116	20	20	49000	24	0.323	22141.62
117	30	30	17000	48	0.264	20483.59
118	50	40	26000	24	0.218	11416.23

Run	Stripe width (μm)	Space width (μm)	Plating density (cells/cm^2)	Culture time (h)	Mean vector length	Terminal density (cells/cm^2)
SC						
1	10	30	17000	48	0.673	42936.1
2	50	40	26000	48	0.713	57098.45
3	10	40	17000	72	0.659	43143.35
4	30	10	26000	48	0.733	32366.15
5	40	30	49000	48	0.761	46994.82
6	20	20	49000	72	0.742	62867.01
7	20	10	49000	48	0.739	49930.92

8	30	20	49000	48	0.776	49879.1
9	30	10	49000	48	0.777	41986.18
10	50	50	26000	72	0.674	67702.94
11	20	50	26000	72	0.724	57029.36
12	30	10	17000	72	0.675	23661.49
13	10	10	26000	48	0.731	39067.36
14	10	30	26000	72	0.771	68428.32
15	50	20	49000	72	0.711	48791.02
16	10	40	49000	48	0.717	61571.68
17	40	20	17000	48	0.75	29464.59
18	30	50	26000	72	0.729	55803.11
19	10	10	17000	48	0.658	16718.48
20	10	10	49000	72	0.725	67582.04
21	10	20	49000	72	0.803	70690.85
22	50	10	49000	48	0.739	33402.42
23	40	40	26000	72	0.732	58221.07
24	20	40	49000	72	0.665	89896.37
25	20	30	17000	72	0.578	50155.44
26	30	20	26000	72	0.649	66027.63
27	50	10	17000	72	0.55	26234.89
28	50	20	26000	48	0.6	39792.75
29	40	40	26000	48	0.662	53903.28
30	40	30	26000	72	0.646	72348.88
31	50	40	49000	48	0.738	53229.71
32	20	30	26000	48	0.72	47806.56
33	20	40	17000	72	0.584	44110.54
34	20	20	17000	48	0.65	28221.07
35	20	50	17000	48	0.68	21364.42
36	10	50	17000	72	0.532	49775.47
37	30	30	17000	72	0.595	48704.66
38	30	30	49000	72	0.659	93333.33
39	50	20	17000	72	0.552	36476.68
40	10	20	26000	48	0.679	33264.25
41	50	50	17000	48	0.681	29740.93
42	30	50	17000	48	0.724	15319.52
43	30	40	49000	48	0.722	63056.99
44	30	40	26000	72	0.671	69447.32
45	40	10	17000	48	0.717	34145.08
46	40	50	49000	72	0.679	73661.49
47	40	50	17000	48	0.685	24490.5
48	40	40	17000	72	0.571	45215.89
49	20	40	26000	48	0.73	48480.14

50	20	20	49000	48	0.761	67685.66
51	50	30	26000	48	0.696	39585.49
52	20	30	49000	72	0.784	73367.88
53	30	30	17000	48	0.59	22953.37
54	50	50	49000	48	0.726	53108.81
55	40	20	26000	72	0.704	44628.67
56	50	30	17000	72	0.638	23488.77
57	10	50	26000	48	0.653	37651.12
58	40	10	49000	72	0.682	43868.74
59	10	10	26000	72	0.729	49689.12
60	50	40	49000	48	0.722	42918.83
61	20	30	17000	72	0.61	28445.6
62	40	20	26000	72	0.676	34093.26
63	10	50	26000	48	0.725	45509.5
64	30	10	17000	72	0.632	23955.09
65	50	50	49000	48	0.747	66027.63
66	20	20	17000	48	0.684	20293.61
67	30	40	26000	72	0.765	44956.82
68	40	10	49000	72	0.709	52607.94
69	30	50	17000	48	0.662	28981
70	50	20	26000	48	0.734	30811.74
71	20	50	26000	72	0.722	54024.18
72	30	10	49000	48	0.743	56839.38
73	40	40	26000	48	0.73	44991.36
74	50	30	17000	72	0.672	36960.28
75	30	20	49000	48	0.754	55561.31
76	40	30	26000	72	0.742	62607.94
77	10	40	17000	72	0.755	58929.19
78	50	10	49000	48	0.662	70932.64
79	20	40	49000	72	0.732	99516.41
80	40	50	17000	48	0.707	34697.75
81	50	50	17000	48	0.763	39982.73
82	30	20	26000	72	0.732	44058.72
83	10	40	49000	48	0.794	81416.23
84	50	50	26000	72	0.68	94352.33
85	20	10	49000	48	0.753	60898.1
86	40	10	17000	48	0.766	29723.66
87	10	30	26000	72	0.806	74905.01
88	20	20	49000	72	0.674	76683.94
89	40	40	17000	72	0.742	53056.99
90	30	50	26000	72	0.761	63661.49
91	40	30	49000	48	0.786	55371.33

92	20	50	17000	48	0.713	43834.2
93	20	30	26000	48	0.729	33143.35
94	30	10	26000	48	0.736	38566.49
95	40	50	49000	72	0.676	90500.86
96	10	20	49000	72	0.794	80673.58
97	30	30	49000	72	0.666	88238.34
98	10	20	26000	48	0.709	68445.6
99	50	20	49000	72	0.627	54680.48
100	10	30	17000	48	0.671	38065.63
101	20	40	17000	72	0.73	48583.77
102	10	10	26000	72	0.773	60051.81
103	10	10	17000	48	0.673	32107.08
104	20	30	49000	72	0.732	75785.84
105	50	30	26000	48	0.757	32607.94
106	10	10	49000	72	0.641	100932.6
107	30	30	17000	48	0.748	45509.5
108	40	20	17000	48	0.743	32936.1
109	30	40	49000	48	0.736	72797.93
110	10	50	17000	72	0.756	56511.23
111	50	20	17000	72	0.695	39153.71
112	20	40	26000	48	0.743	47754.75
113	50	10	17000	72	0.659	39257.34
114	40	40	26000	72	0.689	34110.54
115	10	10	26000	48	0.752	57115.72
116	20	20	49000	48	0.759	59827.29
117	30	30	17000	72	0.74	59516.41
118	50	40	26000	48	0.748	45146.8

Table 2.8. Effect estimates for alignment from the result of Design Expert analysis before linear regression to eliminate insignificant variables.

	Factor	Coefficient (Actual Factor)	Coefficient (Coded Factor)	Standard Error (Coded)	Percent Contribution	P-value
A7	Model					<0.0001*
	Intercept	0.808	0.440	0.009		
	A-space width	1.47×10^{-3}	-0.030	0.013	12.1%	0.0202*
	B-stripe width	-7.14×10^{-3}	-0.052	0.013	34.2%	<0.0001*
	C-cell density	-1.09×10^{-5}	-0.012	0.010	2.6%	0.2621
	D-culture time	-2.68×10^{-3}	0.014	0.009	5.5%	0.1160
	AB	-3.77×10^{-6}	-0.002	0.017	0.02%	0.9293
	AC	4.06×10^{-8}	0.013	0.015	1.6%	0.3898
	AD	-1.16×10^{-4}	-0.028	0.012	11.3%	0.0246*
	BC	8.74×10^{-8}	0.028	0.015	7.6%	0.0634
	BD	4.98×10^{-5}	0.012	0.012	2.0%	0.3364
	CD	1.76×10^{-7}	0.034	0.010	22.9%	0.0015*
	Lack of fit					0.9445**
HUVEC	Model					0.0001*
	Intercept	0.292	0.290	0.007		
	A-space width	-4.80×10^{-4}	-0.026	0.009	24.1%	0.0068*
	B-stripe width	-3.43×10^{-3}	-0.035	0.010	40.9%	0.0005*
	C-cell density	4.63×10^{-7}	0.016	0.008	13.4%	0.0406*
	D-culture time	3.26×10^{-3}	0.010	0.007	6.7%	0.1445
	AB	2.37×10^{-5}	0.009	0.013	1.7%	0.4606
	AC	2.58×10^{-8}	0.008	0.011	1.7%	0.4682
	AD	-6.62×10^{-5}	-0.016	0.009	9.4%	0.0864
	BC	2.02×10^{-8}	0.006	0.011	1.0%	0.5660
	BD	9.08×10^{-6}	0.002	0.009	0.2%	0.8158
	CD	-2.30×10^{-8}	-0.004	0.008	1.0%	0.5730
	Lack of fit					0.7667**
SC	Model					<0.0001*
	Intercept	0.639	0.710	0.005		
	A-space width	4.03×10^{-3}	-0.016	0.007	12.4%	0.0261*
	B-stripe width	-2.46×10^{-3}	0.004	0.007	0.8%	0.5624
	C-cell density	3.66×10^{-6}	0.021	0.006	33.3%	0.0003*
	D-culture time	3.41×10^{-4}	-0.016	0.005	25.7%	0.0015*
	AB	2.54×10^{-5}	0.010	0.009	2.8%	0.2794
	AC	-4.46×10^{-8}	-0.014	0.008	7.0%	0.0888
	AD	-6.83×10^{-5}	-0.016	0.007	14.3%	0.0165*
	BC	8.47×10^{-11}	-0.00003	0.008	2.6%	0.9974
	BD	3.17×10^{-5}	0.008	0.007	3.0%	0.2683
	CD	-1.65×10^{-8}	-0.005	0.006	0.7%	0.5814
	Lack of fit					0.7150**

Table 2.9. Effect estimates for terminal density from the result of Design Expert analysis before linear regression to eliminate insignificant variables.

	Factor	Coefficient (Actual Factor)	Coefficient (Coded Factor)	Standard Error (Coded)	Percent Contribution	P-value
A7	Model					<0.0001*
	Intercept	-5950	49600	1430		
	A-space width	-802	758	2050	0.06%	0.7127
	B-stripe width	429	6530	2080	4.0%	0.0022*
	C-cell density	-0.176	20200	1700	57.9%	<0.0001*
	D-culture time	1080	12200	1420	30.0%	<0.0001*
	AB	5.77	2310	2780	0.3%	0.4072
	AC	0.0141	4520	2460	1.4%	0.0691
	AD	5.58	1340	2000	0.2%	0.5035
	BC	0.0170	5450	2440	2.0%	0.0277*
	BD	-23.3	-5590	2030	3.1%	0.0069*
	CD	0.0141	2700	1700	1.0%	0.1150
	Lack of fit					0.1150**
HUVEC	Model					<0.0001*
	Intercept	-10400	28100	848		
	A-space width	176	-785	1220	0.5%	0.5203
	B-stripe width	-34.9	1060	1240	0.8%	0.3928
	C-cell density	0.547	7290	1010	58.5%	<0.0001*
	D-culture time	694	4820	842	36.7%	<0.0001*
	AB	-2.41	-962	1650	0.4%	0.5601
	AC	-1.96×10^{-4}	-62.6	1460	0.002%	0.9659
	AD	-3.80	-913	1180	0.7%	0.4423
	BC	4.24×10^{-3}	1360	1450	1.0%	0.3512
	BD	0.563	135	1200	0.01%	0.9107
	CD	-5.90×10^{-3}	-1130	1010	1.4%	0.2633
	Lack of fit					0.9611**
SC	Model					<0.0001*
	Intercept	17300	53400	1040		
	A-space width	339	-5920	1490	6.1%	0.0001*
	B-stripe width	-1270	7990	1520	10.7%	<0.0001*
	C-cell density	0.841	14900	1240	55.7%	<0.0001*
	D-culture time	52.7	7110	1030	18.2%	<0.0001*
	AB	8.60	3440	2020	1.1%	0.0912
	AC	-0.0159	-5100	1790	3.1%	0.0053*
	AD	-6.13	-1470	1450	0.4%	0.3133
	BC	8.92×10^{-3}	2850	1780	1.0%	0.1111
	BD	18.6	4470	1480	3.5%	0.0030*
	CD	4.99×10^{-3}	958	1240	0.2%	0.4404
	Lack of fit					0.2699**

Table 2.10. Numerical optimization of culture conditions (answers of equal desirability).

	Space width (μm)	Stripe width (μm)	Plating density (cells/cm^2)	Culture time (h)	Mean vector length	Terminal density (cells/cm^2)
CONFLUENT						
A7						
Input Bounds	10-50	10-50	17-49K	24-48		85-125K
	30	47	46818	48		86440
	49	47	44597	45		86710
	17	50	48969	48		85237
	25	42	48730	47		85685
	33	49	47266	44		85515
	47	49	46883	40		87616
	25	42	48724	48		85766
	41	47	46739	45		87998
	40	50	49000	48		95595
	44	27	48736	46		85121
	21	49	48625	46		85061
	50	50	48857	33		86824
	48	50	46330	39		86242
	46	48	48725	44		93592
	49	23	48145	47		85653
	48	40	44905	47		86697
	18	50	48813	47		85002
	49	27	47537	47		85802
	26	50	48957	43		85246
	33	33	48803	48		86209
	33	34	48759	48		86491
	36	33	47939	47		85291
	49	17	48957	48		85152
	27	37	48611	48		85376
	47	47	46113	46		90505
	29	39	48589	47		85892
	50	26	48825	45		85406
	34	50	46233	46		85917
	26	44	47976	47		85409
	28	49	48954	43		86009
	36	33	48525	47		85551
	48	50	45429	40		85628
	50	20	49000	48		87008
	40	41	48049	47		89840
	49	45	48567	39		87464
	41	25	48838	47		85008

	19	50	48968	47	85475
	35	34	48848	48	87061
	44	48	48632	40	87977
	31	49	48878	43	87041
	49	50	48961	33	86189
	50	46	48725	36	86316
	46	20	48872	48	85771
	24	44	48761	47	85224
	47	49	46564	39	85667
	46	42	48652	47	93279
	49	36	48094	46	89796
	49	23	48703	48	87084
	47	23	48693	47	85621
	48	41	45726	46	86883
	36	50	48929	39	86284
	41	47	47513	46	90132
	39	30	48498	47	86108
	39	35	48756	47	88376
	49	42	47185	41	85680
	37	49	48948	38	85070
	28	42	48143	47	85483
	47	23	48823	48	86700
	25	46	48772	47	86744
	29	47	48638	46	87820
	49	50	48643	33	85519
HUVEC					
Input Bounds	10-50	10-50	17-49K	24-48	32-50K
	43	42	32523	48	33062
	10	10	49000	48	39838
	11	26	32060	48	32864
	11	14	46274	46	37853
	29	48	29420	48	32115
	13	16	42308	36	32057
	16	15	48815	38	35432
	48	12	38536	47	34135
	46	48	48758	36	35725
	17	15	48691	31	32545
	18	42	48339	32	34019
	11	40	47302	31	33011
	30	43	48619	28	32049
	18	27	41862	42	34525
	21	15	48729	39	36072

13	42	48745	27	32041
46	11	34444	47	32116
15	24	46364	37	34624
12	42	39322	47	36374
49	45	48756	31	33256
20	30	49000	48	40516
20	40	49000	48	40956
20	20	49000	48	40076
18	26	45703	35	33330
43	29	33864	48	32980
30	43	30622	47	32320
27	15	35123	48	33232
19	48	29420	48	32317
30	30	49000	48	40314
14	12	48661	32	32873
18	29	44241	33	32187
48	49	48714	29	32437
23	12	48572	33	33045
27	14	48648	32	32727
48	46	37147	46	34558
18	39	40770	47	36884
11	13	33833	47	32762
14	50	46424	32	33742
49	49	30814	48	32398
40	50	49000	48	40992
40	10	49000	48	39231
17	49	34634	48	34913
17	11	48594	33	33267
45	35	47563	30	32116
47	48	48449	37	35735
12	49	30452	48	33128
41	46	46559	34	33883
44	28	48627	30	32128
43	19	33864	48	32540
31	33	33508	47	33108
48	48	43672	40	34996
15	47	45476	30	32373
44	48	45945	32	32500
34	10	47626	34	32999
41	41	46092	37	34719
21	11	36578	44	32471
37	27	42520	36	32072

	25	31	43902	34	32199
	26	32	38194	41	32489
	25	45	43276	34	32706
	48	13	46494	38	33691
	12	48	46085	39	36388
	25	44	33241	45	32719
	40	41	48051	38	36068
	38	36	34180	48	33629
	17	38	35277	47	34321
	41	23	33588	48	32826
	25	35	34053	44	32332
	29	24	39691	41	32859
	23	45	34990	45	33555
	26	16	48184	32	32725
	28	32	45125	39	34740
	29	20	36981	47	33997
	14	13	46546	36	33793
	14	18	41408	41	33614
	38	28	35628	47	33770
	25	30	36461	42	32269
	37	48	32450	46	32657
	48	50	38648	48	35965
	12	29	28668	56	34905
SC					
Input Bounds	10-50	10-50	17-49K	48-72	41-69
	43	27	22657	69	44145
	17	11	46648	69	68348
	34	26	46200	70	67290
	30	40	49000	48	63410
	20	30	27463	51	44900
	12	38	47100	48	67870
	44	32	18778	71	45187
	43	22	37676	51	44563
	10	12	23665	48	41091
	47	33	28400	50	41541
	19	11	41908	66	61238
	30	40	26000	72	59197
	10	10	26000	48	43603
	50	25	36210	49	42219
	20	20	49000	48	62672
	40	20	26000	72	44540
	50	30	17000	72	42385

11	48	25691	50	43047
30	30	17000	72	44681
47	42	28400	50	44374
11	25	24671	51	42724
50	40	49000	48	55582
10	20	26000	48	43017
40	30	26000	72	51008
49	49	37580	65	66483
10	10	26000	72	50980
30	20	26000	72	47982
50	20	49000	72	54486
49	50	20690	51	41694
15	17	23300	53	41292
48	12	48200	49	43347
20	10	49000	48	60346
50	50	26000	72	63083
30	10	49000	48	53850
26	14	28800	50	42157
30	20	49000	48	57037
20	30	26000	48	41321
40	40	26000	48	41095
23	16	21725	70	43332
41	20	40022	54	47592
10	50	26000	48	41261
20	50	26000	72	65666
40	40	26000	72	57476
10	40	17000	72	50062
40	40	17000	72	49198
24	16	46200	70	66847
20	42	35987	64	66841
20	40	26000	48	41596
20	40	17000	72	49774
20	30	17000	72	45829
25	29	27822	50	43574
12	24	38216	50	56942
36	47	38786	59	64563
29	32	32548	68	59246
19	11	37176	62	55476
37	39	32814	48	46771
47	22	34155	70	48175
38	18	26958	61	41676
16	29	44331	51	63866

	18	43	25531	54		45944
	32	45	43973	54		64996
	13	16	41134	63		65054
	46	40	42062	68		66976
	43	20	38866	49		44093
	22	38	40898	53		61694
	34	25	28574	51		42276
	48	33	28718	71		52749
	37	42	45874	57		66743
	19	29	22750	71		51679
	27	11	34738	56		47448
	21	25	21406	60		42558
	26	34	22171	71		51531
	49	40	34933	50		48152
	39	26	32818	67		51720
	42	28	46005	63		59442
	44	18	32357	57		42045
	34	10	30379	71		43611
	45	34	22178	66		46694
	15	20	35525	68		61893
	46	31	45973	48		51404

OPTIMAL ALIGNMENT AT CONFLUENCE (LARGER RANGE)

A7						
Input Bounds	1-100	1-100	0-100K	0-72	maximize	85-125K
	7	27	61625	67	0.704	116074
	4	22	74567	63	0.701	123437
	3	37	66129	69	0.769	121983
	7	65	68092	60	0.720	123106
	4	18	62676	67	0.698	115582
	7	44	63686	63	0.699	114319
	12	62	64920	63	0.713	122879
	4	22	72780	64	0.698	122499
	6	41	67908	63	0.710	119357
	6	66	63336	67	0.770	116450
	10	53	61680	71	0.770	120545
	5	30	58163	72	0.738	115881
	6	7	59892	72	0.705	122958
	3	21	67325	69	0.741	124083
	4	26	67230	65	0.702	117742
	6	44	64171	68	0.749	118950
	2	50	72751	59	0.713	121868
	4	27	64558	67	0.718	116874

5	52	60090	68	0.748	111700
5	20	54176	71	0.701	111922
8	96	62643	58	0.697	118979
2	38	66231	61	0.693	111601
15	63	60100	67	0.706	117511
4	30	55993	68	0.706	107837
1	1	53612	70	0.694	113484
9	35	62852	66	0.698	117100
7	20	65219	70	0.721	124381
2	19	67355	68	0.733	121487
13	62	58513	67	0.712	113113
4	48	58625	64	0.695	105421
6	49	54197	69	0.711	103080
9	29	54872	71	0.699	112522
4	20	68274	65	0.699	119365
2	37	68447	61	0.697	114585
3	37	62314	63	0.696	109785
3	43	67996	61	0.704	116245
1	24	65877	66	0.722	116453
8	28	53756	71	0.698	110958
7	27	60332	69	0.714	117149
2	19	74858	65	0.712	124271
1	17	80676	62	0.693	124799
15	45	61167	69	0.710	122403
7	31	62309	66	0.699	115360
9	53	52794	71	0.708	102802
6	42	60172	67	0.720	112632
14	59	55364	69	0.701	108667
4	9	56088	70	0.694	115455
4	45	63294	69	0.761	117276
3	33	72183	63	0.720	122572
4	79	54143	66	0.724	94680
7	25	72358	64	0.700	124575
5	6	64776	69	0.698	122774
14	93	57894	68	0.750	109763
10	53	60733	66	0.709	114612
20	60	57654	72	0.708	119228
16	44	56486	71	0.694	116128
1	51	64592	66	0.763	114425
4	53	64958	68	0.784	118720
4	68	62243	67	0.780	113138
31	99	57235	71	0.696	123635

	1	12	72372	66	0.702	121329
	3	37	63960	69	0.760	117742
	15	86	55278	71	0.740	104912
	4	18	62073	68	0.706	116965
	1	38	79214	58	0.694	124806
	4	13	66546	69	0.711	122993
	3	10	59813	69	0.701	116436
	7	56	69256	60	0.712	123203
	2	2	49653	72	0.694	112623
	9	42	64663	64	0.703	118574
	2	21	63601	66	0.702	112977
	1	14	50283	71	0.700	107000
	18	60	59528	72	0.734	121438
	2	34	51245	69	0.708	100262
	1	73	67422	59	0.728	118057
SC						
Input Bounds	1-100	1-100	17-49K	0-96	maximize	41-69K
	19	46	67907	15	0.825	53559
	3	16	59620	15	0.817	63608
	49	57	77977	19	0.818	52660
	40	31	65731	11	0.810	41569
	34	7	87140	36	0.810	68214
	19	31	64668	21	0.810	59503
	3	18	58458	16	0.815	62229
	38	7	75772	5	0.828	47486
	12	29	76607	3	0.853	59249
	2	10	47194	6	0.808	50714
	39	34	89616	17	0.839	60696
	20	5	64523	13	0.813	59970
	32	29	71976	19	0.815	55492
	31	8	71537	5	0.827	52061
	41	48	82224	11	0.837	50310
	4	31	59714	6	0.830	48489
	1	4	58984	12	0.817	68476
	23	40	76342	4	0.847	49380
	25	13	73208	7	0.832	56648
	16	54	70375	7	0.842	45490
	7	14	61348	17	0.814	64944
	17	3	66709	9	0.822	62408
	13	4	54865	8	0.808	56269
	24	62	65716	19	0.817	52278
	27	39	82082	2	0.855	49859

3	13	61261	6	0.829	61065
8	25	76260	1	0.856	62406
29	67	73192	20	0.824	60017
10	1	61374	13	0.814	66102
10	41	57270	11	0.819	43369
12	42	77909	0	0.861	52448
2	11	56368	19	0.806	65041
46	31	92705	6	0.853	45445
47	48	92974	6	0.856	47241
4	38	56186	17	0.813	51476
49	67	77977	19	0.820	54673
1	3	49550	2	0.816	56459
10	4	60577	19	0.807	66384
27	34	86993	9	0.852	62215
24	9	67739	3	0.829	53649
4	1	54518	14	0.807	64395
32	6	67310	14	0.809	52213
34	39	90239	2	0.863	51596
42	71	69766	14	0.820	43041
11	13	60860	16	0.812	61819
16	20	60528	7	0.819	50937
1	12	58226	8	0.823	60861
7	97	57222	31	0.808	58516
32	95	63799	20	0.814	48577
5	97	69454	17	0.844	50691
1	4	56493	15	0.810	67006
19	71	72650	15	0.838	53732
78	71	96879	30	0.817	64926
24	40	65631	21	0.810	56339
23	71	62537	20	0.813	49614
7	28	62228	24	0.809	67052
84	67	94608	21	0.821	45214
29	88	75330	17	0.836	56707
21	98	72303	17	0.838	53656
36	66	77300	9	0.839	44838
47	79	69150	21	0.809	52532
60	58	91864	17	0.834	51778
44	5	96329	23	0.833	53607
7	69	63661	27	0.816	65947
43	8	92013	22	0.829	54166
62	69	73684	16	0.810	43428
35	33	77574	28	0.810	65409

35	20	94554	20	0.843	67742
12	9	67991	14	0.824	67517
28	57	72779	24	0.818	65080
66	86	92230	14	0.842	54080
11	38	74257	16	0.837	67770
25	95	80615	12	0.854	54254
2	60	56034	23	0.811	50424
33	12	86535	15	0.837	60075
4	12	44884	1	0.809	44072
60	14	96488	33	0.813	42732

Chapter 3 Anisotropic biomimetic and bioinspired topographies guide neurite outgrowth

Understanding the cues that guide axons and how we can optimize these cues to achieve directed neuronal growth is imperative for advances in neural tissue engineering. Cells in the local environment influence neuronal growth with a rich mixture of topographical and biochemical cues. This study moves toward breaking down the complex mixture of cues involved in cell-cell guidance by isolating the topographical information presented by support cells and determining the capacity of these topographies to guide navigating neurons. We generated materials presenting isolated oriented astrocyte, endothelial cell, and Schwann cell (SC) topographies as well as geometric features inspired by the contours of aligned SCs. These anisotropic cellular topographies were shown to be sufficient for guiding neuronal growth despite distinct topographies and anisotropies presented by these materials. Clustering analysis and uniformity tests suggest that dorsal root ganglia (DRG) alignment was strongest on SC biomimetic materials followed by astrocyte materials with more uniform orientation to endothelial cell materials. DRG neurons, support cells, and neurites demonstrated the most directed response on bioinspired materials which presented anisotropic features of >3 μm height with 90° edges. These results suggest that the topography of anisotropic tissue structures is sufficient to guide neuronal growth, but the features presented by cellular topography may not be optimal for directed control of neuronal growth.

3.1 Introduction

The lack of optimistic outcomes for spinal cord injury (SCI) lies in the fact that nerve regeneration does not occur spontaneously within the central nervous system (CNS). Inherent differences between CNS and peripheral nervous system (PNS) post-injury environments explain their contrasting capacities for regeneration. While Schwann cells (SCs) in the PNS provide supportive cues to regeneration in the post-injury environment,[1, 2] oligodendrocytes and reactive astrocytes in the CNS contribute inhibitory cues.[3] The goal of neural tissue engineering for SCI includes determining cues that neurons must be given to overcome this inhibitory post-injury environment and generating biomaterial therapies to present these cues to support successful regeneration and improve the quality of life of SCI patients.

Contact guidance is a promising approach for guiding regenerating axons toward their targets. Substrate topography is one type of directive cue that has been evaluated substantially *in vitro* and *in vivo*. Edges, fibers, and grooves in the micrometer and nanometer range have been shown to guide and promote neurite outgrowth depending on the depth and width of such features.[4] While grooves and fibers as narrow as 50 nm,[5] as wide as 100 μm,[6] as shallow as 14 nm,[4] and as deep as 40 μm[7] have directed neurite growth, the systematic analysis of topographical parameters that influence neurite growth has not previously been carried out. Geometric features help to obtain precise knowledge of the factors that influence cellular growth and alignment including the range of dimensions that are useful for topographical guidance, but they oversimplify the topography of the *in vivo* environment.

It is important to consider that geometric materials presenting feature widths in the range of 4 to 30 μm[4, 8] and depths greater than 1 μm[9, 10] seem to be most effective for directing neurite growth. This range of feature sizes is similar to the sizes of features presented by cells and extracellular matrix *in vivo*. Accordingly, neurons have been shown to be guided by anisotropic tissue structures *in vitro*

and *in vivo*. Neurons can align to tissues such as nerve,[11, 12] white matter,[13] muscle,[14-16] and blood vessels,[17-19] and in co-cultures with aligned astrocytes,[20-23] SCs,[5, 24, 25] meningeal cells,[26] olfactory ensheathing cells,[22] and fibroblasts.[26, 27] In these studies, it is difficult to separate the influence of topography of these cells and tissues from chemical and electrical influences of the guiding cells. Recent worked has moved toward breaking down the complex mixture of topographical and biochemical cues involved in cell-cell guidance. Fixed aligned astrocyte cultures have been shown to guide neurite outgrowth,[23] and the powerful tool of replicating cellular topography in polymer materials has shown that materials presenting isolated aligned SC topographies can direct neuron growth.[28]

It is well recognized that the different chemical cues presented by SCs and astrocytes after injury contribute to the varied capacities for regeneration in the PNS and CNS, but it has not yet been shown if their topographical features also contribute to the promotion of axon guidance. It was our aim to characterize the topographical information presented by these distinct glia and the contribution of these physical features to the promotion of neurite guidance. We also looked at a non-glial cell type, endothelial cells, to determine if anisotropy of any tissue or cell type is sufficient for neuronal guidance or if a glial phenotype is necessary. Further, we used computer aided design and lithography to fabricate poly(dimethylsiloxane) (PDMS) materials with repeating geometries insipired by the features of aligned SCs toward determining which topographical features – dimensions and/or shape – encode critical guidance information to a navigating neuron.

3.2 Materials and methods

3.2.1 Fabrication of materials presenting replicated cellular topographies

A summary of the sequence of fabrication methods involved in this study are presented in Figure 1.

3.2.2 Cell culture

Cell culture reagents were from Invitrogen Life Technologies (Carlsbad, CA, USA) unless otherwise indicated. Cultures were incubated at 37°C with 5% CO_2 in a humidified environment. SCs from rat sciatic nerve, a generous gift of Dr. Mary Bunge (University of Miami, Coral Gables, FL, USA), were cultured on tissue culture plastic dishes coated with 100 μg/ml poly(L-lysine) (PLL; Sigma, St. Louis, MO, USA) in Dulbecco's modified eagle's medium (DMEM) with 10% fetal bovine serum (FBS), 4 mM L-glutamine, 100 U/ml penicillin and 100 μg/ml streptomycin supplemented with 2 μM forskolin (Sigma), 10 μg/ml bovine pituitary extract (Sigma) and 2 μM heregulin (generous gift from Genentech, Vacaville, CA, USA) (SC media). Cells used in experiments were between passage 5 and 7. A7 astrocytes (A7s), a generous gift of Dr. Herbert Geller (Developmental Neurobiology Section, NHLBI, NIH, Bethesda, MD, USA), were cultured on tissue-culture plastic dishes in DMEM with 10% FBS, 4 mM L-glutamine, 100 U/ml penicillin and 100 μg/ml streptomycin supplemented with 5μg/ml insulin from bovine pancreas.[29] Cells used in experiments were between passage 8 and 12. Human umbilical vein endothelial cells (HUVECs) (PCS-100-010, ATCC, Manassas, VA, USA) were cultured on tissue-culture plastic dishes in endothelial growth media-2 (EGM-2) (Cambrex, Rockland, ME, USA). Cells used in experiments were between passage 4 and 6.

3.2.3 Substrate preparation

Substrates were prepared as previously described.[28] For aligned SCs and aligned A7s, poly(dimdethylsiloxane) (PDMS) (Dow Corning, Midland, MI,USA) microstamps with plateaus of 10 mm length, 50 μm width and 10 and 20 μm pitch were coated with laminin (LN) and stamped onto glass chamber slides (Nunc, Thermo Fisher Scientific, Rochester, NY, USA) with micro-contact printing. For aligned HUVECs, slides were microstamped with plateaus of 10 mm length, 10 μm width and 10 μm pitch coated with human fibronectin (FN) stripes. SCs, A7s, and HUVECs were plated on the appropriate substrates at 49K cells/cm^2 and incubated for 48 h. Cells were fixed with 2% paraformaldehyde (Sigma) in 0.1 M phosphate-buffered saline (PBS). For randomly oriented

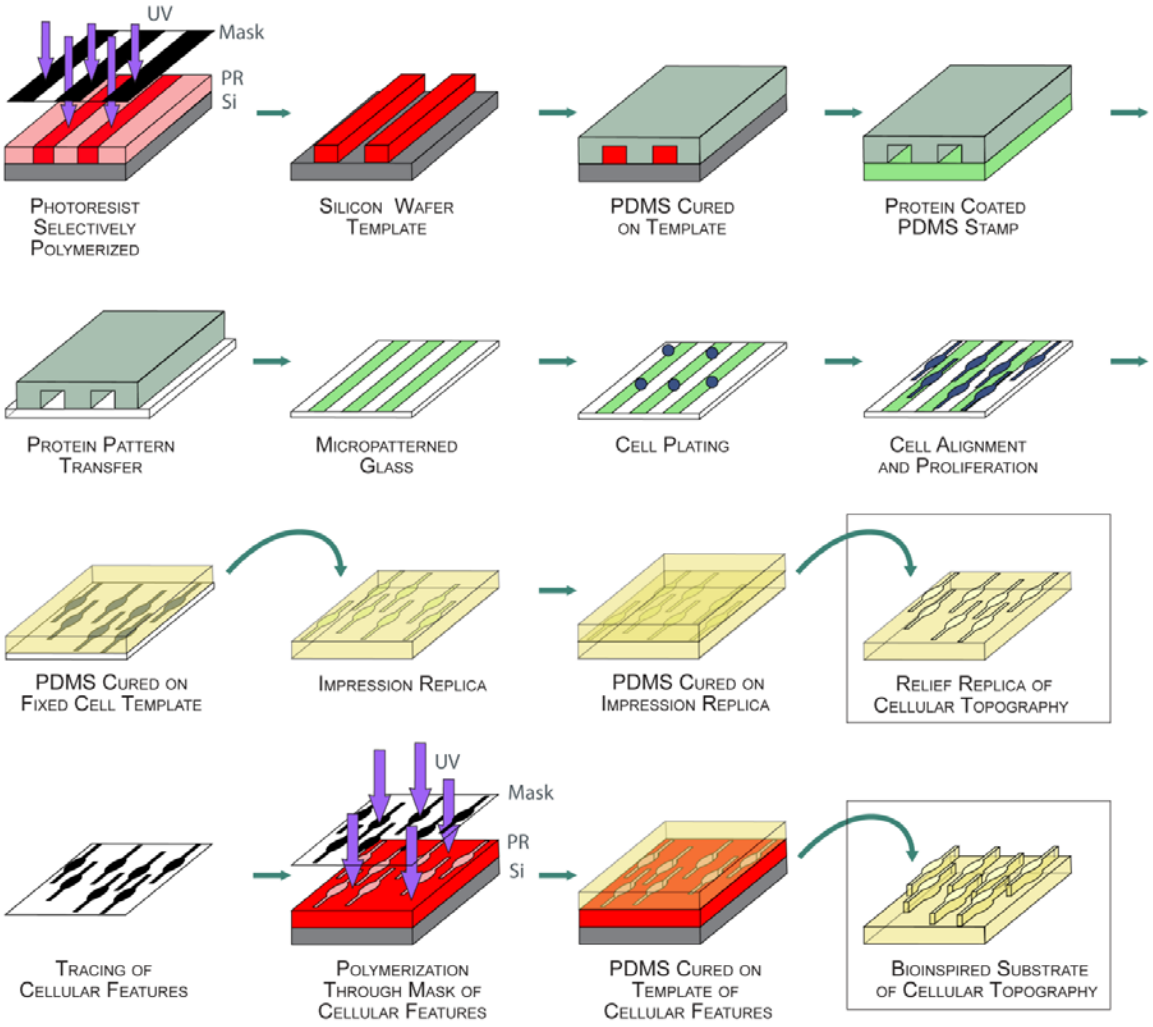

Figure 3.1. Methods of fabrication of topographical platforms.
Schematic overview of the techniques used to fabricate anisotropic biomimetic and bioinspired materials highlighting photolithography, microcontact printing, cell culture, replica molding, and a second photolithography step. Materials used for the investigation of DRG response are shown in boxes.

substrates, coverslips coated uniformly with LN or FN were also plated at this cell density and fixed at 48 h. Glass chamber slides were rinsed 3 times with PBS after fixation, and the media chamber and gasket were removed and saved for use in the molding process. Slides were placed in Coplin jars (Thermo Fisher Scientific) for post-fixation in Karnovsky's fixative (Electron Microscopy Sciences, Hatfield, PA, USA) for at least 3 h. Samples were then rinsed with 0.1M sodium cacodylate, fixed in 1% osmium tetroxide in 0.1M sodium cacodylate for 1 h, rinsed 3 times with water, incubated in 1% thiocarbohydrazide in water for 1 h, rinsed 3 times with water, and incubated in 1% osmium

tetroxide in water for 1 h (Electron Microscopy Sciences). Substrates were then dehydrated through serial rinses with increasing gradations of ethanol up to 100%, air dried, and sputter-coated with gold palladium. Sputter coated, post-fixed cells were then used as templates to create PDMS molded impressions of the cells, which were in turn used to create PDMS replicas of the cellular topography. The precursor to PDMS was poured over the SEM fixed cell template at a 3-4 mm thickness, and PDMS was cured at 95°C overnight. The impression mold was peeled from the template and placed face up. Media chambers from the culture chambers were fit into the molded area, 3-4 mm of PDMS precursor was poured into the chamber, and PDMS was cured at 95°C for at least 4 h. The chamber was then removed, this PDMS layer was peeled from the impression mold, and the resulting PDMS substrate with protruding cellular topography was characterized and used in culture experiments as described below.

3.2.4 Fabrication of topographical materials inspired by features of aligned SCs

A phase contrast image taken at 200x magnification of a replica presenting aligned SC topography was opened in Adobe Photoshop CS2 (Adobe, San Jose, CA, USA). A field of view 200 μm by 200 μm was traced, outlining each cell. The background image was then removed leaving a continuous outline of the cells. Each unit was mirrored and arrayed end-to-end first horizontally and then vertically to fill a 1 cm by 1 cm square. The design was printed in chrome on a quartz mask (Advanced Reproductions Corporation, Andover, MA, USA) with a guaranteed resolution of 1.6 μm. Photolithography techniques similar to those used to generate microstamps were used to create the geometric patterns on 3 inch silicon (Si) wafers (Silicon Sense Inc., Nashua, NH, USA) but negative tone Nano SU-8 2 (MicroChem Co., Newton, MA, USA) was used instead of SU-8 50 in order to generate a thickness of approximately 5 μm, and appropriate baking time, exposure and developing were used. As with microstamps, the precursor to PDMS was poured over the silicon wafer to a

thickness of 3-4 mm. It was then baked at 95°C for 2 h, cooled, and peeled from the silicon wafer, creating a replica of the raised cell-shaped stripes.

3.2.5 Characterization of topographical materials

Cell length, width, and projected surface area were measured by manual tracing with ImageJ v1.36. In four fields of view (FOV) per cell type, one hundred cells were randomly selected and measured. For A7s and HUVECs, the cells were traced with the Freehand Selections tool (Figure 2). The Measure function was used to fit the traced area to an ellipse and to measure the major and minor axes as the length and width of the cell. The projected surface area of the cell was also measured with this function. For SCs, the somas were traced by the Freehand Selections tool, and the length, width, and projected surface area of SC somas were measured by the same method as for A7s and HUVECs (Figure 2). The length and width of the processes were measured with the Straight Line Selections tool and Measure function (Figure 2). The total projected surface area of SCs was approximated by $Area_{soma} + 2* Length_{processes} * Width_{processes}$.

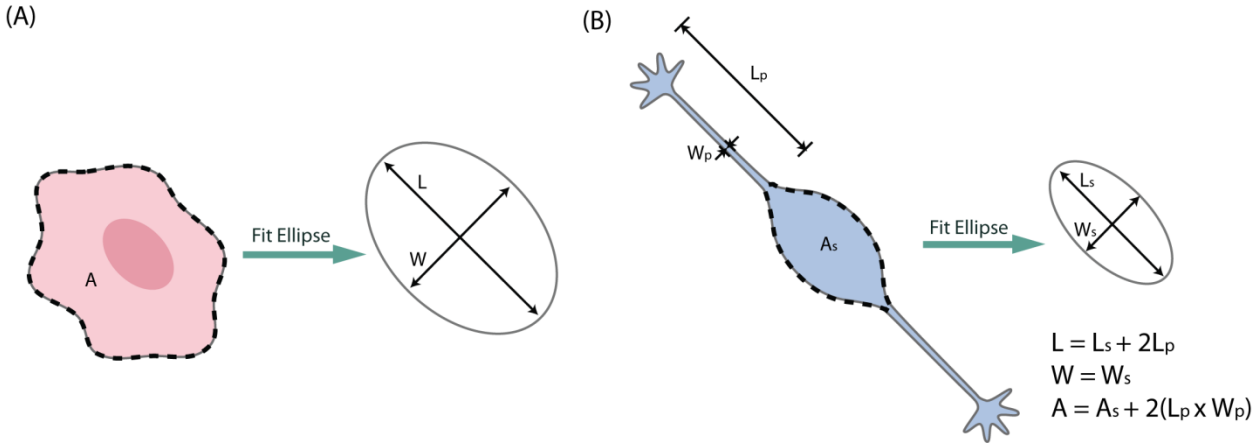

Figure 3.2. Quantitative assessment of cellular widths, lengths, and projected areas.
Drawings of measurement methods. A7s and HUVECs were traced and fit with ellipses to estimate widths and lengths (A). SC somata were similarly traced and fit with ellipses (B). SC process widths and lengths were estimated with straight lines (B).

Cell height profiles were recorded by white light interferometry (WIM). WIM data files were recorded at 10X objectives and 1X zoom with a Zygo New View 6000 3D profiler (Zygo Co., Middlefield, CT, USA). Data files were analyzed with Gwyddion 2.0 software. The data was leveled by fitting a plane through three flat areas between cells (zero points) chosen by the user. Twelve cells per FOV were randomly selected, and the height profile of a horizontal cross-section of the cell was generated using Extract Profile function (Figure 3). For A7s, HUVECs, and SC somata, height profiles were fit to a second order polynomial function with a custom Matlab program (Matlab r2008b, The MathWorks, Natick, MA, USA), and the average value and maximum value of this function were recorded for each cell. For processes, the maximum height was recorded as the maximum value of the profile extracted in Gwyddion.

One-way analysis of variance (ANOVA) tests were performed on length, widths, heights, mean vector lengths, percentages, and cell counts. *Post hoc* multiple comparison analyses were performed using the Bonferroni test. Again, a *P* value of 0.05 was taken to be significant.

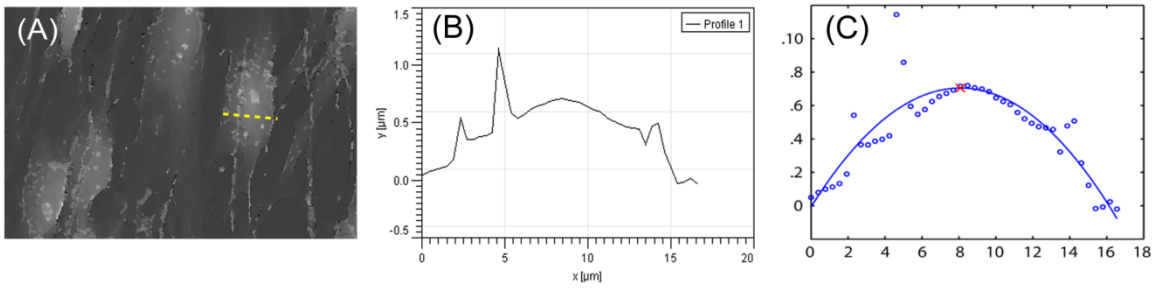

Figure 3.3. Quantitative assessment of cellular heights.
WIM profile map of aligned SCs (A). The height profile of a cross-section (indicated by yellow dotted line) of a cell was extracted and graphed (B). This height profile was fit to a second order polynomial function (C), and the average and maximum (red x) values were recorded for each cell.

3.2.6 Study of dorsal root ganglia alignment

All PDMS topographical substrates were coated with 100 μg/ml pLL for 1 h, rinsed with Hank's Balanced Salt Solution (HBSS), and coated with 50 mg/ml LN for 1 h. Dorsal root ganglia (DRG) were dissected from the spinal column of postnatal (P3) rats. DRG explants were cleaned of axons and blood vessels, incubated in 0.05% trypsin-EDTA in HBSS for 45 min at 37°C, triturated in DMEM with 10% FBS, 4 mM L-glutamine, 100 U/ml penicillin and 100 μg/ml streptomycin supplemented with 50 ng/ml nerve growth factor (NGF), and plated at 41,000 cells/cm^2 in 12-well plates.

3.2.7 Visualization of neurite and nuclear alignment

After 5 days, cells were fixed and blocked for 1 h at room temperature with 10% goat serum (Jackson Immuno Research Laboratories, West Grove, PA, USA) and 1% bovine serum albumin (Sigma), in 0.1 M phosphate buffered saline (PBS) with the addition of 0.1% Triton X-100 (VWR, West Chester, PA, USA) for permeabilization. To visualize neurites, samples were incubated overnight at 4°C with monoclonal anti-neuronal class III beta tubulin primary antibody (Covance Research Products, Inc., Berkeley, CA, USA) diluted 1:500 in blocking buffer. Samples were rinsed in PBS, incubated for 1 h at room temperature with Cy3-conjugated goat anti-mouse secondary antibody (Jackson Immuno Research Laboratories) diluted 1:200 in blocking buffer and rinsed again in PBS. To visualize nuclei, a 1:100 solution of 4,6-diamidino-2-phenylindole (DAPI) (Sigma) in PBS was added to each sample for 1 h.

3.2.8 Microscopy

12-bit images were obtained at 100× magnification with a 30-ms exposure for epifluorescent imaging of DAPI, 200-ms exposure for epifluorescent imaging of neurites, and 10-ms exposure for imaging of phase contrast and analyzed as described below.

For quantitative assessment of alignment, ten FOVs of 664 μm × 872 μm were acquired at 100× magnification on a Nikon Eclipse TE2000-S microscope equipped with phase-contrast and epifluorescence optics and software-controlled motorized stage. Samples were oriented so that substrate topographical alignment direction was uniform between samples. Corresponding phase and epifluorescence images were captured using a Hamamatsu Orca-ER camera, an Orbit shutter controller, and a Ludl stage controller, outputting to OpenLab v4.0.4 (Improvision, Lexington, MA, USA). A custom stage automation was written which allowed the user to select the area of protein patterning, choose 10 points at random within this area, and obtain corresponding images of phase, DAPI, and stained neurites.

3.2.9 Quantification of nuclear alignment

DAPI images were converted to 8-bit greyscale with Adobe Photoshop CS2, inverted, and the contrast was adjusted using the level and curve functions. Nuclei numbers were assessed with ImageJ v1.36, using the Otsu function of the multithresholder plugin and the particle analyzer plugin with size filter set to 50–850 pixels to exclude image artifacts and cell clusters. For alignment and confluence analysis, DAPI images were processed as described, and nuclei number and angle of orientation were assessed with ImageJ. This data was analyzed with Oriana v2.02c (Kovach Computing Services, Pentraeth, UK). Circular analysis was used to analyze the angular distributions of the major axes of the nuclei.[30] Circular mean vectors were calculated, where the length of the mean vector corresponds to the degree of clustering of the data, and the direction of the mean vector corresponds to the mean direction of the data. Uniformity of the distribution of nuclei was assessed using a Rao's spacing test and alignment of nuclei in the direction of the substrate pattern was assessed with a V–test. One-way analysis of variance (ANOVA) tests were performed on mean vector lengths. *Post hoc* multiple comparison analyses were performed using the Bonferroni test. For all cases, a P value of 0.05 was taken to be significant.

3.2.10 Quantification of neurite alignment

Images of neurites stained for neuronal class III beta tubulin were thresholded and converted to 8-bit grayscale images with custom Matlab software. Images were opened in ImageJ, processed with a fast Fourier transform (FFT), and analyzed with a custom oval profile plugin. Pixel intensities along radii at each angle for each image were normalized by the mean intensity in that image, and normalized intensities at each angle were averaged. Average normalized intensity was plotted against angles from 0° to 179°, generating an intensity peak.

3.3 Results

Recent work in our lab has described the generation of biomimetic polymer materials presenting isolated aligned SC topographies and their ability to direct neuron growth.[28, 31] The type of cell replicated by this technique is not limited. Thus we generated materials presenting aligned A7, HUVEC, and SC topographies by culturing these cells under optimized conditions[32] and preparing replicas as previously described.[31] The topography presented by aligned monolayers of these three types differed in surface appearance (Figure 4A-C). A7s and HUVECs presented broader topographical features while SCs had smaller cell bodies with thin, long extensions. While similarly broad, A7s were much rockier in appearance than HUVECs. The surfaces of HUVECs were not completely smooth, however, but had small protrusions near the centers of the somata. A7s were most closely packed together of the 3 cell types followed by HUVECs and then SCs. While all three cell types presented anisotropy, SCs appeared more elongated in the direction of the micropatterned cue. HUVECs appeared more elongated than A7s.

Quantitative image analysis of cell morphology supported these observations. HUVECs were the largest cell type in both length and width (Figure 5A). HUVECs were 62.3 ± 8.1 μm in length and 24.9 ± 3.8 μm in width with a projected area of 1215 ± 246 μm. A7s projected a 41% smaller surface area

of 712 ± 191 μm with a length of 46.1 ± 8.0 μm and width of 19.2 ± 2.8 μm. SC somata were the smallest in both length and width. SC somata were 36.1 ± 4.1 μm in length and 13.3 ± 2.0 μm in width. SC processes were considerably longer than other cellular features with length of 52.5 ± 17.4 μm and width of 1.8 ± 0.3 μm. Even including the contribution of the processes, SC projected area was 54% smaller than HUVEC area at 564 ± 88 μm. Despite their small size, SCs presented the most elongated somata with an aspect ratio of 2.73 ± 0.26 ($p \leq 0.05$). HUVEC somata had an aspect ratio of 2.50 ± 0.25 μm, and A7 somata were the least elongated with an aspect ratio of 2.39 ± 0.27 ($p \leq 0.05$). SC processes were the most elongated cellular feature with an aspect ratio of 30.0 ± 5.7 ($p \leq 0.05$).

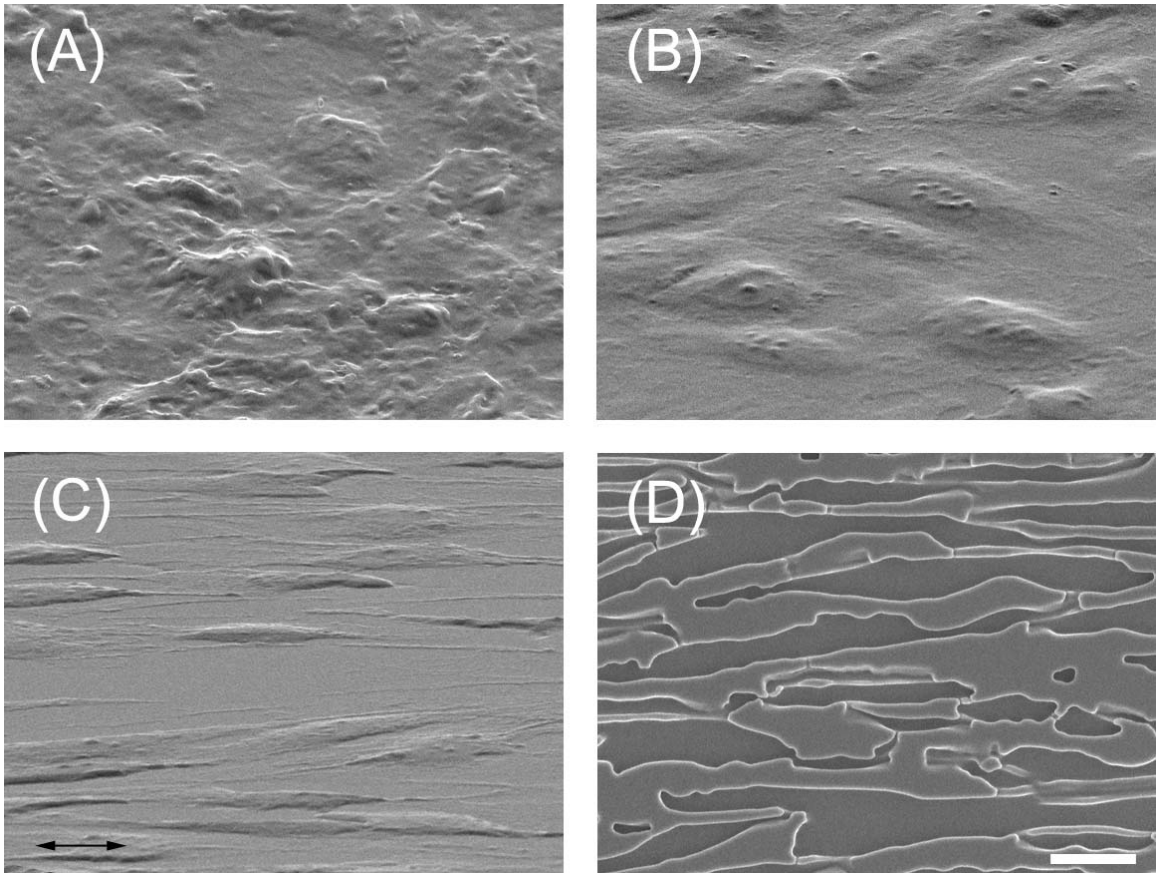

Figure 3.4. Topographical platforms presented distinct topographies to navigating neurons.
Scanning electron micrographs of PDMS materials presenting aligned A7 topography (A), aligned HUVEC topography (B), aligned SC topography (C), and geometric traces of SC topography (D). Arrow indicates orientation of topography. Scale bar, 20 μm.

While the widths and lengths of topographic features presented by these cell types were considerably different, the heights of features were not significantly different among the cell types, as analyzed from WIM images (Figure 5B). The average soma height across the soma was 0.73 ± 0.27 μm for A7s, 0.74 ± 0.14 μm for HUVECs, and 0.79 ± 0.20 μm for SCs. The maximum height presented across a soma was 1.00 ± 0.39 μm for A7s, 1.14 ± 0.31 μm for HUVECs, and 0.95 ± 0.27 for SCs. SC processes presented much flatter topographical features with a maximum height of 0.49 ± 0.24 μm.

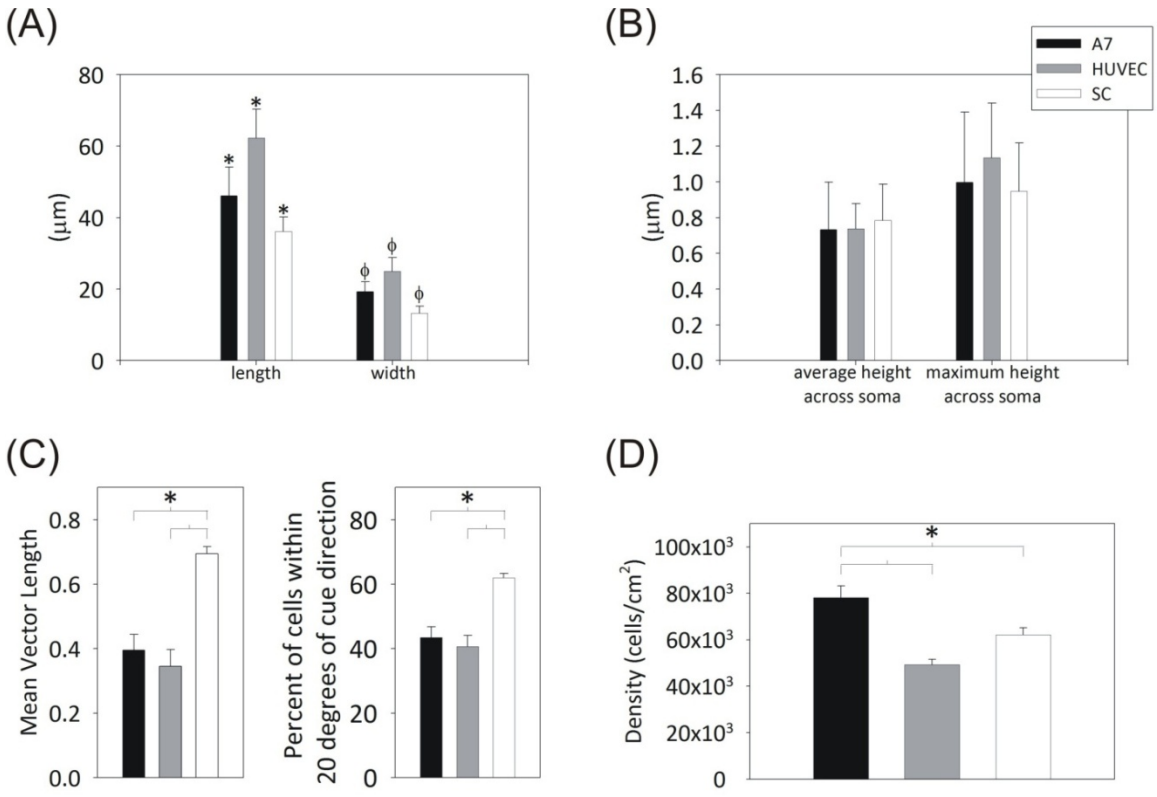

Figure 3.5. Topographies of each cell type varied in length, width, height, and clustering of alignment. Graphs characterizing the topographical features of aligned A7, HUVEC, and SC topographies. Soma length and width (A), soma average and maximum height (B), nuclear alignment (C), and cell density (D) were measured for each cell type. Mean ± SEM are presented, *, ϕ, $p<0.05$ by ANOVA.

The anisotropy of the topography presented by these cell types was also distinct (Figure 5C). As previously noted, SCs exhibited a stronger capacity for alignment on micropatterned substrates than

A7s and HUVECs.[32] Circular mean vectors were calculated, where the length of the mean vector corresponds to the degree of clustering of the data, and the direction of the mean vector corresponds to the mean direction of the data. The nuclear alignment of SCs was almost twice as clustered as the alignment of A7s and HUVECs (mean vector lengths of 0.695 ± 0.022 for SCs, 0.395 ± 0.045 for A7s, 0.345 ± 0.052 for HUVECs). The stronger alignment of SCs was also demonstrated in the higher proportion of SCs aligned within 20° of the pattern (61.9 ± 1.4% for SCs, 43.5 ± 3.3% for A7s, and 40.6 ± 3.4% for HUVECs). While the overall alignment of SCs was stronger than that of A7s, the number of aligned cells presented in these monolayers was more similar. A7 monolayers had a larger cell density of 86,500 ± 4,500 cells/cm^2 than SC monolayers with a density of 62,000 ± 3,000 cells/cm^2. The number of A7 somata aligned within 20° of the mean direction was 37,000 ± 200 cells/cm^2 which was similar to the number of aligned SC somata at 38,500 ± 100 cells/cm^2. HUVECs had the lowest density of 49,200 ± 2,300 cells/cm^2, and the lowest number of cells aligned within 20° of the mean, 20,000 ± 100 cells/cm^2.

Bioinspired SC topographies were also generated using computer-aided design and lithography to present anisotropic topographical information to navigating neurons. Traces of SC somas with processes were replicated with PDMS (Figure 4D). The width of SC "somata" was 8.8 ± 1.8 μm which was 34% smaller than the feature width presented by biomimetic molded replicas of SC topography. The width of bioinspired "processes" was 2.5 ± 0.3 μm which was 39% wider than the width of molded replicas. The most significant difference between biomimetic and bioinspired topographical features was feature height. The feature height on bioinspired substrates was uniform and significantly higher (3.5 ± 0.1 μm, data not shown) than biomimetic SC topography (max height 0.95 ± 0.27 μm). The topography of bioinspired substrates was also presented with a 90° edge while the topography of cell replicas has a more gradual slope.

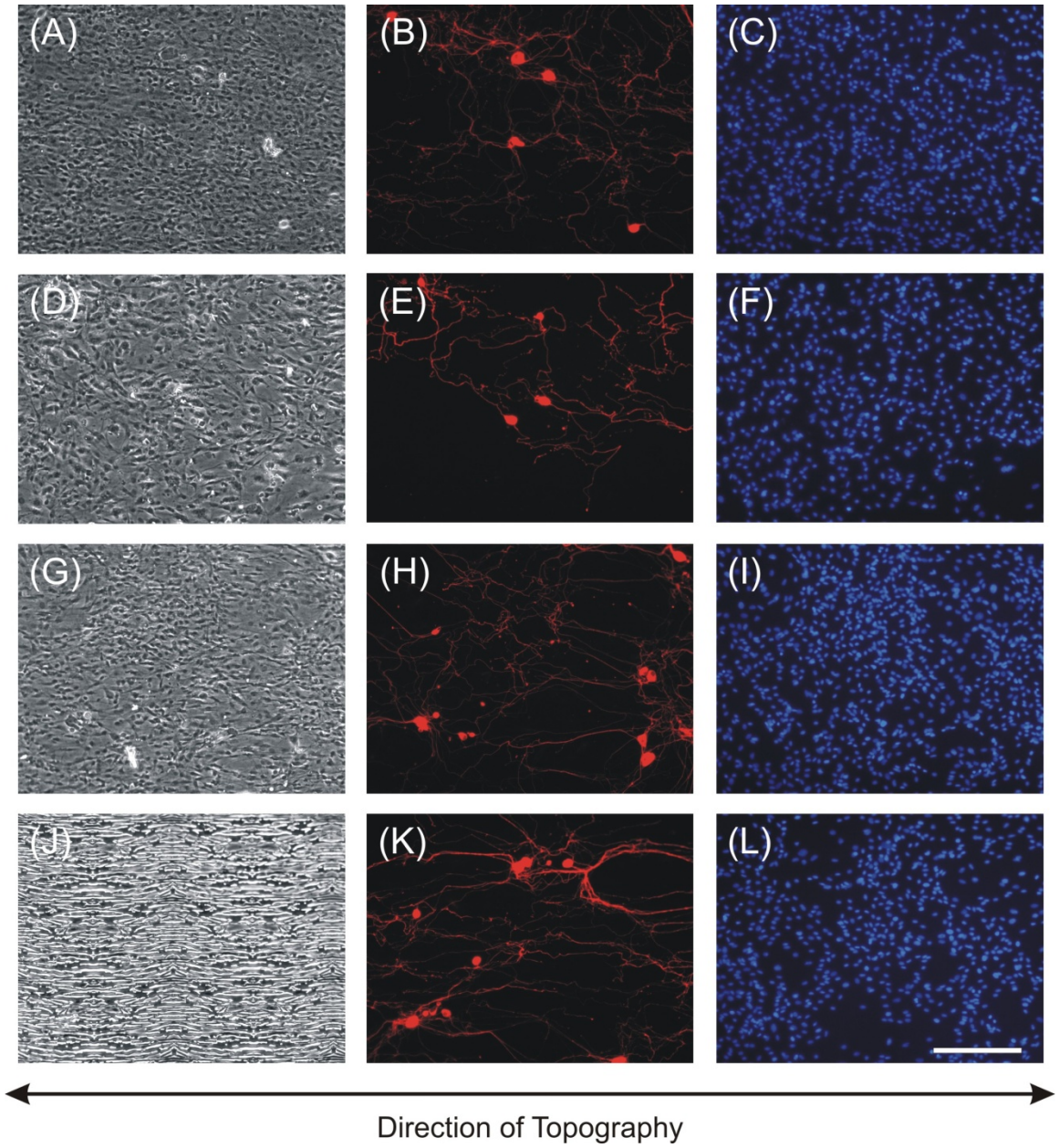

Figure 3.6. Neurons, support cells, and neurites were influenced by the topography of biomimetic support cells. Corresponding phase contrast(A, D, G, J) and epifluorescent images (B, C, E, F, H, I, K, L) of DRGs cultured on PDMS materials presenting aligned A7 topography (A, B, C), aligned HUVEC topography (D, E, F), aligned SC topography (G, H, I), and geometric traces of aligned SC topography (J, K, L). Neurites were stained with anti-class III beta tubulin (B, E, H, K), and nuclei were stained with DAPI (C, F, I, L). Scale bar, 200 μm.

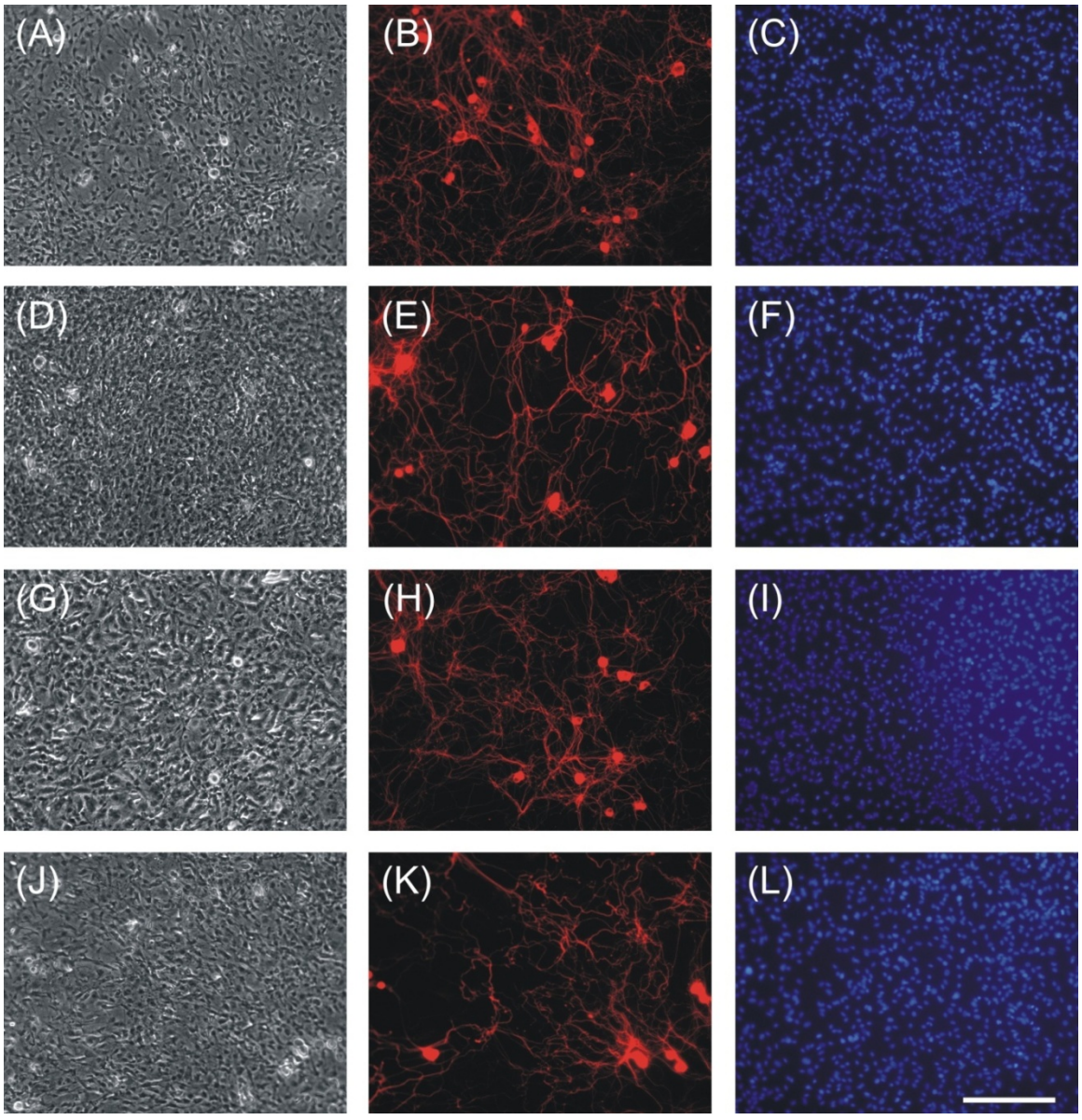

Figure 3.7. Cells and neurites were randomly oriented on flat and isotropic cellular topographies. Corresponding phase contrast (A, D, G, J) and epifluorescent images (B, C, E, F, H, I, K, L) of DRGs cultured on flat PDMS (A, B, C) or PDMS materials presenting random A7 topography (D, E, F), random HUVEC topography (G, H, I), and random SC topography (J, K, L). Neurites were stained with anti-class III beta tubulin (B, E, H, K), and nuclei were stained with DAPI (C, F, I, L). Scale bar, 200 μm.

When DRGs were cultured on anisotropic biomimetic and bioinspired materials as well as isotropic biomimetic and flat materials, DRGs demonstrated some degree of alignment to all anisotropic materials presented (Figure 6) while orientation of nuclei and neurites was random on flat and isotropic materials (Figure 7). Comparison of DRG responses to substrates presenting varying aligned features by quantitative circular analysis of the distribution of nuclear angles revealed varied

influences on alignment (Figure 8). The distribution of nuclear angles on all experimental replicates on bioinspired and biomimetic SC materials was significantly different from a uniform distribution of angles by Rao's spacing test ($p<0.05$), and the mean angle of the distribution was not significantly different from the direction of the underlying topography (V-test for 0° or 180°, $p<0.05$) (Figure 8C, D). Similarly, there was no significant difference between the direction of the underlying topography and the mean angle of the distribution of nuclear angles on biomimetic A7 and HUVEC materials (V-test for 0° or 180°, $p<0.05$) (Figure 8A, B). On A7 and HUVEC materials, however, the distribution of angles on some experimental replicates taken individually was statistically similar to uniform distribution (Figure 9, 10). On A7 materials, the distributions were uniform on 2 of 6 of the replicates, and on HUVEC materials, the distributions were uniform in 4 of 6 of the replicates.

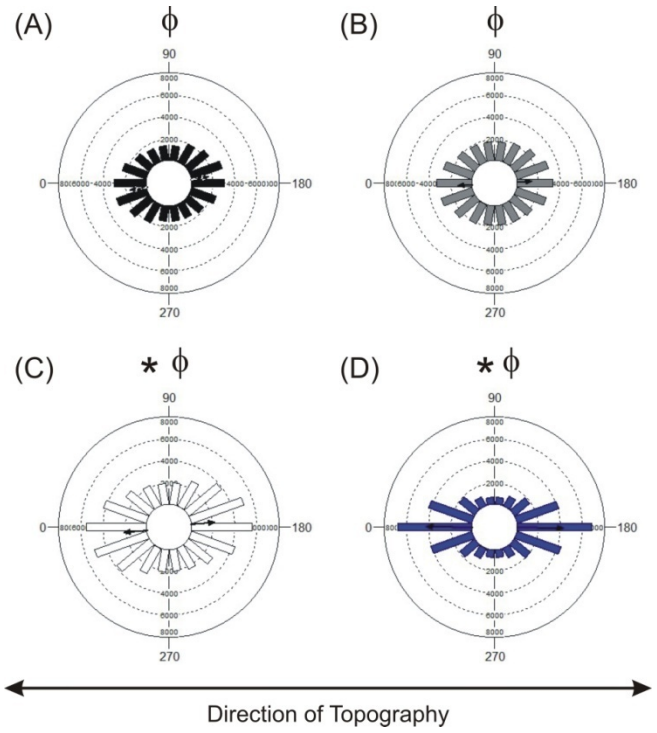

Figure 3.8. Quantitative analysis of cellular alignment on anisotropic topographies revealed different clustering of cellular alignment in the direction of underlying topography.

Circular histograms of nuclear angle distributions of DRGs cultured on PDMS substrates presenting aligned A7 topography (A), aligned HUVEC topography (B), aligned SC topography (C), and geometric traces of SC topography (D). *Indicates difference from a uniform distribution by Rao's spacing test ($p<0.05$). ϕ, Indicates mean vector angle in the direction of the topographical cue by V-test ($p<0.05$).

Comparison of the mean vector lengths of all alignment distributions on biomimetic and bioinspired topographies (Figure 11) showed that clustering of nuclear alignment around the mean angle was twice as strong on bioinspired geometric SC features (0.544 ± 0.030) than on other materials (0.188 ± 0.022 on A7, 0.159 ± 0.030 on HUVEC, 0.265 ± 0.014 on SC). Clustering around the mean on biomimetic SC features was also significantly stronger than on biomimetic HUVEC features. Comparison of the percent of DRG nuclei aligned within 20° of the underlying topography also showed significantly more nuclei were aligned on bioinspired materials (54.8 ± 2.3%) than on biomimetic materials (30.6 ± 0.9% on A7, 29.5 ± 1.7% on HUVEC, 34.4 ± 0.7% on SC). The clustering of nuclear angles on flat and isotropic materials was not significantly different from a uniform distribution of angles by Rao's spacing test (data not shown).

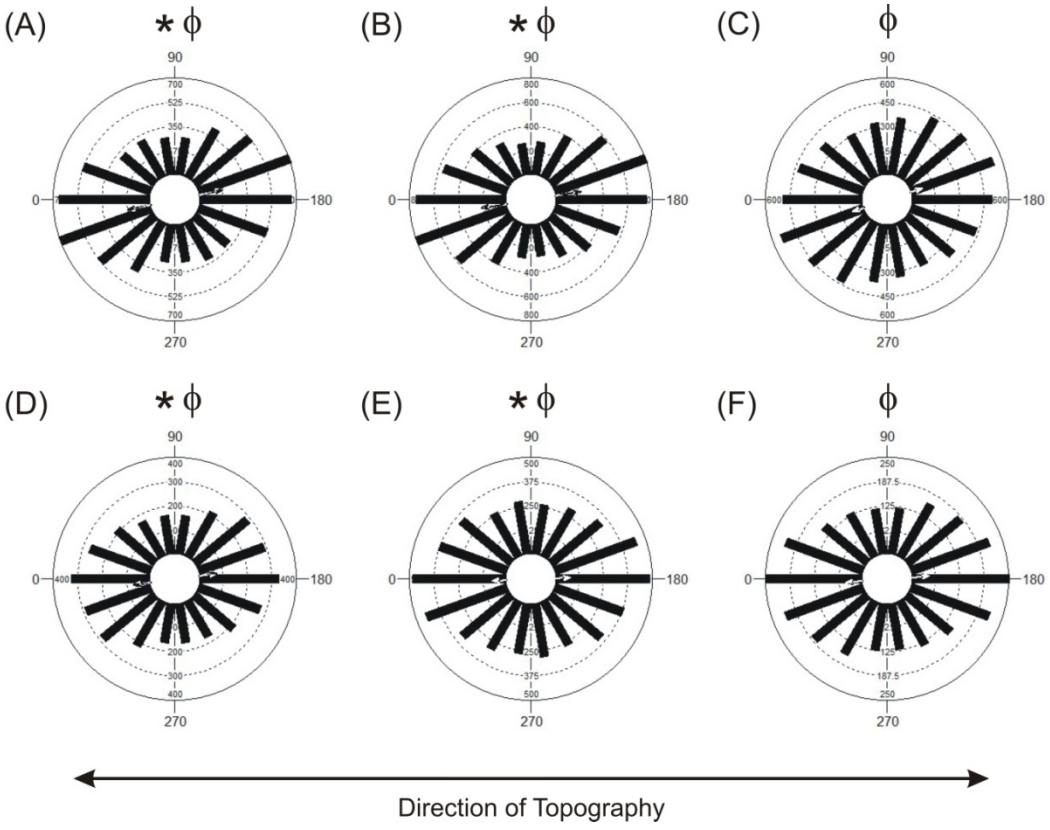

Figure 3.9. Quantitative analysis of cellular alignment on anisotropic A7 topographies revealed different clustering of alignment in the direction of underlying topography.

Circular histograms of nuclear angle distributions of replicate experiments of DRGs cultured on PDMS substrates presenting aligned A7 topography (A-F). *Indicates difference from a uniform distribution with by Rao's spacing test ($p<0.05$). ϕ, Indicates mean vector angle in the direction of the topographical cue by V-test ($p<0.05$).

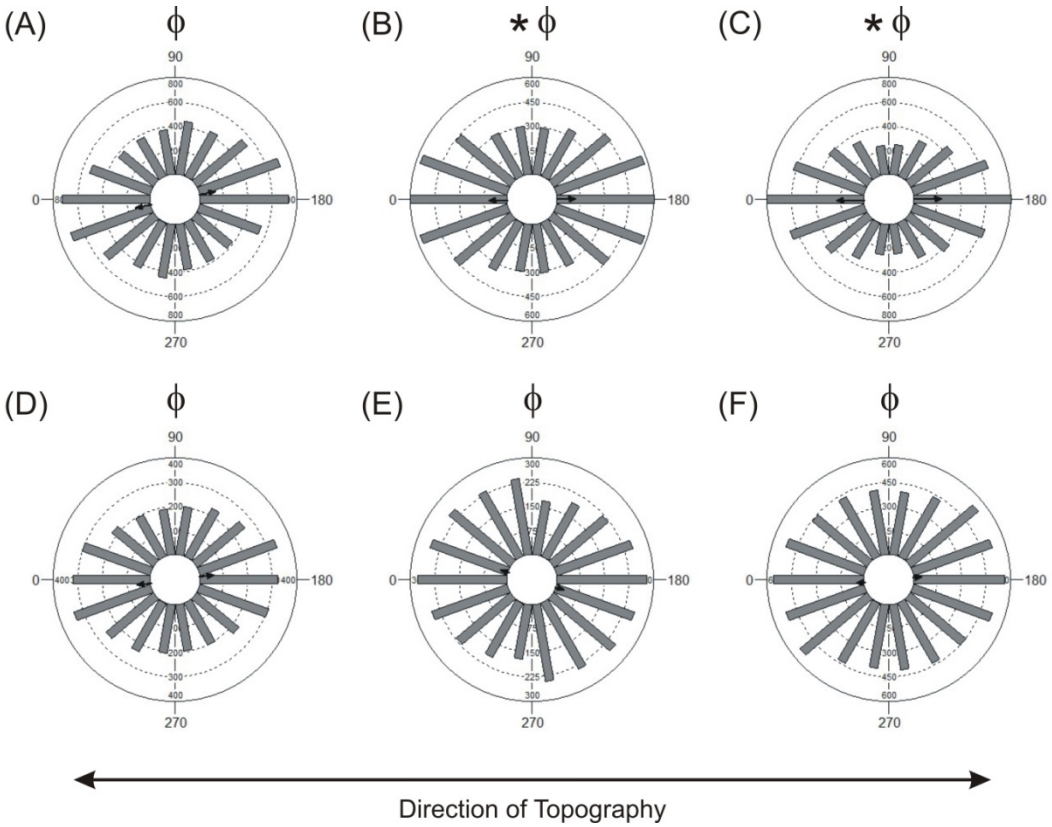

Figure 3.10. Quantitative analysis of cellular alignment on anisotropic HUVEC topographies revealed different clustering of alignment in the direction of underlying topography.

Circular histograms of nuclear angle distributions of replicate experiments of DRGs cultured on PDMS substrates presenting aligned HUVEC topography (A-F). *Indicates difference from a uniform distribution with by Rao's spacing test ($p<0.05$). ϕ, Indicates mean vector angle in the direction of the topographical cue by V-test ($p<0.05$).

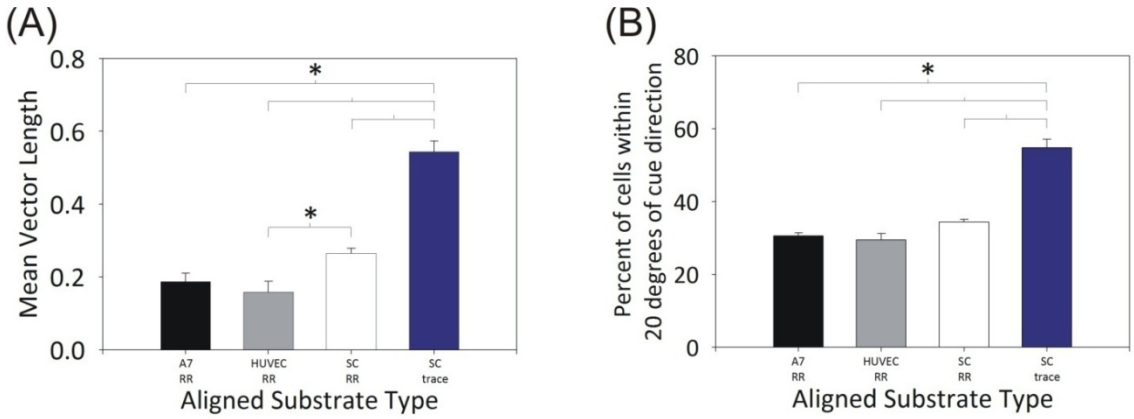

Figure 3.11. Alignment on geometric topographies was stronger than on cellular topographies.

Graph of mean vector length of nuclear angle distributions of DRGs plated on PDMS substrates coated with pLL-LN at 200K cells/well for 5 days. Mean ± SEM are presented, n=6 for each condition, *, $p<0.05$ by ANOVA.

Analysis of neurites by FFT revealed similar trends in the response of neurites to these anisotropic materials. An intensity peak centered at 90° was present in all spectra of neurites cultured on anisotropic materials (Figure 12). As FFT processing shifts directional data 90°, these peaks correspond to directed neurite growth along the direction of the topographical cue presented. Similar to the trends of nuclear alignment observed, alignment on bioinspired SC features was strongest as indicated by the highest intensity peak (Figure 10D). Alignment on biomimetic SC features was suggested to be stronger than on A7 and HUVEC features as indicated by the clear intensity peak compared to the noisy and flatter intensity peaks on A7 and HUVEC substrates (Figure 10A, 10B, 10C). The variability of responses of nuclear alignment on A7 and HUVEC replicates was also supported by FFT analysis of neurite alignment. Replicates with nuclear distributions that were not significantly different from uniform distributions did not generate clear intensity peaks when neurites were analyzed by FFT (data not shown).

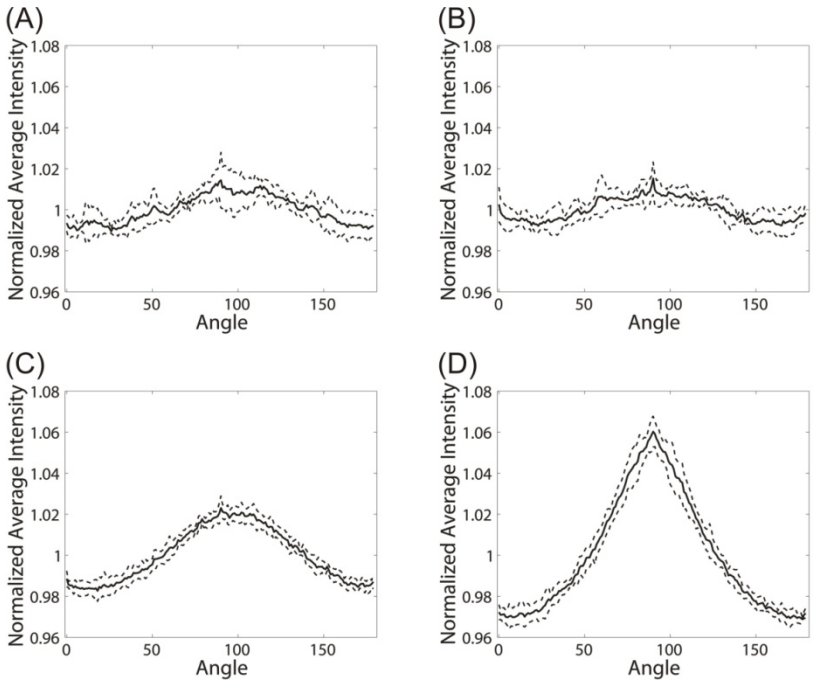

Figure 3.12. Alignment of neurites was stronger on geometric topographies than on cellular topographies. Graphs of normalized pixel intensities of FFT along radii from 0-179°. Epifluorescent images stained for neurites of DRGs cultured on PDMS substrates presenting aligned A7 topography (A), aligned HUVEC topography (B), aligned SC topography (C), and geometric traces of SC topography (D) with anti-neuronal class III beta tubulin were processed with FFT. Mean, dark grey solid line; Plus and minus standard deviation, grey dotted lines.

3.4 Discussion

The main objective of this study was to gain insights into the shapes and dimensions of topographical features that encode critical guidance information to navigating neurons. In previous studies, edges, fibers, grooves, and cellular topographies have been shown to influence directed neurite outgrowth.[4, 28, 33, 34] Our micromolding and lithographic approach provided several advantages in this study; 1) substrates were generated that contained micro- and nano-scale replication of cellular features; 2) by changing the types of cells aligned and replicated, a variety of topographical shapes and sizes whose influence has not been previously investigated were presented to navigating neurons; and 3) generation of bioinspired geometric features allowed edges and cellular topographies to be compared in the same study for the first time. DRG orientation was directed on all anisotropic materials presented while the growth of DRGs was randomly oriented on flat and isotropic materials. DRG alignment was similar on anisotropic biomimetc features. Comparison of mean vector length of nuclear clustering showed no difference between DRG cellular alignment on SC materials versus A7 materials. Comparison of uniformity tests, however, points toward more isotropic orientation on A7 materials. Stronger neurite alignment on SC materials was also suggested by FFT processing of DRG neurite response. Similarly, clustering of alignment on A7 materials was not significantly different from clustering on HUVEC materials, but uniformity tests suggest more uniform orientation on HUVEC materials. Taken together, clustering analysis and uniformity tests suggest that DRG alignment was strongest on SC materials followed by A7 materials with more uniform orientation to HUVEC materials. DRG neurons, support cells, and neurites demonstrated the most directed response on bioinspired materials which presented anisotropic features of variable length and width and >3 μm depth with 90° edges.

In order to study the response of DRGs to these anisotropic substrates, we were interested in assessing cellular and neurite alignment. DRG plating density and culture duration were chosen based on conditions in previous work shown to be most effective for alignment of DRGs on materials replicating Schwann cell alignment.[28] Circular statistical analysis and mean vector length of nuclear

angles were chosen to measure alignment because circular orientation data such as alignment is better described by a resultant vector rather than an arithmetic mean and the mean vector length corresponds to the clustering of the angles of the nuclei.[30] Changes in cellular shape have been shown to affect the shape of the nucleus,[35, 36] and previous work has shown that the angle of the major axis of the nucleus is an effective measure of cellular orientation.[32, 37] FFT was also performed as there is evidence that nuclear alignment is indicative to cellular alignment, but the exact correlation between nuclear alignment and neurite alignment has not been established. FFT has been shown to be effective for processing and representing anisotropic neurite outgrowth.[23, 38]

A7s and SCs were chosen because while it is well recognized that the different chemical cues presented by SCs and astrocytes after injury contribute to the varied capacities for regeneration in the PNS and CNS, it has not yet been shown whether their topographical features also contribute to the promotion of axon guidance. The development of a micromolding technique to replicate cellular topographies facilitates the deconstruction of the local cellular cues present *in vivo*. We were also interested in determining if guidance by anisotropic tissues was limited to the features of glial cells, so HUVECs were chosen for characterization as a non-glial cell type. Astrocytes, ECs, and SCs have been cultured to aligned confluence previously, but not in the same manner so that their influence on neuron growth can be compared in the same experiments. Our biomimetic materials present a complex range of surface heights that vary from tens of nanometers to single micrometers, and by changing the types of cells aligned and replicated, a variety of topographical shapes and sizes whose influence has not been previously investigated were presented to navigating neurons.

DRG alignment was most strongly directed by materials presenting oriented features inspired by the projections of SCs. The projected area of features on these substrates was comparable to replicas of SC topographies, but the features on these substrates were higher, had sharper edges, and presented continuous features to navigating neurons. Considering these observations, it is not surprising that

these materials were better at directing neurite outgrowth. Studies by Clark et al. suggest that the contribution of height or depth to directing cellular alignment is greater than pitch and size of these features.[9] Several studies have suggested that depth must exceed 1 μm before effectively guiding neurons.[4, 9, 10] Chick cerebral neurons were unaffected by 8 μm grooves with 20 μm plateaus with 1 μm height, but growth on 2 μm high patterns was markedly aligned.[9] Hippocampal neurons were optimally aligned on features that were 1.1 μm in height and separated by 4 μm in one study,[4] and controlled alignment of these cells was also achieved by using microfabricated silicon surfaces with 1 μm high pillars.[39] Another study showed that the alignment of DRG neurites was significantly induced by substrates with roughness of at least 250 nm on polystyrene modified by contact molding,[40] and Britland et al. showed that DRG neurites did not align to gratings when height was less than 1 μm.[10] Our bioinspired substrates presented a uniform height of >3 μm which is significantly greater than this 1 μm threshold. Cellular topographies, however, presented a maximum topography of approximately 1 μm.

Another attribute of our bioinspired topographical materials that increases their capacity to guide neurons is the sharp edges of these features. Neurites have shown a bias for growth in the direction of minimum curvature,[34] and other studies have suggested that axons grow in directions that minimize turning.[41] From these observations it would follow that neurites would be less likely to change their direction when extending in grooves or along edges as it would require a 90° turn. Cellular topographies present a more gradual curvature so extension perpendicular to a feature would not require such a drastic turn. Our lithographically generated materials also present continuous interconnected plateau structures while cellular monolayers present spatially varying heights and spaces. Previous studies have shown discontinuous structures in the form of pillars to guide neurite growth, but a larger amount of growth perpendicular to these structures is also seen.[39]

This study has isolated cellular topographic cues to achieve a better understanding of how these cues guide developing axons. We also sought to find a correlation between the topographical features presented and their ability to guide neurons. It was not surprising that cellular topographies guided neurite outgrowth as previous studies have shown alignment on SC topography or on more geometric features on the order of cellular sizes.[4, 10, 28, 42] Comparison of alignment among DRGs on cellular replicas is not as drastic as comparison to more geometric bioinspired topography, but subtle differences in alignment can be attributed to the features presented by these substrates. Materials presenting SC topography demonstrated the strongest capacity for guiding neurites and demonstrated a stronger capacity than HUVECs for directing alignment of DRG cells. A7 topography did not enhance cellular or neurite alignment in comparison to HUVEC topography, and cellular alignment on these substrates was not different from cellular alignment on SC topography.

Our cellular topographies presented similar adhesive surface coatings and heights. All substrates were coated with pLL-LN. While LN is expressed by A7s, ECs, and SCs at some level,[43-45] the uniform presentation of this molecule on these cellular topographies may have made their capacity for guidance more uniform. The average and maximum height across the somata presented by each of these cell types was also not significantly different. Contrasting features of cellular topographies included size, degree of alignment, and pitch. HUVECs presented the largest areas of protruding topography to navigating neurons as they were both longer and wider than A7s and SCs. This size contrast was especially pronounced between HUVECs and SCs as HUVECs were 54% larger than SCs. Growth cones are typically 1 to 10 μm in diameter and are likely to react differently to a feature that is 62 x 25 μm than to one that is 36 x 13 μm. The larger size of HUVECs may thus play a role in the decreased capacity for directing DRG alignment in comparison to SCs.

Contrast in the degree of alignment of our substrates did not appear to strongly contribute to the ability of these topographies to guide outgrowth. SC materials presented topography with a stronger

degree of alignment as the clustering of nuclear angles of cells in these materials was double the clustering of the other two cell types, and 20% more of SCs were aligned within 20° of the overall cue direction than A7s or HUVECs aligned within 20°. Based on the findings of previous work, the higher degree of alignment on SC materials should similarly improve the alignment of neurons to these materials. In one study, the pattern of neurite elongation from chick DRGs into magnetically aligned collagen gels was more directed in collagen gels with a higher degree of alignment.[5] Similarly, Corey et al. found greater DRG neurite alignment on more highly aligned electrospun nano-fibers.[38] Based on these findings, we would expect a significant increase in DRG alignment on SC materials, but cellular alignment was not increased compared to growth on A7 materials, and the increase in cellular alignment compared to HUVEC materials and neurite alignment compared to A7 and HUVEC materials was not similar in magnitude to the increased anisotropy of SC materials.

The lack of effect by increased clustering of alignment of SC materials may point to an important role for the frequency of guidepost cues rather than the overall degree of orientation of these cues. While the distribution of SC alignment was more directed than other cell types, the number of topographical cellular features directing toward the overall orientation of the material was similar for A7 and SC materials. A7s packed together more closely at confluence so while a lower percentage of cells oriented in the direction of alignment, the number of aligned cells was similar to the number of aligned SCs. HUVECs had a lower packing density than both A7s and SCs so the percentage of aligned HUVECs as well as the number of aligned HUVECs was smaller. All three types of cellular topographies presented features on the order of 1 μm in depth. Clark et al. suggested that the effect of spacing is of minor importance at depths of 2 μm or more, but cellular response to repeating features of 1 μm height or less is more pronounced than reaction to single features of the same magnitude.[9] At smaller depths, alignment is generally inversely proportional to spacing.[9] The spacing of aligned features in A7 and SC materials was lower than the space between aligned HUVEC features which may improve their ability to elicit guidance. This observation is also relevant to axon guidance during development. Guidepost cells are thought to play an integral part in directing

neurites to their appropriate targets. Such cells are present along the path of growing axons, are contacted by axonal growth cones, and are separated from one another but within filopodial reach of one another similar to the topographical cues presented by our materials. In development the route is not straight so these cells are not continuously present along the axon path; instead they are present at discrete points, providing non-continuous positional information that sequentially guides axonal growth.[46] As guidepost cells may contain cues that could reorient the trajectory of the axon at the strategic points, these results suggest that these cues attributed to guidepost cells may be at least partly topographical.

Contact guidance of cells by physical contours has been shown to be a promising approach for guiding neurons in a variety of studies, but less is known about the cellular events of contact sensing and their transduction into directional growth, especially in neuronal growth cones. It has been proposed that microtubules and actin filaments within the cytoplasm are inflexible and do not allow significant bending of filopodia to accommodate topographical features. Microchannel walls may limit the set of angles over which microtubules and actin filaments within the neurite shaft and growth cone accumulate, assemble, and orient to advance the growing neurite. Neurons and neurites were not trapped in grooves on our substrates allowing for more flexibility of the cytoskeleton. Guidance was elicited by our substrates, however, pointing to a different mechanism of topographical sensing. Others have recognized that oriented growth of neurites is not merely due to physical constraint within the grooves because individual growth cones often span several groove and ridge repeats.[4] Xenopus and hippocampal neurons grew parallel to grooves too small to restrain them physically, suggesting that parallel orientation was not merely due to neurites being trapped within grooves. Although filopodia were predominately aligned parallel to grooves, they were not essential for contact guidance.[47] These observations suggest that the alignment response of neurons to grooved substrata requires active sensation and integration of cues rather than being a consequence of passive restraint. Even when not due to steric hindrance the cytoskeleton is likely involved in topographical sensing. Cells which lack cytoskeletal organization are less susceptible to

topographical guidance on glass fibers and microgrooved substrata as demonstrated by Clark et al. They found that neutrophil leukocytes, whose cytoskeletal organization is highly labile, were unresponsive to single steps to which other cell types would react strongly. Less responsive cell types are also generally less adhesive so contact-induced cell spreading may also play a role in cellular alignment to topographical features.[9]

These results suggest a capacity for anisotropic cellular topographies to orient the growth of neurons, support cells, and neurites. DRG cultures are heterogeneous, containing not only neurons, but also proliferating SCs and fibroblasts. When neurites in DRG cultures align in the direction of SC topography, they may be responding directly to the topography and/or directly to support cells which have aligned to the topography. The results of this study suggest some contribution by support cells or at least by the overall cellular orientation. When the cellular distribution on an anisotropic A7 or HUVEC substrate was similar to a uniform distribution, FFT processing did not indicate alignment. These results can be attributed to a reduced capacity for the features of these substrates to align support cells (to which neurites then align) or a reduced capacity to guide all cells and neurites. Neurites and glial cells have shown different capacities for interacting with guidance features. Adhesive patterns that inhibit Neu7 cell adhesion promote the adhesion and growth of DRG neurites. Specifically, neurites can grow freely through the array of hydrogels spaced 2 μm apart from each other.[48] Neurons have also been shown to be less responsive to ultrafine gratings than astrocytes.[49] This difference is attributed to the lack of high-order F-actin and focal adhesions in neurons. The role of other cells in alignment to topographical features has been previously recognized. Observations by Clark et al. suggested that on grooved substrata, baby hamster kidney cell alignment increases with population density.

Other studies have observed longer neurites lengths, increased rate of growth in the preferred direction, fewer neurites per neuron, alteration in the sites at which neurites emerge from somata,

increased mobility, and increased synaptic connections on anisotropic materials.[4, 8, 39, 41] Our study was not well suited to study these effects as the density of growth at the timepoint investigated made it difficult to assess these factors. It will be important in future studies to explore other densities and time points to explore the contributions of cellular topographies to these neuronal functions.

3.5 Conclusion

We aimed to describe the directional effects of substratum contours on neuronal guidance as a first step toward elucidating the mechanism for topography-induced guidance. There is a need to understand the cues that guide axons and how we can manipulate these cues to achieve directed neuronal growth. Anisotropic cellular topographies were shown to be sufficient for guiding neuronal growth despite distinct topographies and anisotropies presented by these materials. Biomimetic SC materials guided neurons more effectively than astrocyte and HUVEC materials, but neurons, support cells, and neurites demonstrated the most directed response on bioinspired materials which presented anisotropic features of >3 μm depth with 90° edges. These results suggest that the topography of anisotropic tissue structures are sufficient for neuronal growth, but the features presented by cellular topography may not be optimal for directed control of neuronal growth. When trying to develop a method to direct axons toward specific targets, an understanding of the cell to cell interactions present in the damaged nervous system is essential, and elucidation of the critical dimensions of cues presented in that matrix will allow for a more rigorous construction of effective therapeutics toward CNS regeneration.

3.6 References

1. Schmidt, C. E. and J. B. Leach. Neural tissue engineering: Strategies for repair and regeneration. Annu Rev Biomed Eng. 5: 293-347, 2003.

2. Chen, Y. Y., D. McDonald, C. Cheng, B. Magnowski, J. Durand and D. W. Zochodne. Axon and schwann cell partnership during nerve regrowth. Journal of Neuropathology and Experimental Neurology. 64: 613, 2005.

3. Silver, J. and J. H. Miller. Regeneration beyond the glial scar. Nat Rev Neuroscience. 5: 146-156, 2004.

4. Rajnicek, A., S. Britland and C. McCaig. Contact guidance of cns neurites on grooved quartz: Influence of groove dimensions, neuronal age and cell type. J Cell Sci. 110 (Pt 23): 2905-13, 1997.

5. Dubey, N., P. C. Letourneau and R. T. Tranquillo. Guided neurite elongation and schwann cell invasion into magnetically aligned collagen in simulated peripheral nerve regeneration. Exp Neurol. 158: 338-50, 1999.

6. Britland, S. and C. McCaig. Embryonic xenopus neurites integrate and respond to simultaneous electrical and adhesive guidance cues. Exp Cell Res. 226: 31-8, 1996.

7. Zhang, N., C. Zhang and X. Wen. Fabrication of semipermeable hollow fiber membranes with highly aligned texture for nerve guidance. J Biomed Mater Res A. 75: 941-9, 2005.

8. Mahoney, M. J., R. R. Chen, J. Tan and W. M. Saltzman. The influence of microchannels on neurite growth and architecture. Biomaterials. 26: 771-8, 2005.

9. Clark, P., P. Connolly, A. S. Curtis, J. A. Dow and C. D. Wilkinson. Topographical control of cell behaviour: Ii. Multiple grooved substrata. Development. 108: 635-44, 1990.

10. Britland, S., C. Perridge, M. Denyer, H. Morgan, A. Curtis and C. Wilkinson. Morphogenetic guidance cues can interact synergistically and hierarchically in steering nerve cell growth. Experimental Biology Online. 1: 1-15, 1997.

11. David, S. and A. J. Aguayo. Axonal elongation into peripheral nervous system "Bridges" After central nervous system injury in adult rats. Science. 214: 931-3, 1981.

12. Richardson, P. M., U. M. McGuinness and A. J. Aguayo. Axons from cns neurons regenerate into pns grafts. Nature. 284: 264-5, 1980.

13. Pettigrew, D. B. and K. A. Crutcher. White matter of the cns supports or inhibits neurite outgrowth in vitro depending on geometry. J Neurosci. 19: 8358-66, 1999.

14. Glasby, M. A., S. G. Gschmeissner, R. J. I. Hitchcock and C. L. H. Huang. The dependence of nerve regeneration through muscle grafts in the rat on the availability and orientation of basement membrane. Journal of Neurocytology. 15: 497-510, 1986.

15. Keynes, R. J., W. G. Hopkins and L. H. Huang. Regeneration of mouse peripheral nerves in degenerating skeletal muscle: Guidance by residual muscle fibre basement membrane. Brain Res. 295: 275-81, 1984.

16. Hall, S. Axonal regeneration through acellular muscle grafts. Journal of Anatomy. 190: 57-71, 1997.

17. Anderson, P. N. and M. Turmaine. Axonal regeneration through arterial grafts. Journal of Anatomy. 147: 73, 1986.

18. Chiu, D. T., I. Janecka, T. J. Krizek, M. Wolff and R. E. Lovelace. Autogenous vein graft as a conduit for nerve regeneration. Surgery. 91: 226-33, 1982.

19. Foidart-Dessalle, M., A. Dubuisson, A. Lejeune, A. Severyns, Y. Manassis, P. Delree, J. M. Crielaard, R. Bassleer and G. Lejeune. Sciatic nerve regeneration through venous or nervous grafts in the rat. Experimental Neurology. 148: 236-246, 1997.

20. Biran, R., M. D. Noble and P. A. Tresco. Directed nerve outgrowth is enhanced by engineered glial substrates. Exp Neurol. 184: 141-52, 2003.

21. Recknor, J. B., D. S. Sakaguchi and S. K. Mallapragada. Growth and differentiation of astrocytes and neural progenitor cells on micropatterned polymer films. Ann N Y Acad Sci. 1049: 24-7, 2005.

22. Deumens, R., G. C. Koopmans, C. G. Den Bakker, V. Maquet, S. Blacher, W. M. Honig, R. Jerome, J. P. Pirard, H. W. Steinbusch and E. A. Joosten. Alignment of glial cells stimulates directional neurite growth of cns neurons in vitro. Neuroscience. 125: 591-604, 2004.

23. Alexander, J. K., B. Fuss and R. J. Colello. Electric field-induced astrocyte alignment directs neurite outgrowth. Neuron Glia Biol. 2: 93-103, 2006.

24. Miller, C., S. Jeftinija and S. Mallapragada. Micropatterned schwann cell-seeded biodegradable polymer substrates significantly enhance neurite alignment and outgrowth. Tissue Eng. 7: 705-15, 2001.

25. Thompson, D. M. and H. M. Buettner. Neurite outgrowth is directed by schwann cell alignment in the absence of other guidance cues. Ann Biomed Eng. 34: 161-8, 2006.

26. Walsh, J. F., M. E. Manwaring and P. A. Tresco. Directional neurite outgrowth is enhanced by engineered meningeal cell-coated substrates. Tissue Eng. 11: 1085-94, 2005.

27. Stepien, E., J. Stanisz and W. Korohoda. Contact guidance of chick embryo neurons on single scratches in glass and on underlying aligned human skin fibroblasts. Cell Biol Int. 23: 105-16, 1999.

28. Bruder, J. M., A. P. Lee and D. Hoffman-Kim. Biomimetic materials replicating schwann cell topography enhance neuronal adhesion and neurite alignment in vitro. Journal of Biomaterials Science, Polymer Edition. 18: 967-982, 2007.

29. Geller, H. M. Antigenic and functional characterization of a rat central nervous system-derived cell line immortalized by a retroviral vector. Journal of Cell Biology. 107: 1977-1986, 1988.

30. Li, G. N. Y. and D. Hoffman-Kim. Evaluation of neurite outgrowth anisotropy using a novel application of circular analysis. Journal of Neuroscience Methods. 2008.

31. Bruder, J. M., N. C. Monu, M. W. Harrison and D. Hoffman-Kim. Fabrication of polymeric replicas of cell surfaces with nanoscale resolution. Biomaterials. 27: 460-472, 2006.

32. Kofron, C. M. and D. Hoffman-Kim. Optimization by response surface methodology of confluent and aligned cellular monolayers for nerve guidance. Ann Biomed Eng. submitted: 2009.

33. Clark, P., P. Connolly, A. S. Curtis, J. A. Dow and C. D. Wilkinson. Topographical control of cell behaviour. I. Simple step cues. Development. 99: 439-48, 1987.

34. Smeal, R. M., R. Rabbitt, R. Biran and P. A. Tresco. Substrate curvature influences the direction of nerve outgrowth. Ann Biomed Eng. 33: 376-82, 2005.

35. Dalby, M. J., M. O. Riehle, S. J. Yarwood, C. D. Wilkinson and A. S. Curtis. Nucleus alignment and cell signaling in fibroblasts: Response to a micro-grooved topography. Exp Cell Res. 284: 274-82, 2003.

36. Maniotis, A. J., C. S. Chen and D. E. Ingber. Demonstration of mechanical connections between integrins, cytoskeletal filaments, and nucleoplasm that stabilize nuclear structure. Proc Natl Acad Sci U S A. 94: 849-54, 1997.

37. Yim, E. K., R. M. Reano, S. W. Pang, A. F. Yee, C. S. Chen and K. W. Leong. Nanopattern-induced changes in morphology and motility of smooth muscle cells. Biomaterials. 26: 5405-13, 2005.

38. Corey, J. M., D. Y. Lin, K. B. Mycek, Q. Chen, S. Samuel, E. L. Feldman and D. C. Martin. Aligned electrospun nanofibers specify the direction of dorsal root ganglia neurite growth. Journal of Biomedical Materials Research Part A. 2007.

39. Dowell-Mesfin, N. M., M. A. Abdul-Karim, A. M. Turner, S. Schanz, H. G. Craighead, B. Roysam, J. N. Turner and W. Shain. Topographically modified surfaces affect orientation and growth of hippocampal neurons. J Neural Eng. 1: 78-90, 2004.

40. Gomez, N., Y. Lu, S. Chen and C. E. Schmidt. Immobilized nerve growth factor and microtopography have distinct effects on polarization versus axon elongation in hippocampal cells in culture. Biomaterials. 28: 271-284, 2007.

41. Li, N. and A. Folch. Integration of topographical and biochemical cues by axons during growth on microfabricated 3-d substrates. Exp Cell Res. 311: 307-16, 2005.

42. Nagata, I., A. Kawana and N. Nakatsuji. Perpendicular contact guidance of cns neuroblasts on artificial microstructures. Development. 117: 401-8, 1993.

43. Grimpe, B., S. Dong, C. Doller, K. Temple, A. T. Malouf and J. Silver. The critical role of basement membrane-independent laminin gamma 1 chain during axon regeneration in the cns. Journal of Neuroscience. 22: 3144, 2002.

44. Sorokin, L., W. Girg, T. Gopfert, R. Hallmann and R. Deutzmann. Expression of novel 400-kda laminin chains by mouse and bovine endothelial cells. European Journal of Biochemistry. 223: 603-610, 1994.

45. Bixby, J. L. and W. A. Harris. Molecular mechanisms of axon growth and guidance. Annu Rev Cell Biol. 7: 117-59, 1991.

46. Chao, D. L., L. Ma and K. Shen. Transient cell-cell interactions in neural circuit formation. Nat Rev Neurosci. 10: 262-271, 2009.

47. Rajnicek, A. and C. McCaig. Guidance of cns growth cones by substratum grooves and ridges: Effects of inhibitors of the cytoskeleton, calcium channels and signal transduction pathways. J Cell Sci. 110 (Pt 23): 2915-24, 1997.

48. Krsko, P., S. Sukhishvili, M. Mansfield, R. Clancy and M. Libera. Electron-beam surface-patterned poly (ethylene glycol) microhydrogels. Langmuir. 19: 5618-5625, 2003.

49. Webb, A., P. Clark, J. Skepper, A. Compston and A. Wood. Guidance of oligodendrocytes and their progenitors by substratum topography. J Cell Sci. 108 (Pt 8): 2747-60, 1995.

Chapter 4 Combinations of Schwann cell topography and patterned molecular cues influence neuron growth

This study investigated the collaborative and hierarchical effects of combinations of permissive or inhibitory molecular cues and biomimetic materials presenting anisotropic Schwann cell (SC) topography on directed neuronal growth. We utilized the versatility of micro-contact printing to present single, cooperating, and competing directive cues to dorsal root ganglia neurons. Poly(dimethyl siloxane) (PDMS) replicas presenting anisotropic SC topography were micro-contact printed with stripes of laminin (LN), chondroitin sulfate proteoglycans (CSPGs), or a mix of the two proteins. Protein stripes were patterned either parallel or perpendicular to anisotropic topography. Single cue platforms of protein stripes on flat materials or topographic materials uniformly coated with protein were also examined for their capacity to guide neuronal growth. We investigated the effects of protein concentration, pattern dimensions, and pattern type on the preference of neurons to align on directive biomimetic replicas. Neurons exhibited a preference for directive biochemical cues over directive biomimetic topographical cues over the range of protein concentrations and geometries tested. The findings of this study suggest that the hierarchy of directive cues does not depend solely on the type of cue presented. The relative strength of each cue individually is important, but comparison of the relative strengths of cues when presented individually does not completely predict their hierarchy or accord when presented together.

4.1 Introduction

Neurons process and transmit information in the nervous system, but in order for their intricate networks to be formed and maintained, neurons must be promoted to grow, follow a directed path, and connect or reconnect to the appropriate targets. Pathfinding neurons are endowed with a variety of cues to interpret and integrate, including substrate bound and diffusible chemical factors, electrical signals from neighboring cells, and physical and topographical features from the morphology of surrounding cells and the extracellular matrix (ECM). Neuronal response to individual cues has been studied extensively, and cues are often presented in platforms that are classified as having an overall positive or negative influence on growth including permissive, inhibitory, outgrowth promoting, outgrowth suppressing, attractive, repulsive, or directive, but integration of these cues in competing or cooperative platforms is not well understood. Studies that incorporate the collective influences of the rich mixture of cues in the local environment are imperative for understanding the decisions neurons make *in vivo*.

Individually, guidance by anisotropic topography or proteins has been established. Oriented fibers,[1, 2] plateaus and grooves,[3] and cellular topographies[4, 5] have all demonstrated the influence of topography as a directive cue for nerve guidance, and effective features range from nanometers to micrometers, similar to the sizes of features presented by cells and ECM *in vivo*.[3, 6, 7] Substrate bound chemical cues have also been shown to influence directed neurite outgrowth. Chemical cues are often presented in boundary lines and parallel stripes in order to investigate their ability to direct growth.[8-11] Two such cues that are of particular relevance in the nervous system are laminin (LN) and chondroitin sulfate proteoglycans (CSPGs). LN is an adhesive and growth-promoting ECM glycoprotein present in developing and regenerating axon tracts.[12] Inhibitory CSPGs are also present in many regions of the developing nervous system and are a major contributor to the inhibitory nature of the glial scar formed in the central nervous system after injury.[13] Neurons align on LN tracks and between CSPG tracks *in vitro*.[9, 11, 13-17] Neurons have also been shown to be guided by

anisotropic cellular structures *in vitro* and *in vivo*.[18-20] Cellular tracks present both topographies with the capacity to guide neurites[5] and directive molecular cues including LN, CSPGs, and cell adhesion molecules. The relative and cooperative contributions of each of these directive elements are therefore unknown. In order to determine their full potential as guidance molecules *in vivo*, directive topographical and biochemical cues must be evaluated together. The recent isolation of cellular topography via biomaterial replicas provides a useful platform for presentation of multiple cellular cues to navigating neurons.[21]

Initial research of multi-cue environments has shown additive and hierarchical effects of directive cues. Parallel presentation of microgrooves and LN increased alignment of neurites relative to microgrooves or LN stripes alone.[22] Similarly, presentation of microchannels and immobilized nerve growth factor (NGF) stimulated growth of longer neurites relative to microchannels or NGF alone,[23] and simultaneous presentation of microchannels and poly-L-lysine tracks promoted geometric control of neurite connections between microelectronic circuit nodes.[24] When conflicting information was presented, neurons exhibited preference for extension into a LN-rich matrix rather than along poly-D-lysine topography.[25] When LN or CSPG tracks were presented in conjunction with three-dimensional (3D) collagen matrices, the response was protein dependent.[11] When LN was presented, neurites showed preference for guided extension along two dimensional (2D) LN tracks. When CSPG was presented, neurites were not directed at the 2D surface, but instead were guided away from the CSPG surface in 3D. Britland et al. studied both parallel and orthogonal presentation of cues. Parallel presentation of LN tracks and microgrooves increased neurite alignment. When these cues were presented orthogonally, more neurites aligned to LN tracks with groove depths of less than 1 μm, but neurites aligned in the direction of the topography with deeper grooves.[26] Recent studies in our lab of parallel and orthogonal presentation of LN tracks and anisotropic cellular topographies have shown trends similar to those seen by Britland et al. for topographical features of less than 1 μm in height.[27] These studies are an important first step in the investigation of multi-cue

environments, but further study is necessary to gain insights into the complex features of the topography and proteins of the *in vivo* environment.

This study aimed to investigate the additive and hierarchical effects of combinations of permissive or inhibitory molecular cues and biomimetic materials presenting Schwann cell (SC) topography on directed neuronal growth. Our first set of conditions supported the conclusion that neurons exhibit preference for biochemical directive cues, but these results were tested over a limited range of protein concentrations and geometry. We also hypothesized that there exists a set of conditions where the cellular topography dominates over biochemical patterning wherein neurons preferentially align to the underlying topography. Toward this end, we aimed to investigate the effects of protein concentration, pattern dimensions, and pattern type on the preference of neurons to align on directive biomimetic replicas.

4.2 Materials and methods

4.2.1 Generation of biomimetic materials presenting SC topography

Biomimetic materials presenting aligned SC topographies were generated as previously described.[28] Briefly, photolithography and soft lithography were used to make poly (dimethylsiloxane) (PDMS) (Dow Corning, Midland, MI, USA) stamps with repeating micron-scaled grooves and plateaus. These patterns were then used to transfer LN protein patterns to glass via micro-contact printing. SCs from rat sciatic nerve, a generous gift of Dr. Mary Bunge (University of Miami, Coral Gables, FL, USA), were cultured on the protein patterns and aligned parallel to the protein stripes in Dulbecco's modified eagle's medium (DMEM) (Invitrogen Life Technologies, Carlsbad, CA, USA) with 10% fetal bovine serum (FBS) (Invitrogen), 4 mM L-glutamine (Invitrogen), 100 U/ml penicillin (Invitrogen), and 100 μg/ml streptomycin (Invitrogen) supplemented with 2 μM forskolin (Sigma, St. Louis, MO, USA), 10 μg/ml bovine pituitary extract (Sigma), and 2 μM heregulin (generous gift from Genentech, Vacaville,

CA, USA). Cultures were incubated at 37°C with 5% CO_2 in a humidified environment. The cells were fixed at confluence, and PDMS was used to make an impression mold of the cells. A second layer of PDMS was cast from the impression mold to form a relief replica presenting aligned SC topography with micro- and nano-scale resolution of features.

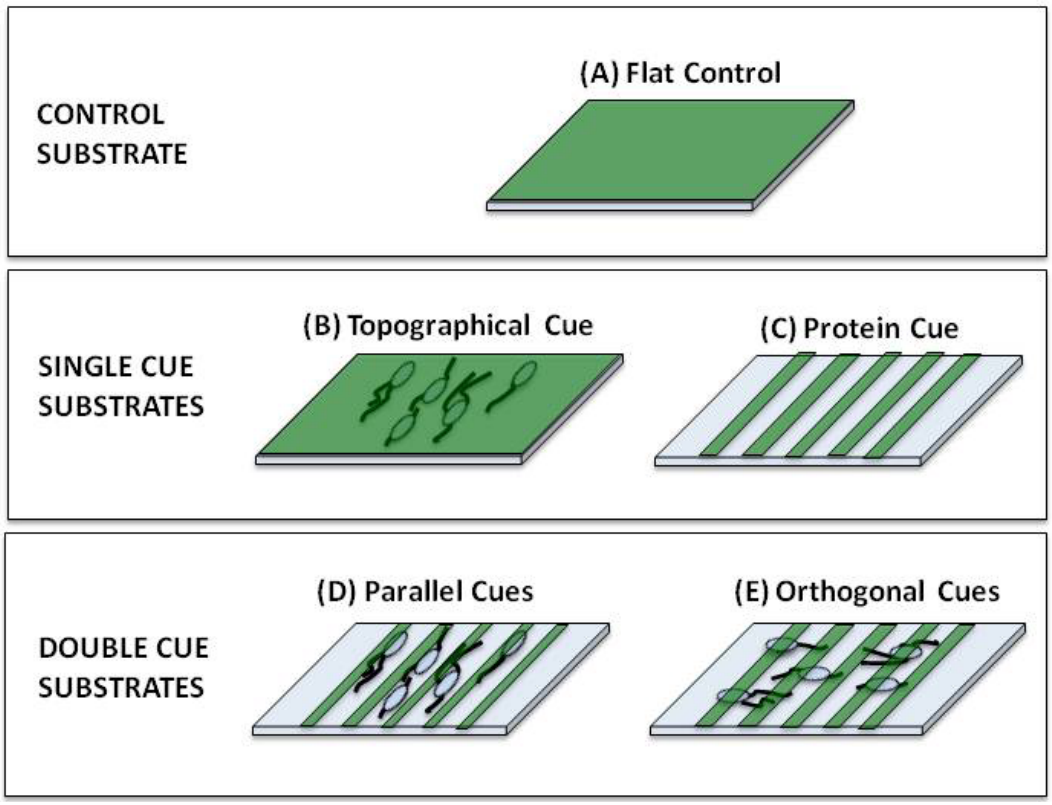

Figure 4.1. Single- and multi-cue platforms investigated.
Schematic of individual (A, B, C), cooperative (D), and competitive (E) presentation of directive cues. Platforms included: protein absorbed on flat PDMS (no directive cue) (A), protein absorbed on PDMS materials presenting anisotropic SC topography (B), microcontact printed protein on flat PDMS (C), protein microcontact printed parallel to SC topography (D), and protein microcontact printed orthogonal to SC topography (E).

4.2.2 Generation of multi-cue platforms for neuron guidance

Five different single- or double-cue platforms were generated: a flat fully coated control (flat control), a fully coated SC replica (single topographical cue), protein patterned flat PDMS (single protein cue), a SC replica with protein patterned parallel to the underlying topography (parallel

cues), or a SC replica with protein patterned orthogonal to the underlying topography (orthogonal cues) (Figure 1). Protein type(s), protein concentration, protein pattern geometry, and protein pattern dimensions were varied (summarized in Table 1). Mouse LN (Invitrogen) was tested at 5, 10, and 50 μg/ml. Embryonic chick CSPGs (Chemicon, Temecula, CA, USA) was tested at either 10 μg/ml. On substrates with a full protein coat, the protein was suspended in Hank's balanced salt solution (HBSS) (Invitrogen), deposited on a plasma-activated PDMS substrate, and allowed to adsorb to the surface for at least 1 h. Before cell plating, the excess protein was pipetted off, and the substrate was rinsed with water.

Patterned proteins were transferred to the PDMS substrates via micro-contact printing. PDMS stamps were coated with approximately 200 μl of the appropriated protein solution in HBSS for at least 1 h. Excess protein was removed, and the stamps were rinsed with distilled water and dried with a pressurized air stream. The stamps were then inverted onto plasma-activated flat or topographical PDMS to transfer the pattern for cell culture. Light pressure was applied to the back of the stamps to ensure even contact. Stamps were left in contact overnight and peeled off directly before cell culture. Proteins were either patterned in repeating straight lines or in bioinspired shapes mimicking the features of aligned SCs. Bioinsipred materials were generated as previously described.[5] Protein stripe width ranged from 50 to 500 μm and space width varied from 10 to 100 μm.

4.2.3 Study of dorsal root ganglia alignment

Dorsal root ganglia (DRG) explants were dissected from the spinal cords of postnatal rat pups (P0-P4). The explants were cleaned of any blood, axons, or connective tissue, incubated in 0.05% trypsin-EDTA (Invitrogen) in HBSS for 45 minutes, and dissociated by trituration. Dissociated DRG cells were cultured at 37°C and 5% CO_2 in DMEM with 10% FBS, 4 mM L-glutamine, 100 U/ml penicillin and

Table 4.1. Single- and multi-cue platforms investigated.

Protein concentration (μg/ml)	Micropattern Stripe (μm)-Space (μm) (orientation of cues)	Topographical cue	n	Rao's test	V-test	Mean vector length
CS10	50-50 (protein)	flat	3	p<0.05	p<0.05	0.554 ± 0.061
CS10	50-50 (orthogonal)	SC replica	2	p<0.05 (n=1); p>0.05 (n=1)	p<0.05	0.442 ± 0.028
CS10-LN50	(flat)	flat	3	p>0.05	p>0.05	0.023 ± 0.009
CS10-LN50	(topography)	SC replica	4	p<0.05	p<0.05	0.276 ± 0.020
CS10-LN50	50-50 (protein)	flat	5	p<0.05	p<0.05	0.370 ± 0.032
CS10-LN50	50-50 (parallel)	SC replica	5	p<0.05	p<0.05	0.510 ± 0.018
CS10-LN50	50-50 (orthogonal)	SC replica	6	p<0.05 (n=4); p>0.05 (n=2)	p<0.05	0.209 ± 0.029
LN 50	(flat)	flat	3	p>0.05	p>0.05	0.027 ± 0.006
LN 50	(topography)	SC replica	3	p<0.05	p<0.05	0.260 ± 0.018
LN 50	50-50 (protein)	flat	3	p<0.05	p<0.05	0.578 ± 0.027
LN 50	50-50 (parallel)	SC replica	3	p<0.05	p<0.05	0.604 ± 0.008
LN 50	50-50 (orthogonal)	SC replica	3	p<0.05	p<0.05	0.498 ± 0.061
LN 5	500-50 (protein)	flat	3	p<0.05 (n=1); p>0.05 (n=2)	p<0.05	0.150 ± 0.022
LN 5	500-50 (orthogonal)	SC replica	3	p>0.05	p>0.05	0.077 ± 0.015
LN 10	50-10 (protein)	flat	3	p<0.05	p<0.05	0.283 ± 0.021
LN 10	50-10 (orthogonal)	SC replica	2	p>0.05	p<0.05	0.084 ± 0.013
LN 10	trace (protein)	flat	6	p<0.05 (n=4); p>0.05 (n=2)	p<0.05	0.461 ± 0.013
LN 10	trace (orthogonal)	SC replica	5	p>0.05	p<0.05 (n=2); p>0.05 (n=3)	0.078 ± 0.021

100 μg/ml streptomycin supplemented with 50 ng/ml nerve growth factor (Invitrogen). Cells were plated at 41,000 cells/cm^2 and cultured for 5 days. DRG cells were fixed with 2% parafomaldehyde (Electron Microscopy Sciences, Hatfield, PA, USA) in phosphate buffered saline (PBS) (Invitrogen) for 15-20 min and then rinsed 3 times with PBS. Cell nuclei were stained with 1% 4,6-diamidino-phenylindole (DAPI) (Sigma) and 0.1% Triton-X VWR International, West Chester, PA, USA) in PBS. On substrates with CSPGs patterning or coating, neurites were stained with anti-GAP 43 (1:500)

primary antibody (Santa Cruz Biotechnology, Inc., Santa Cruz, CA, USA) and Cy3 conjugated goat anti-rabbit (1:200) secondary antibody (Jackson Immuno Research Laboratories, West Grove, PA, USA). CSPGs were stained with CS56 (1:200) primary antibody (Sigma) and FITC conjugated goat anti-mouse (1:150) secondary antibody (Sigma). On substrates with LN patterning or coating, neurites were stained with mouse anti-neurofilament (RT97) (Developmental Studies Hybridoma Bank, Iowa City, IA, USA) (1:200) or anti-β(III)tubulin (1:500) primary antibody (Covance Research Products, Inc., Berkeley, CA, USA) and Cy3 conjugated goat anti-mouse secondary antibody (1:200) (Jackson). LN was stained with rabbit anti-LN (1:200) primary antibody (Biomedical Technologies, Stoughton, MA, USA) and Cy2 conjugated goat anti-rabbit (1:200) secondary antibody (Jackson). Non-specific staining was blocked by incubating samples with 10% normal goat serum (Jackson) and 0.1% Triton-X in PBS for 60 minutes. Samples were then incubated with the first primary antibody overnight at 4°C and rinsed with PBS. Next, samples were incubated with the second primary antibody overnight at 4°C and rinsed. Finally, samples were incubated with the first secondary antibody for 1 h at room temperature, rinsed with PBS, incubated with the second secondary antibody for 1 h at room temperature, and rinsed 3 times. During and after this step, the samples were protected from light with aluminum foil. Wells with no primary antibodies and wells with cross-matched primary and secondary antibodies were kept as controls.

4.2.4 Microscopy and analysis

Phase contrast and fluorescent images were captured with a Nikon Eclipse TE200-S microscope at 100X, and outputted to OpenLab v4.0.4 (Improvision, Lexington, MA, USA). 10 fields of view (FOV) with the corresponding channels for phase, DAPI, protein, and neurite staining were captured for each sample. Nuclear alignment was analyzed via DAPI staining and used to indicate cellular alignment. DAPI images were converted to 8-bit grayscale, inverted and contrast adjusted using the levels function in Adobe Photoshop CS2 (Adobe, San Jose, CA, USA). Nuclear orientation was evaluated using ImageJ v1.36 with the Otsu function of the multithresholder plugin and the particle

analyzer plugin. Briefly, an ellipse was fit to each nucleus, and the angle of the long axis of the ellipse and a reference angle were measured.

4.2.5 Statistical analysis

Circular analysis was used to analyze the angular distributions of the major axes of the nuclei (Li et al 2008).[29] Circular mean vectors were calculated, where the length of the mean vector corresponds to the degree of clustering of the data, and the direction of the mean vector corresponds to the mean direction of the data. Uniformity of the distribution of nuclei was assessed using a Rao's spacing test and alignment of nuclei in the direction of the substrate pattern was assessed with a *V*–test. Oriana v3.00 (Kovach Computing Services, Pentreth, UK) software was used for circular statistical analysis. For all cases, a *P* value of less than 0.05 was taken to be significant. One-way analysis of variance (ANOVA) tests were performed on mean vector lengths and cell counts. *Post hoc* multiple comparison analyses were performed using the Bonferroni test. Again, a *P* value of less than 0.05 was taken to be significant.

4.3 Results

Protein micropatterns can be absorbed to plasma-activated PDMS surfaces easily and reproducibly. We utilized the versatility of this technique in conjunction with PDMS biomaterial replicas of aligned SC topography to present single, cooperating, and competing cues to DRGs (Figure 1). Flat PDMS and PDMS presenting anisotropic SC topography were coated or microstamped with proteins. Permissive LN or mixes of inhibitory CSPG and permissive LN were microcontact printed parallel and orthogonal to aligned SC topography (Figure 2) to generate double cue platforms. Stripes appeared continuous and uninterrupted by the topography, and the topographical features were unaffected by the microcontact printing. Flat PDMS was microcontact printed and anisotropic SC materials were

fully coated to serve as single cue platforms. Fully coated, flat PDMS served as a non-directive control.

When DRGs were cultured on anisotropic biomimetic SC materials coated with 50 μg/ml of LN (LN50), neurons, support cells, and neurites demonstrated alignment in the direction of topographical cue (Figure 3 G, H, I). Similarly, DRGs cultured on PDMS micropatterned with this concentration of LN in stripes with 50 μm width and pitch (50-50) were aligned in the direction of the micropatterns (Figure 3 D, E, F). DRGs cultured on substrates presenting these cues in parallel appeared aligned in the direction of both cues (Figure 3 J, K, L). When these cues were presented orthogonally, DRGs appeared to preferentially align along protein stripes (Figure 3 M, N, O).

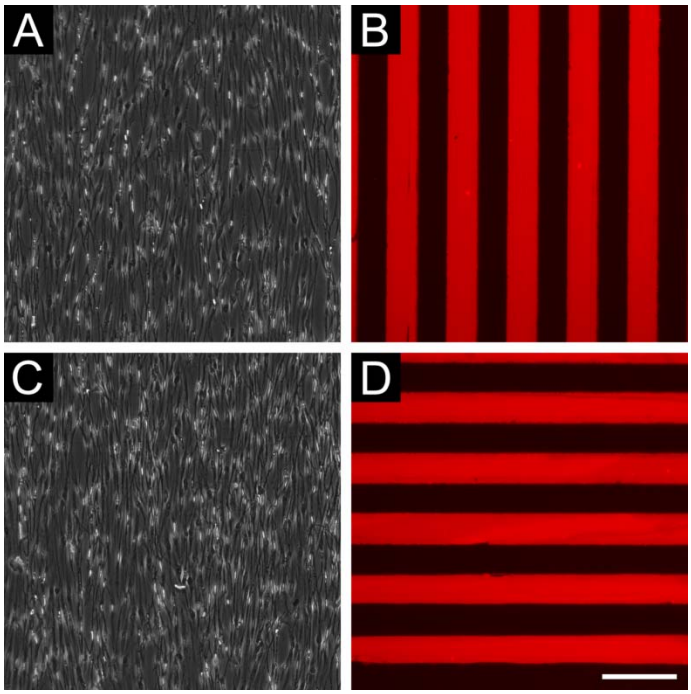

Figure 4.2. Microcontact printed proteins on materials presenting anisotropic SC topography presented cooperative and competitive directive cues.

Phase (A, C) and fluorescence (B, D) micrographs of corresponding fields of view of parallel cue (A, B) and orthogonal cue (C, D) samples showing independence of orientation of topographical (A, C) and biochemical cues (B, D). A and C display confluent biomimetic vertically aligned SC-shaped surface morphology under phase illumination. B and D show corresponding fields of view with vertical (B) and horizontal (D) immunofluorescently labeled laminin stripes under fluorescence illumination. Scale bar, 100 um. *Figure from Bruder, J. M. Neuron guidance by biomimetic topographical cues. Ph.D. dissertation, Brown University, 2008.*[27]

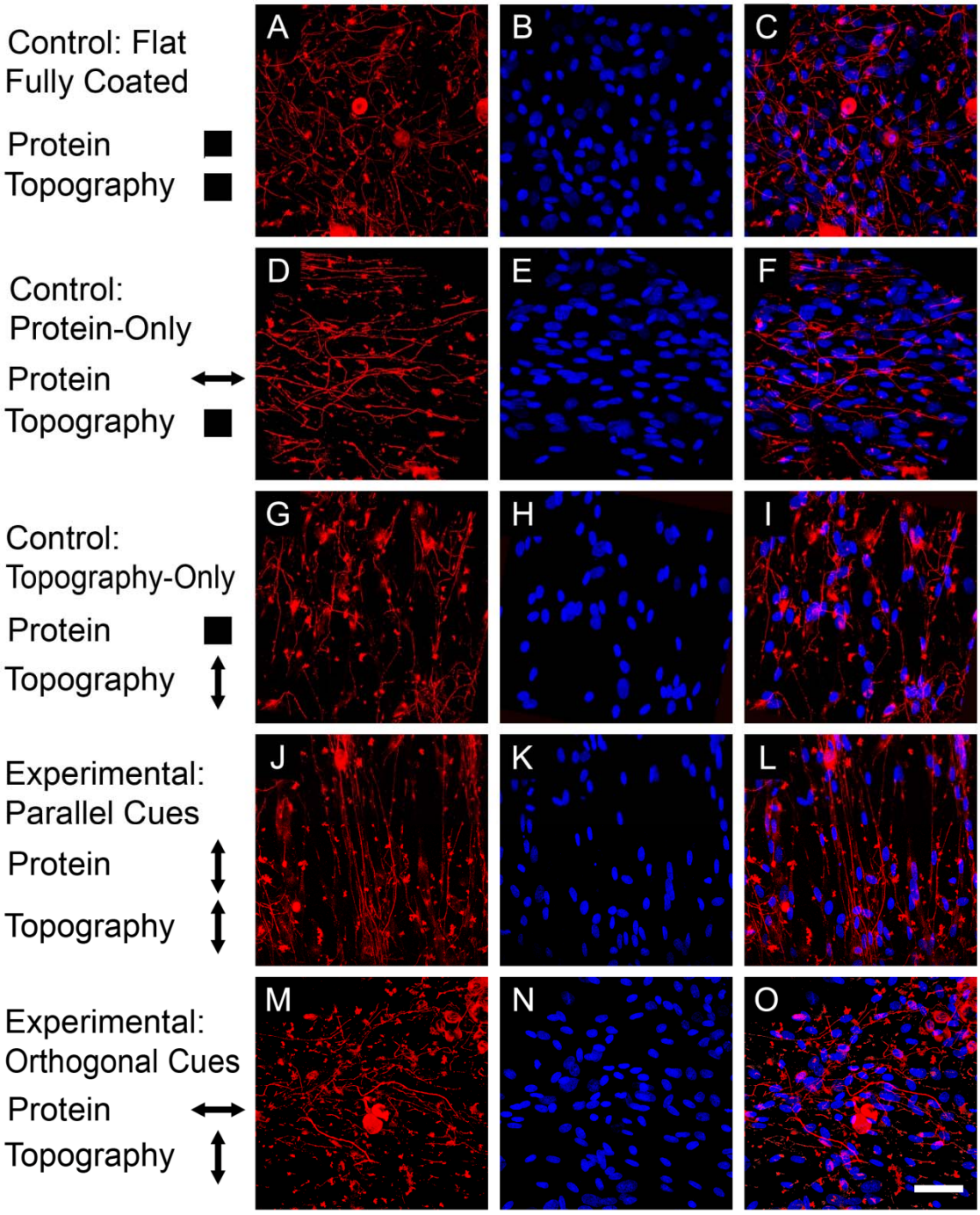

Figure 4.3. Neurons, support cells, and neurites are influenced by presentation of anisotropic biomimetic topography with directive patterns of LN.

Staining and immunolabeled are grouped by column, and substrate type is grouped by row. A, D, G, J, and M are labeled for neurofilament. B, E, H, K, and M are corresponding fields of view stained with DAPI to visualize nuclei location and orientation. C, F, I, L, and O are corresponding overlays of the two images in the same row. The nature and direction of laminin patterning and topography for each row is indicated to the left of each row. Scale bar, 50 um. *Figure from Bruder, J. M. Neuron guidance by biomimetic topographical cues. Ph.D. dissertation, Brown University, 2008.*[27]

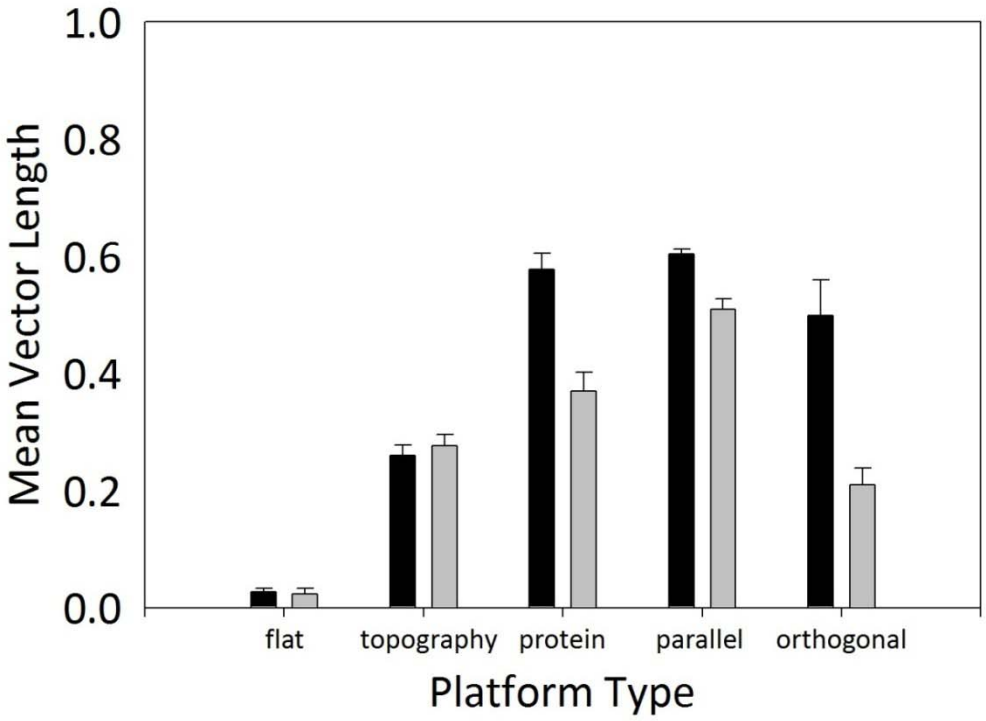

Figure 4.4. Alignment on platforms with directive protein cues was stronger than on platforms presenting uniform protein presentation.

Graph of mean vector length of nuclear angle distributions of DRGs cultured on PDMS substrates presenting individual and multiple directive cues. 50μg/ml LN (black bars) or a mix of 10μg/ml CS and 50μg/ml LN (grey bars) was used for the protein. Mean ± SEM are presented.

p-values		Flat		topography		protein		parallel		Orthogonal	
		LN	CSPG-LN	LN	CSPG-LN	LN	CSPG-LN	LN	CSPG-LN	LN	CSPG-LN
flat	LN	X	1.000	0.001	<0.001	<0.001	<0.001	<0.001	<0.001	<0.001	0.004
	CSPG-LN		X	1.000	<0.001	0.001	<0.001	<0.001	<0.001	<0.001	0.003
topography	LN			X	1.000	<0.001	0.563	<0.001	<0.001	0.001	1.000
	CSPG-LN				X	<0.001	1.000	<0.001	<0.001	0.002	1.000
protein	LN					X	0.006	1.000	1.000	1.000	<0.001
	CSPG-LN						X	<0.001	0.023	0.183	0.003
parallel	LN							X	1.000	1.000	<0.001
	CSPG-LN								X	1.000	<0.001
orthogonal	LN									X	<0.001
	CSPG-LN										X

Orientation of cells and neurites was random on flat materials (Figure 3 A, B, C). Comparison of DRG responses to these platforms by quantitative circular analysis of the distributions of nuclear angles supported these qualitative observations (Figure 4, Table 1). Uniformity of the distribution of nuclei was assessed using a Rao's spacing test and alignment of nuclei in the direction of each cue was assessed with a *V*–test. The distribution of nuclear angles on all platforms containing directive cues was significantly different from a uniform distribution by Rao's spacing test ($p \leq 0.05$), and the mean angle of the distribution was not significantly different from the direction of the underlying topography or protein cue (V-test for 0° or 180°, $p \leq 0.05$). Circular mean vectors were calculated,

where the length of the mean vector corresponds to the degree of clustering of the data, and the direction of the mean vector corresponds to the mean direction of the data. Comparison of the mean vector lengths on these platforms showed that clustering of nuclear angles around the direction of the protein cue was not significantly different when this cue was presented alone (0.578 ± 0.027), parallel to biomimetic topography (0.604 ± 0.008), or orthogonal to biomimetic topography (0.498 ± 0.061). Clustering of nuclear alignment was significantly lower when biomimetic topography was presented alone (0.260 ± 0.018). The clustering of nuclear angles on flat and isotropic materials was not significantly different from a uniform distribution of angles by Rao's spacing test.

When DRGs were cultured on anisotropic biomimetic SC materials coated with 50 μg/ml of LN mixed with 10 μg/ml of CSPG (CSPG10-LN50), DRGs demonstrated alignment in the direction of the topographical cue (Figure 5 D, E). Similarly, DRGs cultured on PDMS micropatterned with this protein mix in 50-50 stripes were aligned in the direction of the micropatterns (Figure 5 G, H). DRGs cultured on substrates presenting these cues in parallel appeared aligned in the direction of both cues (Figure 5 J, K). When these cues were presented orthogonally, DRGs appeared to preferentially align along protein stripes (Figure 5 M, N). Orientation of cells and neurites was random on flat materials (Figure 5 A, B). Again, comparison of DRG responses to these platforms by quantitative circular analysis of the distributions of nuclear angles supported these qualitative observations (Figure 5, Table 1). The mean angle of the distribution was not significantly different from the direction of the underlying topography or protein cue on all platforms containing directive cues (V-test for 0° or 180°, $p \leq 0.05$), and the distributions of nuclear angles on all platforms containing only topographic cues, only protein cues, and parallel cues were significantly different from a uniform distribution by Rao's spacing test ($p \leq 0.05$). On platforms presenting orthogonal cues, however, the distribution of angles was not significantly different from a uniform distribution on 2 of 6 experimental replicates. Comparison of the mean vector lengths of alignment distributions on these platforms showed that clustering of nuclear alignment was similar on both single cue platforms (0.276 ± 0.020 on topography only and 0.370 ± 0.032 on protein only). Clustering of nuclear

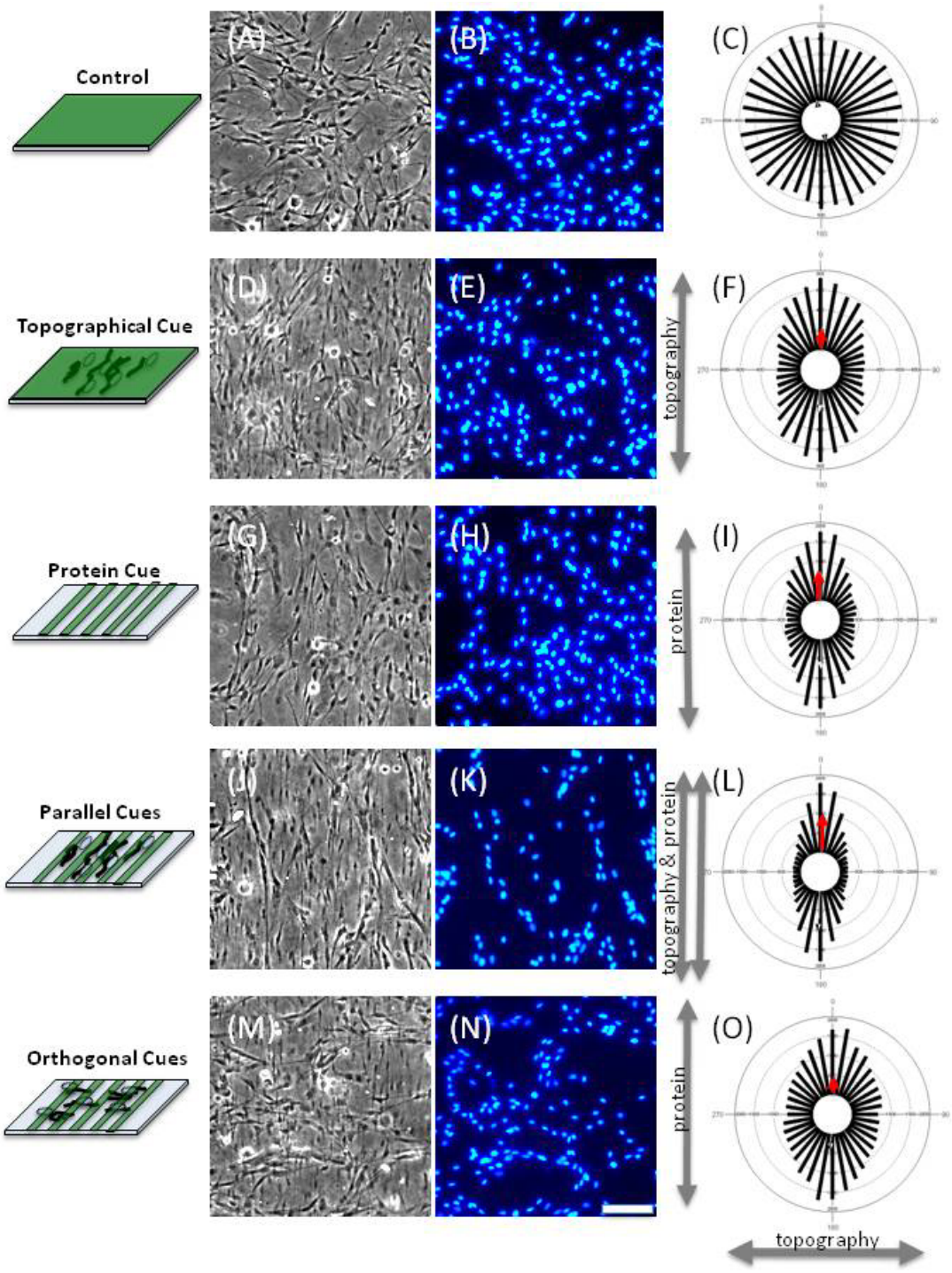

Figure 4.5. Neurons, support cells, and neurites are influenced by presentation of anisotropic biomimetic topography with directive patterns of CSPG and LN.

Corresponding phase (A, D, G, J, M) and epifluorescent images (B, E, H, K, N) of DRGs cultured on PDMS materials presenting flat (A, B, G, H) or aligned SC topography (D, E, J, K, M, N) with parallel (G, H, J, K) or orthogonal (M, N) patterns of CSPG/LN. In all conditions, a mix of 10µg/ml CS and 50µg/ml LN (CS10/LN50) was used for the protein. Nuclei were stained with DAPI (B, E, H, K, N). Circular histograms of nuclear angle distributions on these substrates are also presented (C, F, I, L, O). Scale bar, 100 µm.

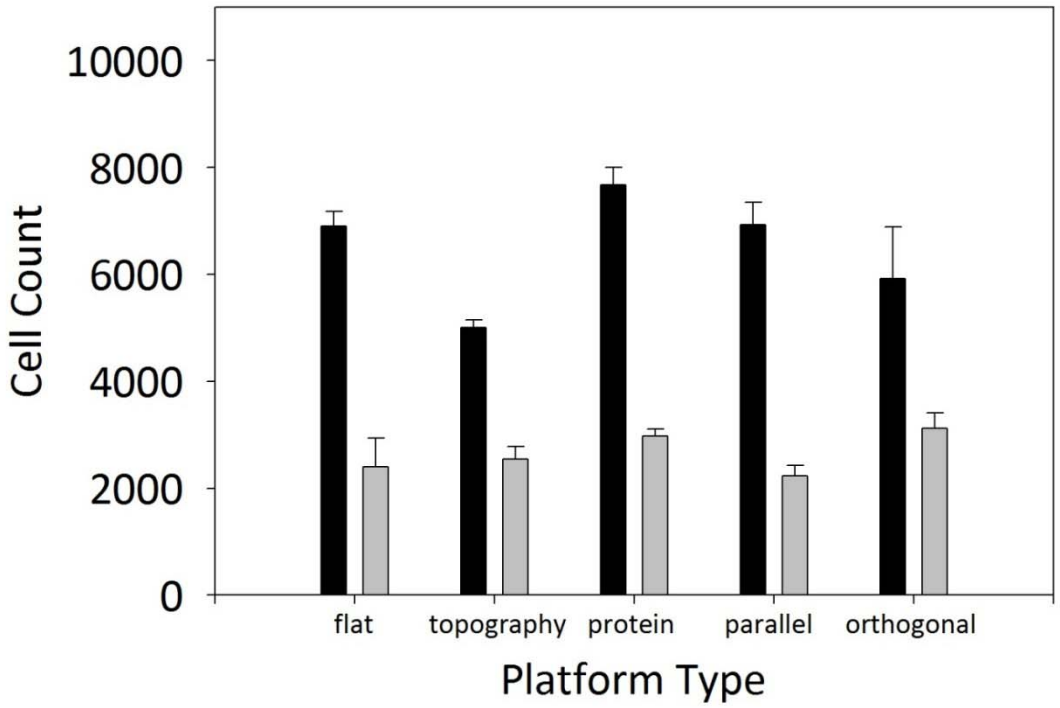

Figure 4.6. Presentation of CSPG with LN reduced the number of cells present at the end of the experiments. Graph of cell counts of DRGs cultured on PDMS substrates presenting individual and multiple directive cues. 50μg/ml LN (black bars) or a mix of 10μg/ml CS and 50μg/ml LN (grey bars) was used for the protein. Mean ± SEM are presented.

p-value		flat		topography		protein		Parallel		Orthogonal	
		LN	CSPG-LN	LN	CSPG-LN	LN	CSPG-LN	LN	CSPG-LN	LN	CSPG-LN
flat	LN	X	<0.001	0.127	<0.001	1.000	<0.001	1.000	<0.001	1.000	<0.001
	CSPG-LN		X	0.006	1.000	<0.001	1.000	<0.001	1.000	0.001	1.000
topography	LN			X	0.011	0.014	0.026	0.116	0.001	1.000	0.039
	CSPG-LN				X	<0.001	1.000	<0.001	<0.001	<0.001	1.000
protein	LN					X	<0.001	1.000	<0.001	0.518	<0.001
	CSPG-LN						X	<0.001	1.000	<0.001	1.000
parallel	LN							X	<0.001	1.000	<0.001
	CSPG-LN								X	<0.001	1.000
orthogonal	LN									X	<0.001
	CSPG-LN										X

alignment was also similar along protein stripes presented orthogonally to biomimetic topography (0.209 ± 0.029). Alignment was enhanced when CSPG10-LN50 50-50 tracks were presented parallel to topographical anisotropy (0.510 ± 0.018). The clustering of nuclear angles on flat materials was not significantly different from a uniform distribution of angles by Rao's spacing test.

The addition of CSPG10 to LN50 coating of biomimetic substrates did not affect the clustering of nuclear alignment on these substrates (Figure 4). The addition of CSPG10 to LN50 50-50 tracks reduced the clustering of alignment along these tracks (0.578 ± 0.027 vs. 0.370 ± 0.032), and similarly, alignment was reduced along protein CSPG10-LN50 stripes presented orthogonally to

biomimetic topography. While alignment was enhanced when CSPG10-LN50 tracks were presented parallel to topography versus when CSPG10-LN50 tracks were presented alone, alignment was similar to that on parallel cues with LN50 as the protein (0.510 ± 0.018 vs. 0.604 ± 0.008). The addition of CSPG10 also significantly reduced the terminal cell density of DRGs on all of these substrates versus those that only presented LN (Figure 6).

When DRGs were cultured on PDMS micropatterned with 5 μg/ml of LN (LN5) in stripes with 500 μm width and 50 μm pitch (500-50), DRGs were aligned in the direction of the micropatterns (Figure 7 A, C, E, G). When this cue was presented orthogonally to oriented SC topography, DRG growth appeared randomly oriented (Figure 7 B, D, F, H). Comparison of DRG responses to these platforms by quantitative circular analysis of the distributions of nuclear angles supported these qualitative observations (Figure 7 I, J, Table 1). When protein was presented alone, the mean angle of the distribution was not significantly different from the direction of the protein cue (V-test for 0° or 180°, $p \leq 0.05$), but the distribution of nuclear angles was not significantly different from a uniform distribution on 2 of 3 experimental replicates (Figure 8). On platforms presenting orthogonal cues, the mean angle of the distribution was significantly different from the direction of the protein cue and from the direction of the topographical cue (V-test for 0°, 90°, 180°, or 270°), and the distribution of angles was not significantly different from a uniform distribution.

When DRGs were cultured on PDMS micropatterned with 10 μg/ml of LN (LN10) in stripes with 50 μm width and 10 μm pitch (50-10), DRGs were strongly aligned in the direction of the micropatterns (Figure 9 A, C, E, G). When this cue was presented orthogonally to oriented SC topography, DRG cells appeared more randomly oriented, and neurites were aligned to the protein cue (Figure 9 B, D, F, H). Comparison of DRG responses to these platforms by quantitative circular analysis of the distributions of nuclear angles supported these qualitative observations (Figure 9 I, J, Table 1). When protein was presented alone, the mean angle of the distribution was not significantly different

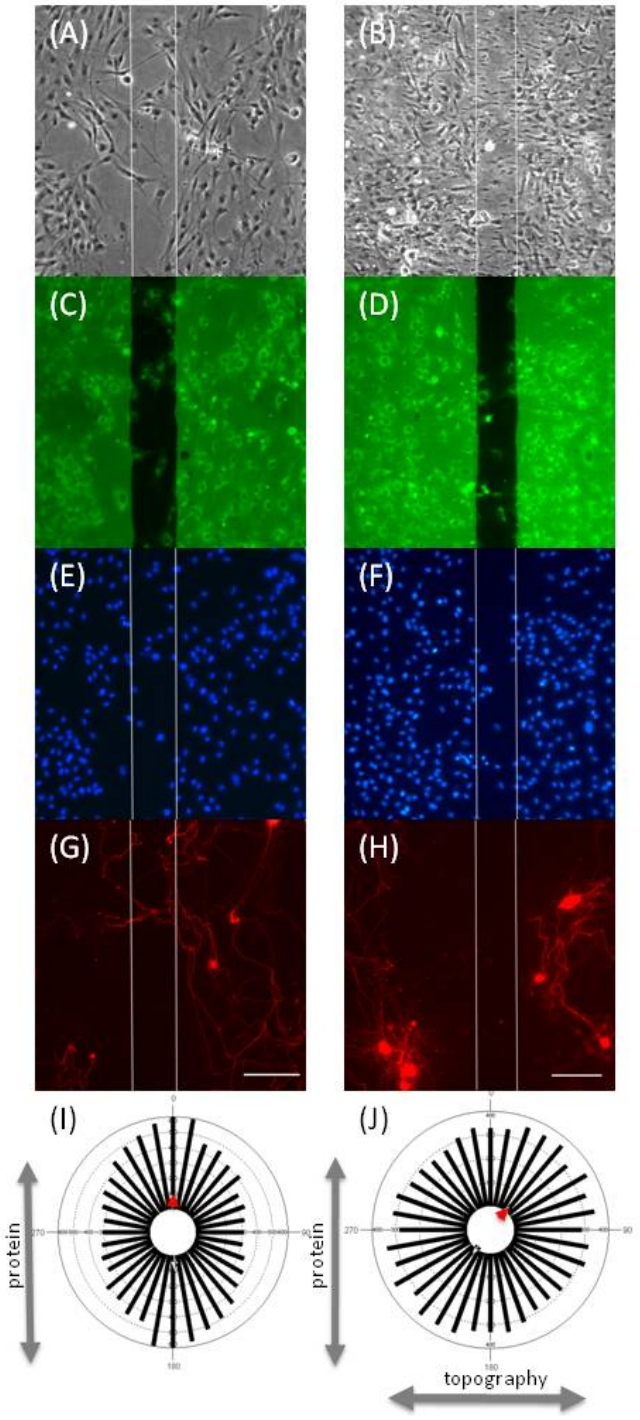

Figure 4.7. Presentation of anisotropic SC topography orthogonal to large stripes of low concentration LN increased the uniformity of nuclear angle distribution.

Phase contrast and epifluorescent images of platforms presenting 500 μm stripes of 5 μg/ml of LN with 50 μm spaces on flat PDMS (A, C, E, G) or orthogonal to aligned SC topography (B, D, F, H). Protein cues were stained with anti-LN (C,D), nuclei were stained with DAPI (E, F), and neurites were stained with anti-class III beta tubulin (G, H). Circular histograms of nuclear angle distributions on these substrates are also presented (I, J). Scale bar, 100 μm.

from the direction of the protein cue (V-test for 0° or 180°, p≤0.05), and the distribution of nuclear angles was significantly different from a uniform distribution by Rao's spacing test (p≤0.05). On platforms presenting orthogonal cues, the mean angle of the distribution was not significantly different from the direction of the protein cue (V-test for 0° or 180°, p≤0.05), but the distribution of angles was not significantly different from a uniform distribution.

When DRGs were cultured on PDMS micropatterned with LN10 in the shape of bioinspired anisotropic micropatterns (trace), DRGs were strongly aligned in the direction of the micropatterns (Figure 10 A, C, E, G). When this cue was presented orthogonally to oriented SC topography, DRGs

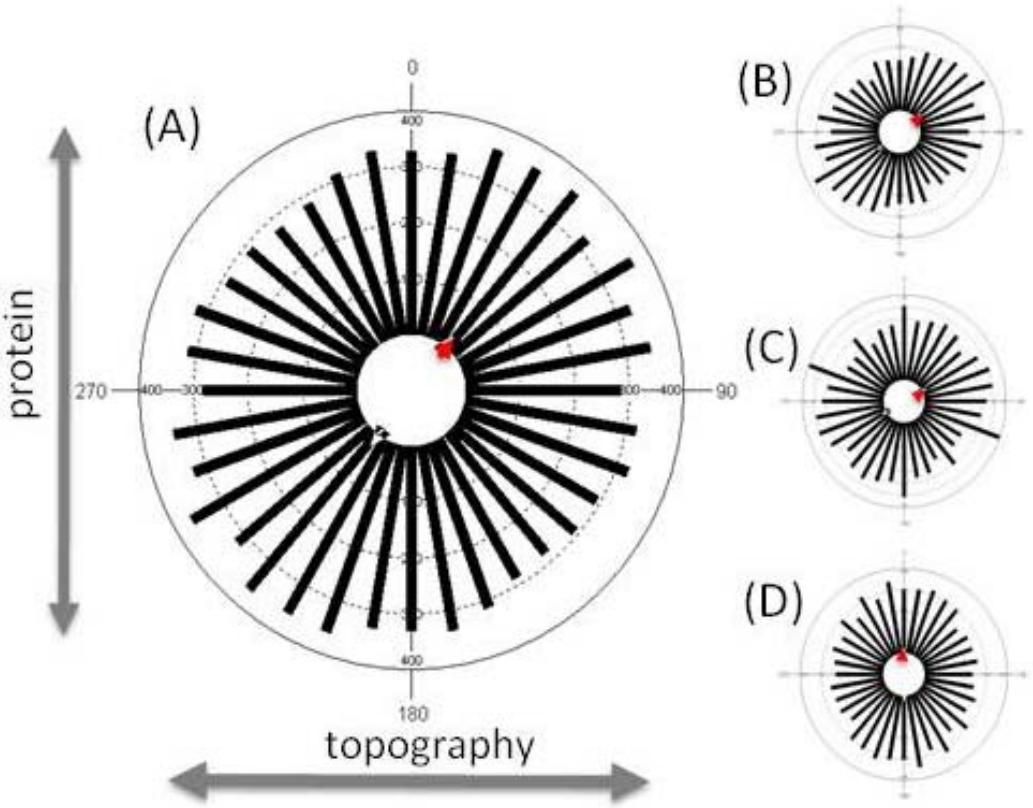

Figure 4.8. The response to presentation of anisotropic SC topography orthogonal to large stripes of low concentration LN varied among replicates.
Circular histograms of nuclear angle distributions of DRGs cultured on platforms presenting 500 μm stripes of 5 μg/ml of LN with 50 μm spaces orthogonal to aligned SC topography.

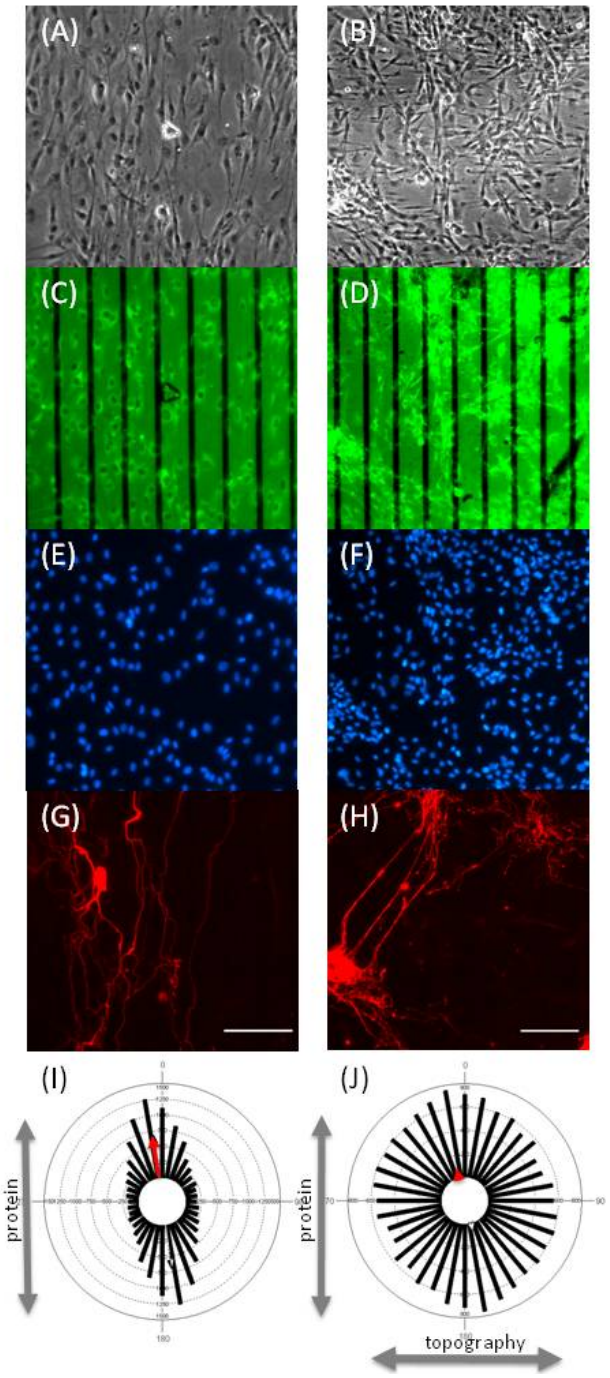

Figure 4.9. Presentation of anisotropic SC topography orthogonal to stripes of lower concentration LN with small spaces between stripes decreased alignment of DRGs.

Phase contrast and epifluorescent images of platforms presenting 50 μm stripes of 10 μg/ml of LN with 10 μm spaces on flat PDMS (A, C, E, G) or orthogonal to aligned SC topography (B, D, F, H). Protein cues were stained with anti-LN (C,D), nuclei were stained with DAPI (E, F), and neurites were stained with anti-class III beta tubulin (G, H). Circular histograms of nuclear angle distributions on these substrates are also presented (I, J). Scale bar, 100 μm.

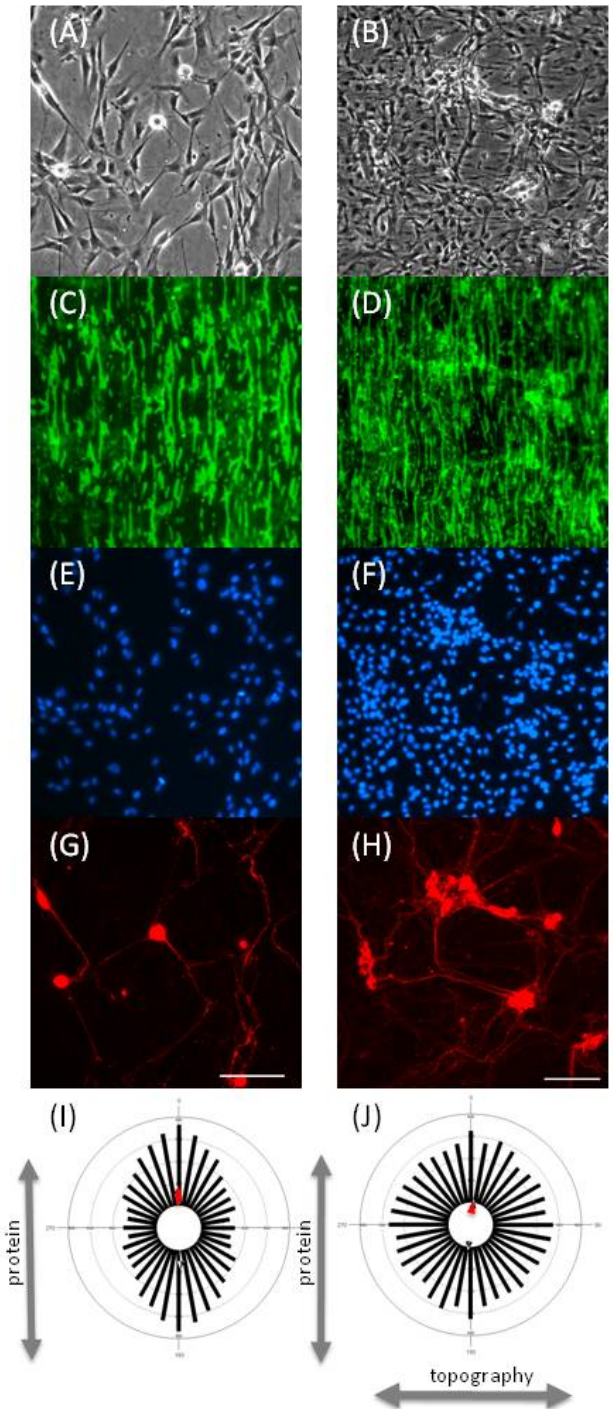

Figure 4.10. Presentation of anisotropic SC topography orthogonal to bioinspired micropatterns of lower concentration LN decreased alignment of DRGs.

Phase contrast and epifluorescent images of platforms presenting 50 μm stripes of 10 μg/ml of LN with 10 μm spaces on flat PDMS (A, C, E, G) or orthogonal to aligned SC topography (B, D, F, H). Protein cues were stained with anti-LN (C,D), nuclei were stained with DAPI (E, F), and neurites were stained with anti-class III beta tubulin (G, H). Circular histograms of nuclear angle distributions on these substrates are also presented (I, J). Scale bar, 100 μm.

appeared more randomly oriented (Figure 10 B, D, F, H). Comparison of DRG responses to these platforms by quantitative circular analysis of the distributions of nuclear angles supported these qualitative observations (Figure 10 I, J, Table 1). When protein was presented alone, the mean angle of the distribution was not significantly different from the direction of the protein cue (V-test for 0° or 180°, $p \leq 0.05$), but the distribution of nuclear angles was not significantly different from a uniform distribution on 2 of 6 replicates. On platforms presenting orthogonal cues, the mean angle of the distribution was significantly different from the direction of the protein cue or the direction of the topographical cue on 3 of 5 replicates (V-test for 0°, 90°, 180°, or 270°), and the distribution of angles was significantly different from a uniform distribution.

When DRGs were cultured on PDMS micropatterned with CSPG10 in 50-50 stripes, DRGs were aligned in the direction of the micropatterns (Table 1). When protein was presented alone, the mean angle of the distribution was not significantly different from the direction of the protein cue (V-test for 0° or 180°, $p \leq 0.05$), and the distribution of nuclear angles was significantly different from a uniform distribution by Rao's spacing test ($p \leq 0.05$). On platforms presenting orthogonal cues, the mean angle of the distribution was not significantly different from the direction of the protein cue (V-test for 0° or 180°, $p \leq 0.05$), and the distribution of angles was not significantly different from a uniform distribution on 1 of 2 replicates.

Comparison of the mean vector lengths of nuclear alignment distributions on these platforms (Figure 11) showed that clustering of nuclear alignment was not significantly different when protein patterns were presented with LN50 50-50 stripes on flat PDMS (0.578 ± 0.027) or orthogonal to topography (0.498 ± 0.061), CSPG10 50-50 stripes on flat PDMS (0.554 ± 0.061) or orthogonal to topography (0.442 ± 0.028), or LN10 50-10 stripes on flat PDMS. Clustering of nuclear alignment on platforms presenting protein patterns of CS10-LN50 50-50 on flat PDMS (0.370 ± 0.032) or LN10 trace on flat PDMS (0.461 ± 0.013) were also not significantly different from CS10 50-50 orthogonal to topography, LN 50 50-50 orthogonal to topography, or LN10 50-10 on flat PDMS. Alignment on

these platforms was also not different from each other. LN10 trace on flat PDMS was also not significantly different from CS10-LN50 50-50 orthogonal to topography (0.209 ± 0.029), LN5 500-50 on flat PDMS or orthogonal to topography (0.150 ± 0.022 and 0.077 ± 0.015), LN10 trace orthogonal to topography (0.078 ± 0.021), and LN10 50-10 orthogonal to topography (0.084 ± 0.013). Alignment on these platforms was also not significantly different from each other.

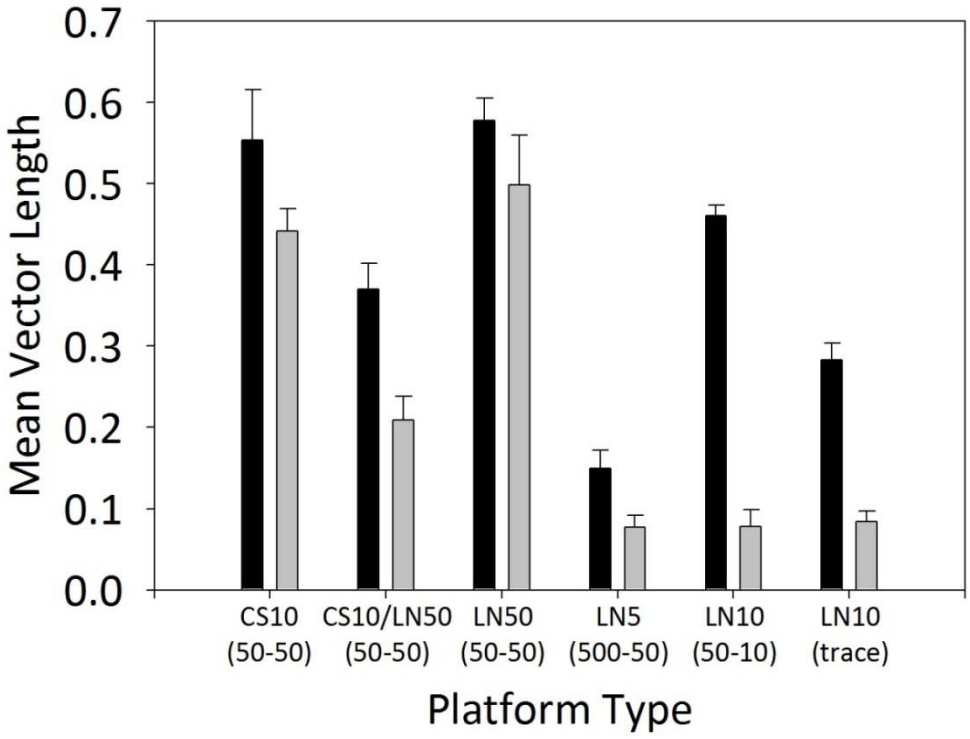

Figure 4.11. Alignment of DRGs to directive protein patterns decreased when orthogonal topographical cue is introduced.

Graph of mean vector length of nuclear angle distributions of DRGs cultured on PDMS substrates presenting only directive protein cues (black bars, P) or orthogonal protein and topographical cues (grey bars, O). Mean ± SEM are presented.

p-value		CS10 (50-50)		CS10/LN50 (50-50)		LN50 (50-50)		LN5 (500-50)		LN10 (50-10)		LN10 (trace)	
		P	O	P	O	P	O	P	O	P	O	P	O
CS10	P	X	1.000	0.027	<0.001	1.000	1.000	<0.001	<0.001	1.000	<0.001	0.004	<0.001
(50-50)	O		X	1.000	0.007	1.000	1.000	0.002	<0.001	1.000	<0.001	1.000	<0.001
CS10/LN50	P			X	0.016	0.031	0.600	0.003	<0.001	1.000	<0.001	1.000	<0.001
(50-50)	O				X	<0.001	0.016	0.397	<0.001	<0.001	0.208	1.000	0.572
LN50	P					X	1.000	<0.001	<0.001	1.000	<0.001	0.004	<0.001
(50-50)	O						X	<0.001	<0.001	1.000	<0.001	0.054	<0.001
LN5	P							X	1.000	<0.001	1.000	1.000	1.000
(500-50)	O								X	<0.001	1.000	0.084	1.000
LN10	P									X	<0.001	0.291	<0.001
(50-10)	O										X	0.053	1.000
LN10	P											X	0.113
(trace)	O												X

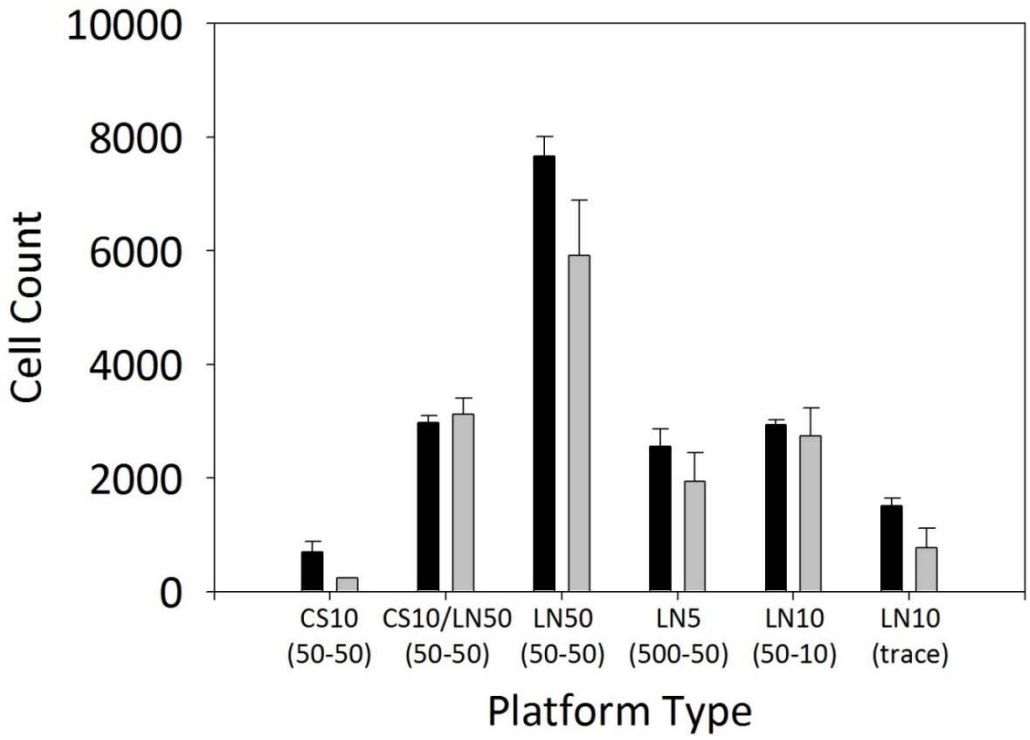

Figure 4.12. Lower concentrations of LN and higher concentrations of CSPG reduced the number of cells present at the end of the experiments.

Graph of cell counts of DRGs cultured on PDMS substrates presenting only directive protein cues (black bars, P) or orthogonal protein and topographical cues (grey bars, O). Mean ± SEM are presented.

p-value		CS10 (50-50)		CS10/LN50 (50-50)		LN50 (50-50)		LN5 (500-50)		LN10 (50-10)		LN10 (trace)	
		P	O	P	O	P	O	P	O	P	O	P	O
CS10	P	X	1.000	0.006	0.019	<0.001	<0.001	0.347	1.000	0.072	0.091	1.000	1.000
(50-50)	O		X	0.011	0.005	<0.001	<0.001	0.147	1.000	0.035	0.044	1.000	1.000
CS10/LN50	P			X	1.000	<0.001	0.001	1.000	1.000	1.000	1.000	1.000	0.027
(50-50)	O				X	<0.001	0.001	1.000	1.000	1.000	1.000	0.912	0.009
LN50	P					X	1.000	<0.001	<0.001	<0.001	<0.001	<0.001	<0.001
(50-50)	O						X	0.001	<0.001	0.003	<0.001	<0.001	<0.001
LN5	P							X	1.000	1.000	1.000	1.000	0.465
(500-50)	O								X	1.000	1.000	1.000	1.000
LN10	P									X	1.000	1.000	0.098
(50-10)	O										X	1.000	0.126
LN10	P											X	1.000
(trace)	O												X

Terminal cell density on LN50 was significantly higher than on lower concentrations of LN, mixes of CSPG-LN, or CSPG alone (7670 ± 340 protein only and 5920 ± 970 orthogonal to topography). Terminal cell density was similar on CS10-LN50 (2980 ± 120 protein only and 3120 ± 280 orthogonal to topography), LN5 (2560 ± 310 protein only and 1940 ± 510 orthogonal to topography), and LN10 (2940 ± 80 protein in 50-10 stripes, 2740 ± 490 orthogonal 50-10 stirpes and topography, and 1570 ± 140 protein in trace micropattern) except on LN 10 trace pattern orthogonal to

topography (770 ± 350). Terminal cell density was lowest on substrates with CSPG10 alone (690 ± 190 protein only and 240 ± 10 orthogonal to topography).

4.4 Discussion

This study aimed to investigate the collective influences of permissive or inhibitory molecular cues and biomimetic materials presenting Schwann cell (SC) topography on directed neuronal growth. Neuronal response to individual cues has been studied extensively via platforms that have an overall positive or negative influence on neuronal growth. Here we presented navigating neurons with multiple cues competing or combining in direction and/or permissiveness. To determine cooperative and competitive interactions of these cues, they were presented to neurons independently, simultaneously in parallel, or simultaneously but orthogonally opposed. When presented together orthogonally, neurons can respond to one cue over another or to both cues to produce a resultant response. Exposure to one cue may results in altered sensitivity to a subsequent cue. When presented in parallel, neurons can respond to predominantly one cue or both cues additively or synergistically. Cells that are unresponsive to one cue may have been recruited under the combined influence of both cues. LN and CSPG were chosen as representative molecules because LN is known to promote neuronal adhesion, migration, and neurite extension while CSPG is an inhibitor of neuronal growth. To counter the nonadhesive nature of CSPG in culture, LN was mixed with CSPGs prior to micro-stamping or coating the substrates. It has been shown that LN at the concentrations used in this study does not mask the directive effects of CSPGs,[30] and can therefore be used to promote adhesion on substrates where CSPGs are present in high concentration. Platforms presenting oriented SC topography were investigated in combination as these materials have been previously shown to induce directed neuronal growth,[4, 5] but the relative strength of these directive cues to other cues has not yet been investigated. DRG plating density and culture duration were chosen based on conditions in previous work shown to be most effective for alignment of DRGs on materials replicating Schwann cell alignment.[4] Thus, DRGs were plated at 200,000 cells/well for 5 d. To study the response of DRGs to these anisotropic substrates, we assessed cellular and neurite

alignment. The shape of the nucleus has been shown to change in response to cellular elongation.[31] The angle of the major axis of the nucleus was used as an indicator of cellular orientation, circular statistical analysis was used to assess the distributions of these angles, and mean vector length of nuclear angles was used to measure alignment.[29]

Our first sets of experiments supported the conclusion that neurons exhibit directional preference for biochemical cues. DRG growth was directed by both cell-shaped topography and protein micropatterns when presented as single directive cues with strongest alignment to LN micropatterns. Alignment to LN50 micropatterning was so strong that the addition of a parallel topographical cue did not enhance alignment and competing topographical anisotropy did not disrupt alignment. While alignment to cell-shaped topography was similar whether coated with LN50 or CSPG10-LN50, alignment to LN50 micropatterns was more focused than alignment to CSPG10-LN50 micropatterns. Alignment on CSPG10-LN50 micropatterns was similar to alignment on cellular topography coated with CSPG10-LN50. CSPG10-LN50 micropatterns appeared to have an enhanced effect with topography to align neurons when presented in parallel. CSPG10-LN50 in parallel with topography increased alignment over both of these cues presented singly. LN in parallel with topography did not substantially increase alignment over either individual cue, but these results may indicate that a threshold for alignment under these conditions has been reached. This hierarchy of these protein cues over SC topography was further demonstrated as growth was oriented in the direction of protein pattern when cues were presented orthogonally. Stronger guidance by LN than CSPG10-LN50 was also reiterated. Directed growth to LN tracks was not deterred by orthogonal presentation of topography compared to presentation of LN tracks alone. Comparison of mean vector lengths also shows no difference between CSPG10-LN50 tracks presented alone and presented orthogonal to topography. Comparison of uniformity tests, however, points toward less directed alignment on platforms presenting these cues orthogonally as 2/3 of experimental replicates displayed nuclear angle distributions that were not different from a uniform distribution.

We also hypothesized that there exists a set of conditions where the cellular topography has dominant influence on alignment over biochemical patterning, and neurons preferentially align to the underlying cellular topography. Perhaps the cues were mismatched with regard to their relative magnitudes especially when comparing LN coated topography with LN stripes. CSPG-LN cues were more balanced, but biochemical cues still prevailed. Toward this end, we aimed to investigate the effects of protein concentration, pattern dimensions, and pattern type on the preference of neurons to align on directive biomimetic replicas. Lower concentrations were chosen and CSPG only conditions were chosen because a different set of orientation behaviors might be expected if adhesiveness of LN tracks was reduced. With strong concentrations of LN, cells may interact more with LN than other cells. Larger micropatterned stripes and smaller micropattern pitch were also investigated. Previous work has shown that neurons were most highly oriented on 30 and 40 μm stripe widths with 40 μm spacing which is similar to the initial conditions of this study.[17] It was our hypothesis that presentation of stripes 10 times as large would reduce the influence of LN tracks as the frequency of stripe borders would be reduced. Smaller spaces were hypothesized to allow neurons to interact across more than one stripe. Matching the biomimetic nature of cues was also employed as a means of matching the influence of these cues.

When larger stripes of permissive LN5 (500 μm), smaller spaces between stripes of LN10 (10 μm), repeating geometries inspired by the features of aligned SCs, or stripes of CSPG10 without LN50 were micro-contact printed either perpendicular to aligned SC topography or on flat PDMS, the response of neurons to these more balanced directive cues was complex. Examining clustering of nuclear alignment supports the conclusion that presentation of a highly permissive or highly inhibitory cue without competing anisotropy or permissiveness is most effective for neuronal guidance as presentation of LN50 and CS10 in stripes of 50 μm stripes and pitch exhibited the highest mean vector length. These single cues are so strong that presentation of orthogonal topography did not significantly deter guidance. Strength of DRG alignment was also similarly clustered on a lower concentration of LN (10) with smaller pattern pitch (10 μm). This substrate was

theoretically less permissive and adhesive so the similarity in influence on neurite guidance points to more favorable micropattern dimensions. This hypothesis is also supported by previous work in our lab that found the optimal pattern dimensions for SC alignment to be 50 μm stripes with 10 μm spaces[32]; SC alignment is relevant since SCs account for a large percentage of cells in these heterotypic DRG cultures grown for 5 days. Bioinspired micropatterns and large stripes appear to be less favorable micropatterns for guiding neurite outgrowth. Alignment on bioinspired micropattern showed a trend toward directed growth (V-test $p \leq 0.05$), but the clustering of this growth was reduced, and growth on 1/3 of experimental replicates was similar to a uniform distribution. Alignment on 500 μm stripes also showed a trend toward directed growth, but the clustering of this growth was further reduced, and growth on 2/3 of experimental replicates was similar to a uniform distribution. The relative strength of these cues appeared to be more balanced when compared to anisotropic SC topography. Orthogonal presentation of SC micropatterns and SC topography resulted in 70% less clustering of alignment compared to SC micropatterning alone and in a uniform distribution of neurite outgrowth. Growth on 2/5 of these substrates trended toward micropattern direction. Orthogonal presentation of large LN stripes and SC topography did not significantly reduce clustering of neurite alignment compared to these stripes alone but resulted in a uniform distribution of neurite outgrowth and the mean direction of growth was not toward either cue. The complexity of the combination of permissive and inhibitory molecules in anisotropic presentation reduced the clustering of nuclear alignment when compared to the influence of each of these molecules alone. The addition of LN as a molecule with conflicting permissiveness to CSPG micropatterns reduced clustering of alignment by 33% while the addition of conflicting topographical anisotropy reduced clustering of alignment by 43%. The most dramatic decrease in alignment due to the addition of competing anisotropic topography occurred when topography was presented orthogonally to LN micropatterns with small spaces. Clustering of alignment was significantly reduced by 83%, and while alignment trended toward the direction of the protein cue, the distribution of angles was not significantly different from a uniform distribution.

While the addition of aligned topography orthogonal to directive micropatterns reduced or balanced the alignment of neurons as compared to micropatterns alone, a set of conditions where the cellular topography dominates over biochemical patterning and neurons preferentially align to the underlying cellular topography was not found in this study. Previous study of competing topographic and biochemical cues demonstrated conditions in which topographic cues exhibited hierarchical guidance over biochemical cues. Britland et al. found that neurites aligned preferentially to adhesive tracks positioned perpendicularly over shallow grooves, but aligned increasingly to grooves with increasing depth. At groove depths between 0.5 and 1.0 μm, cues were balanced. The balanced response of alignment in their study manifested as a cross pattern of neurites, neurites growing parallel to one cue or the other. The lack of conditions by which biomimetic SC topography can overcome biochemical cues presented supports the observation that growth Is more directed by geometric materials as compared to growth on cellular topographies.[5] Previous work also showed that neurite guidance was enhanced by the parallel presentation of adhesive tracks and topographic gratings.[26] Cooperative presentation of LN tracks and biomimetic topography did not enhance alignment in our study, again pointing to the relative strength of biomimetic versus geometric topographies. The addition of the relatively weaker biomimetic cue did not influence directed outgrowth more than the stronger LN cue. When a relatively weaker biochemical cue was used (CSPG10-LN50), alignment was enhanced by parallel presentation.

The main objective of this study was to investigate the effects of topographical and molecular cues on directed growth, but our study also gives insight into the relative permissiveness of our substrates for adhesion and growth of DRGs. Terminal cell density was highest on substrates patterned with LN50 as this was the strongest concentration of the permissive molecule LN presented. As expected, due to its anti-adhesive and inhibitory nature, the addition of CSPG10 to LN50 50-50 stripes reduced substrate permissiveness, and further, cell density was lowest on substrates where CSPG10 was presented alone. This trend contrasts with the capacity of these cues for guidance. Directed neuron growth was influenced more significantly by LN50 or CSPG10 50-50 tracks compared to CSPG10-

LN50 50-50 tracks. Similarly, a reduction in concentration of LN to LN5 or LN10 reduced adhesiveness and permissiveness compared to growth on LN50. Terminal cell density was similar between LN5 500-50 and LN10 50-10 on flat PDMS and orthogonal to topography, but alignment on LN10 50-10 on flat PDMS was significantly higher than alignment to LN5 500-50 on flat PDMS. Alignment was similar, however, for orthogonal presentation of these patterns. Taken together, these results point toward separation of the mechanisms of adhesion and extension versus guidance and alignment. Previous work has also shown evidence that neuronal responses such as adhesion and extension are mediated differently than directed neuronal growth. For example, neurons directed by the border between A7 and Neu7 astrocytes continue to be guided by this boundary even when neurite extension is prohibited by enzymatic treatment.[33]

This study suggests several trends for the influence of parameters such as protein concentration, protein type, micropattern stripe width, micropattern spacing, and relative orientation of cues on directing and promoting growth and adhesion of neuronal growth. For example, reducing the concentration of LN from 50 μg/ml to 10 μg/ml presented orthogonal to topography seems to shift neuronal preference for guidance to the biochemical cue to a more balanced response to both the biochemical and topographical cues. This balanced response may also be due to the reduction of space between the protein tracks (50 μm to 10 μm). One approach to separating the effects of these two factors on neuronal alignment response would be to change the levels of each variable separately over a range of concentrations and then protein spacing. This would require a large number of experiments, and the interactions of these parameters with each other would be ignored. The problem-solving power of combined design of experiments (DOE) and response surface methodology (RSM) has recently been demonstrated as an efficient and informative approach to probe cellular response to various and multiple factors. These experiments provide insights into effective parameters and ranges of inputs that could be employed in a future designed experiment to statistically model and optimize the interactions of these parameters and cues.

Axon navigation is often focused on decision making at the growth cone, but decision making in multi-cue environments may be more complex. Mechanisms of biochemical and topographic guidance may be common or separate mechanisms. Biochemical ligands bind to specific receptors including integrins and adhesion molecules eliciting responses in the cells.[34] Growth cone motility, which allows neurites to contact these cues in the local environment, is dependent on dynamic remodeling of the actin cytoskeleton.[35] Therefore, biochemical cues elicit appropriate motile responses at least in part by regulating dynamics and structure of the cytoskeleton. Physical signals are likely transduced by cytoskeletal tension in the neurite and in the soma. Guidance in microgrooves such as those employed in previous studies of biochemical and topographical cues[26] can be attributed to physical constraints on the cytoskeleton, but contact sensing and transduction into directional growth on topographical substrates such as ours where growth is not constrained is not as easily explained. The cytoskeleton likely plays a role as cells which lack cytoskeletal organization such as leukocytes are less susceptible to topographical guidance.[6] Thus, neuron sensing points to the cytoskeleton, but the exact mechanism or mechanisms are not understood.

4.5 Conclusion

The findings of this study suggest that the hierarchy of directive cues depends not only on the type of cue presented. The relative strength of each cue individually is important. As neuronal guidance to LN50 50-50 stripes presented with no other directive cue was stronger than guidance to anisotropic cellular topography coated with LN50, it followed that neuronal response to orthogonal presentation of these cues showed a strong preference for biochemical guidance by LN50. The relative strength of cues when presented individually, however, is not the only factor involved in guidance on multi-cue platforms. Despite the directive strength of LN10 50-10 stripes presented with no other directive cue, neuronal response was balanced when this biochemical cue was presented orthogonal to anisotropic cellular topography. Our study presents a well-defined platform for study of multiple cues. Continued development and investigation of neurons in multi-cue environments will gain a more complete understanding of neurite navigation.

4.6 References

1. Dubey, N., P. C. Letourneau and R. T. Tranquillo. Guided neurite elongation and schwann cell invasion into magnetically aligned collagen in simulated peripheral nerve regeneration. Exp Neurol. 158: 338-50, 1999.

2. Smeal, R. M., R. Rabbitt, R. Biran and P. A. Tresco. Substrate curvature influences the direction of nerve outgrowth. Ann Biomed Eng. 33: 376-82, 2005.

3. Rajnicek, A., S. Britland and C. McCaig. Contact guidance of cns neurites on grooved quartz: Influence of groove dimensions, neuronal age and cell type. J Cell Sci. 110 (Pt 23): 2905-13, 1997.

4. Bruder, J. M., A. P. Lee and D. Hoffman-Kim. Biomimetic materials replicating schwann cell topography enhance neuronal adhesion and neurite alignment in vitro. Journal of Biomaterials Science, Polymer Edition. 18: 967-982, 2007.

5. Kofron, C. M., Y.-T. Liu, J. C. Rollo, J. E. Pallay and D. Hoffman-Kim. Anisotropic biomimetic and bioinspired topographies guide neurite outgrowth. In preparation. 2009.

6. Clark, P., P. Connolly, A. S. Curtis, J. A. Dow and C. D. Wilkinson. Topographical control of cell behaviour: Ii. Multiple grooved substrata. Development. 108: 635-44, 1990.

7. Mahoney, M. J., R. R. Chen, J. Tan and W. M. Saltzman. The influence of microchannels on neurite growth and architecture. Biomaterials. 26: 771-8, 2005.

8. Snow, D. M., V. Lemmon, D. A. Carrino, A. I. Caplan and J. Silver. Sulfated proteoglycans in astroglial barriers inhibit neurite outgrowth in vitro. Exp Neurol. 109: 111-30, 1990.

9. Clark, P., S. Britland and P. Connolly. Growth cone guidance and neuron morphology on micropatterned laminin surfaces. J Cell Sci. 105 (Pt 1): 203-12, 1993.

10. Esch, T., V. Lemmon and G. Banker. Local presentation of substrate molecules directs axon specification by cultured hippocampal neurons. J Neurosci. 19: 6417-26, 1999.

11. Kofron, C. M., V. J. Fong and D. Hoffman-Kim. Neurite outgrowth at the interface of 2d and 3d growth environments. Journal of Neural Engineering. 6: 016002, 2009.

12. Luckenbill-Edds, L. Laminin and the mechanism of neuronal outgrowth. Brain Research Reviews. 23: 1-27, 1997.

13. Hoke, A. and J. Silver. Proteoglycans and other repulsive molecules in glial boundaries during development and regeneration of the nervous system. Prog Brain Res. 108: 149-63, 1996.

14. Hammarback, J. A., S. L. Palm, L. T. Furcht and P. C. Letourneau. Guidance of neurite outgrowth by pathways of substratum-adsorbed laminin. J Neurosci Res. 13: 213-20, 1985.

15. Yeung, C. K., L. Lauer, A. Offenhausser and W. Knoll. Modulation of the growth and guidance of rat brain stem neurons using patterned extracellular matrix proteins. Neurosci Lett. 301: 147-50, 2001.

16. Song, H. K., B. Toste, K. Ahmann, D. Hoffman-Kim and G. T. Palmore. Micropatterns of positive guidance cues anchored to polypyrrole doped with polyglutamic acid: A new platform for characterizing neurite extension in complex environments. Biomaterials. 27: 473-84, 2006.

17. Song, M. and K. E. Uhrich. Optimal micropattern dimensions enhance neurite outgrowth rates, lengths, and orientations. Ann Biomed Eng. 35: 1812-20, 2007.

18. David, S. and A. J. Aguayo. Axonal elongation into peripheral nervous system "Bridges" After central nervous system injury in adult rats. Science. 214: 931-3, 1981.

19. Alexander, J. K., B. Fuss and R. J. Colello. Electric field-induced astrocyte alignment directs neurite outgrowth. Neuron Glia Biol. 2: 93-103, 2006.

20. Thompson, D. M. and H. M. Buettner. Neurite outgrowth is directed by schwann cell alignment in the absence of other guidance cues. Ann Biomed Eng. 34: 161-8, 2006.

21. Goldner, J. S., J. M. Bruder, G. Li, D. Gazzola and D. Hoffman-Kim. Neurite bridging across micropatterned grooves. Biomaterials. 27: 460-72, 2006.

22. Miller, C., S. Jeftinija and S. Mallapragada. Synergistic effects of physical and chemical guidance cues on neurite alignment and outgrowth on biodegradable polymer substrates. Tissue Eng. 8: 367-78, 2002.

23. Gomez, N., Y. Lu, S. Chen and C. E. Schmidt. Immobilized nerve growth factor and microtopography have distinct effects on polarization versus axon elongation in hippocampal cells in culture. Biomaterials. 28: 271-284, 2007.

24. Zhang, N., C. Zhang and X. Wen. Fabrication of semipermeable hollow fiber membranes with highly aligned texture for nerve guidance. J Biomed Mater Res A. 75: 941-9, 2005.

25. Li, N. and A. Folch. Integration of topographical and biochemical cues by axons during growth on microfabricated 3-d substrates. Exp Cell Res. 311: 307-16, 2005.

26. Britland, S., C. Perridge, M. Denyer, H. Morgan, A. Curtis and C. Wilkinson. Morphogenetic guidance cues can interact synergistically and hierarchically in steering nerve cell growth. Experimental Biology Online. 1: 1-15, 1997.

27. Bruder, J. M. Neuron guidance by biomimetic topographical cues. Ph.D. dissertation, Brown University, 2008.

28. Bruder, J. M., N. C. Monu, M. W. Harrison and D. Hoffman-Kim. Fabrication of polymeric replicas of cell surfaces with nanoscale resolution. Biomaterials. 27: 460-472, 2006.

29. Li, G. N. Y. and D. Hoffman-Kim. Evaluation of neurite outgrowth anisotropy using a novel application of circular analysis. Journal of Neuroscience Methods. 2008.

30. Snow, D. M., J. D. Smith and J. A. Gurwell. Binding characteristics of chondroitin sulfate proteoglycans and laminin-1, and correlative neurite outgrowth behaviors in a standard tissue culture choice assay. Journal of Neurobiology. 51: 2002.

31. Dalby, M. J., M. O. Riehle, S. J. Yarwood, C. D. Wilkinson and A. S. Curtis. Nucleus alignment and cell signaling in fibroblasts: Response to a micro-grooved topography. Exp Cell Res. 284: 274-82, 2003.

32. Kofron, C. M. and D. Hoffman-Kim. Optimization by response surface methodology of confluent and aligned cellular monolayers for nerve guidance. Ann Biomed Eng. submitted: 2009.

33. Powell, E. M., J. W. Fawcett and H. M. Geller. Proteoglycans provide neurite guidance at an astrocyte boundary. Molecular and Cellular Neurosciences. 10: 27-42, 1997.

34. Reichardt, L. F. and K. J. Tomaselli. Extracellular matrix molecules and their receptors: Functions in neural development. Annual review of neuroscience. 14: 531-570, 1991.

35. Gallo, G. and P. C. Letourneau. Axon guidance: A balance of signals sets axons on the right track. Curr Biol. 9: R490-2, 1999.

Chapter 5 Neurite outgrowth at the interface of 2D and 3D growth environments

Growing neurons navigate complex environments, but *in vitro* systems for studying neuronal growth typically limit the cues to flat surfaces or a single type of cue, thereby limiting the resulting growth. Here we examined the growth of neurons presented with two-dimensional (2D) substrate-bound cues when these cues are presented in conjunction with a more complex three-dimensional (3D) architecture. Dorsal root ganglia (DRG) explants were cultured at the interface between a collagen I matrix and a glass coverslip. Laminin (LN) or chondroitin sulfate proteoglycans (CSPG) were uniformly coated on the surface of the glass coverslip or patterned in 50 μm tracks by microcontact printing. Quantitative analysis of neurite outgrowth with a novel grid system at multiple depths in the gel revealed several interesting trends. Most of the neurites extended at the surface of the gel when LN was presented whereas more neurites extended into the gel when CSPG was presented. Patterning of cues did not affect neurite density or depth of growth. However, neurite outgrowth near the surface of the gel aligned to LN patterns, and these extensions were significantly longer than neurites extended in other cultures. In interface cultures, DRG growth patterns varied with the type of cue where neurite density was higher in cultures presenting LN than in cultures presenting CSPG. These results represent an important step toward understanding how neurons integrate local structural and chemical cues to make net growth decisions.

5.1 Introduction

Complete and correct nerve regeneration is difficult to achieve after injury to the nervous system because of the complex post-injury environment that contains multiple, often conflicting cues. In order to overcome the post-injury environment and ultimately elucidate therapies for nerve injury, an understanding of neural response to guidance cues is required. Growing neurons navigate complex environments by integrating a variety of cues, including diffusible factors,[1-4] substrate-bound factors,[5-7] electrical and magnetic fields,[8-10] and topographical features.[11-13] *In vitro* systems for studying neuronal growth typically limit the cues presented to a single type of cue on a two dimensional (2D) substrate; this may in turn limit the resulting growth and its applicability to the more complicated *in vivo* situation.

One type of cue that has been well studied in simplified cell culture systems is substrate-bound chemical factors. Boundary lines or parallel stripes of molecular cues are commonly employed on 2D cell culture substrates in order to investigate their ability to direct growth.[14-16] Molecules that have been investigated in this manner include those that are purely adhesive such as poly-L-lysine,[17] poly-D-lysine,[18] polyornithine,[19] and silane derivatives[20]; those that are adhesive and growth promoting such as laminin (LN), fibronectin, and collagen I[21]; and those that are inhibitory such as chondroitin sulfate proteoglycan (CSPG).[22] It has been recognized, however, that guidance factors cannot properly be defined in standard dissociated cell culture conditions. The limitations of these methods lie in the poor approximation that the flatness of these 2D surfaces provides of the more complex three-dimensional (3D) architecture that neurons navigate *in vivo.* This architecture includes the astrocyte derived extracellular matrix (ECM) in the CNS[23] and the Schwann cell-derived basement membrane in the peripheral nervous system (PNS).[24] To determine their full potential for axon guidance *in vivo*, the molecular components of the neuronal environment must be evaluated in more complex 3D culture systems *in vitro*.

Scaffold materials are widely used to mimic the 3D extracellular environment. A variety of synthetic polymers such as polyethylene glycol and polyvinyl alcohol have been used as hydrogels for 3D cell culture, and many of the natural components of the ECM can be used *ex vivo*, including agarose, alginate, chitosan, collagen I, fibrin, gelatin, and hyaluronic acid.[25-28] Differences in the morphology of neurons grown in 2D versus 3D have been observed.[29, 30] For example, neurite extensions within a 3D collagen I matrix were longer than on a 2D collagen I substrate.[31] The growth cones of neurons grown in 3D agarose appear more globular than the lamellar morphology of neuronal growth cones in 2D.[32] The influence of dimensionality on neurite outgrowth has been established, but the effects of dimensionality on the ability of growth cones to interpret guidance cues have not been investigated. This is particularly important in the context of advances in nerve guidance channel (NGC) technology, where guidance channels have been designed to incorporate combinations of soluble factors, matrices, and cells, encompassing varying geometries and configurations.[33-35]

In this study, we aimed to characterize the capacity of 2D substrate bound molecular cues to influence neurite growth in conjunction with a more complex 3D environment**.** We developed a novel cell culture system which combined microcontact printing of permissive or inhibitory molecular guidance cues with hydrogel matrices in order to culture dorsal root ganglia (DRG) explants at the interface of 2D and 3D cues. This method allowed us to present these cues simultaneously for the first time and to determine how neurite outgrowth changed in response to multiple cues. DRG growth was evaluated with phase contrast, fluorescence, and confocal microscopy and quantified with a novel grid system for comparison across conditions**.** These outcomes provide an important step toward understanding how neurons integrate local structural and chemical cues to make net growth decisions.

5.2 Methods

All materials were purchased from Invitrogen (Carlsbad, CA) unless otherwise specified.

5.2.1 Preparation of 2D surfaces

Microcontact printing was used to create 2D patterns of proteins on glass coverslips. The micropattern consisted of parallel 50 μm stripes of 1 cm length separated by 50 μm spaces and was designed in AutoCAD LT 2004 (Autodesk, Inc., San Rafael, CA) and printed at 10,000 DPI onto a mylar mask (CAD/Art Services, Inc., Bandon, OR). Photolithography was used to transfer the pattern to silicon wafers (Silicon Sense Inc, Nashua, NH). Wafers were spin coated with a 50 μm layer of Nano SU-8 50 photoresist (MicroChem Co., Newton, MA), exposed to UV light through the mask with a Karl Suss mask aligner (MJBs UV300) at 5.3 mW/cm^2 for 1.1 min to crosslink the photoresist, baked, rinsed to remove the uncrosslinked photoresist, and baked again. Tridecafluoro-1,1,2,2-tetrahydrooctyl-1-tricholosilane (United Chemical Technologies, Inc., Bristol, PA) was coated onto finished wafers under vacuum to reduce adhesiveness. Polydimethylsiloxane (PDMS) microstamps were created by pouring Sylgard 184 PDMS (Dow Corning, Midland, MI) elastomer base mixed with curing agent at a 10:1 ratio onto the wafers at a thickness of 1-2 mm and curing at 95ºC for 1 hr. The stamps were then peeled from the silicon wafers and coated with 10% sodium dodecyl sulfate (SDS) (Sigma-Aldrich, St. Louis, MO) in distilled water to facilitate protein release. To generate protein tracks, these stamps were coated with 50 μg/ml mouse laminin (LN) or 10 μg/ml embryonic chick chondroitin sulfate proteoglycans (CSPG) (Chemicon, Temecula, CA) in Hank's Balanced Salt Solution without calcium or magnesium (HBSS-CMF) for one hour. Glass coverslips were plasma activated at 10.5 W for 60 sec with a plasma cleaner/sterilizer (PDC – 32 G, Med RF level, Harrick, Pleasantville, NY), and the protein tracks were transferred by inverting the stamps and leaving them in contact with the glass surface overnight. To generate a uniform surface coating of protein, flat pieces of PDMS were used as stamps in the same manner.

5.2.2 Cell culture

Dorsal root ganglia (DRG) were dissected from the spinal columns of postnatal (P1-P4) rat pups as previously described. DRG were either cultured as intact explants or dissociated. For culture of

dissociated cells, DRG were incubated in 0.05% trypsin-EDTA in HBSS-CMF at 37°C for 60 min and dissociated by trituration. Cells and explants were cultured in neuronal media, consisting of Dulbecco's Modified Eagle's Medium (DMEM), 10% fetal bovine serum, 4mM L-glutamine, 100 μg/ml penicillin, 100 μg/ml streptomycin, and 50 ng/ml nerve growth factor (NGF).

5.2.2.1 Culture on 2D substrates

For culture on 2D substrates, either DRG explants or dissociated DRG plated at 150,000 cells/ml were cultured on glass slides stamped with micropatterned LN, micropatterned CSPG, or no cue.

5.2.2.2 Culture at the interface of 2D and 3D cues

For interface cultures (summarized in figure 1), the 3D component of the system consisted of a collagen gel matrix prepared immediately prior to cell culture using a 4:1 mixture of purified bovine collagen I (PureCol, Inamed Co., Fremont, CA) and 5X DMEM with 1N NaOH as necessary for neutralization of the mixture. For each experiment, 2 ml of this neutralized solution was pipetted into either (1) each well of a 6-well plate; or (2) a tissue culture insert (Millipore, Billerica, MA) for subsequent confocal microscopy; and placed into a 37°C, humidified incubator for one hour to induce gelation. Three whole DRG explants were added to the surface of each gel using forceps, a coverslip was inverted on the explants, and neuronal media was added. Coverslips included LN and CSPG patterned; LN and CSPG coated; and no patterned or coated cue (plain glass).

5.2.3 Immunostaining

Samples were fixed with 2% paraformaldehyde (Electron Microscopy Sciences, Hatfield, PA), 4% sucrose in 0.1M phosphate buffer solutions (pH 7.4) (PBS). Prior to immunostaining, nonspecific staining was blocked by incubating with a block solution consisting of 10% goat serum, 2% bovine

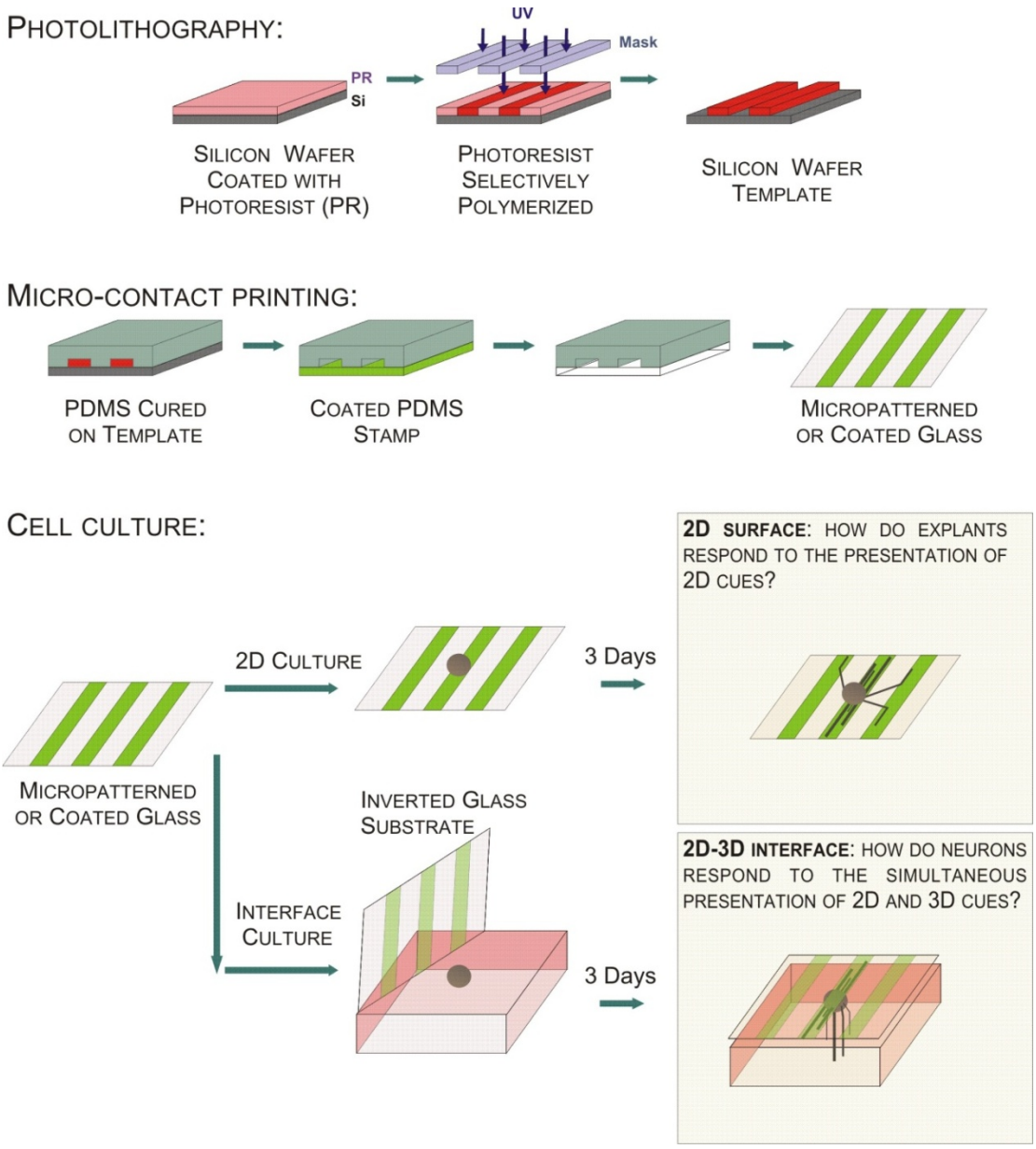

Figure 5.1. Production of cultures.
Schematic overview of the techniques used to fabricate 2D surface cultures and 2D-3D interface cultures highlighting photolithography, micro-contact printing and cell culture on a 2D glass surface or at the interface between a collagen I matrix and a glass substrate. Note, in interface cultures, the micropatterned or coated glass surface was inverted to expose the molecular cue to the explant. Not drawn to scale.

serum albumin (BSA) (Sigma-Aldrich), and 0.1% Triton X (VWR International, West Chester, PA) in PBS for 3h. Samples were incubated overnight at 4°C with primary antibody diluted 1:200 in working solution consisting of 10% goat serum and 2% BSA. Primary antibody was rabbit anti-LN (Biomedical Technologies, Stoughton, MA), mouse anti-CS56 (Sigma-Aldrich), or mouse anti-

neurofilament (RT-97; Developmental Studies Hybridoma Bank, Iowa City, IA). Samples were shaken for 30 min at room temperature before the antibody was removed, and washed with PBS three times for 10 min each. Samples were incubated for 1 h for 2D cultures or 12 h for interface cultures with fluorescent secondary antibodies (The Jackson Laboratory, Bar Harbor, ME) diluted 1:200 in working solution. Secondary antibodies were Cy2 goat anti-rabbit IgG for LN samples, Cy3 goat anti-mouse IgG for CSPG samples, and Cy2 goat anti-mouse IgG for neurofilament samples. Samples were rinsed with PBS three times. Controls included samples reacted without primary antibodies, to confirm no non-specific staining by the secondary antibodies.

5.2.4 Qualitative assessment of neurite outgrowth with confocal microscopy

A Leica TCS SP2 AOBS spectral confocal microscope was utilized to obtain 3D stacks of fixed explants. A krypton-argon laser was used to excite the samples at the proper wavelength, and emission was collected with a 10X objective lens. Due to the short working distance of the confocal microscope, inserts were removed from the tissue culture inserts and inverted so that the images were taken through the glass coverslip on which the chemical cue was presented. In order to image to the depth of the explant, the z-wide control function of the Leica software was employed. 3D renderings were constructed using Leica software.

5.2.5 Acquisition of phase contrast images of DRG explants

Fixed samples were examined and imaged on a Nikon Eclipse TE2000-S microscope under phase contrast optics at 100X with a Hamamatsu Orca-ER camera and Orbit shutter controller (Improvision, Lexington, MA), outputting to OpenLab v4.02 (Improvision). Images were captured to record the extent of neurite growth in x, y, and z directions, extending from the level of the glass coverslip into the collagen gel. Images were obtained at depths spaced 50 μm apart, and each image overlapped with the next image by 30%. Once the 100X images were obtained, they were merged

together to form larger images using the photomerge function in Photoshop CS2 (Adobe, San Jose, CA).

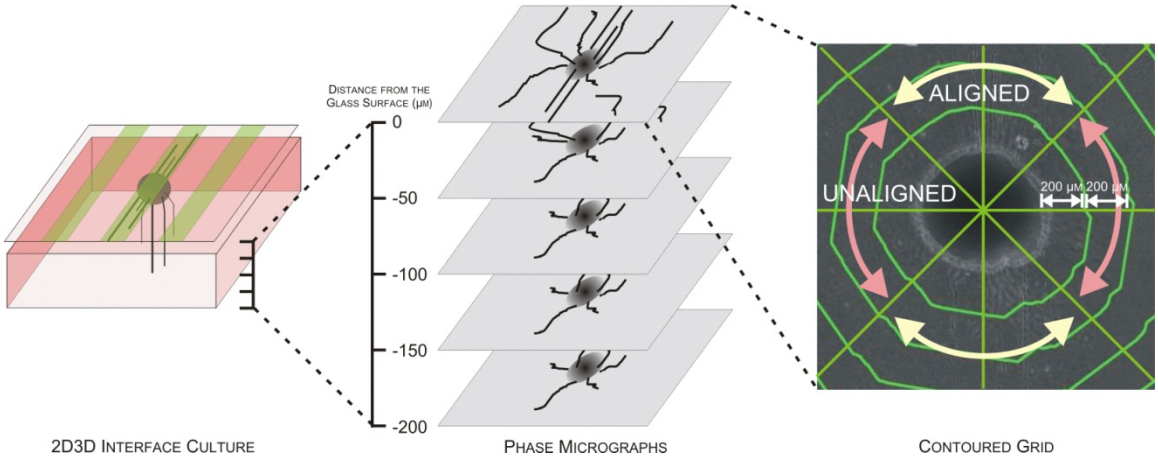

Figure 5.2. Quantitative assessment of neuronal growth.
The entire culture system is imaged in a z-stack at depth intervals of 50 μm. For images at each depth, a grid is overlaid and centered on the body of the explant beginning 200 μm from the explant boundary. Each grid contour line mimics the shape of the explant and is spaced 200 μm from the previous contour. The axis of the grid is aligned in the direction of the micropatterned tracks. Neurites in the four sections that border the axis aligned to the cue are considered aligned, and neurites in the other four sections are considered unaligned.

5.2.6 Quantitative assessment of neurite outgrowth with a novel grid analysis method

We developed a novel grid-based analysis method to quantify neurite outgrowth from fixed DRG explants (summarized in figure 2). Phase-contrast images of each explant and its neurite extensions at a single focal plane were merged in Adobe Photoshop CS2, and the outline of each explant was traced. To form the analysis grid, this outline was overlaid sequentially with outlines of identical shape whose size increased by 200 μm increments in all directions, thus forming a radially expanding grid that accounted for the size and shape of each explant. To facilitate analysis of neurite extension and alignment (see below), the grid was further organized into eight sections of equivalent size corresponding to 45 degree regions around the axis of the center of the explant.

For evaluation of neurite extension, the number of neurite segment extensions present within each grid area was counted. Thus for example, a neurite that was 650 μm long would have segments counted in the first four radial zones, i.e. 0-200 μm, 200-400 μm, 400-600 μm, and 600-800 μm. For evaluation of neurite alignment, the analysis grid was oriented so that the 0-180 degree axis was oriented parallel to the direction of the micropattern. Extensions were defined as aligned if they were within a region of the grid that bordered this axis, i.e. 0-45, 135-180, 180-225, or 315-360 degrees. For cultures that included 3D substrates, extension, alignment, and migration analyses were repeated at each plane of focus. DRG explants were considered to have healthy neurite outgrowth and were analyzed if they had at least 100 extensions within the analysis grid.

Paired t-test, one-way analysis of variance (ANOVA), two-way ANOVA, and multi-variable ANOVA (MANOVA) tests were performed. Post hoc multiple comparison analyses were performed using the Bonferroni test. $P<0.05$ was considered significant.

5.3 Results

5.3.1 Experimental model and analysis

DRG explants have the capacity to generate neurites that emerge from a single explant and extend in multiple directions, providing a good model for the study of neurite outgrowth at the interface between 2D and 3D substrates. In this study DRG explants exhibited healthy growth, with multiple neurites. In the presence of 3D substrates, neurites extended into the gels. Since this pattern of growth often made it difficult to trace each individual neurite through multiple planes of depth, we developed a novel analysis method to evaluate the complex neurite outgrowth from explants. The analysis method quantifies the neurite outgrowth, including the "halo" of neurites that typically extends near an explant as well as the longer "traceable" neurites (figure 2). Neurites were quantified at 5 focal planes separated by 50 μm; these focal planes corresponded to specific depths

within the gel. At each depth, neurites were counted in concentric radial zones that were 200 μm apart. This approach accounts for multiple short neurites present within one radial zone and at one depth, as well as individual long neurites present in multiple zones and/or at multiple depths.

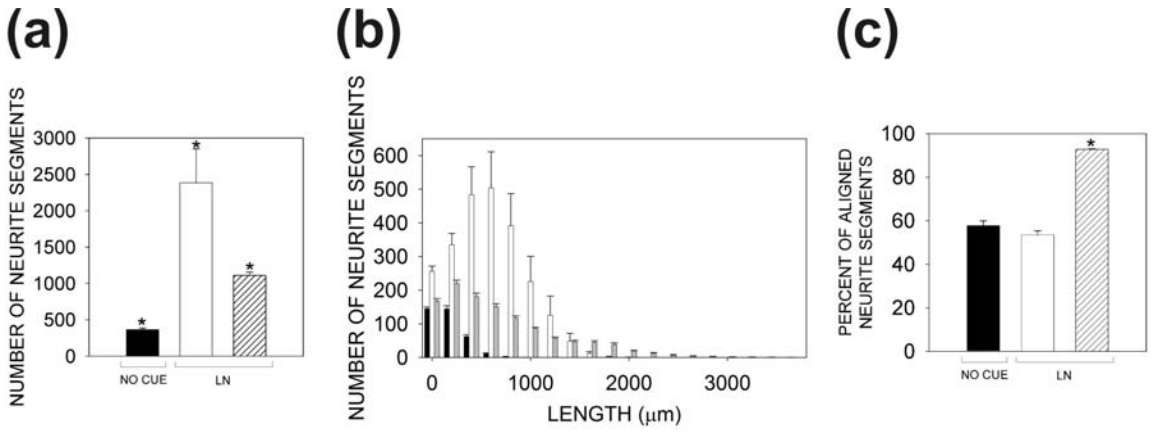

Figure 5.3. On 2D surface cultures, neurite density and length increased with LN cues.
(a) Graph of the total number of neurite segments from DRG explants cultured for 3 days in a 2D surface culture with no cue (black bars), coated LN (white bars), or micropatterned LN (white striped bars). (b) Graph of the number of neurite segments in a series of concentric contours separated by 200 μm. (c) Graph of the percent of neurite segments in aligned regions. Mean ± SEM are presented, n=9 for each condition, *, p≤0.01 by t-test.

5.3.2 In 2D surface cultures, DRG extended neurites on LN stripes and between CSPG stripes.

Before undertaking experiments with the 2D-3D interface model, we first evaluated neurite outgrowth in traditional 2D environments. To evaluate neurite outgrowth in response to extracellular matrix cues presented in 2D, DRG explants were cultured on glass coverslips coated homogeneously with LN or CSPG, on glass coverslips coated with micropatterned LN or CSPG stripes, and on uncoated glass coverslips. Explants did not adhere and thus did not extend neurites on any of the coverslips containing CSPG. DRG explants adhered and extended neurites on coverslips with LN or no cue. Total numbers of neurite segments varied with substrate type, with 366 $\pm$ 19 neurite segments on uncoated, 2384 $\pm$ 470 neurite segments on coated LN, and 1158 $\pm$ 47 neurite segments on micropatterned LN coverslips (figure 3(a); n=9 for each condition). A t-test showed significant

differences between all three conditions with $p<0.01$. Further analysis revealed that these total numbers of neurite segments reflected contributions from both neurite length and neurite number.

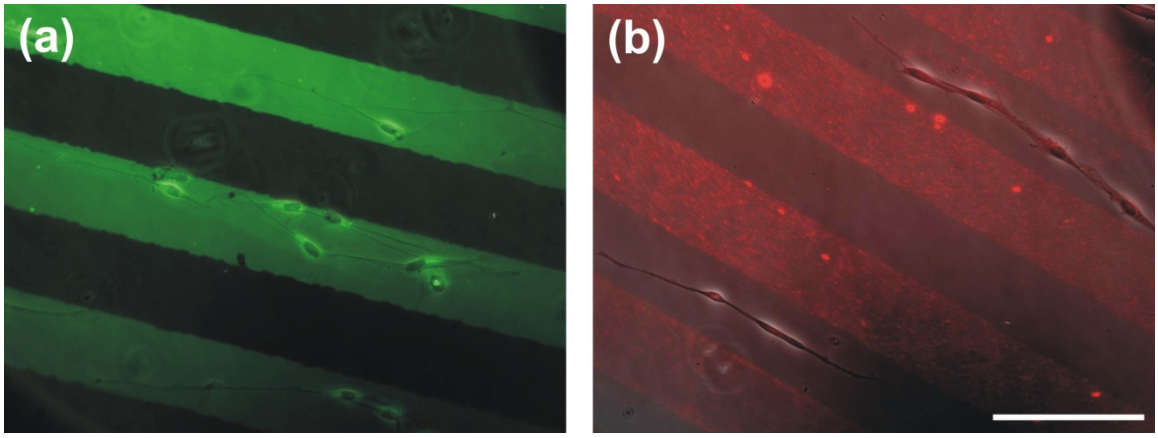

Figure 5.4. On 2D surfaces, DRG cells aligned on LN patterns and between CSPG patterns.
Overlaid phase contrast and fluorescent micrographs of dissociated DRG cells cultured on 2D surfaces micropatterned with LN (a) or CSPG (b) stripes of 50 μm thickness. Cultures were stained with anti-LN (a) or anti-CS56 (b) immunohistochemistry. Scale bar, 100 μm.

Neurite lengths differed between the substrate types, with the longest neurites reaching 1.0 mm on uncoated, 2.0 mm on coated LN, and 3.6 mm on micropatterned LN coverslips (figure 3(b)). Neurite density in each radial zone also varied among types of substrates, where the number of neurites reaching radial zones 400-800 μm from the explant was significantly higher in LN coated samples than in the other samples (figure 3(b); n=9 for each condition). In LN micropatterned cultures, the number of neurites reaching a radial distance of 1.4 mm from the explant exceeded the number of neurites reaching this distance in any other condition. LN micropatterned cultures were also the only cultures that supported neurite extension reaching 2.2 to 3.6 mm from the explant (figure 3(b)). On LN micropatterned substrates, more than 90% of the neurite segments from explants extended in the direction of the patterns, while no alignment was observed in 2D cultures of explants on control substrates (figure 3(c); n=9 for each condition).

A second type of alignment experiment allowed the qualitative comparison of neurite alignment to 2D micropatterned LN and CSPG cues. Although CSPG substrates did not support adhesion of DRG explants, 2D micropatterned CSPG substrates did allow growth of dissociated DRG neurons and qualitative assessment of neurite growth. Dissociated DRG cultured on these substrates adhered to the glass regions between CSPG tracks and extended neurites between the CSPG regions, along the direction of the pattern (figure 4(b). In contrast, dissociated DRG cultured on LN tracks adhered preferentially and extended neurites that aligned on the protein pattern (figure 4(a)).

5.3.3 In interface cultures, DRG explants displayed different outgrowth patterns depending on the surface cue.

Explants exhibited healthy morphology and extended neurites when grown at the interface between 2D surface and 3D gel substrates. With both confocal (figure 5) and phase contrast microscopy used for evaluation, the majority of neurite outgrowth from explants in these cultures was imaged. The only neurites that could not be imaged clearly were those located directly below the explant; these neurites were obstructed from view by the explant itself.

When an uncoated glass slide was presented at the interface, the majority of neurite growth was visible at the interface – along the glass and at the surface of the collagen gel (figure 5(a)). Neurites extended randomly in all directions and were often longer than the diameter of the explant from which they were growing. Most of the neurites grew in the x-y plane. Fascicles were occasionally seen at the plane of the glass. In levels below the plane of the glass within the collagen gel, neurites also extended in all directions, but were typically shorter than the diameter of the explant from which they were growing. Neurites also were in focus at multiple depths. Few neurites were seen below 200 μm deep into the collagen gel, i.e. 200 μm below the interface.

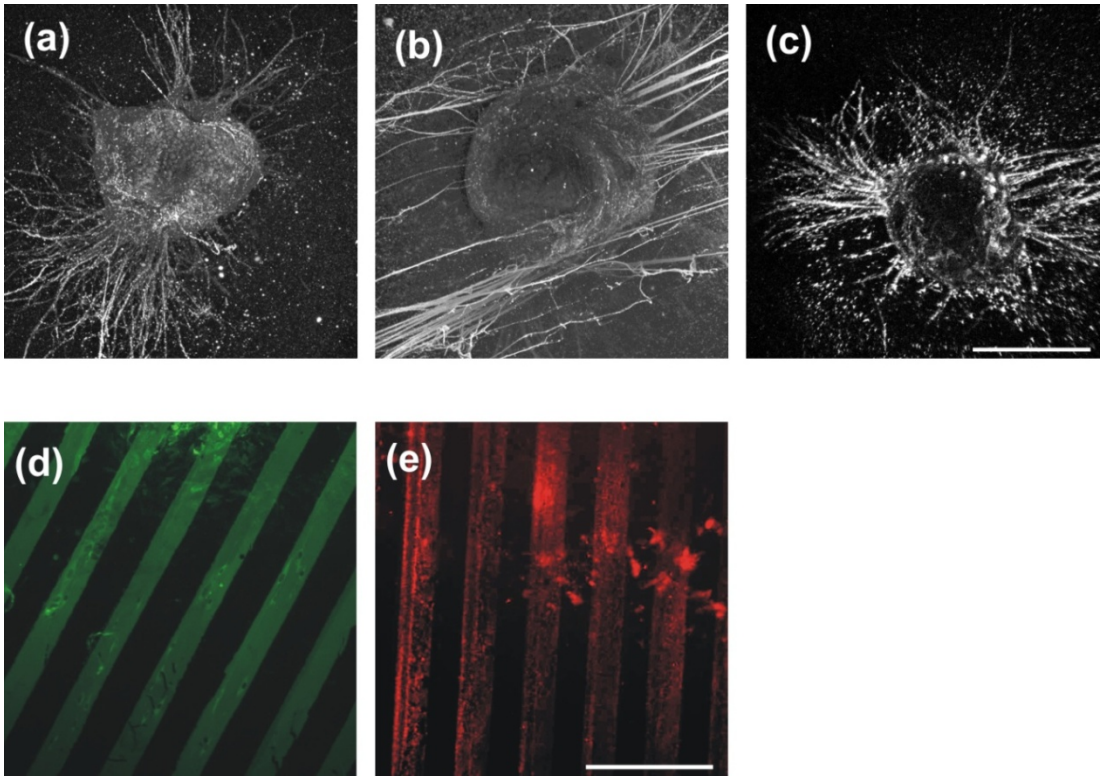

Figure 5.5. In interface cultures, DRG explant growth patterns varied with interface cue.
a, b, c: 2D summations of maximum projections of a confocal stack of DRG explants grown for 3 days in interface cultures with no cue (a), micropatterned LN (b), or micropatterned CSPG (c) and stained for anti-neurofilament immunocytochemistry. Movies of these summations are provided in Supplemental Information. d, e: Coverslips removed from separate interface cultures with micropatterned LN (d) and micropatterned CSPG (e) and immunostained for anti-LN (d) and anti-CSPG (e). Top scale bar, 500 μm; bottom scale bar, 200 μm.

When LN was presented as a cue at the interface, the majority of neurite growth was seen along the LN coated glass - at the surface of the gel (figure 5(b)). Here more neurites and longer neurites were observed, with neurites often two to three times longer than the explant body. The increase in length was especially pronounced in cultures where LN was presented in micropatterned tracks. Neurites initiated at the plane of the glass often remained at the plane of the glass, extending along the LN surface or pattern. Most of the neurites initiated within 50 μm of the LN surface grew up through the gel to the surface cue. Neurites that reached the LN surface cue were rarely seen to extend downward into the gel, i.e. their growth was along the LN surface or pattern. This phenomenon decreased the total density of outgrowth directly below the surface of the gel because although neurites were still initiating at these levels, they tended to extend upward and along the LN surface

rather than at the depth at which they were initiated. Neurites that were present below 50 μm into the gel extended in all directions and were typically shorter than the diameter of the explant.

Less neurite growth was seen at the interface when CSPG was presented to explants (figure 5(c)) than when other cues were presented (figure 5(a), 5(b)). Neurites extended in all directions, fasciculation of neurites was rarely seen, and neurites were typically shorter than the size of the explant at all levels. At all depths imaged, neurites were visible. Neurite outgrowth was similar when the interface cue was either coated CSPG or micropatterned CSPG.

5.3.4 In interface cultures, complex neurite outgrowth patterns varied with length, depth, and cue.

A grid system was used to quantify neurite outgrowth from explants in the interface cultures (figure 2). This technique allowed us to account for the number and length of all neurites growing from the explants and to assess their direction in three dimensions. Total neurite density was higher when LN was present at the interface than when CSPG was present at the interface**.** Total numbers of neurite segments were 397 $\pm$ 25 with no cue presented (n=10), 593 $\pm$ 36 with coated LN presented (n=10), 567 $\pm$ 36 with micropatterned LN presented (n=10), 258 $\pm$ 21 with coated CSPG presented (n=9), and 239 $\pm$ 10 with micropatterned CSPG presented (n=13) (figure 6(a)). An ANOVA showed significant differences between LN and CSPG cues with $p<0.01$.

The spatial patterns of neurite outgrowth from explants in interface cultures varied based on the cue presented at the interface (figure 6(b)-6(e)). Results were normalized to the proportion of the total outgrowth densities (figure 6(a)) to allow for comparison among cues. Statistical analysis of this data by multi-variate ANOVA revealed that the type of interface cue significantly affected the density of neurite outgrowth. Post-hoc analysis showed no significant difference between micropatterned

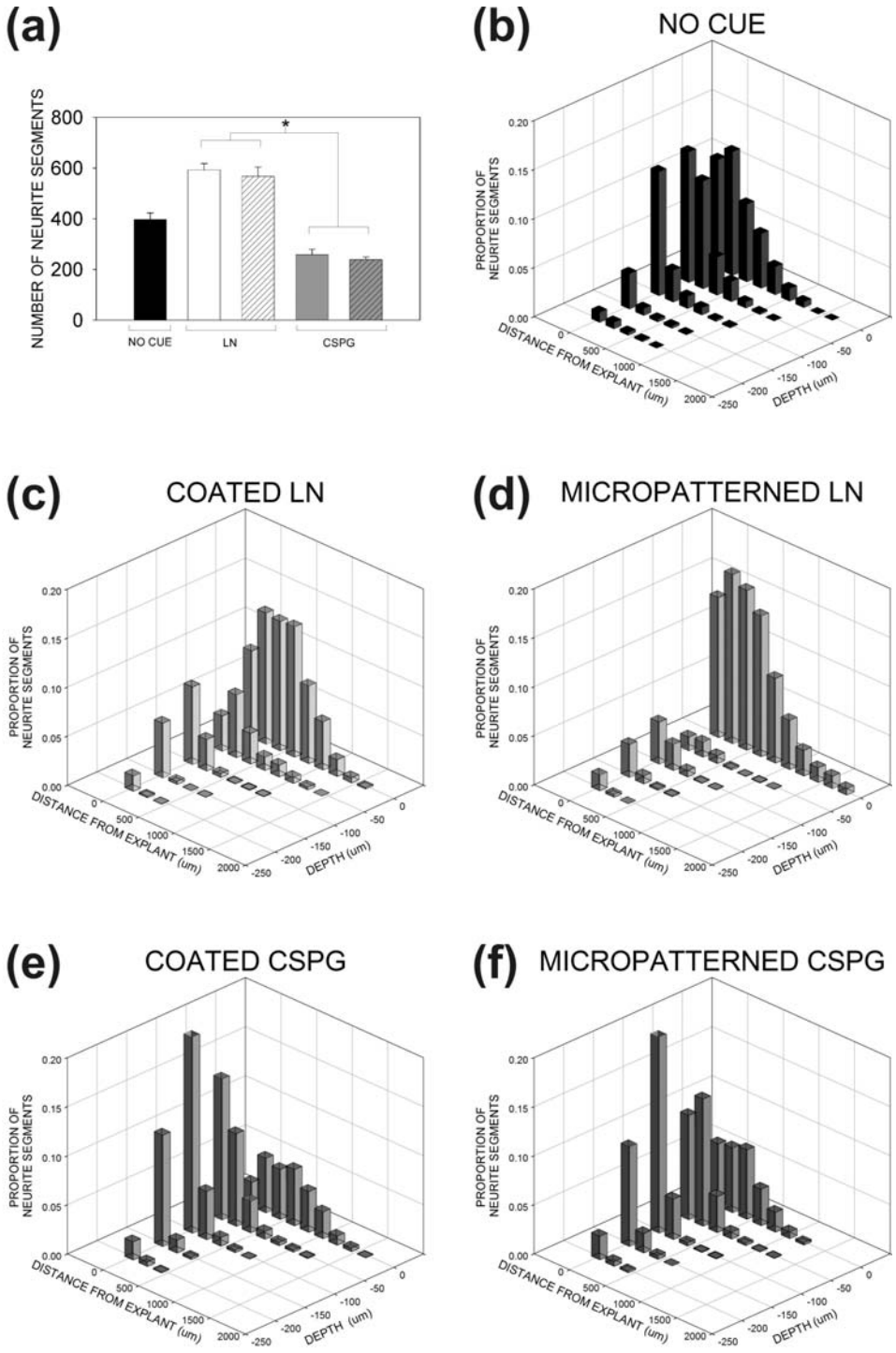

Figure 5.6. In interface cultures, DRG explants exhibited distinct growth patterns depending on the interface cue. (a) Graph of the total number of neurite segments from DRG explants cultured for 3 days in an interface culture with no cue (black bars, n=10), coated LN (white bars, n=10), micropatterned LN (white striped bars, n=10), coated CSPG (grey bars, n=9), or micropatterned CSPG (grey striped bars, n=13). Mean ± SEM are presented, *, p≤0.01 by ANOVA. (b-f) Graph of proportion of DRG neurite segments found at varying radial distance and varying depth from the explant for no cue (b), coated LN (c), micropatterned LN (d), coated CSPG (e), and micropatterned CSPG (f).

versus uniformly coated proteins for both LN and CSPG, respectively. In all samples, the longest neurites were found at the interface, and neurite length decreased with increasing depth into the collagen gel. With no cue at the interface, the largest fractions (11-13%) of neurite segments were found within a 200 μm radius at either 0, 50, or 100 μm depths from the surface. Neurite density at the interface decreased as radial distance from the explant increased. With LN cues at the interface, the largest fractions (8-17%) of neurite segments were found within a 800 μm radius of the explant and at the surface of the gel (0 μm depth). Neurite density was similar within a 800 μm radius of the explant and then decreased with radial distance from the explant. With CSPG cues at the interface, more than 23% of neurite segments was found within a 200 μm radius of the explant and at a 100 μm depth below the interface. Similar in trend to the no cue cultures, neurite density decreased as radial distance from the explant increased.

5.3.5 The type of cue presented in interface cultures affected the depth of neurite outgrowth.

In order to evaluate the effect of interface cue on the depth of neurite outgrowth, neurite density at specific depths was compared across interface cues (figure 7). Two-way ANOVA confirmed that the type of cue significantly affected the density of neurite outgrowth, and showed that neurite density varied significantly with depth. Neurite density did not differ significantly between LN coated and LN micropatterned samples nor between CSPG coated and CSPG micropatterned samples. Comparison across cues showed that in samples presented with no interface cue, 42% of neurite growth occurred at the interface and was not significantly different than growth at 50 μm below the interface. In cultures with LN at the interface, neurite growth at the level of the interface was significantly greater than growth at all other depths, with 64-82% of all growth occurring along the interface. In CSPG cultures, growth at the interface (27%) was not significantly different than growth at 50 μm or 100 μm below the interface. Examination at specific depths revealed that the proportion of neurite outgrowth at the interface was significantly greater in LN samples than in CSPG

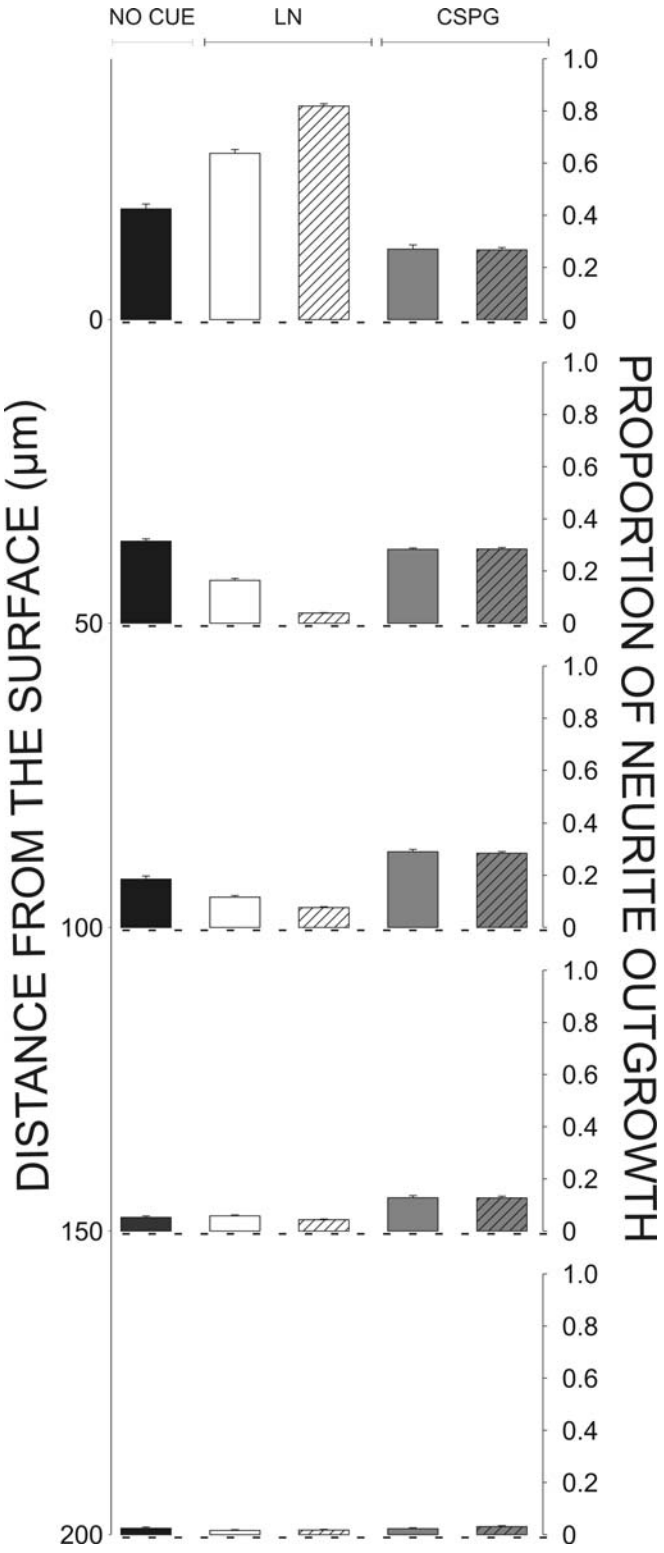

Figure 5.7. The type of interface cue affected the depth of neurite growth.
Graph of the proportion of neurite segments found at varying depths from DRG explants cultured for 3 days in an interface culture with no cue (black bars), coated LN (white bars), micropatterned LN (white striped bars), coated CSPG (grey bars), or micropatterned CSPG (grey striped bars). Mean ± SEM are presented.

samples. Fifty microns below the interface, the proportion of neurite outgrowth in LN samples (4-16%) was significantly less than all other conditions. One hundred microns below the interface, 29% of neurite outgrowth occurred in CSPG cultures, and this was significantly greater than the 7-11% counted in LN cultures. At 150 and 200 μm below the interface, there was no difference in neurite outgrowth (2-6%) across cues.

5.3.6 The type and patterning of cue presented in interface cultures affected the length and alignment of neurite outgrowth.

In order to evaluate the effect of cue presentation on the length of neurite outgrowth, total neurite density in concentric cylindrical zones was compared across cues (figure 8). Two-way ANOVA confirmed that the type of cue significantly affected the length of neurite outgrowth, and showed that neurite density varied significantly with distance from the explant. Within a 200 μm radius of the

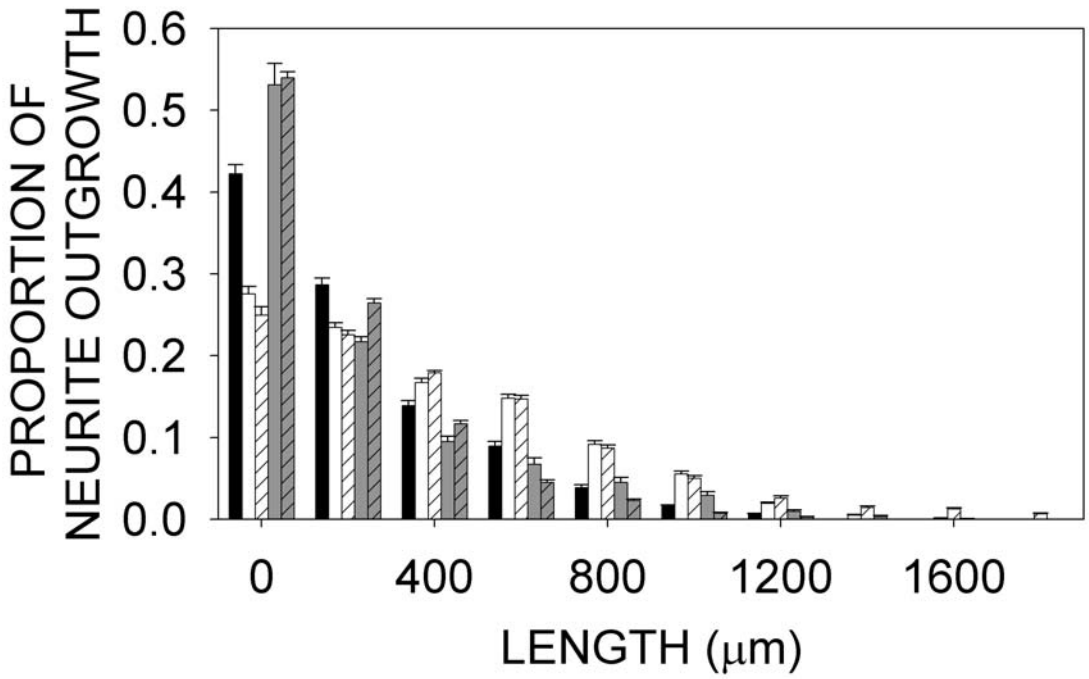

Figure 5.8. DRG explants presented with LN tracks extended the longest neurites.
Graph of the proportion of neurite segments found at varying radial intervals from DRG explants cultured for 3 days in an interface culture with no cue (black bars), coated LN (white bars), micropatterned LN (white striped bars), coated CSPG (grey bars), or micropatterned CSPG (grey striped bars). Mean ± SEM are presented.

explant, the density of neurite outgrowth was not significantly different across cues. The average number of neurites initiating from the explant (counted in the first 200 μm radius) across all cues was 131 ± 6. The number of neurites reaching 400 μm and 600 μm from the explant was significantly greater in LN cultures than in CSPG cultures. In cultures presenting LN, an average of 107 ± 7 neurites (17-18% of the total density) extended into the 400 μm radial zone and 89 ± 6 (15% of the total density) extended into the 600 μm radial zone, whereas in CSPG cultures only 31 ± 3 (5-7% of the total density) extended into the 400 μm radial zone and 20 ± 3 (2-5% of the total density) extended into the 600 μm radial zone. The average number of neurites reaching 1.6 mm was 10 ± 1 (1.2% of the total density) in cultures with micropatterned LN at the interface while all other conditions averaged less than one neurite reaching this length (<0.1% of total density**).** Neurite lengths differed between the substrate types, where the longest neurites reached 1.6 mm with no cue presented, 1.6 mm with coated LN presented, 1.8 mm with micropatterned LN presented, 1.6 mm with coated CSPG presented, and 1.2 mm with micropatterned CSPG presented. More than 90% of neurite outgrowth at the interface was aligned to the pattern in the LN patterned cultures (figure 9), while no alignment was observed in cultures with micropatterned CSPG at the interface. The alignment of neurites at the surface of interface cultures with LN stripes was not significantly different from the alignment of neurites in 2D cultures with LN stripes (figure 3(b)).

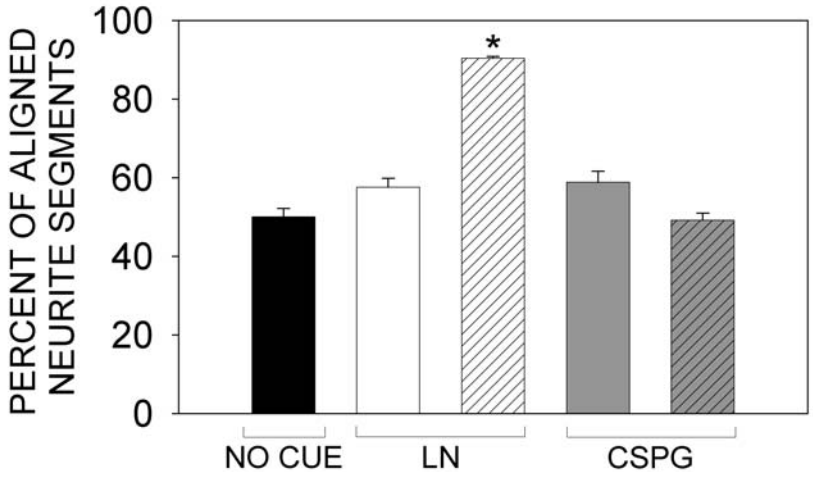

Figure 5.9. In interface cultures, DRG explants aligned neurites to LN but not CSPG interface cues.
Graph of the percent of neurite segments in aligned regions at the interface from DRG explants cultured for 3 days in an interface culture with no cue (black bars), coated LN (white bars), micropatterned LN (white striped bars), coated CSPG (grey bars), or micropatterned CSPG (grey striped bars). Mean ± SEM are presented, *, p≤0.01 by ANOVA.

5.4 Discussion

The overarching goal of this study was to evaluate the effects of dimensionality on the response of neurites to 2D molecular guidance cues. Toward this end, we developed a novel cell culture system that allowed us to assess the outgrowth of neurites presented with 2D cues in the context of a 3D growth environment**.** The presentation of a LN cue at the 2D surface increased the overall density of neurite outgrowth when compared to cultures presenting a CSPG cue at the surface. When the surface cue was LN, most of the neurites extended at the surface of the gel, whereas when CSPG was presented, more neurites extended into the collagen I matrix. Patterning of cues did not affect the density or depth of growth. However, outgrowth near the surface of the gel was aligned to LN patterns, and these extensions were significantly longer than neurites in other cultures.

LN and CSPG were chosen as representative molecules because LN is known to promote neuronal adhesion, migration, and neurite extension while CSPG is an inhibitor of neuronal growth. Collagen I is an established hydrogel that is compatible with cell culture and was thus chosen as a representative 3D matrix. Neurons have receptors to both collagens and laminins,[36, 37] and DRG neurons have been specifically shown to express $\alpha_1\beta_1$ integrin, $\alpha_3\beta_1$ integrin, and low levels of $\alpha_6\beta_1$ integrin.[38] Pilot experiments confirmed that collagen I did not guide neurites in this model; when either coated collagen or micropatterned collagen was presented as a potential cue at the interface, neurite growth was not significantly different from neurite growth when no cue was presented at the interface (data not shown). Whole DRG explants were used to allow for precise placement at the interface. Additionally, explants allow for straightforward assessment of neurite outgrowth given that the neurite starting points can be easily determined without the need for timelapse microscopy.

Previous quantitative methods used to evaluate neurite outgrowth from explants[39-47] were not well suited to characterize the complex 3D outgrowth observed from explants in our culture system as we aimed to assess the density, length, and depth of neurite outgrowth. We developed a quantification

method that modified the Sholl method of concentric circles for analyzing the branching pattern of neurons.[13, 48] In our analysis method, the total numbers of neurite segments reflect contributions from both neurite length and neurite number in the focal planes analyzed. Our analysis method also confirms and extends the results that we observed with confocal and phase contrast microscopy.

2D culture of explants was employed in our study for analysis of the neurite response to 2D molecular cues in the absence of a 3D architecture. After 3 days in culture, a larger surface area of LN coating (full coat vs. micropatterned) resulted in a higher density of neurite outgrowth, but the longest outgrowth was seen along LN micropatterned stripes. A previous study observed a higher rate of growth from chick DRG on LN coated surfaces than on micropatterned LN surfaces with a shorter culture time – one day of culture.[40] The pattern size (30 μm stripes) and analysis method were also different, making it difficult to compare the two studies. Because of the lack of adhesion of explants to CSPG surfaces, dissociated DRG were used to confirm the ability of CSPG to guide neurites in the 2D cultures. Similar to previous studies, dissociated DRG avoided the stripes of CSPG,[16] extending neurites aligned along the CSPG stripes but between them. This growth contrasted with growth of dissociated DRG on LN stripes, where DRG extended neurites aligned to the LN stripes and directly on top of them. Thus, in 2D cultures, both permissive and inhibitory molecular cues can direct neurite growth along micron-scale stripes; however, the mechanisms differ. The permissive LN attracts neurite growth along the LN stripe, while the inhibitory CSPG confines neurites to the stripe between the CSPG stripes.

Our interface cultures revealed more complex neurite growth profiles in response to a combined 2D and 3D growth environment (figure 10). Neurite density throughout the complex 3D interface cultures was higher with LN versus CSPG at the interface. This result is similar to what we observed in 2D, where neurite density was higher in response to LN than to no cue. Our analysis method allowed us to directly compare quantitative data within the interface culture experiments. Because

the 2D data represents the total neurite outgrowth from the explant while the interface data represents the neurite outgrowth found at 5 distinct depths in the gel, we compared the neurite density data from 2D cultures with interface cultures solely in a qualitative manner.

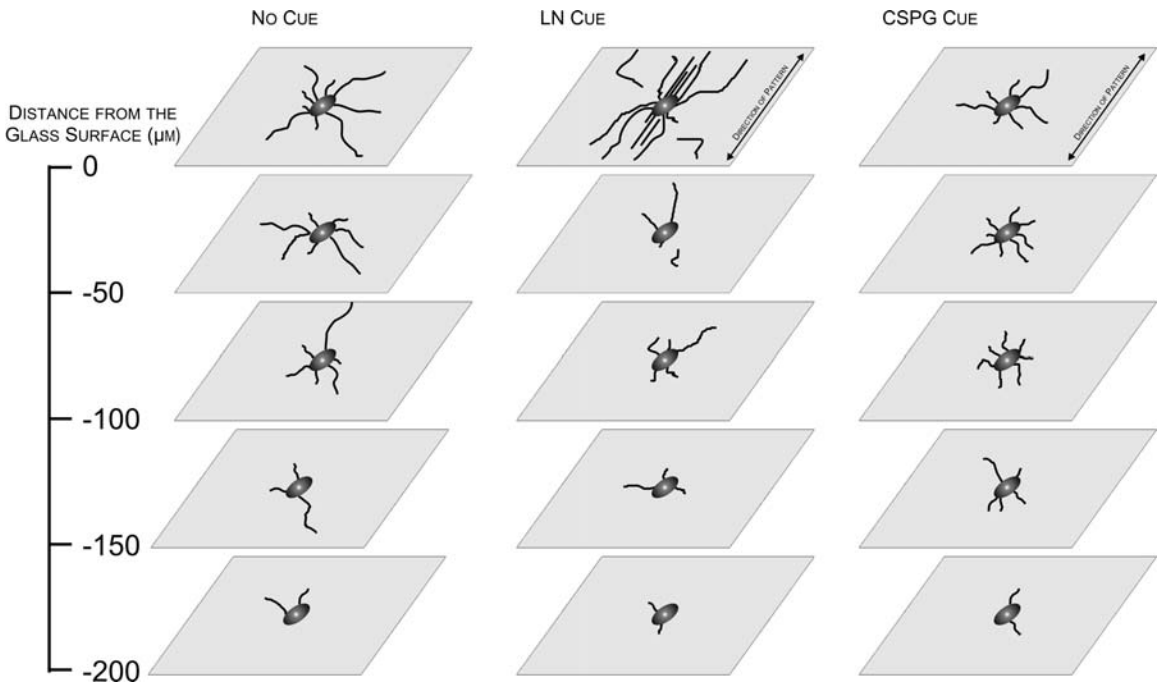

Figure 5.10. Summary of distinct growth patterns in interface cultures.

Micropatterned LN maintained its ability to guide neurite outgrowth when presented in conjunction with a more complex 3D environment. Interestingly, this guidance seemed to be effective over a distance of at least 50 μm, since most neurites that initiated their extensions within 50 μm of the glass surface grew upward toward the surface and extended along uniform or micropatterned LN. Of all the substrate cues tested, the presentation of patterned LN resulted in the longest neurites in interface cultures, where the longest neurites extended along the LN stripes at the surface of the gel. This cue-specific result is similar to that seen in 2D. In addition, in both the 2D and interface cultures, the presentation of LN also increased the number of neurites reaching intermediate distances (i.e. 1.4 mm for 2D and 800 μm for interface cultures). Of note, the longest neurites that extended on

patterned LN on 2D surfaces were twice as long as the longest neurites extended on patterned LN in interface cultures. The presence of the 3D gel in the interface cultures provides neurites with more choices as they navigate this more complex environment; as a result, the more complicated decision process may potentially slow neurite extension.

While neurites avoided CSPG in both the 2D surface cultures and the interface cultures, patterned CSPG did not maintain its ability to direct neurite outgrowth within the x-y plane at the interface. Rather, neurites avoided both fully coated and patterned CSPG by growing into the 3D gel. Further, more neurites grew deeper into the gel when they were presented with a surface cue of CSPG as compared to LN. Taken together, these results point to a strong ability of CSPG to direct neurite growth away from itself, and suggest that the pattern of CSPG is less important than its presence for avoidance in 3D architectures. Yu and Bellamkoda have demonstrated that fewer chick DRG neurites extended into areas of agarose hydrogels cross-linked with CS than into areas of unmodified gels.[49] Their results showing the inhibitory effects of CS on 3D neurite outgrowth are consistent with those of the present study. While these experiments have not excluded the possibility that a soluble gradient may form in our system and play a role in attracting or repelling neurites from the surface cue, the presence of the cues and fidelity of the micropattern after 3 days (figure 5(d), 5(e)) suggest a primary role for the cues at the surface. It will be interesting to investigate the dynamic profiles of guidance cues in future studies.

Other studies have begun to explore the capacity of cues traditionally presented to cells adhered to flat surfaces. Luo and Shoichet have examined the neurite response to 3D tracks of adhesive fibronectin peptide fragments in non-adhesive hydrogels.[50] Comparable to the neurite response to patterned peptides on 2D substrates,[51] neurites oriented to and grew through these 3D tubes of adhesive proteins. When Li and Folch gave neurites the choice of growing along poly-D-lysine-coated, microfabricated PDMS or into a 3D Matrigel matrix, neurites in the poly-D-lysine-coated grooves

grew along the groove walls despite having the option of growing upward into the Matrigel matrix.[18] Similar to the results with LN in our study, their study showed that the topographical cues maintained their ability to guide when combined with the introduction of a 3D environment.

The results of this study provide insights into the spatial integration of permissive and inhibitory molecular cues and 3D architecture. Our platform can be extended to integrate other *in vitro* models for axon guidance[52] that incorporate and investigate a diverse array of molecular and/or topographical cues.[30, 49, 53, 54] These results are also of interest in the context of a recent study demonstrating functional improvement in rats after spinal cord injury, when the rats were implanted with poly(2-hydroxyethyl methacrylate-*co*-methyl methacrylate) NGCs. Improvement was observed when the NGC lumens contained either of two distinct geometries: a fibrin matrix or multiple smaller NGCs.[55]

In conclusion, the potential of nerve guidance channels or open matrix therapies to promote nerve regeneration hinges on their ability to maintain guidance through the complex 3D *in vivo* environment. As more complex, well-defined biomaterial substrates and matrices are developed, we will expect to gain a more complete understanding of neurite navigation in multiple dimensions.

5.5 Acknowledgments

The authors thank Grace Li for helpful discussion of the manuscript and Johnathon Rollo for assistance with experiments. This work was funded by an NSF CAREER grant to DHK, an AAUW dissertation fellowship to CK, and a MRSEC REU grant to VF.

5.6 References

1. Boyd, J. G. and T. Gordon. Neurotrophic factors and their receptors in axonal regeneration and functional recovery after peripheral nerve injury. Molecular Neurobiology. 27: 277-323, 2003.

2. Jones, D. M., B. A. Tucker, M. Rahimtula and K. M. Mearow. The synergistic effects of ngf and igf-1 on neurite growth in adult sensory neurons: Convergence on the pi 3-kinase signaling pathway. Journal of Neurochemistry. 86: 1116, 2003.

3. Kato, A. C. and R. M. Lindsay. Overlapping and additive effects of neurotrophins and cntf on cultured human spinal cord neurons. Experimental Neurology. 130: 196, 1994.

4. Taylor, L., L. Jones, M. H. Tuszynski and A. Blesch. Neurotrophin-3 gradients established by lentiviral gene delivery promote short-distance axonal bridging beyond cellular grafts in the injured spinal cord. Journal of Neuroscience. 26: 9713, 2006.

5. Le Beau, J. M., F. J. Liuzzi, A. S. Depto and A. I. Vinik. Up-regulation of laminin b2 gene expression in dorsal root ganglion neurons and nonneuronal cells during sciatic nerve regeneration. Experimental Neurology. 134: 150-155, 1995.

6. Li, G. N., J. Liu and D. Hoffman-Kim. Multi-molecular gradients of permissive and inhibitory cues direct neurite outgrowth. Annals of Biomedical Engineering. 36: 889-904, 2008.

7. Tom, V. J., M. P. Steinmetz, J. H. Miller, C. M. Doller and J. Silver. Studies on the development and behavior of the dystrophic growth cone, the hallmark of regeneration failure, in an in vitro model of the glial scar and after spinal cord injury. J Neurosci. 24: 6531-9, 2004.

8. Blackman, C. F., S. G. Benane and D. E. House. Evidence for direct effect of magnetic fields on neurite outgrowth. The FASEB Journal. 7: 801-806, 1993.

9. Patel, N. and M. M. Poo. Orientation of neurite growth by extracellular electric fields. Journal of Neuroscience. 2: 483-496, 1982.

10. Shi, R. and R. B. Borgens. Three-dimensional gradients of voltage during development of the nervous system as invisible coordinates for the establishment of embryonic pattern. Developmental Dynamics. 202: 1995.

11. Bruder, J. M., A. P. Lee and D. Hoffman-Kim. Biomimetic materials replicating schwann cell topography enhance neuronal adhesion and neurite alignment in vitro. Journal of Biomaterials Science, Polymer Edition. 18: 967-982, 2007.

12. Goldner, J. S., J. M. Bruder, G. Li, D. Gazzola and D. Hoffman-Kim. Neurite bridging across micropatterned grooves. Biomaterials. 27: 460-72, 2006.

13. Mahoney, M. J., R. R. Chen, J. Tan and W. M. Saltzman. The influence of microchannels on neurite growth and architecture. Biomaterials. 26: 771-8, 2005.

14. Clark, P., S. Britland and P. Connolly. Growth cone guidance and neuron morphology on micropatterned laminin surfaces. J Cell Sci. 105 (Pt 1): 203-12, 1993.

15. Esch, T., V. Lemmon and G. Banker. Local presentation of substrate molecules directs axon specification by cultured hippocampal neurons. J Neurosci. 19: 6417-26, 1999.

16. Snow, D. M., V. Lemmon, D. A. Carrino, A. I. Caplan and J. Silver. Sulfated proteoglycans in astroglial barriers inhibit neurite outgrowth in vitro. Exp Neurol. 109: 111-30, 1990.

17. Gundersen, R. W. Response of sensory neurites and growth cones to patterned substrata of laminin and fibronectin in vitro. Dev Biol. 121: 423-31, 1987.

18. Li, N. and A. Folch. Integration of topographical and biochemical cues by axons during growth on microfabricated 3-d substrates. Exp Cell Res. 311: 307-16, 2005.

19. Letourneau, P. C. Cell-to-substratum adhesion and guidance of axonal elongation. Dev Biol. 44: 92-101, 1975.

20. Kleinfeld, D., K. H. Kahler and P. E. Hockberger. Controlled outgrowth of dissociated neurons on patterned substrates. J Neurosci. 8: 4098-120, 1988.

21. Luckenbill-Edds, L. Laminin and the mechanism of neuronal outgrowth. Brain Research Reviews. 23: 1-27, 1997.

22. Hoke, A. and J. Silver. Proteoglycans and other repulsive molecules in glial boundaries during development and regeneration of the nervous system. Prog Brain Res. 108: 149-63, 1996.

23. Silver, J. and J. H. Miller. Regeneration beyond the glial scar. Nat Rev Neuroscience. 5: 146-156, 2004.

24. Chernousov, M. A. and D. J. Carey. Schwann cell extracellular matrix molecules and their receptors. Histol Histopathol. 15: 593-601, 2000.

25. Gelse, K., E. Poschl and T. Aigner. Collagens--structure, function, and biosynthesis. Adv Drug Deliv Rev. 55: 1531-46, 2003.

26. Hoffman, A. S. Hydrogels for biomedical applications. Ann N Y Acad Sci. 944: 62-73, 2001.

27. Lee, K. Y. and D. J. Mooney. Hydrogels for tissue engineering. Chem Rev. 101: 1869-79, 2001.

28. Wallace, D. G. and J. Rosenblatt. Collagen gel systems for sustained delivery and tissue engineering. Adv Drug Deliv Rev. 55: 1631-49, 2003.

29. Hayman, M. W., K. H. Smith, N. R. Cameron and S. A. Przyborski. Enhanced neurite outgrowth by human neurons grown on solid three-dimensional scaffolds. Biochem Biophys Res Commun. 314: 483-8, 2004.

30. Pittier, R., F. Sauthier, J. A. Hubbell and H. Hall. Neurite extension and in vitro myelination within three-dimensional modified fibrin matrices. J Neurobiol. 63: 1-14, 2005.

31. Li, G. N., L. L. Livi, C. M. Gourd, E. S. Deweerd and D. Hoffman-Kim. Genomic and morphological changes of neuroblastoma cells in response to three-dimensional matrices. Tissue Engineering. 13: 1035-1047, 2007.

32. Balgude, A. P., X. Yu, A. Szymanski and R. V. Bellamkonda. Agarose gel stiffness determines rate of drg neurite extension in 3d cultures. Biomaterials. 22: 1077-84, 2001.

33. Belkas, J. S., M. S. Shoichet and R. Midha. Axonal guidance channels in peripheral nerve regeneration. Operative Techniques in Orthopaedics. 14: 190-198, 2004.

34. Huang, Y. C. and Y. Y. Huang. Biomaterials and strategies for nerve regeneration. Artificial organs. 30: 514-522, 2006.

35. Pfister, L. A., M. Papaloizos, H. P. Merkle and B. Gander. Nerve conduits and growth factor delivery in peripheral nerve repair. Journal of the Peripheral Nervous System. 12: 65, 2007.

36. Reichardt, L. F. and K. J. Tomaselli. Extracellular matrix molecules and their receptors: Functions in neural development. Annual review of neuroscience. 14: 531-570, 1991.

37. Venstrom, K. A. and L. F. Reichardt. Extracellular matrix. 2: Role of extracellular matrix molecules and their receptors in the nervous system. The FASEB Journal. 7: 996-1003, 1993.

38. Tomaselli, K. J., P. Doherty, C. J. Emmett, C. H. Damsky, F. S. Walsh and L. F. Reichardt. Expression of beta 1 integrins in sensory neurons of the dorsal root ganglion and their functions in neurite outgrowth on two laminin isoforms. Journal of Neuroscience. 13: 4880-4888, 1993.

39. Ebendal, T.Nerve growth factors. Bath: Wiley, 1989.

40. Tai, H. C. and H. M. Buettner. Neurite outgrowth and growth cone morphology on micropatterned surfaces. Biotechnol Prog. 14: 364-70, 1998.

41. Borasio, G. D., S. Horstmann, J. M. Anneser, N. T. Neff and M. A. Glicksman. Cep-1347/kt7515, a jnk pathway inhibitor, supports the in vitro survival of chick embryonic neurons. Neuroreport. 9: 1435-9, 1998.

42. Steiner, J. P., G. S. Hamilton, D. T. Ross, H. L. Valentine, H. Guo, M. A. Connolly, S. Liang, C. Ramsey, J. H. Li, W. Huang, P. Howorth, R. Soni, M. Fuller, H. Sauer, A. C. Nowotnik and P. D. Suzdak. Neurotrophic immunophilin ligands stimulate structural and functional recovery in neurodegenerative animal models. Proc Natl Acad Sci U S A. 94: 2019-24, 1997.

43. Masuda, T., N. Okado and T. Shiga. The involvement of axonin-1/sc2 in mediating notochord-derived chemorepulsive activities for dorsal root ganglion neurites. Dev Biol. 224: 112-21, 2000.

44. Wen, X. and P. A. Tresco. Effect of filament diameter and extracellular matrix molecule precoating on neurite outgrowth and schwann cell behavior on multifilament entubulation bridging device in vitro. J Biomed Mater Res. 76A: 626-37, 2006.

45. Bilsland, J., M. Rigby, L. Young and S. Harper. A rapid method for semi-quantitative analysis of neurite outgrowth from chick drg explants using image analysis. J Neurosci Methods. 92: 75-85, 1999.

46. Bilsland, J. G. and S. J. Harper. Cep-1347 promotes survival of ngf responsive neurones in primary drg explants. Neuroreport. 14: 995-9, 2003.

47. Harper, S., J. Bilsland, L. Young, L. Bristow, S. Boyce, G. Mason, M. Rigby, L. Hewson, D. Smith, R. O'Donnell, D. O'Connor, R. G. Hill, D. Evans, C. Swain, B. Williams and F. Hefti. Analysis of the neurotrophic effects of gpi-1046 on neuron survival and regeneration in culture and in vivo. Neuroscience. 88: 257-67, 1999.

48. Sholl, D. A. Dendritic organization in the neurons of the visual and motor cortices of the cat. J Anat. 87: 387-406, 1953.

49. Yu, X. and R. V. Bellamkonda. Dorsal root ganglia neurite extension is inhibited by mechanical and chondroitin sulfate-rich interfaces. J Neurosci Res. 66: 303-10, 2001.

50. Luo, Y. and M. S. Shoichet. Light-activated immobilization of biomolecules to agarose hydrogels for controlled cellular response. Biomacromolecules. 5: 2315-23, 2004.

51. Ranieri, J. P., R. Bellamkonda, E. J. Bekos, J. A. Gardella, Jr., H. J. Mathieu, L. Ruiz and P. Aebischer. Spatial control of neuronal cell attachment and differentiation on covalently patterned laminin oligopeptide substrates. Int J Dev Neurosci. 12: 725-35, 1994.

52. Li, G. N. and D. Hoffman-Kim. Tissue-engineered platforms of axon guidance. Tissue Engineering Part B: Reviews. 14: 33-51, 2008.

53. Krewson, C. E., S. W. Chung, W. Dai and W. M. Saltzman. Cell aggregation and neurite growth in gels of extracellular matrix molecules. Biotechnology and Bioengineering. 43: 555-62, 1994.

54. Baldwin, S. P., C. E. Krewson and W. M. Saltzman. Pc12 cell aggregation and neurite growth in gels of collagen, laminin and fibronectin. Int J Dev Neurosci. 14: 351-64, 1996.

55. Tsai, E. C., P. D. Dalton, M. S. Shoichet and C. H. Tator. Matrix inclusion within synthetic hydrogel guidance channels improves specific supraspinal and local axonal regeneration after complete spinal cord transection. Biomaterials. 27: 519-533, 2006.

Chapter 6 Conclusions and Future Directions

The conventional tissue engineering approach of substituting engineered replacement tissue for injured tissue does not promote the precise regrowth and reconnections required to overcome nerve injury. Individual cues have been studied extensively, but single guidance cues are not sufficient to overcome the inhibitory post-injury environment. Coordinated presentation of multiple cues is likely required for successful and functional nerve regeneration. The main objective of this thesis was to break down the complex mixture of cues involved in neuronal guidance *in vivo* and to begin to recombine these cues in defined *in vitro* platforms toward determining the net neuronal response to multiple directive cues. The topographical information presented by oriented cells was isolated from the myriad of biochemical cues involved in cell-cell guidance and examined for critical topographical guiding information. The contribution of these materials to directed neuronal growth in combination or in competition with biochemical cues was also investigated. Finally, biochemical cues were investigated in conjunction with 3D architecture.

The first objective of this thesis was to gain insights into the critical topographical features required for directed neuronal growth. We characterized the topographical information presented by distinct glial cells, astrocytes and SCs, as well as endothelial cells. Chapter 3 demonstrated that despite contrasts in cellular sizes, degree of alignment, and positional frequency, the topography of all of these cell types was sufficient for guidance. This study points to some correlation between the topographical features presented and their ability to guide neurons. The decreased capacity for guidance on aligned endothelial cell features may be attributed to presentation of cellular features more than 50% larger in area than more directive SC features. In addition to smaller feature size, SC

features also presented a substantially more clustered distribution of orientation of features. DRG alignment was increased on SC materials, but this increase was not proportionate to the increase in clustering of aligned features which may point to the importance of the frequency of guidepost features in reorienting the trajectory of axons as the number of aligned SCs was similar to the number of aligned astrocytes.

Further insights toward critical feature parameters required for directed neuronal growth were gained from comparison to more geometric bioinspired SC topographies. These bioinspired features which were higher, had sharper edges, and presented continuous features to navigating neurons were also shown to be better suited for more precise guidance. Further, work presented in Appendix C points again to the importance of continuity of features as continuous approximations of SC contours had a stronger directive influence than discontinuous approximations of SC somas. This work also suggests that alignment to straight approximations of SC processes was stronger than alignment to contoured approximations.

These findings point future studies to the design and investigation of bioinspired materials that incorporate and vary more geometric approximations of cellular topography, provide more bioinspired heights and slopes, and incorporate positional frequency of biomimetic topographies toward determining the dimensions and shapes of features that provide critical topographical guidance information to navigating neurons. The physical cues presented in these studies were biomimetic in topographical information, but other physical properties of these substrates including stiffness and dimensionality do not mimic biological tissues. Future studies should investigate the capacity for cellular topographies to guide when presented at more biomimetic stiffness which may include variable stiffness across cellular topography and move toward 3D replication of cellular cues.

It is well recognized that the different chemical cues presented by SCs and astrocytes after injury contribute to the varied capacities for regeneration in the PNS and CNS, but this work points to the multifaceted importance of glial cells suggesting that the physical features of SCs and astrocytes may contribute to the difference in regeneration capacity in the CNS and PNS as DRG alignment was stronger on SC materials than on astrocyte materials. It was also demonstrated that guidance of nerve cells is not limited to glial cell topography as endothelial topography was also sufficient for directing neuronal growth. To determine their full capacity as regenerative cues, further examination of cellular response on biomimetic and bioinspired topographies such as length of neurites, rate of growth in the preferred direction, number of neurites per neuron, position of neurites emerging from somata, cell mobility, and number of synaptic connections should be carried out.

Future studies should also work to elucidate the mechanisms by which neurons align to topographical features. The cytoskeleton is likely involved in topographical sensing. Toward this end, the guidance of DRGs on these materials when molecules involved in cytoskeletal organization are inhibited should be investigated in the future. Another approach to elucidating the role of the cytoskeleton in topographical sensing and guidance is to look at interactions at the receptor level. Integrin receptors and cell adhesion molecules are coupled to the cytoskeleton through intermediaries. Pilot studies presented in Appendix B suggest that varying the molecular coating of biomimetic topography influences the alignment of DRGs to these cues. Adhesion to these substrates and activation of signaling pathways should also be investigated for their role in neuronal sensing of topographical cues.

While this work demonstrates that both DRG cells and neurites preferentially align to the direction of the underlying topographical cues, it is not clear whether neurites are responding directly to the topography and/or directly to support cells which have aligned to the topography. DRG cultures are

heterogeneous, containing not only neurons, but also proliferating SCs and fibroblasts, and work presented in Appendix A suggests that SCs and fibroblasts each have the capacity to align to biomimetic SC features. In order to fully characterize the response of DRGs to biomimetic topography the role of these two mechanisms in influencing the resulting alignment must be determined.

It was an underlying goal to determine optimal conditions for alignment of glial and non-glial cell types in an efficient and illuminating manner. Chapter 2 demonstrated statistical design and analysis methods as effective tools for modeling the interactions of several culture parameters and determining optima. Insights into the general mechanisms of cellular adhesion, alignment, and monolayer formation were also elucidated. Future directions include application of the insights gained in this study to apply statistical design and analysis to other multi-factorial guidance platforms and to predict guidance and monolayer formation of other cell types. These multi-factorial platforms can include multiple cues such as combinations of chemical and topographical cues or multiple factors contributing to one type of cue such as duration, onset, strength, and frequency of electrical stimulation.

Another goal of this thesis was to investigate new combinations of directive cues and structural microenvironments. Chapter 4 suggested dominance of directive biochemical cues over biomimetic cellular topographies or balance of the two directive cues in the limited range tested, but more importantly, this study pointed to the importance of investigating multi-cue environments as the relative strengths of individual cues was not completely predictive of neuronal response to combinations of these cues. Alignment to directive protein cues was strengthened by reducing pattern pitch, but neuronal preference to orthogonal preference of this strong individual cue more balanced. Other trends and interactions of cues were also observed. Alignment to directive protein cues was weakened by reducing the adhesiveness of the protein cue by reducing the concentration of

adhesive protein or mixing with an anti-adhesive molecule, and neuronal preference was shifted from for strong guidance to the biochemical cue to more balanced to both cues or a less consistent alignment response to the biochemical cue. Future studies should seek to interpolate these suggested trends and interactions. Statistical design and analysis should be a useful tool toward this end. Further, combinations of directive biochemical cues and geometric or bioinspired topographies should be studied. Future studies will also benefit from the discernment of the mechanisms by which cells sense and respond to topographical cues. Comparing and contrasting these mechanisms to those which contribute to the sensing of biochemical cues will also advance the understanding of the integrated response of neurons to multiple cues in their local environment.

Chapter 5 demonstrated the persistence of biochemical guidance on permissive and adhesive tracks in 3D and illustrated a more complex response to inhibitory molecules. These studies were conducted in a specific range of conditions. Different types of cues such as topography or electrical stimulation should be incorporated into 3D platforms. These studies will also be informed by insights into the mechanisms by which cells sense and respond to multiple cues.

In conclusion, the work presented in this thesis contributes to a deeper understanding of neuronal guidance at a basic science level through the breakdown and recombination of features mimicking the *in vivo* environment in defined *in vitro* platforms. An extensive toolbox of engineering and biological techniques including photolithography, soft lithography, micro-contact printing, micromolding, immunocytochemistry, microscopy, image anlaysis, circular statistics, and FFT image processing was utilized to fabricate and examine these platforms, but in addition, DOE, RSM, novel platforms for the presentation of multiple cues, and novel analysis of 3D neurite growth were added to this toolbox during the investigations of this thesis. Breakdown of the complex mixture of cues presented by cellular cues revealed the multifaceted importance of glial cells as topographical features of glial cells were shown to contribute to their guidance capacities. Steps toward

reconstruction of the complex *in vivo* environment through the presentation of biochemical cues with biomimetic topographies or 3D matrices pointed to the precision by which neurons navigate their local environment. Neurons exhibited a guided response to more complex environments and/or demonstrated integration of cues in these complex environments rather responding to only one type of cue at a time in the local environment. As repairing injury in the CNS will require synergistic presentation of multiple cues to overcome the inhibitory post-injury environment, these studies point toward the importance of investigating these cues *in vitro* in platforms that consider the complexity *in vivo*.

Appendix A Biomimetic materials presenting Schwann cell topography direct growth of neurons and support cells

Directed growth is required for successful regeneration and reconnection after nerve injury. Previous work has shown that biomimetic materials presenting Schwann cell (SC) topography enhance alignment of dorsal root ganglia (DRG) cells in a cell density-dependent manner. DRG cultures are heterogeneous, containing not only neurons, but also proliferating SCs and fibroblasts (Fbs). When neurons in DRG cultures align in the direction of SC topography, they may be responding directly to the topography and/or directly to support cells which have aligned to the topography. We examined the alignment of SCs, Fbs, and neuron-enriched DRG cultures individually to gain insight into the mechanisms by which cells align to biomimetic substrates. Each cell type was seeded at 21,000 cells/cm^2 for 3 and 5 days. Cellular alignment was assessed by determining the distribution of nuclear alignment and (for neurons) by neurite alignment. Angular distributions of all cell types at both time points were significantly non-uniform with mean vectors directed parallel to SC topography, except for SC cultures at 3 days. Clustering of angular distributions was stronger when cells were more confluent, independent of cell type. Fbs showed the strongest alignment and were also the most confluent at analyzed time points. These results suggest that direction of cells by SC biomimetic topography is a complex process that is cell density-dependent and influenced by neighboring cell and neurite alignment.

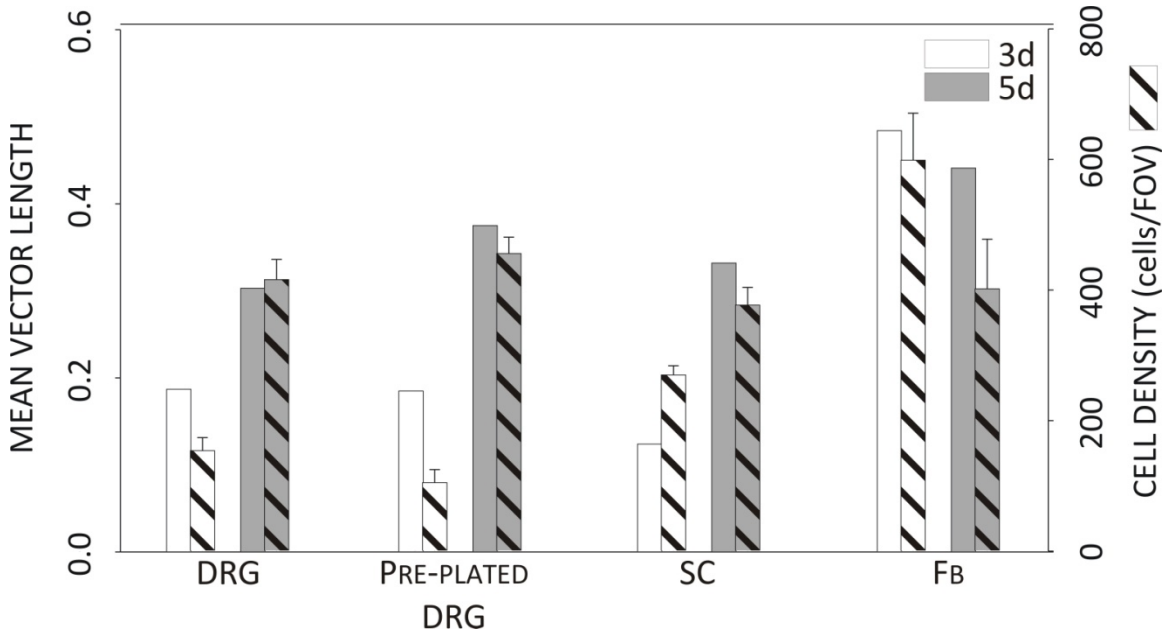

Figure A.1. Cellular alignment was stronger when cells were more confluent, independent of cell types. Graph of mean vector length of nuclear angle distributions (solid bars) and terminal cell density (striped bars) of DRGs, pre-plated DRGs, SCs, or Fbs plated on PDMS substrates for 3 (white bars) or 5 days (grey bars). Mean ± SEM are presented.

Appendix B Guided neurite outgrowth on biomimetic materials presenting adhesive molecules, extracellular matrix molecules, or cell adhesion molecules

Contact guidance of neurons by physical contours of the substrate is well recognized, but less is known about the cellular events of contact sensing and their transduction into directional growth. Microtubules and actin filaments of the cytoskeleton contribute to contact sensing of topographical features. Interactions of neurons with molecules in their local environment may be important for relaying mechano-physical information. Laminin (LN) and neural cell adhesion molecule (NCAM) are known to promote adhesion, migration, and extension. LN is bound by neurons through integrin receptors which are connected through talin, vinculin, and α-actinin to actin filaments of the cytoskeleton. NCAM is also coupled to actin filaments through spectrin. Topographical substrates are often coated with adhesive or growth-promoting molecules, but the role of these molecules in the capacity for neurons to sense and respond to the topographical information presented has not be characterized. Previous work has shown that biomimetic materials presenting Schwann cell (SC) topography enhanced alignment of dorsal root ganglia (DRG) cells when these materials were uniformly coated with LN. We examined the alignment DRGs to these materials when coated with LN, NCAM, and poly-L-lysine (pLL). pLL is adhesive, but the cell surface receptors mediating neurite outgrowth on pLL are not known. Substrates coated with each molecule were plated with 41,000 cells/cm^2 for 1, 3, and 5 days in neurobasal media. Angular distributions of nuclear angles were not significantly different from a uniform distribution on NCAM and pLL coated substrates at day 1. Clustering of nuclear alignment on LN coated surfaces was stronger than on other coatings at each time point with alignment increasing on all coating types over time. There was noticeable aggregation of cells on NCAM coated substrates between day 1 and day 3. These results suggest that

directional growth on materials presenting cellular topography is influenced by the type of coating used on these materials.

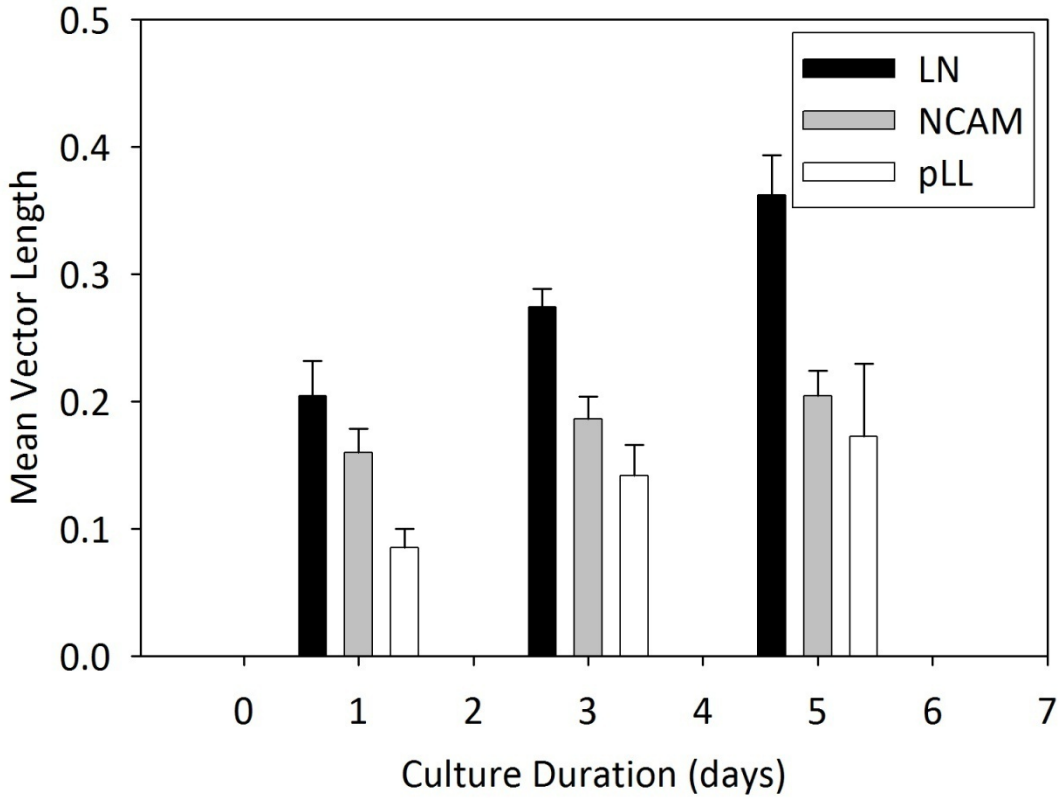

Figure B.1. Alignment was stronger on material coated with LN.
Graph of mean vector length of nuclear angle distributions of DRGs plated on PDMS substrates coated with LN (black bars), NCAM (grey bars), or pLL (white bars) at 200K cells/well for 5 days. Mean ± SEM are presented.

Appendix C Bioinspired topographies for guided neurite outgrowth

Cellular and geometric features have been shown to direct neuronal growth, but the dimensions and shapes of topographical features that encode critical guidance information to navigating neurons have yet to be determined. We used computer aided design and lithography to fabricate PDMS materials with repeating geometries inspired by the features of aligned SCs. Geometric approximations of SC somas with processes consisted of ovals of 14.3 μm length and 5.6 μm width connected by rectangles of 66.2 μm length and 1.6 μm length with 8.7 μm spaces between rows of rectangles. Geometric approximations of SC somas alone consisted of ovals of 14.3 μm length and 5.6 μm width with 5 μm spaces between rows and columns of ovals. Substrates were plated with 41,000 dorsal root ganglia (DRG) cells/cm^2 for 5 days. Angular distributions of nuclear angles of these cells were significantly different from a uniform distribution. Alignment on geometric topographies had a stronger influence on cellular alignment than biomimetic cellular topographies. Nuclear alignment was strongest on geometric approximations of SC somas and processes, and nuclear alignment on geometric approximations of SC somas was not significantly different from alignment on biomimetic SC topography. Fast Fourier transform (FFT) analysis of neurite orientation also suggested strongest alignment on geometric approximations of SC somas and processes. These results begin to deconstruct the features of cellular topography encoding critical guiding information to navigating neurons.

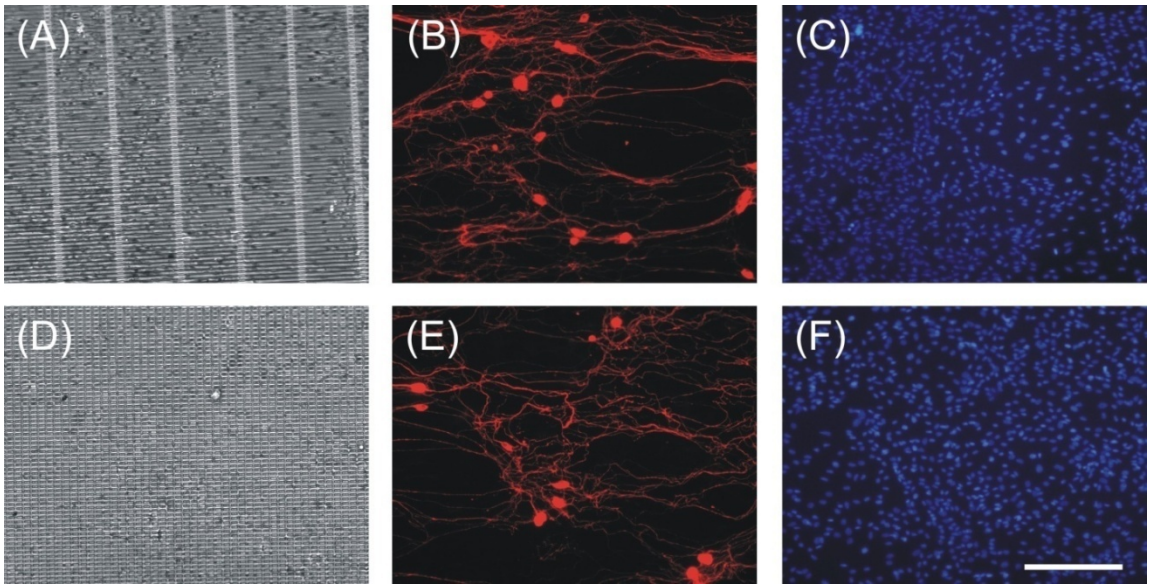

Figure C.1. Neurons, support cells, and neurites aligned strongly to cellular inspired topographies with 90° edges. Corresponding phase (A, D) and epifluorescent images (B, C, E, F) of DRGs cultured on PDMS materials presenting geometric approximations of SC somas and processes (A, B, C) and geometric approximations of SC somas (D, E, F). Neurites were stained with anti-class III beta tubulin (B, E), and nuclei were stained with DAPI (C, F). Scale bar, 200 μm.

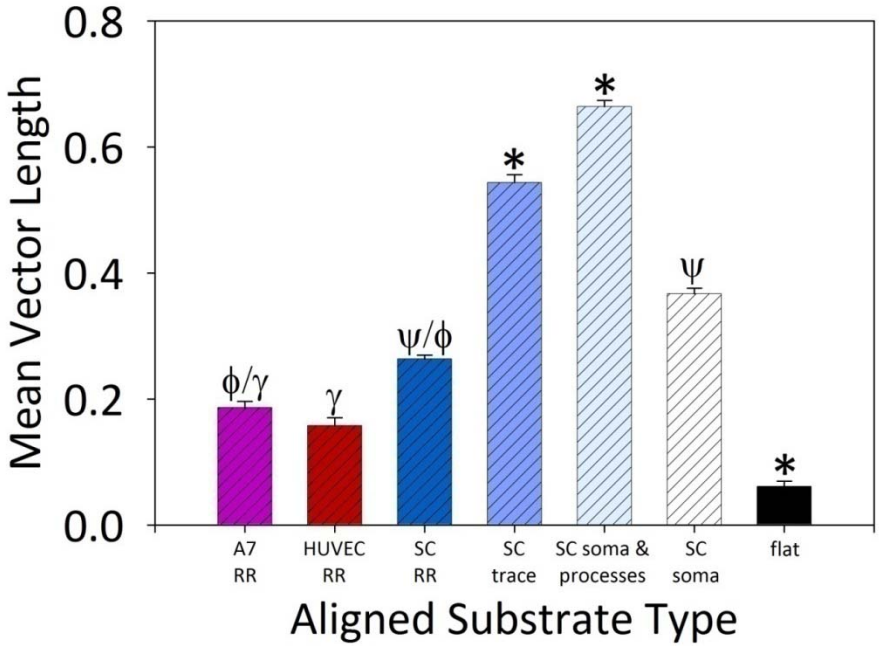

Figure C.2. Cellular alignment was strongest on geometric topographies. Graph of mean vector length of nuclear angle distributions of DRGs plated on PDMS substrates coated with pLL-LN at 41K cells/cm² for 5 days. *, p≤0.05 by ANOVA vs. all other conditions. Ψ, φ, γ; p≤0.05 by ANOVA vs. all other conditions except those with same symbol.

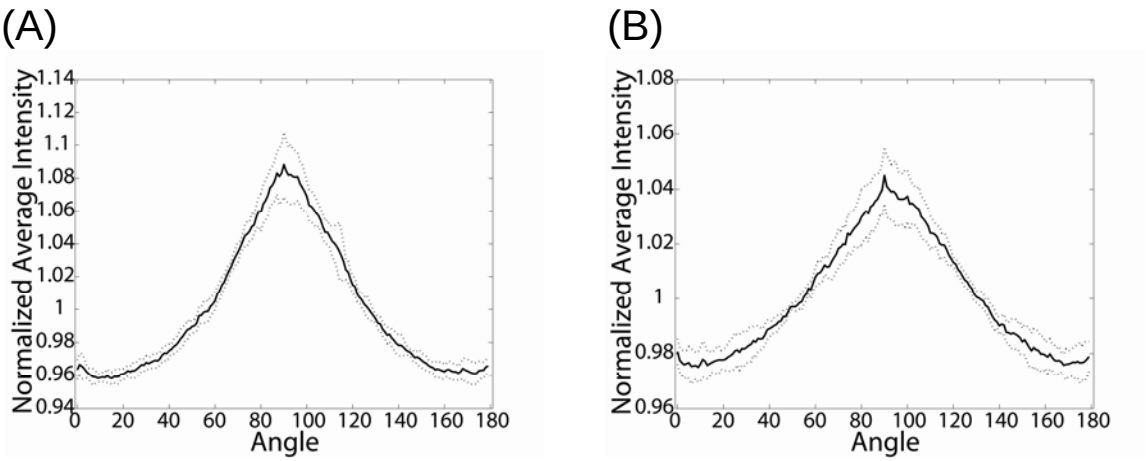

Figure C.3. Alignment of neurites was stronger on geometric approximations of SC somas and processes than on approximations of SC somas.

Graphs of normalized pixel intensities of FFT along radii from 0-179°. Epifluorescent images stained for neurites of DRGs cultured on PDMS substrates presenting geometric approximations of SC somas and processes (A) or SC somas (B) were processed with FFT. Mean, solid line; Plus and minus standard deviation, dotted lines.